Self-Sensing Permanent Magnet Servo Motors

Jack Stephen Bottomley MEng. (Hons)

Thesis submitted to the University of Nottingham
for the degree of Doctor of Philosophy, April, 2014

Abstract

The use of Permanent Magnet Synchronous Machines (PMSMs) has become widespread across numerous applications and industries. Their high power density, efficiency and accuracy of control make them excellent choices, leading them to become the industrial standard. Two issues concerning PMSMs use in recent years have been associated with the elevated cost of rare earth materials required for the Permanent Magnet (PM) rotor poles and the reliance on a direct rotor position sensor such as an encoder.

PMSMs require an accurate rotor position feedback within the control scheme, traditionally provided by an encoder or resolver. These devices are excellent at providing the real-time rotor position accurately but have a negative impact on the machine as a whole. Their use increases the size, weight and cost of the electrical machine, while reducing reliability and often limiting use in extreme environments. This has created motivation for sensorless control of PMSMs, which removes the need for a position sensor.

Sensorless control can be categorized into two distinctive aspects. The first is the control scheme and focuses on how position dependent properties can be used to estimate rotor position. The second, which has had less focus, is the machine design. This is focused on the ability of a machine to act as a position sensor with clear position dependent properties. Self-sensing machine design is the common term applied to this field since in essence the machine acts as its own position sensor.

This thesis is concerned with self-sensing oriented design. The work presented is focused on PMSMs with inset rotor topologies. A methodology was developed to assess the position tracking capability of a machine and incorporated within a traditional machine design optimization routine. The conceptual design of the machine emphasized a generic geometrical topology, accounting for practical material selections and construction techniques. This ensured the design outcome had widespread implications, as opposed to a novel machine design with limited commercial relevance.

Acknowledgements

I would like express my gratitude to my supervisors, Dr. Chris Gerada and Prof. Mark Sumner for all their help, support and guidance over the course of this work.

Thank you to the PEMC group for creating an excellent work environment and offering support whenever needed. Thanks must go to Dr. Jesus Arellano-Padilla and Dr. Michael Galea. And in particular to the friendships of Gary Buckley, James Foster and Nicholas Shattock.

Alex, Dan, Jim and Jo, thank you for the advice and providing a welcome escape over the years. Finally, I would like to thank my family for their continued support over the duration of the project. To my brother and sister for the continuous pestering during my four years. To my parents for keeping me motivated and having complete confidence in me.

Contents

1 Introduction **1**
- 1.1 Permanent Magnet Servo Motors . . . 1
- 1.2 Sensorless Control of PMSMs . . . 1
  - 1.2.1 Motivations . . . 1
  - 1.2.2 Sensorless Control Theory . . . 2
- 1.3 Self-Sensing Machine Properties . . . 4
- 1.4 Saliency Oriented Design . . . 9
- 1.5 Thesis Plan . . . 10

2 Literature Review of Related Research **13**
- 2.1 Introduction . . . 13
- 2.2 Self-Sensing Capability and Control of PM Machines . . . 13
- 2.3 Self-Sensing Oriented Design of PM Machines . . . 15
- 2.4 Genetic Algorithm Optimization of PMSMs . . . 22
  - 2.4.1 Optimization of Machine Design Process . . . 22
  - 2.4.2 Optimization Algorithm Adoption . . . 26
- 2.5 Summary . . . 28

3 FEA for Determining Self-Sensing Properties **29**
- 3.1 Introduction . . . 29
- 3.2 FEA Oriented Design . . . 29
- 3.3 Calculation of PMSMs Incremental Inductances . . . 30
- 3.4 Experimental Measurement of Incremental Inductances . . . 31
  - 3.4.1 Discrepancies with Experimental Results . . . 34
- 3.5 Geometrical and Saturation Saliencies . . . 35
- 3.6 Influence of Stator Dimensions on Self-Sensing Properties . . . 36
  - 3.6.1 Influence of Slot Opening . . . 38
  - 3.6.2 Influence of Tooth Width . . . 42
  - 3.6.3 Influence of Back Iron Thickness . . . 45
- 3.7 Influence Rotor Geometry . . . 50
- 3.8 Influence of Variable Stator Tooth Widths . . . 52
- 3.9 Feasibility of Zigzag Flux of Inducing Reverse Saliency . . . 56
- 3.10 Summary . . . 60

4 Development of Variable Machine Topology **63**
- 4.1 Introduction . . . 63
- 4.2 Automated Machine Design . . . 63
- 4.3 Matlab Machine Script . . . 65
  - 4.3.1 Stator Design . . . 66
  - 4.3.2 Rotor Design . . . 68
  - 4.3.3 Material Selection . . . 70

4.3.4 Slot/Pole Combinations for Optimization 71
4.3.5 Phase Windings 72
4.4 Equivalent Thermal Model 74
4.5 Design Constraints and Requirements 79
4.6 Machine Scripting Flow Diagram 79
4.7 Summary 80

5 Development of Optimization Design Process 81
5.1 Introduction 81
5.2 GA Optimization 81
5.2.1 GA Optimization Process 81
5.2.2 Selection of GA Operation Parameters 83
5.2.3 Single vs Multi-Stage Optimization 84
5.2.4 Single vs Multi-Objective Optimization 85
5.3 Selection of GA Design Parameters 85
5.3.1 Optimization Objectives 86
5.4 Two Stage, Single-Objective Optimization Routine 88
5.4.1 Stage One 88
5.4.2 Stage Two 95
5.5 Single Stage, Multi-Objective Optimization Routine 97
5.6 Optimization Design Routine Flow Diagram 100
5.7 Summary 101

6 Optimization Results 103
6.1 Introduction 103
6.2 Machine Design Specifications 103
6.3 Two Stage, Single-Objective GA Optimization Results 105
6.3.1 9s8p Optimization 105
6.3.2 12s10p Optimization 109
6.3.3 18s16p Optimization 112
6.3.4 18s20p Optimization 115
6.3.5 24s20p Optimization 118
6.4 Feasibility & Trend Analysis of Optimum Topologies 121
6.4.1 18s20p Inverse Saliency Machine 127
6.4.2 24s20p Traditional Saliency Machine 130
6.5 Single Stage, Multi-Objective Genetic Algorithm Results 133
6.5.1 MGA Routine with Eight Design Variables 134
6.5.2 Penalty Function Approach 137
6.5.3 MGA Routine with Seven Design Variables 144
6.5.4 MGA Routine with Six Design Variables 147
6.6 Trend Analysis 150
6.7 Summary 152

7 Case Study of Existing PMSM 157
7.1 24s16p Traction Machine 157
7.2 Performance Analysis of Traction Machine 159
7.3 Self-Sensing Optimization of Traction Machine 162

7.4 24s20p & 48s16p Machine Alternatives 165
7.5 Summary 167

8 Conclusion **169**
8.1 Limitations and further development 171

Bibliography **173**

Acronyms **181**

Glossary **183**

List of Figures **185**

List of Tables **189**

Appendix A Matlab Scripts **191**
A.1 Single-Objective GA Master Script 191
A.2 Multi-Objective GA Master Script 193
A.3 Single-Objective Fitness Function 194
A.4 Multi-Objective Fitness Function 196
A.5 Machine Script 199
A.6 Machine Subscripts 206
A.6.1 Toothlines 206
A.6.2 MakeStatorComponents 206
A.6.3 ExtractStatorEdges 207
A.6.4 ExtractMagnetEdges 207
A.6.5 MakeWindings 208
A.6.6 CalculateSlotArea 209
A.6.7 SetCircuitLdq 209
A.6.8 ThermalRatedLoad 212

Appendix B Paper Publications **216**
B.1 PEMD, March 2012 216
B.2 WEMDCD, March 2013 222

Chapter 1: Introduction

1.1 Permanent Magnet Servo Motors

The use of PM motors has become the industry standard across servo applications. The use of PMSMs has grown due to their simplistic construction, high efficiency, power density and accuracy of control. The similarity of the stator topology to those of induction machines means the traditional construction methods have been easily transferred. While the variety of rotor topologies allows the various advantages of each to target their desired application. These are grouped into three main types based of the position of the PM poles relative to the rotor surface; surface mount, inset and buried.

Despite the industrial uptake of PMSMs there are still a number of challenges associated with this form of electrical machine. Along with the overall design challenge where traditional compromises between efficiency, size, weight, cost and power take place, there are two particularly relevant issues around today. In recent years the global price of rare earth materials for high quality PMs has risen sharply and this looks unlikely to change. This has caused a direct rise in the manufacturing costs of machines and as such is now even more important to consider during topological design.

The second challenge is the dependence on rotor position feedback. In order to accurately control PMSMs active rotor position feedback is required. This rotor position is provided by an encoder or resolver incorporated during construction. The negative aspects that are associated with the use of encoders and resolvers are discussed in the next section.

1.2 Sensorless Control of PMSMs

1.2.1 Motivations

The past decade has seen a dramatic increase in the use of PMSMs, since these offer advantages in reliability, power density, efficiency, ease of control and torque-to-inertia ratio. In order to provide accurate control of PMSMs the rotor position

is required, and traditionally this is obtained through the use of an encoder or resolver. These provide fast, accurate position sensing. However, their introduction into the machine unit creates several issues. Most notably, these devices add considerable size and cost to the overall machine. Their incorporation often limits a machines use in more extreme environments due to sensitivity to mechanical stress. While in general they cause a reduction in reliability due to the introduction of a additional failure mode. Incorporating a position sensor requires additional hardware, with special electronic condition circuitry often necessary when the motor is distant to the control drive. All of these have provided a large amount of motivation to control PMSMs without the need for a direct position sensor. In order to do this, sensorless control techniques have been developed. The two main approaches to sensorless control use either the fundamental excitation from the machine or High Frequency (HF) injection to track the real-time rotor position.

As discussed above, removing the need for a position sensor is advantageous to reducing machine size, weight and cost. With a transition to sensorless control it is possible to remove the position sensor all together. The use of HF injection techniques also provides further opportunities. A major benefit allows for integrated health monitoring, which could lead to the removal of further machine sensors. Integrating online health monitoring can enable fault detection such as winding faults, PM faults and even mechanical faults, that at present require additional machine sensors. This means the implementation of HF injection sensorless control can contribute to several additional benefits.

1.2.2 Sensorless Control Theory

Fundamental excitation sensorless control uses a feedback estimator to derive the flux and speed vectors of the machine from the Back Electromotive Force (B-EMF). The estimator requires precise knowledge of the machine parameters in order to work effectively which is a disadvantage as these change as a function of temperature and operating conditions. However, using the B-EMF of the machine is a relatively simple process; it involves measuring the B-EMF from the machine supply and comparing it to the machine model to determine its position. The overriding issue with this control scheme is that it fails when the machine is at low or zero speed. At low or zero speed the B-EMF becomes too insignificant to provide adequate feedback. HF injection methods for sensorless control can overcome this issue allowing controllability even at standstill and therefore is a

more desirable control scheme to use. These control schemes take advantage of machine saliencies, caused by saturation and geometrical features [1]. The salient characteristics of a machine in the D-Q reference frame can be load and/or position dependent.

The control scheme superimposes a high frequency signal onto the fundamental of the machine supply, where generally a high frequency voltage signal is used [2, 3]. The fundamental frequency quantities remain unchanged and continue to be used for electromechanical conversion. The HF signals exploit the position dependent saliency characteristics of the machine, imprinting position information of the output motor currents. The resulting signals from the measured motor currents can then be used to extract position information [4]. Currently the two most common forms of high frequency injection are, $\alpha\beta$ injection and d-axis injection.

The two common sensorless control methods mentioned previously are well established and have been for some time. However, industrial take up of these methods has been slow since the control schemes are dependent on individual machine characteristics. The presence of unwanted effects caused by HF injection; such as audible noise, torque noise and additional losses is an issue. Finally, at present there is a strong degradation within these position estimation techniques with increasing load. This is due to the angular offset caused by the armature reaction, possibility of the saliency disappearing all together and the increased impact of distortions caused by secondary saliencies of a non-sinusoidal nature. The various sensorless control schemes available are presented in Figure 1.1, along with their general classification.

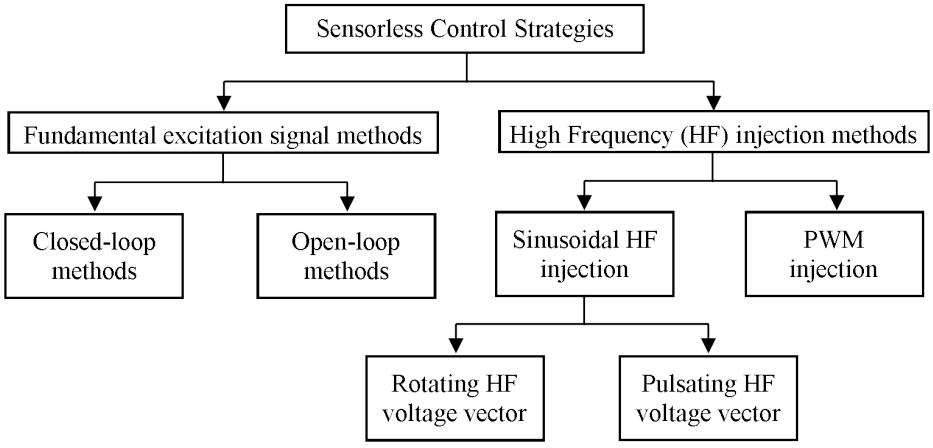

Figure 1.1: Sensorless control strategies and classification

A recent trend has looked at hybrid control schemes that make use of the ad-

vantages of both fundamental excitation and high frequency injection control methods, [5, 6]. These have become increasingly common for obvious reasons, since they can overcome some of the main short comings of each position detection method. They can be particularly useful for certain machines that do not necessarily have good saliency characteristics. The saliency characteristics that determine the HF self-sensing quality of a machine are discussed in the following section.

1.3 Self-Sensing Machine Properties

The use of sensorless control for position estimation relies on the machine to exhibit a variety of HF characteristics. During machine design it is possible to analyse the machine during simulations to determine whether they have good self-sensing characteristics. With self-sensing oriented design the objective is to introduce position dependent saliency or saliencies while still meeting the design specification. With this in mind the various characteristics discussed below can be used to evaluate the sensorless capability of a machine.

The HF injection strategy tracks positional information from the machine incremental inductance on the DQ rotor reference frame. The orientation of the Direct Axis (D-axis) and Quadrature Axis (Q-axis) is illustrated on a 3s2p and 12s10p topology in Figure 1.2.

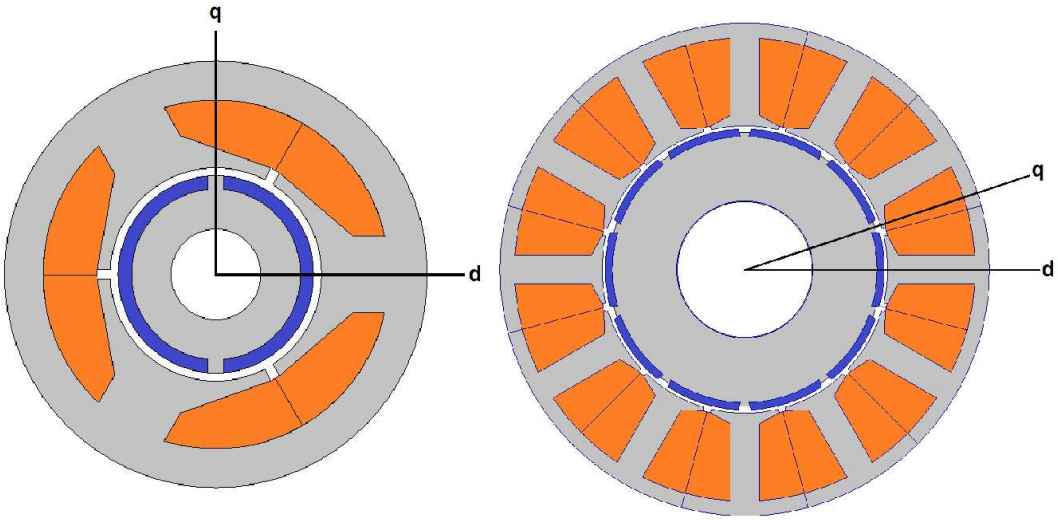

Figure 1.2: DQ-axis reference frame for 3s2p & 12s10p topology

The figure shows the D-axis dissects the centre-point of the rotor pole, meaning

it is aligned with the PM flux linkage phasor ($\bar{\psi}_f$). The Q-axis dissects the inter-pole region 90° (electrical) in advance of D, meaning it is in alignment with the resultant B-EMF phasor ($\bar{E}$).

A machine requires a form of saliency in order to be controlled by high frequency injection. The saliency ratio (ΔL) is determined with the incremental inductances L'_d and L'_q as shown in Equation 1.1. It is a primary design parameter and the level of magnitude improves the Signal-to-Noise Ratio (SNR) of the position tracking signal. A greater saliency ratio improves the accuracy of the position estimation and enables the amplitude of the injection signal to be reduced. The incremental inductances L'_d and L'_q that form the saliency ratio can be calculated as shown in 1.2 and 1.3. These two terms refer to the incremental inductance characteristic of the machine as depicted by the apostrophe, they are not to be confused with the main machine inductance values. The d and q subscript terms are used to identify between the incremental inductance along the D-axis and Q-axis respectively. In general the relative magnitudes is not a concern so long as they are not equal. The level of ripple on the inductance profiles will once again contribute to SNR of tracking signal.

$$\Delta L = \frac{L'_q}{L'_d} \tag{1.1}$$

$$L'_d = \frac{\Delta \Psi_d}{\Delta i_d} \text{ where } \Delta i_q = 0 \tag{1.2}$$

$$L'_q = \frac{\Delta \Psi_q}{\Delta i_q} \text{ where } \Delta i_d = 0 \tag{1.3}$$

In addition to the individual D-axis and Q-axis inductances, each one exhibits an influence on the other. This is referred to as mutual inductance and calculated using 1.4 and 1.5. In the ideal case the mutual inductance is zero, representing a perfect decoupling of the D and Q-axis.

$$L'_{dq} = \frac{\Delta \Psi_d}{\Delta i_q} \text{ where } \Delta i_d = 0 \tag{1.4}$$

$$L'_{qd} = \frac{\Delta \Psi_q}{\Delta i_d} \text{ where } \Delta i_q = 0 \tag{1.5}$$

The two incremental inductances are formed in alignment with their respective D and Q-axis. The magnitude of L'_d and L'_q is dependent on the relative permeability of the materials, such as air or silicon steel. This causes the position dependent characteristic as during rotation the inductance paths will be changing. It means that there is an inherent difference between L'_d and L'_q since the former dissects the

PM pole and the latter the inter-pole lamination. The PM material has a relative permeability close to air and therefore with surface mounted rotor topologies the inherent variation between L'_d and L'_q is removed.

The variation in incremental inductance with rotor position is shown in Figure 1.3. The ripple on each of the D and Q-axis profiles has a fixed period. This is equal to a sixth of the electrical period in a three-phase machine.

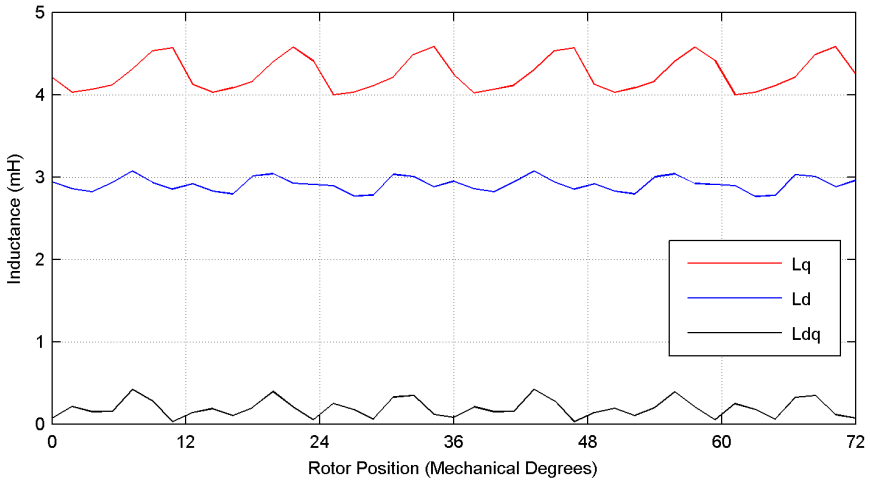

Figure 1.3: Incremental inductance variation with Rotor Position

The source of this ripple frequency is the 6^{th} order space harmonic within the machine that occurs during the transformation to the D-Q reference frame[7]. The data presented shows the variation over 72° which, for the 12s10p example used, is a complete electrical period. The level of ripple is load dependent and determined more by armature reaction than saturation. The level of incremental inductance ripple becomes particularly significant when $\bar{L}'_d$ and $barL'_q$ become close, as the ripple can cause crossover points at certain rotor positions at a fixed loading.

The main HF tracking saliencies of the machine are position dependent as illustrated in Figure 1.3. As well as this they are load dependent, as illustrated in Figure 1.4. The load dependency creates various issues that must be accounted for during design and control. There is a load dependent angular offset that can be seen on the mutual inductance, it is caused by the increasing armature reaction under load. This forces the minimum inductance axis away from the D-axis, causing the estimated DQ reference frame to shift further away from the actual DQ reference frame. This is traditionally accounted for using compensation within the control scheme, with a look-up table developed on the machine

model. The main cause of the angular offset is cross saturation between the D-axis and Q-axis inductance; this is referred to as the mutual inductance where each localized inductance impacts on the other. With increased load the extent of this impact is magnified as demonstrated by the positive gradient of L'_{dq} in Figure 1.4.

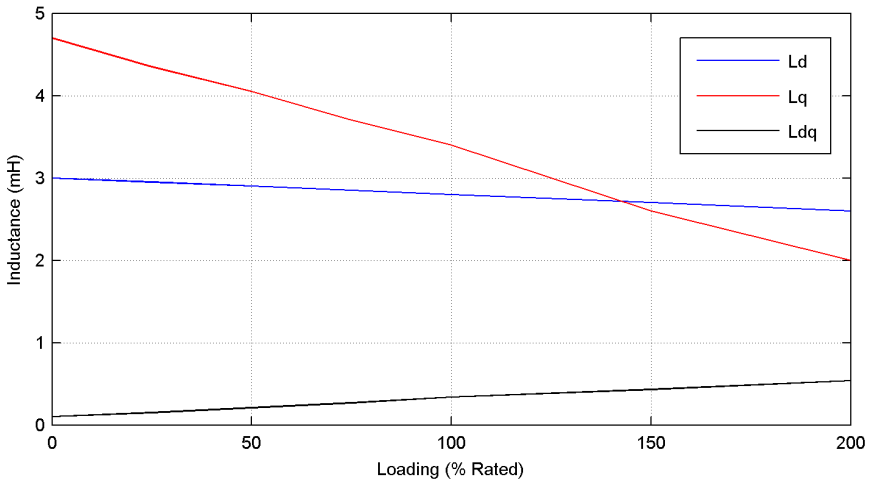

Figure 1.4: Incremental inductance variation with load

The detected angle position moves away from the actual rotor position with increasing Q-axis current [8]. As the stator current increases so too does the main flux and leakage flux level. The increase leakage flux causes the most saturated stator regions to shift. The level of displacement is proportional to the divergence between estimated and actual rotor position. The saliency shift can be demonstrated by Equation 1.6, [7]. The phase shift ψ represents the difference between the actual rotor position and detected rotor position under sensorless control. The L'_{dq} component in the phase shift means that as mutual inductance rises due to the increase in cross-coupling with load so too does the difference angle between actual and detected rotor position.

$$\psi = \frac{1}{2} tan^{-1} \left(\frac{2L'_{dq}(L'_d + L'_q)}{L'^2_d - L'^2_q} \right) \tag{1.6}$$

The loading profiles of L'_d and L'_q are important factors in terms of self-sensing capability. L'_d tends to have a flat profile with very little variation in magnitude due to load. In contrast, L'_q saturates with load and in many cases significantly. This large drop in the magnitude of L'_q introduces a negative characteristic for position tracking. If L'_q saturates enough it will be equal to L'_d, at this loading point the machine has no HF saliency. This zero saliency condition is often re-

ferred to as the saliency crossover point as beyond it the machine has an inverse saliency where $L'_q < L'_d$. The main concern with a zero saliency condition is the inability to estimate rotor position. Since the Q-axis incremental inductance has to saturate enough before this occurs the issue tends to present itself at high loads. In Figure 1.4 a zero saliency condition occurs at approximately 140% load.

This might not be the case if the machine does not have a naturally high level of saliency, such as with Surface Mount Permanent Magnet Synchronous Machines (SPMSMs). Due to a relatively low level of saliency at no load the saliency crossover point can occur at only moderate levels of loading. With sensorless control so long as the crossover point is outside of the operational envelope it will not pose a problem and when rotating above low speed B-EMF tracking methods can be used. It is during start up and overload conditions that the zero saliency condition will generate the most issues, due to the level of loading required.

The two forms of saliency that contribute to self-sensing characteristics are geometrical and saturation. Geometrical saliencies are characterized by physical features within the machine topology that directly impact on the direct and quadrature-axis. Since the DQ-axis orientation is fixed with respect to the rotor geometry it is within the rotor that these geometrical saliencies occur. This simplest form is the PM location. In a surface-mount rotor the D and Q-axis inductance paths are identical since the PM material has a relative permeability close to that of air. This means the airgap observed across the Q-axis and the effective airgap seen across the D-axis are the same. In contrast, inset and interior PM rotor topologies introduce a geometrical rotor saliency. With these rotor configurations the Q-axis passes through a greater amount of rotor back iron, while the D-axis passes through the PM. The relative permeability of these materials are vastly different which will impact the reluctance path. Since $Reluctance = \frac{1}{Inductance}$ this directly affects the D and Q-axis inductances. Additional rotor features can create geometrical saliencies such as air bridges around buried magnets and bore holes for reducing inertia. It is also feasible that with this in mind geometrical features could be introduced to the rotor to create a geometrical saliency. This could be achieved through strategic placement of air bridges and bore holes.

Saturation saliencies are caused by the the relative permeability of the soft magnetic material used for the stator and rotor back iron, with changes in flux density the main contributor. Saturation saliencies by contrast to geometrical saliencies are generally focused in the stator, particularly in fractional-slot SPMSMs. Stator slot leakage causes localized saturation during operation and creates a significant

saturation saliency within the machine. Under increasing load the amount of stator slot leakage increases, and therefore so does the amount of saturation. With fractional slot SPMSMs this is the dominant tracking saliency and caused the load dependent variation [9].

1.4 Saliency Oriented Design

Traditional electrical machine design uses electromagnetic design aimed at meeting and/or exceeding a set of performance requirements. These are focused around standard performance characteristics and tailored towards the ultimate use of the machine. Various operational aspects impact of these characteristics, as well as economic and logistical factors. The machine specifications could be based on torque performance, such as rated torque production or level of torque ripple. Alternatively they could involve overall restraints based on size, weight or cost. The intended operational environment for the machine will influence material selections, power density and efficiency requirements. Finally, within commercial industry the manufacturing techniques needed to mass produce a machine will often limit the structural options available during the initial design stages.

When considering a machine design that will be used under sensorless control there are additional design aspects which must be taken into account. In broad terms, with self-sensing machine design the saliency characteristics are targeted from the initial design stages. The aim of self-sensing design is to design a machine which acts as a position sensor itself. In an ideal case the machine would have a high level of saliency, this would exhibit a solid SNR and allow the injected signal to have a lower amplitude. In addition to this there would be minimal angular offset with load and a low level of cross saturation. The main challenges associated with self-sensing machine design are the variable nature of the machine saliency ratio with load and position. The load dependent characteristics which cause variation of saliency shape and position, and the cross saturation angular offset pose additional challenges.

The aim of this project is to incorporate self-sensing characteristics into a design optimization routine. This means the self-sensing capability will be taken into account during the initial design stages. The targeted design will be carried out while maintaining a strong focus on the fundamental performance of the machine and using established manufacturing techniques. This is a new approach to removing the need for direct position detection. The large majority of work

to this point has focused on either the sensorless control strategies or creating novel machine topologies. Although these novel topologies demonstrate excellent self-sensing capability they have limited industrial take up due to the complexity of design [10, 11].

1.5 Thesis Plan

Chapter 2 discusses the existing research findings relating to sensorless control of PMSMs. These findings are focused on three main aspects of the field. Firstly, machine analysis to determine sensorless capability and its association with the control schemes. Secondly, self-sensing oriented machine design, where the authors have targeted improving the machines ability to act as a position sensor. Lastly, the common approaches to numerical optimization of PMSMs is examined.

Chapter 3 presents the initial processes that were carried out during the project, beginning with analysis techniques to determine saliency characteristics. The preliminary work into the manipulation of machine topology to influence saliency characteristics is then discussed.

Chapter 4 outlines the machine topology designed for the project that is used for the optimization routine. During the chapter the full topological design is presented along with the reasoned decisions that formed it. The impact of various decisions made regarding material and configurations is examined in terms of performance, cost and practicality.

Chapter 5 contains the development of the Genetic Algorithm (GA) optimization routines used during the project. The various options available for the optimization routine are analysed. In each case the preliminary testing with the optimization parameters is presented and their relative impact.

Chapter 6 is the optimization results chapter. It reviews and analyses all of the optimization routines that were performed during the project. Each of the results is evaluated in terms of effectiveness of optimization and feasibility of result. The geometrical trends that determine self-sensing characteristics are then concluded.

Chapter 7 uses the project findings and implements them on a case study of an existing commercial PMSM. The existing topology is analysed first and the

performance characteristics are examined. The chapter then presents the optimization results for targeting enhancement of sensorless capability.

Chapter 8 is the final chapter of the thesis and concludes the findings from the duration of the project.

Chapter 2: Literature Review of Related Research

2.1 Introduction

The following chapter examines the existing research in the relevant subject fields of this project. This is centred around three main areas. The first section is on self-sensing capability, reviewing the analysis and concepts used to determine the effectiveness of sensorless position detection techniques. In the next section self-sensing oriented machine design will be presented, with the emphasis on PMSM topologies. The final section examines publications associated with optimized machine design, particularly the use of GA optimization techniques on PMSMs.

2.2 Self-Sensing Capability and Control of PM Machines

There has been a vast amount of research carried out in developing sensorless control schemes for PM machines, particularly regarding saliency tracking with high frequency injection. Sensorless position estimation techniques such as this are evaluated well in [12] and [13], including hybrid schemes such as [14]. The ability to detect rotor position via sensorless control is not solely dependent on the control scheme adopted or type of injected signal. It is also reliant on the machine topology, with geometrical, magnetic and saturation properties all having an impact. The minimum requirement for HF sensorless control is for the D and Q-axis current vector responses to be different from unity and therefore a saliency condition to exist. With this knowledge, various methods can be adopted in machine analysis to determine self-sensing capability.

In [15, 16] the sensorless capability of fractional-slot inset PMSMs is investigated, under which the saliency and cross-saturation properties are analysed. The results from the saliency analysis are used to demonstrate the sensorless capability of the machine. The findings show a sufficiently high saliency ratio across a large loading range and a particularly strong ratio along the Maximum Torque Per Ampere (MTPA) trajectory. This refers to the current anglle required to produce the maximum amount of torque production for a given supply current. Figure 2.1 shows the results with the blue dotted line indicating the operating current angle

required for MTPA. From this, it is clear the machine exhibits good sensorless properties. Zero saliency ($L'_{dq} = 0$) conditions are discovered for the machine where the HF control scheme would fail, however they occur towards the extremes of loadings tested (Figure 2.1) and well away from the MTPA trajectory for which the machine is operated under.

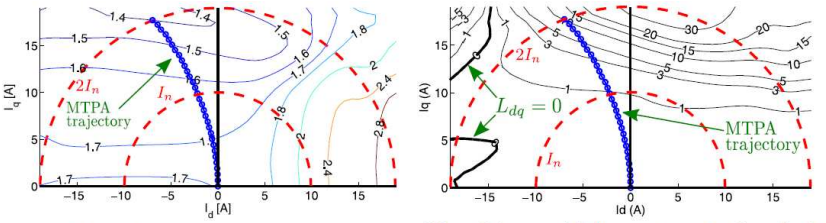

Map of the magnetic saliency ξ_{HF}. Map of the error $|\epsilon|$ due to cross–coupling (deg).

Figure 2.1: Saliency Analysis Results for [15]

Similar analysis has been used to review the sensorless capability of PMSMs in [13, 17, 18].

Although the use of a saliency ratio between incremental inductances is the most common form of HF sensorless control, work has been carried out on exploiting resistance-based saliencies. The benefits of both forms of saliency tracking are explored by the authors in [19]. Resistive losses that are rotor position dependent are tracked. Eddy current losses in SPMSMs are shown to be particularly clear for sensorless control, which could be advantageous since many SPMSMs do not have naturally high saliency ratios for tracking. Primarily due to the same effective airgap along both the D and Q-axis flux paths. Since the PMs have a low permeability and are regarded as air in inductance calculations. High frequency resistance characteristics for sensorless position detection are discussed further in [20, 21]. They offer an alternative to the well established inductance-based schemes, although with very similar short comings. The focus of this project is on self-sensing oriented design of PMSMs, rather than self-sensing control. The shortcomings of traditional sensorless control techniques on current PMSMs enables targeted design to take place. The design processes used later in this work are focused on using inductance based HF injection methods, since they are well developed and have demonstrated accurate position control.

In [8] the author is concerned with the impact of cross-saturation on sensorless control. The work investigates the cross-saturation occurring in a SPMSM, affecting the magnetic axis shift under load and the influence of the operating point on the saliency. It is a well know condition that with increasing q-axis loading

the position error increases as the position estimation diverges further from the actual rotor position. Traditionally this is overcome with compensation in the control scheme, involving a characteristic curve for the machine. When concerned with inductive-based position estimation it has been shown that the primary requirement is a form of HF saliency. In theory this can be very small but a larger saliency ratio simplifies control and improves accuracy.

2.3 Self-Sensing Oriented Design of PM Machines

Electrical machine design is always performed with a set of design specifications in place that are there to be met. This is no different to self-sensing oriented design. The additional focus of generating good saliency characteristics should not detract from the fact the machine needs sufficient fundamental performance. If a machine design is lacking this fundamental performance it is irrelevant how accurately it can be controlled. This concept of designing electrical machines while accounting for sensorless control has been has been explored more frequently in recent years.

In [19] the authors investigate the use of both inductance and resistance based tracking algorithms for low speed position detection of a SPMSM. Although the inductance based method shows clear advantages, the authors also state how this method can often fail when used with surface mounted rotors. To overcome this an improved rotor design is suggested but not investigated further within the paper. The design consideration involves utilizing the holes which have been punched into the rotor to reduce the inertia. Systematically relocating this holes could allow for them to reduce inertia while increasing saliency at the same time.

The authors in [22] analysed the advantages of using an inset PM rotor topology for zero-speed sensorless position detection, compared to a standard Interior Permanent Magnet (IPM) rotor topology, as shown in 2.2. One of the main advantages discussed within the paper is that the larger back iron path in the rotor means saturation occurs at higher current. The two rotors are compared using a high frequency voltage injection technique with identical stators; both Finite Element Analysis (FEA) and experimental results demonstrate the inset rotor performs better, especially at high load. Further work was carried out by the authors in [23], where once again the inset motor is shown to perform well against the IPM motor. Following this the reliability of FEA for assessing saliency characteristics is confirmed through a good match with experimental results.

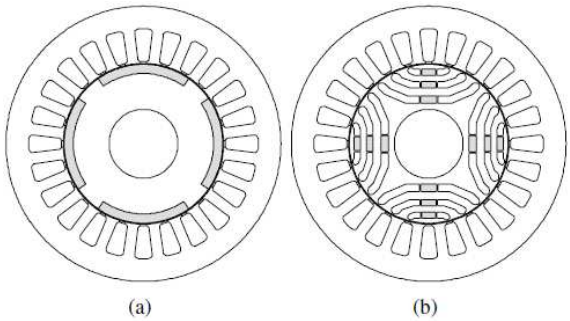

Figure 2.2: PM motors with (a) inset rotor and (b) IPM rotor [22]

A large amount of research has been carried out focusing on the influence of stator dimensions, particularly those associated with the slot opening. In [24], once again a selection of rotor topologies are used during their investigation; embedded PM, surface mounted PM and buried (spoke) PM structures. These are all analysed from a zero-speed sensorless position detection point of view, with the impact of changes to stator slot shape being analysed. Two parameters within the stator slot were investigated, slot opening (s_i) and tooth tip thickness (t_i), these are illustrated in Figure 2.3,. The effect of systematically reducing both parameters to half the initial size is analysed. The results indicate that the slot shape impacts the sensorless characteristics of all the test motors, the authors suggest using these parameters to minimize the sensorless position error and therefore reduce the complexity of the control compensation.

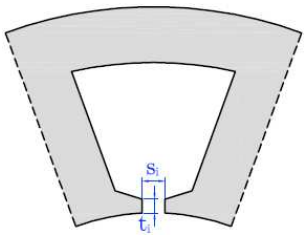

Figure 2.3: Layout of a Single Stator Slot [24]

The influence of stator tooth tip shape is investigated again in [25], using a fixed surface mount PM rotor, with the aim of maximizing the signal-to-noise of position and polarity signals. The work was carried out without compromising the performance of the machine, this type of focus is often not considered with other publications. FEA is used to review a variety of design choices, a 2 Slots/Pole/Phase (Spp) SPMSM, a 1 Spp SPMSM and a 1 Spp SPMSM with stator bridges. In the first stage of their analysis the authors are able to vary

the saliency ratio ($\frac{L'_q}{L'_d}$) in all three of the stator configurations. However as the authors state,

> It is difficult to obtain a large difference in the saliency ratio by changing only the stator structure compared with changing the rotor structure. [25]

Finally some interesting work involves various slot opening options, a 0.5mm bridge, a 0.25 bridge, a normal slot opening and an open slot design. Most notably from this part of the paper, the use and thickness of a slot bridge can play a significant role in improving the sensorless controllability of the machine.

With rotor designs previously proposed in [26] the authors continued work in [27], using a diverse range of Interior Permanent Magnet Synchronous Machine (IPMSM) topologies. The aim was to investigate the effects of fractional pitch and distributed stator windings. A detailed saliency analysis is carried out on all rotor/stator configurations with clear variations occurring between them. The data shown in Figure 2.4 indicates that only some rotor designs suffer from a zero saliency condition, when analysed up to 200% rated load. And with one of these cases the condition is not present with the use of concentrated windings.

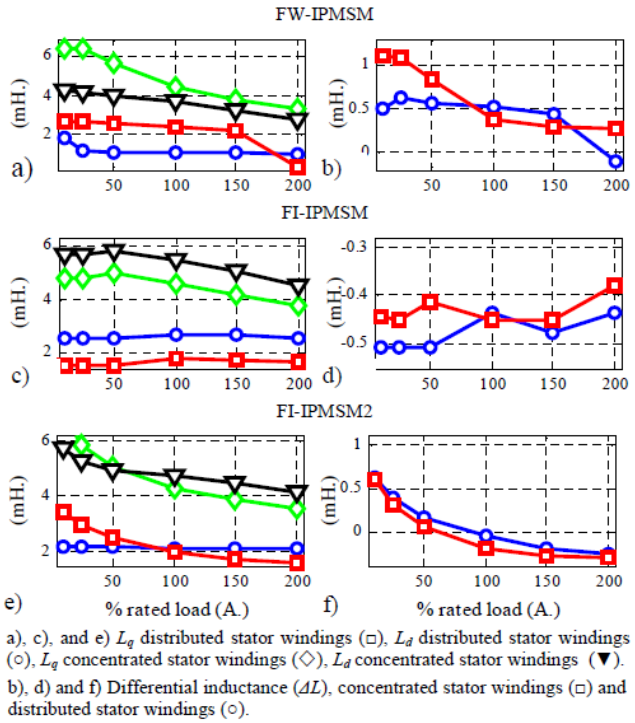

Figure 2.4: L'_{dq} & ΔL vs load current for FW- & FI-IPM designs [27]

In conclusion the paper demonstrated that concentrated windings produced greater

saliency and hence, improved self-sensing capabilities. Although a downside to the use of concentrate windings is higher secondary saliencies, leading to an increased estimated position error.

In a similar way to the above a variety of research has centred on the impact of rotor topology for sensorless position estimation; particularly the influence of changes to a select few parameters. In [28] the impact of PM thickness and width on saliency based position estimation is investigated. The thickness is expressed as a ratio of inner radius of PM to its outer radius, while the width is expressed as a subtended angle relative to the pole pitch. In all, 14 rotor topologies are selected. Figure 2.5 shows that they do not affect the net torque capability, a stated prerequisite of the investigation. Finite elements was used to analyse the saliency ratio for all the design variants, along with the level of cogging torque. This allows simple comparison of topologies before their suitability for zero-speed sensorless position estimation is investigated. For this the authors take advantage of the symmetry of saliency results and therefore only simulate a sixth of the electrical cycle to reduce computational time. The combined results for sensorless control accuracy and torque characteristics then allowed for a suitable topology to be selected.

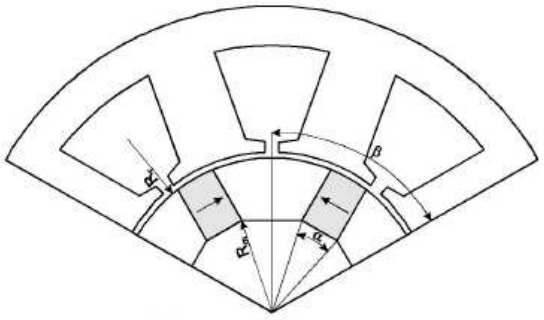

SUMMARY OF ROTOR TOPOLOGIES

Rotor Topology	(α/β)	(R_m/R_r)	χ
1	0.73	0.39	2.35
2	0.73	0.43	2.32
3	0.73	0.51	2.20
4	0.76	0.55	2.08
5	0.80	0.59	1.93
6	0.80	0.59	1.93
7	0.83	0.59	1.79
8	0.83	0.63	1.64
9	0.83	0.63	1.64
10	0.86	0.63	1.50
11	0.90	0.63	1.43
12	0.90	0.66	1.31
13	0.93	0.66	1.23
14	0.93	0.70	1.16

Figure 2.5: PM parameters with 14 suitable selections [28]

An IPMSM is selected to investigate the influence of rotor geometry on the feasibility region for sensorless position estimation in [29] and [30]. The feasibility region is defined as the loading range up to the zero saliency point. The boundary is determined by the loading point where $L'_q = L'_d$, in an ideal case this point occurs above the loading range of a machine. A 9s6p concentrated winding configuration is used with the rotor tooth opening, PM size (expressed in width and length) and the depth they are embedded as geometrical variables. While the stator tooth bridges are bevelled in order to minimize cogging torque. All

of these parameters are expressed graphically in Figure 2.6. The investigation has a clear set of design restrictions and requirements and the parameters are optimized to meet these while successfully increasing the feasibility region.

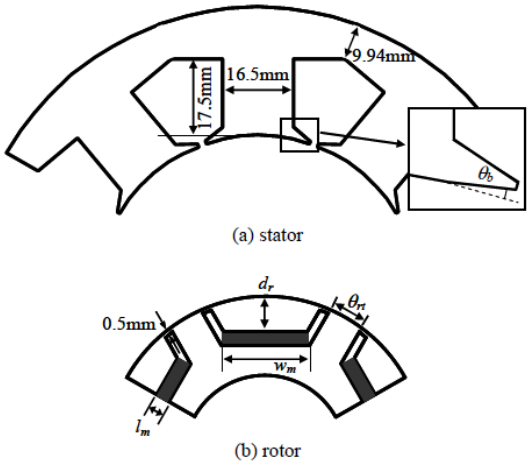

Figure 2.6: Parametrization of test IPM Motor [29]

The authors continue with similar work with concentrated wound IPM motors hybrid electric vehicles in [31]. The design guidelines are once again established to obtain a motor which can maximize torque capability and stability of the sensorless drive. A design sequence is devised where each of the three variable parameters are set prior to the next being investigated.

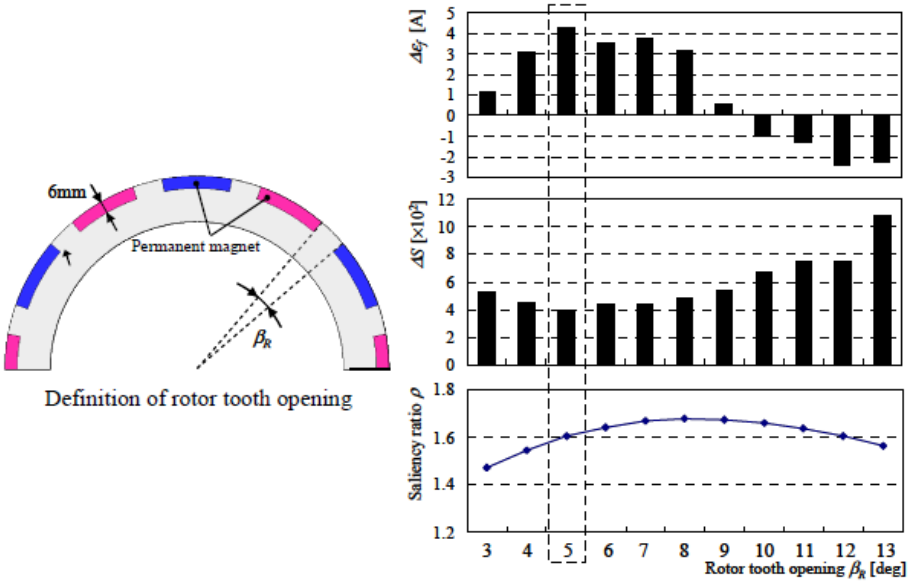

Figure 2.7: Effect of rotor tooth opening on $\Delta\varepsilon_f$ and ΔS [31]

The selection is made using analysis results indicating the effectiveness of sen-

sorless operation ($\Delta\varepsilon_f$ as large as possible) and level of fluctuation in the error signal ε_f (ΔS as small as possible). The analysis results for the first parameter selected, rotor tooth opening, are shown in Figure 2.7. When the parameter is varied all other dimensions are fixed in order for its sole influence to be reflected in the results. The final design process involves optimizing the rotor tooth opening with a fixed magnet length, then optimizing the depth of embedded magnet with a fixed rotor tooth opening and finally the ratio of stator back iron width to tooth width is optimized. The result is IPMSM which exceeds the prerequisite torque requirements and meets its sensorless performance characteristics.

The accuracy of sensorless control is once again investigated with regards to IPMSMs in [32], here changing a rotor topology to include flux barriers. In the paper an improved state-space modelling technique is proposed. The two rotor topologies are designed with geometrical variations focused on reducing position estimation error caused by cross-saturation. The findings indicate that the PM thickness and depth below the rotor surface the PMs are buried are influential factors. In conclusion, the authors determine that cross-saturation is the main cause of position error and therefore a hypothetical machine without cross-saturation would result in almost zero sensorless position error. This statement is a well established notion but as yet has not been achieved where the saturation saliency is dominant.

The review of existing research has shown there is a trend to adapt an existing topology through the optimization of selected parameters. The approach benefits from an existing strong machine design and aims to enhance the saliency characteristics. The compromise between improving sensorless position detection and limiting the impact on fundamental performance is the main design challenge. There is an alternative approach that has been explored in research areas that looks to novel machine design to introduce new position dependent features. The targeted design is aimed at creating HF characteristics that are position dependent and do not deteriorate like the main saturation saliencies. These have demonstrated excellent position tracking properties but due to their novel approaches require additional hardware or construction techniques.

A slight variation to this is shown in the work from the authors in [33]. It introduced an interesting approach to solving a common issue when considering sensorless controllability of permanent magnet machines. The authors proposed designing a machine with inherent reverse saliency, where $L_d > L_q$ across the whole loading range. A machine with this saliency characteristic is of partic-

ular interest in the field of sensorless position estimation. Currently machines with traditional incremental inductance properties, where $L_q > L_d$, suffer from a zero saliency condition or saliency crossover point. This occurs when a machine is operated under increasing load and the Q-axis inductance becomes saturated causing it to decrease. The same effect does not occur with the D-axis inductance and therefore at a certain level of loading the saliency characteristic of the machine will reverse, i.e. when L_d becomes greater than L_q . If operating under sensorless control this crossover point represents a major issue since there will be a loss of controllability. The benefits of a machine with reverse saliency characteristic are that there would be no zero saliency point at higher loads as L_q saturates; in fact under this condition the level of saliency would simply increase.

The papers approach to reverse-saliency design is to use specific slot/pole combinations with double-layer concentrated windings to induce a significant zigzag flux. This term is more common when considering induction machines and is generally referred to as magnet leakage flux in PM machines. The saturation in the tooth bridge occurs when it is aligned with the Q-axis, this therefore adds another reluctance term to the Q-axis equivalent circuit and consequently reduces the Q-axis inductance so that it is lower than the D-axis. The tooth bridge is designed to be relatively thin so that saturation easily occurs; the design used for the magnetic flux plots in Figure 2.8 uses a tooth bridge half the thickness of the airgap. In Figure 2.8b the saturated tooth bridge are indicated by the red shading. Since the saturation occurs in alignment with the Q-axis, L'_q has a lower magnitude due to the increased reluctance. This occurs even at no load, causing $L_d > L_q$ and forming an inverse saliency.

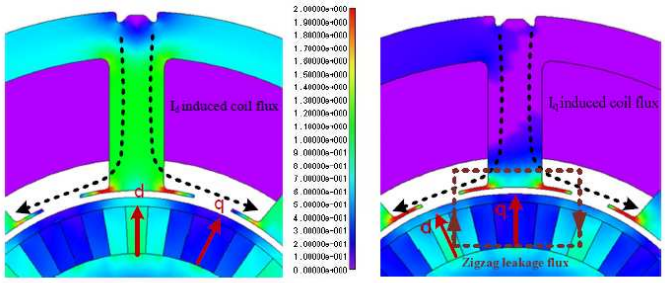

Figure 2.8: FEA magnetic flux density plots from two rotor positions

Investigating the machine parameters that can increase zigzag leakage flux it is shown that reducing the magnet width and having slot/pole combinations with similar values are the most desirable conditions. A suitably thin tooth bridge

is required for sufficient saturation to occur. This tooth bridge feature diverges considerably from a conventional machine design. A thicker tooth bridge is generally used as it contributes to a good fundamental torque, with low distortion This is both in terms of torque per amp and torque per kilogram.

In differing approaches to this, research has looked to venture away from traditional topologies to enhance sensorless capability. The introduction of additional hardware or geometrical features to produce a controllable saliency has been investigated. In [10, 34] the authors apply a copper turn around each rotor pole to investigate modifying the HF D-axis inductance without affecting the Q-axis. The copper turns are implemented onto a 6-pole SPM rotor. The intention of the authors is to create a rotor anisotropy that can be exploited similar to that of an IPM rotor.

The result is successful and produces comparable sensorless performance to an IPM topology. An advantage of this particular rotor design is that the rotor anisotropy introduced is based on the electrical coupling of the rotor rings and stator windings. Therefore the main magnetic saturation becomes less dependent. A significant downside to the machine design is the requirement of thel copper rotor rings that adds additional cost and manufacturing processes.

2.4 Genetic Algorithm Optimization of PMSMs

Numerical optimization techniques have been used extensively in the design of electrical machines. The benefits of systematic numerical algorithms and genetic algorithms have been utilized across a wide variety of optimization problems. When associated with electrical machine design and particularly permanent magnet machines, various approaches to design optimization have been investigated. The overall focus of the optimization routine greatly influences its make up, whether through speed of optimization, accuracy of computerized simulation or complexity of solution.

2.4.1 Optimization of Machine Design Process

A comprehensive investigation into GA optimization of an SPMSM is presented in [35], where the single-objective approach focuses on minimization of PM weight (and effectively motor cost) or maximization of torque. The single objective

approach means the algorithm is optimizing for a single performance indicator, through a solitary objective function. The machine topology is carefully designed in order to reduce the number of geometrical variables; instead certain dimensions are defined using other variables or simple ratio terms. The authors use the example of the external diameter, which is alternatively expressed as a function of three other dimensions (inner diameter, slot height and back iron height). Additionally, a systematic analysis is used to determine the GA crossover and mutation rates, as well at the population size. Some interesting conclusions are drawn by the authors from the investigation. Compared to traditional numerical techniques a GA has the ability to find a global optimum using the whole search space defined by the variable boundaries. Traditional methods often target a local optimum and limit the effectiveness of the process. The greater number of iterations required during a GA routine naturally increases computational time and this is exaggerated when combined with a FEA-based routine, for this reason the authors recommend not using such a comprehensive process within day-to-day design.

Multi-objective optimization techniques have been used for targeted PM machine design, often associated with sensorless control. The approach used by the authors in [36] is to generate an optimal design that improves both the torque production of the machine and HF electro-magnetic saliency; the investigation uses a genetic algorithm to optimize a PM assisted synchronous reluctance machine. The objective functions analyse the torque capability along the MTPA trajectory and the saliency around the nominal working point, using at least two simulations. Both of these are good selections for the objective functions as they provide clear indications of the machine performance and are simple to implement as an objective function. Four design variables are selected for the routine, the three magnet thickness's used in the rotor structure and the coercive force of the PMs. Three cascaded optimizations are performed with the reference for each new routine set as the optimal design from the previous routine. Through the investigation it is shown how the best objective value is achieved within 15 generations, as shown in the left-hand plot in Figure 2.9. The central and right-hand plot show the distribution of the initial population and how by the last (25^{th}) generation the design variables have tended to close values. The paper demonstrates a well structured approach, however has some shortcomings with regards to the result. The optimization leads to an increase in magnet thickness, and therefore volume, particularly across the first barrier which contributes to an increase in the HF saliency. With the rising cost of rare earth materials there

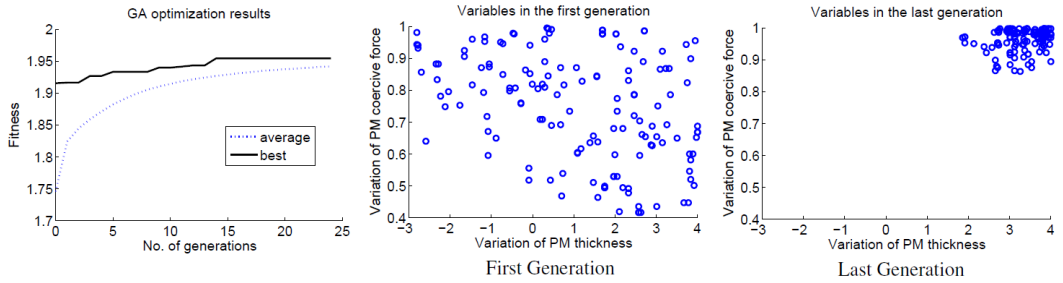

Figure 2.9: Data analysis of first optimization [36]

needs to be some concern regarding the PM volume used within the machine. The use of torque production and level of saliency are sensible selections for objective functions, however, it could be advisable to consider additional properties, such as the amount of torque ripple. HF saliency is calculated at the nominal working point and consequently with a positive ratio at this point there would be not crossover or zero saliency condition. This allows the machine to be sensorlessly controlled up to at least this nominal loading; if operated above this point the zero saliency condition would need to be investigated.

The authors expand on this multi-objective approach further within [37], the same topology is optimized with the definition and number of design variables expanded upon. The investigation focuses on the same two objective functions of torque production and high frequency saliency ratio.

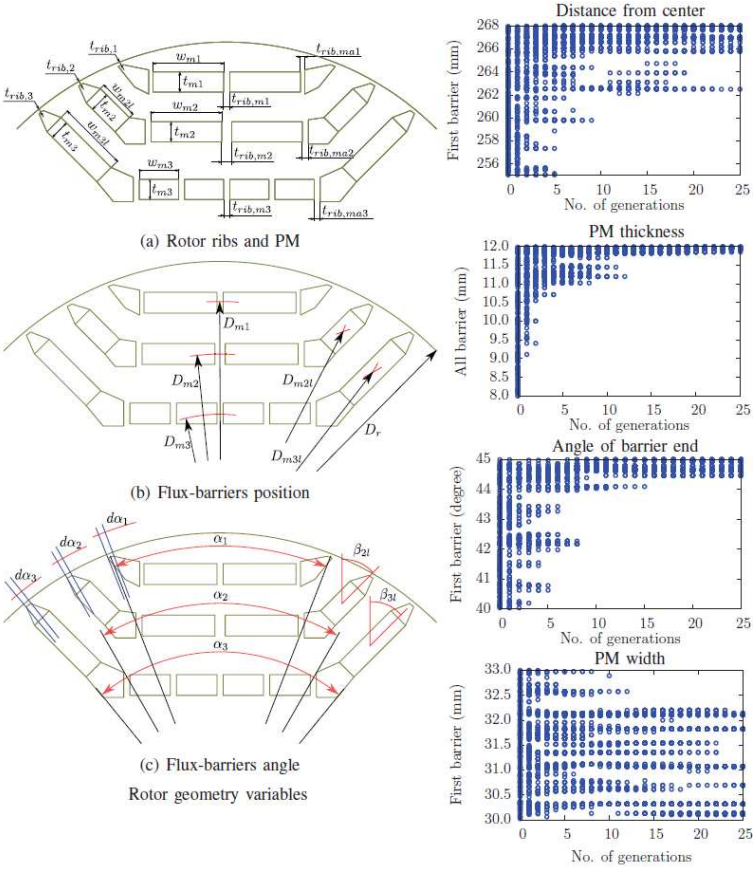

Figure 2.10: Definition of design variables and GA optimization results [37]

The data analysis of the GA results reveals several trends and indicates that certain variables, particularly magnet thickness, have optimal values and therefore through the evolution assume values within a very narrow range. As the authors conclude, this means that these variables have a larger impact on the optimization objective, compared to those which cover a wide range of values in each generation. Figure 2.10 shows the definition of the design variables along with the a selection of the results. The optimization routine is performed with geometrical limits imposed, along with PM demagnetization, and it is found that the two objectives are in opposition. Therefore an optimal design could be considered having met a minimum level of torque or saliency while the remaining objective is maximized. An important note regarding the two stages of the investigations in these papers is that the electromagnetic analysis carried out during the algorithm is performed using Finite Elements (FE).

FEA is again combined with a multi-objective optimization in [38], where the paper focuses on the rotor design due to the IPM structure. As discussed in section 1.3 with interior PMs there is a strong geometrical saliency. Three approaches

are presented to target the three possible objective functions; maximum torque, minimum torque ripple, maximum flux weakening capability. The rotor geometry is optimized with PM angle and height set as parameters, along with PM quality and finally the current phase angle. The findings from a fast 2-objective optimization, a hybrid 2-objective optimization and a 3-objective refinement are examined for their effectiveness and computational time. The authors conclude that acceptable designs can be achieved using a relatively fast 2-objective approach, furthermore manual manipulation of the PM quality can then be used to improve the third objective (constant power speed range). The 3-objective optimization generates higher quality results, but with greatly increased computational time and therefore this must be a consideration.

The work carried out is continued further in [39], with the addition of rotor harmonic losses as an objective function. A comparison is used for two 2-objective and two 3-objective optimizations, with emphasis on the quality of result and computational time. All of the optimal designs demonstrate a similar level of performance, even when rotor losses are not used as an objective function the minimization of torque ripple has a contributing effect of keeping them in control. This shows how careful selection of objective functions can help improve additional machine properties without directly targeting them in the optimization process. The increase in computational time caused by a 3-objective optimization compared to a 2-objective approach is once again significant, in this case the duration increased from 25 hours to 110-130 hours. The direct impact certain design variables have on objective values could be utilized by removing the variable and/or objective, then alternatively manually selecting a value after the optimization to improve upon the optimal design further.

2.4.2 Optimization Algorithm Adoption

There is a large number of numerical optimization techniques readily accessible that can be used to integrate into a machine design process. Optimal search algorithms are categorized by either deterministic methods or stochastic methods. Deterministic methods optimize the solution through systemic algorithms without randomness. The process will always produce the same output by taking advantage of the analytical characteristic of the optimization problem. While they converge to a global optimum solution they are intensive and restrictive [40]. This means they are not often selected for machine design problems. Stochastic methods by contrast explore a search space randomly, this makes them more

efficient and flexible. However, due to the random nature of the algorithm the quality of the final solution cannot be guaranteed.

The use of stochastic (random) methods often require more evaluations but due to their random nature they do not get drawn towards local optimums [41]. Four conventional stochastic optimization methods are discussed below.

- Genetic Algorithms, these are based on replicating natural selection and genetics of biological evolution. They are advantageous in multi-objective problems as variables and objective do not need to be weighted. They are are common choice for electrical machine optimization, [42, 35, 43]
- Particle Swarm Optimization, this method is behaves in a similar way to a swarm of bees searching for the largest concentration of flowers in a space. They perform well in hybrid design models like [44].
- Simulated Annealing, emulates a physical annealing process where an object is heated, freeing the atoms from local minima and during cooling they configure into global minima. The method performs strongly at finding the global optimum but is not efficient when applied to large search spaces [41].
- Differential Evolution, aids the improvement of the next generation by applied scaled differences to the current generation. The method is relatively new to machine design optimization but has been effectively demonstrated in [45].

The use of genetic algorithms is a popular choice when facing a machine design optimization. They are flexible in their implementation, with the choice of single or multiple objective functions. They have been used in numerous ways, with a multilevel process demonstrated in [46] and multi-objective in [47]. Due to the multi-objective nature of the design problem faced in this project, a genetic algorithm optimization method is a suitable choice. The aim is to enhance self-sensing characteristic while ensuring good fundamental performance. These two objectives can be implemented into objective functions in a number of ways. They may not be complementary to each other during design and therefore a single global optimum may not be possible and instead design trade-off's would have to be considered.

2.5 Summary

This chapter has reviewed existing research into sensorless control of PMSMs. The main areas examined were analysing sensorless capability, targeted design and optimization. Through the chapter it is clear that there has not been an approach developed to guarantee good machine design and sensorless capability. Instead what has been demonstrated is that through a design procedure the saliency characteristics of a machine used for HF position tracking can be enhanced, while this often requires compromises. The overall challenge when designing a commercially viable machine is acquiring these saliency characteristics with minimal impact on fundamental performance.

The zero saliency condition, where $L'_d = L'_q$, has repeatedly been raised during previous research as a major cause of concern. The common approach is to ensure that any zero saliency points are located outside the operational envelope. When this is not the case, design iterations are used to shift the zero saliency location. With the continued development of hybrid control schemes this will go some way to overcoming this issue. However, zero saliency conditions tend to occur at high loadings which are often used at start-up or for high torque output. Therefore under these circumstances it can be assumed that HF injection would still be used and not alter the outcome. With this in mind, the best approaches involve manipulation of geometrical parameters to shift the zero saliency point outside the operational envelope. Alternatively, a design approach, as suggested in [33], which fundamentally removes the possibility of a zero saliency condition could be used.

Chapter 3: FEA for Determining Self-Sensing Properties

3.1 Introduction

This chapter firstly introduces the use of FEA for electrical machine design and demonstrates how it can be used to calculate incremental inductances. These are essential for determining HF saliency characteristics. The remainder of this chapter will then present a background into the impact that various geometrical parameters, in SPMSMs, have on both fundamental and saliency properties. These investigations provide an insight into the ability to target machine design to enhance sensorless capability. Throughout, there is reference to the fundamental machine performance, since this is the most significant consideration for the selection of a machine design.

3.2 FEA Oriented Design

FEA uses a computer based model to analysis a material or design under a particular stress to determine specific test results. The process is commonly used in electromagnetic machine design and optimization as it enables the user to verify proposed designs [48]. This reduces the amount of prototype stages required and allows targeted design for machine specifications prior to physical production. In addition to using FEA for fundamental machine design, it can be utilized to analyse machine losses, thermal properties and HF characteristics [49]. With particular reference to the latter, FEA can be used to calculate machine saliency properties and therefore determine sensorless capability during overall machine design.

Throughout this project Infolytica's MagNet [50] is used as the main FEA software, enabling the use of static and transient analysis in both 2D and 3D. Due to its scripting capabilities and data processing tool Matlab is also utilized throughout in conjunction with MagNet. Using the Visual Basic (VB) commands for MagNet and scripting them using Matlab protocols it is possible to send and receive commands and data between MagNet and Matlab. This link allows for

repetitive simulations to be automated and machine model construction to be performed easily. As well as this, the link enables the direct use of Matlab's optimization tools, which are used for machine design during the project.

3.3 Calculation of PMSMs Incremental Inductances

The saliency characteristics of a machine and ultimately self-sensing properties can be analysed using incremental inductances. Determining these incremental inductances, particularly with regards to their variation with load and position is very important. The ability to calculate them using FEA, allows saliency characteristics to be analysed faster and during the design process. As opposed to using lab based experimental results on prototypes. In order to calculate the incremental inductances in the FE environment, a simulation technique was developed. This involved a multi-simulation approach, in this case using Infolytica's MagNet (a FE software environment). With the test machine in place, the windings are connected with a supply circuit as shown in Figure 3.1.

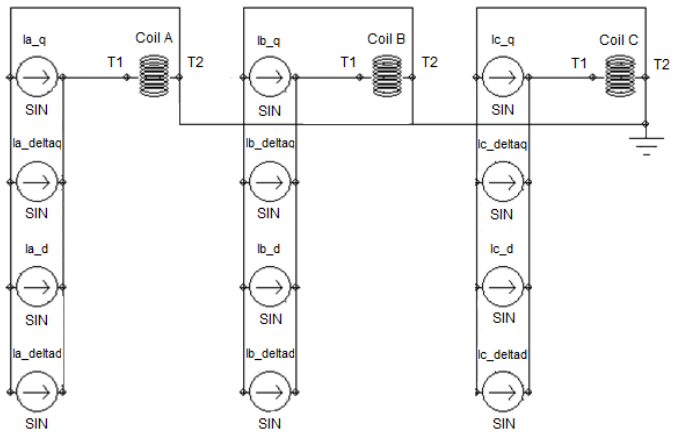

Figure 3.1: Supply circuit diagram for FE inductance measurement

This configuration allows the machine to be operated using D-axis and/or Q-axis current. The current sources are divided into D and Q-axis alignments with their respective 90° phase shift. An initial simulation is used to align the sinusoidal phase shift for three phase windings with the fundamental of the B-EMF. This ensures the correct alignment for the Q-axis and the main machine torque component. All of the Q-axis sources are set to this phase shift with the B and C windings set at their 120° electrical displacements. Finally, each of the D-axis sources are set to lag their corresponding Q-axis sources by 90°. The multiple

sources are used to simplify the process so adjustments can easily be made to the configuration.

The first simulation is carried out under normal conditions, with the desired test loading set in the main Q-axis sources. The two subsequent simulations are performed with an additional current increment applied to the delta D-axis or Q-axis sources each in turn. The current increment must be relatively small in order to obtain an accurate measurement. During post processing the flux linkage results for each phase are transformed into their D-axis and Q-axis components using traditional transformations. The incremental inductances are then calculated with the following equations.

$$L'_d = \frac{\Psi_{d\_d} - \Psi_{d\_n}}{i_i} \tag{3.1}$$

$$L'_q = \frac{\Psi_{q\_q} - \Psi_{q\_n}}{i_i} \tag{3.2}$$

$$L'_{qd} = \frac{\Psi_{q\_d} - \Psi_{q\_n}}{i_i} = L'_{dq} = \frac{\Psi_{d\_q} - \Psi_{d\_n}}{i_i} \tag{3.3}$$

Here the Ψ_{d_d} in 3.1 indicates that it is the D-axis flux from the simulation with an incremental current applied on the D-axis. As can be seen the calculation involves resulting the change in D-axis (or Q-axis) flux and dividing it by the i_i applied during the second and third simulations. The mutual inductance can be calculated in two ways, both of which should return the same result as shown in 3.3 providing the D-axis and Q-axis are correctly aligned during the simulation. The incremental inductance profile has a constant characteristic of sinusoidal shape with six oscillations per electrical period. This means that when simulating to calculate the incremental inductances, and therefore saliency properties, of a machine that the simulation should be carried out over a least a sixth of the electrical period. This means at least one complete oscillation of both the D and Q-axis inductances will be analysed, along with the mutual inductance.

3.4 Experimental Measurement of Incremental Inductances

Experimental measurements were used to verify the FEA of incremental inductances used to determine sensorless capability of PMSMs. Through the use of experimental measurements, the values obtained through the FEA can be verified. With verification this ensures that the design stage analysis of PMSMs can

be used with sufficient knowledge of real world values. The test machine used in the experimental calculations is summarized in Table 3.1.

Slots	18
Poles	6
Rotor Configuration	Surface-Mount
Winding Configuration	Distributed

Table 3.1: Experimental Test Machine

The experimental procedure involves a conventional locked rotor test [51, 52] with AC injection. The overview of the experimental setup is shown in block form in Figure 3.2. The test machine is supplied using a DC bias with AC superposition using a Chroma programmable power supply. The DC bias is supplied based on the locked rotor position, provided by an absolute encoder connected to the coupled DC motor shaft. The machine is locked in the respective D-axis and Q-axis positions so that injection takes place on each in turn. While locked in these axis orientations the DC bias supplied to the machine windings reflects the desired three-phase supply based on the rotor position.

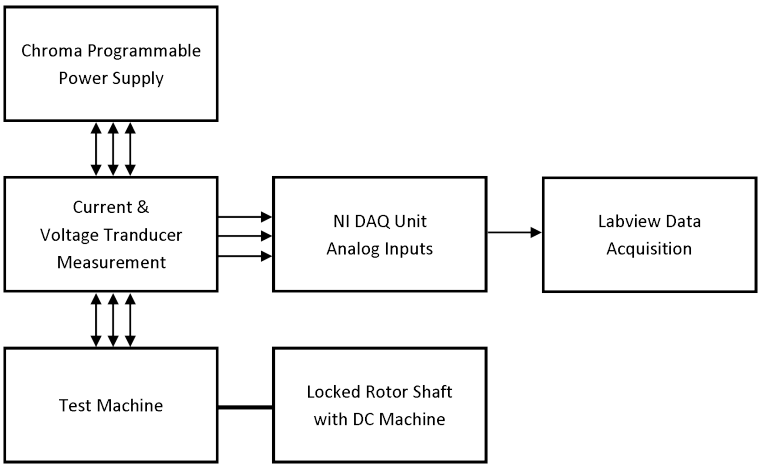

Figure 3.2: Block diagram of experimental setup

The superimposed AC supply is used to deduce the incremental inductance value while the DC bias can then be used to measure the inductance values at various loading points. The measurement technique requires the AC signal to be small enough to ensure accurate measurement. A National Instruments (NI) Data Acquisition Board (DAQ) unit is used in accordance with Labview to gather the motor currents and voltages during testing to calculate the results post-process. The primary concern is the variation in L'_d and L'_q while under Q-axis loading

since this reflects close to MTPA operation. This means that for L'_q measurement the rotor was locked in an alignment such that the AC and DC to be applied on the Q-axis. While for L'_d the rotor was positioned so that the DC bias was applied on the Q-axis and AC on the D-axis. This is illustrated in the phasor diagrams in Figure 3.3.

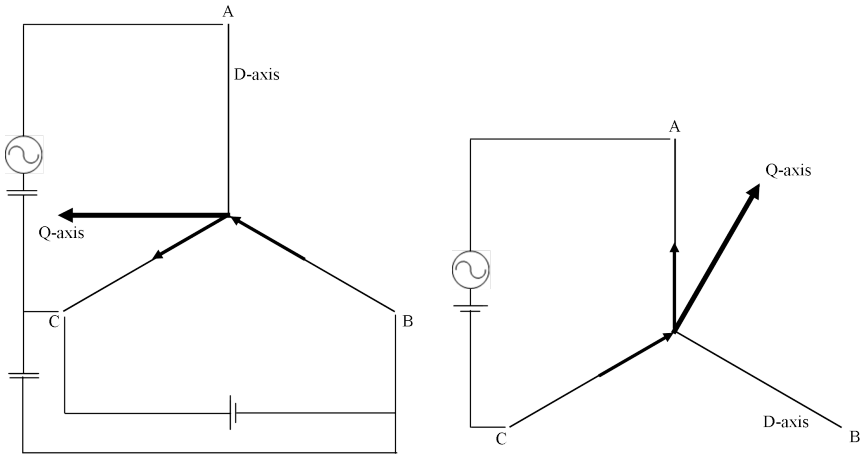

(a) D-Axis Measurement (b) Q-Axis Measurement

Figure 3.3: Phasor alignment for rotor position & loading configuration

The current and voltage waveforms observed from the locked rotor tests are illustrated in Figure 3.4. The AC component of the experimental is kept constant, while the DC bias is gradually increased. This causes the current and voltage waveforms to gradually deviate from zero.

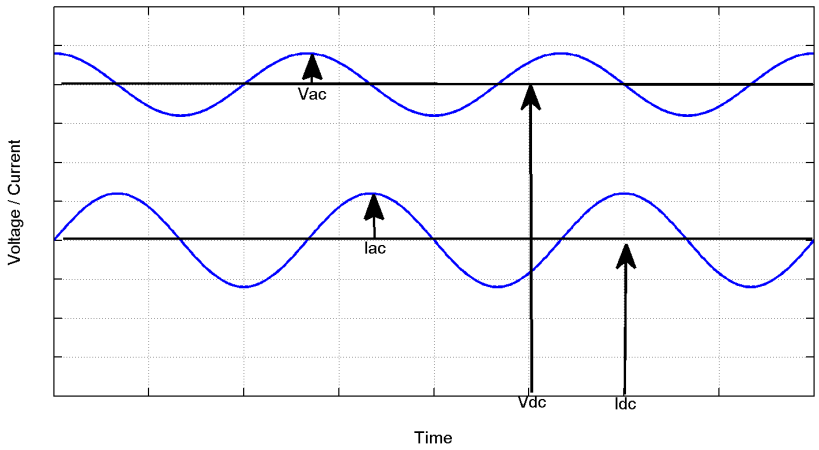

Figure 3.4: Illustration of measured voltage and current waveforms

The DC parts of the two waveforms when under load can be used to calculate the machine resistance that is required for the inductance calculation, Equation

3.4. Finally, L'_d and L'_q can be calculated with Equation 3.5, using the AC part of the waveforms when locked in their respective positions.

$$R = \frac{v_{DC}}{i_{DC}} \tag{3.4}$$

$$L(i) = \frac{\sqrt{v_{AC}^2 - R^2 \cdot i_{AC}^2}}{2 \cdot \pi \cdot f \cdot i_{AC}} \tag{3.5}$$

For the experimental measurements the machine was locked in the two fixed positions detailed in Figure 3.3. The first is in alignment with the Q-axis, before repeating the same test on the D-axis having rotated the machine 90° electrical (30° mechanical with the 6p test machine). The measurements were carried out at numerous DC bias loading points and then compared to the FEA incremental inductance results. The experimental setup for measurement of L'_d with Q-axis loading required an additional current supply to provide the DC bias. This limited the level of loading possible when in this alignment.

The experimental results are presented in Figure 3.5. They demonstrate that the FEA measurements are closely linked to their respective experimental values. Taking this into consideration the FEA method can be used to indicated self-sensing characteristics during machine design.

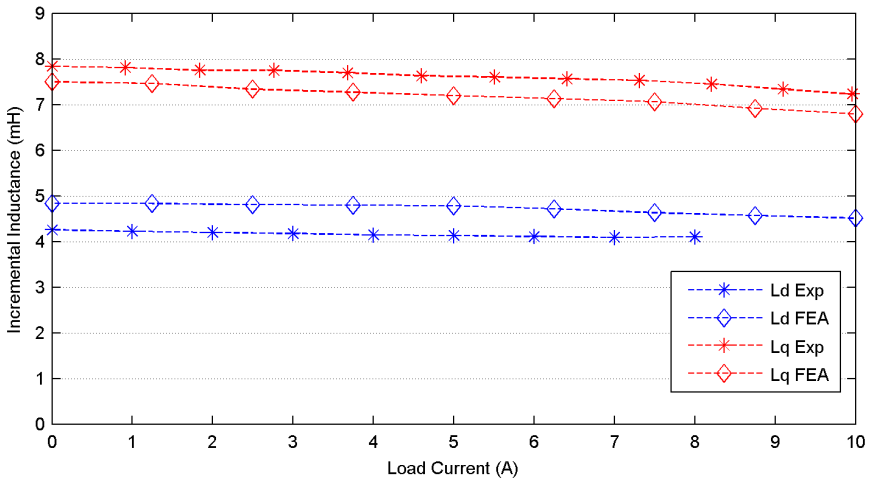

Figure 3.5: Experimental vs. FEA measurement of incremental inductances

3.4.1 Discrepancies with Experimental Results

The FEA results demonstrate a clear correlation to the magnitude and trend of both L'_d and L'_q. Despite this there is a level of deviation between the two values. The variation is caused by a number of factors. The FE simulations take place

within a 2D environment and ignore the machine end-windings, along with there effects. This will inherently cause a separation between FEA and experimental values. Secondly, the incremental inductances are position dependent and have a vary in magnitude over a complete rotation. During the alignment and locking of the rotor, a small deviation for the D and Q-axis will create a disparity.

3.5 Geometrical and Saturation Saliencies

The main tracking saliency observed in traditional PMSMs is caused by saturation. The level of saturation within the stator and rotor back-iron varies during rotation and with changes in load. The differential saliency tracked during HF injection is therefore mostly caused by the main saturation saliency between the D and Q-axis. This is easily demonstrated by comparing the results of a test machine simulated twice. Firstly, under normal conditions with non-linear material properties and then with ideal linear material properties. This second simulation model removes any characteristics caused by saturation so only geometrical saliencies will be observed.

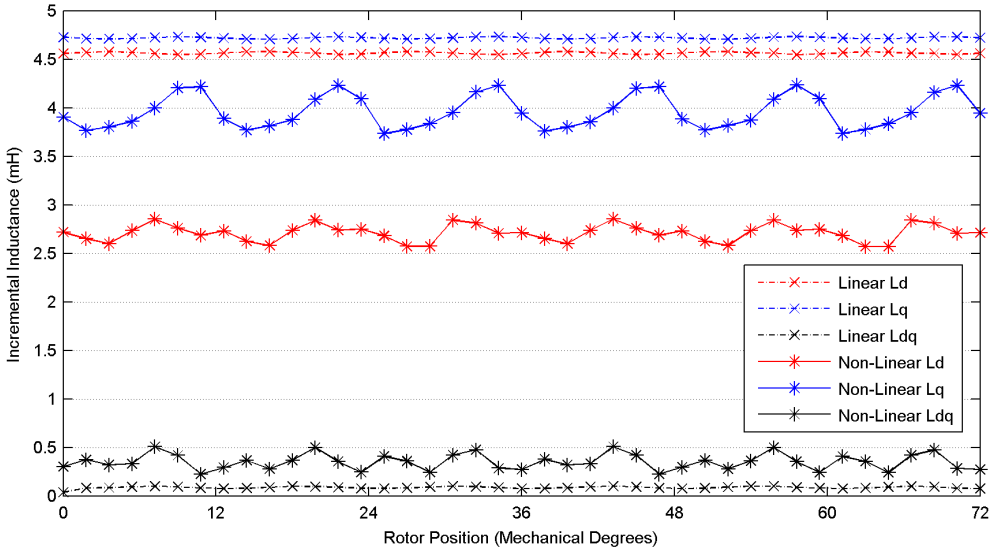

Figure 3.6: Incremental inductance variation with rotor position

The data plot in Figure 3.6 shows the individual and mutual incremental inductances from the two simulations. The comparison between the two sets of data demonstrates that with the inset PMSM topology tested there is very little geometrical saliency present. The plot covers a 72° mechanical rotation which encompasses a complete electrical period for the 12s10p topology tested. The

6^{th} harmonic ripple is evident on the non-linear result but is lost in the linear simulation where only geometrical saliency is taken into account.

The main saturation saliency that is used to track rotor position is demonstrated again in Figure 3.7. The simulations with ideal linear material show no change or deterioration with load. The small difference observed between L'_d and L'_q in the linear simulation is caused by the inset rotor magnets creating a geometrical variation between the main D and Q-axis inductance paths. The load dependent mutual inductance is also confirmed as a saturation induced characteristic in Figure 3.7.

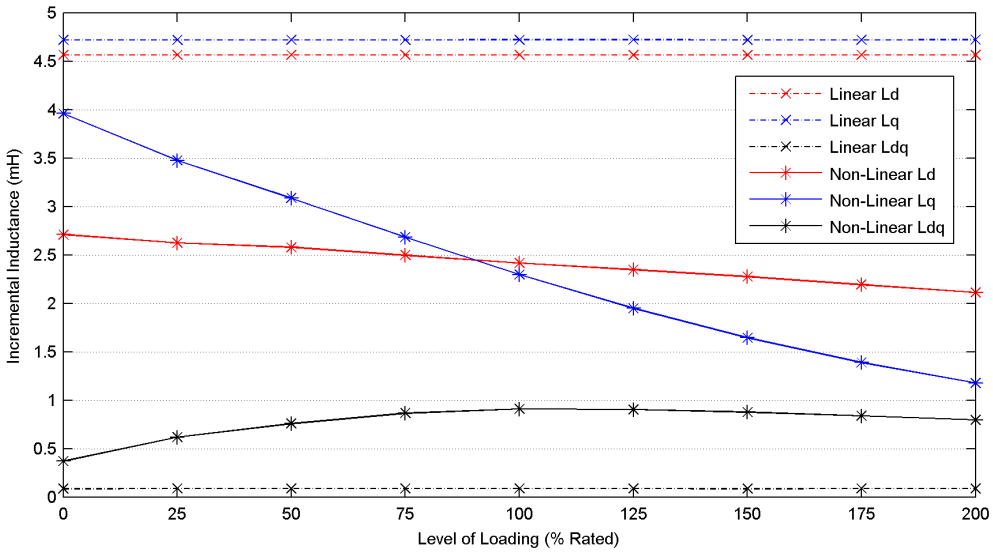

Figure 3.7: Incremental inductance variation with loading

3.6 Influence of Stator Dimensions on Self-Sensing Properties

The calculation approach outlined in section 3.3 allows MagNet to be used when calculating incremental inductances of a machine, and therefore saliency characteristics can be analysed. With this technique the impact of geometrical stator variations on saliency characteristics were investigated. The influence on saliency characteristics was examined for three geometrical parameters in the stator. To determine the significance of each parameter, they were each investigated in turn, with all other machine dimensions remaining unchanged. The impact on saliency characteristics and overall machine performance was analysed, with particular emphasis on the following properties:

- Mean torque production

- Level of cogging torque
- B-EMF
- Incremental inductances
- Level of Saliency
- Saliency Ripple
- Saliency Crossover Point

A 12s10p inset PMSM topology with a simple, radial design was used for illustration purposes. The slot opening, tooth width and back iron thickness were each systematically varied in turn. Here the slot opening is defined as the degrees of opening from the centre of the machine between each tooth bridge tip. The tooth width was simply defined as the width of the parallel sided tooth segment, while the back iron thickness was the distance from the outer surface of the stator back iron to the roof of the stator slots. Figure 3.8 illustrates these three variable parameters on a wireframe model of the test topology.

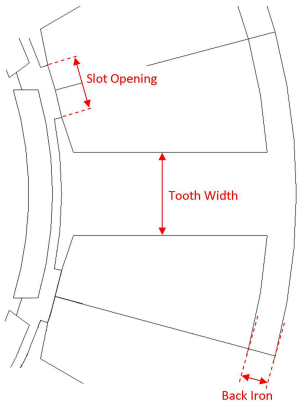

Figure 3.8: Variable geometrical parameters under investigation

During these parameter tests the rotor geometry was kept constant and only the stator was investigated. Due to the dominant saturation saliency the rotor geometry has less of an impact and at this stage was not considered for its saliency influence. The test machine used Double-Layer (DL) concentrated windings with variable loading that maintained constant current density during geometrical changes. A summary of the fixed machine parameters is displayed in Table 3.2.

Stator Outer Radius	67.5mm
Stator Inner Radius	40.0mm
Active Stack Length	87.6mm
Shaft Radius	20mm
Airgap Length	0.75mm
Permanent Magnet Shape	Radial (Segmented)
Permanent Magnet Volume	Fixed
Winding Configuration	Double-Layer Concentrated
Turns per Coil	34 %

Table 3.2: Test Machine Parameters

3.6.1 Influence of Slot Opening

The slot opening was incrementally increased from a near closed slot condition (2°) up to an open slot condition (16°). These were then simulated under various loading conditions to fully analyse the impact on the machine properties detailed previously. The plots in Figure 3.9 show the incremental inductances and level of saliency at each increment, at no load, rated load and 200% rated load.

A 6° slot opening exhibits the greatest saliency ratio under no load, as shown in Figure 3.9(b). However, this is not the case when the machines are simulated under 100% and 200% rated load. Here the level of saliency for slot openings at the low end of the range significantly drop under load, into the inverse saliency range ($\frac{L'_q}{L'_d} < 1$). This occurs due to heavy q-axis saturation under increasing load, caused by the thin tooth bridges becoming saturated when aligned with q-axis during rotation. This condition is less significant with larger slot openings, and to a certain extent an increase in slot opening can reduce the amount L'_q saturates.

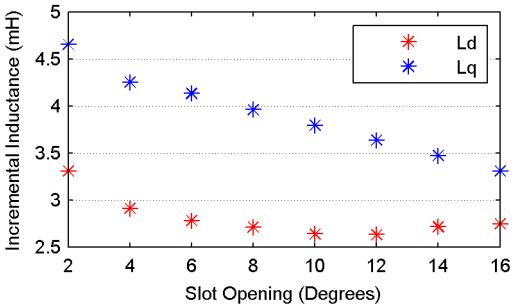

(a) No Load

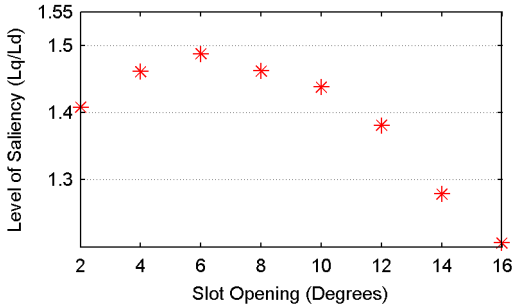

(b) No Load

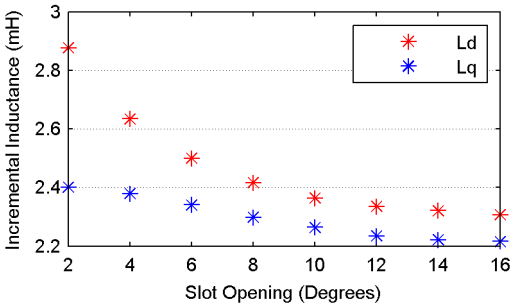

(c) 100% Rated Load

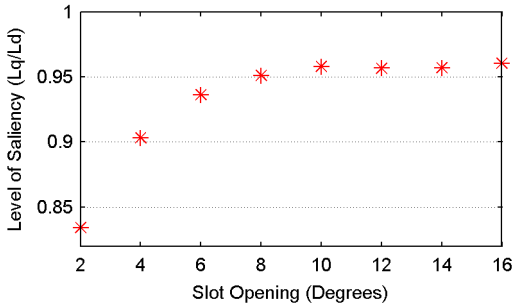

(d) 100% Rated Load

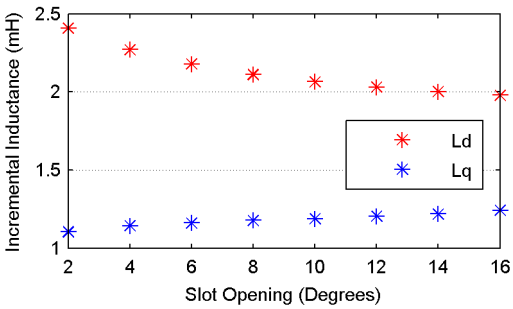

(e) 200% Rated Load

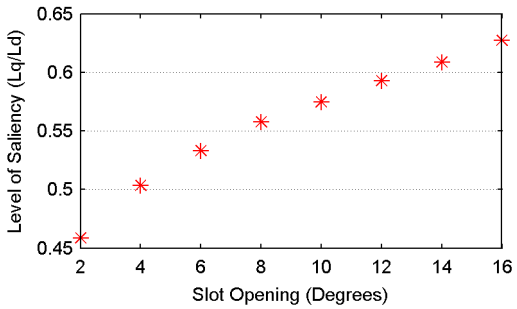

(f) 200% Rated Load

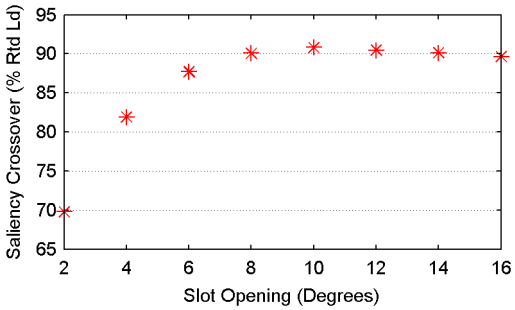

(g) Saliency Crossover Point

Figure 3.9: Influence of SO on Incremental Inductances

These plots along with Figure 3.10 indicate that the slot opening does impact on the incremental inductances. The impact can be seen when analysing the

saliency crossover point, under which there is a zero saliency condition. In Figure 3.9(g), this crossover point is calculated as a percentage of rated load. A 10° slot opening has the highest crossover point, in terms of rated load, although the crossover still occurs below rated load. This indicates that when operated under sensorless control the HF injection method would fail at this loading point. The level of ripple present on the incremental inductance profiles is analysed in Figure 3.11. There is a trend which is common across all levels of loading. An increase in SO leads to a reduction in the amount of ripple on the incremental inductances. The increase in ripple with level of loading and with a reduction in SO mostly likely occurs due to the greater amount of saturation, particularly in the tooth bridges.

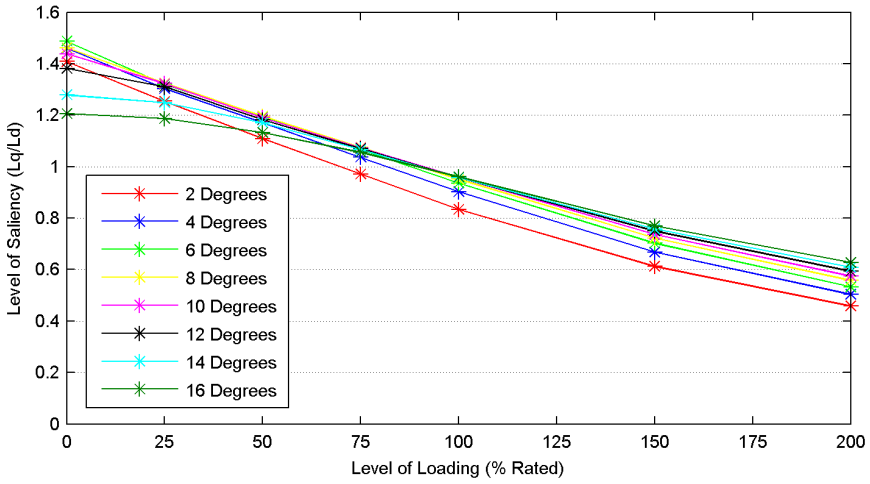

Figure 3.10: Variation of saliency due to loading and SO

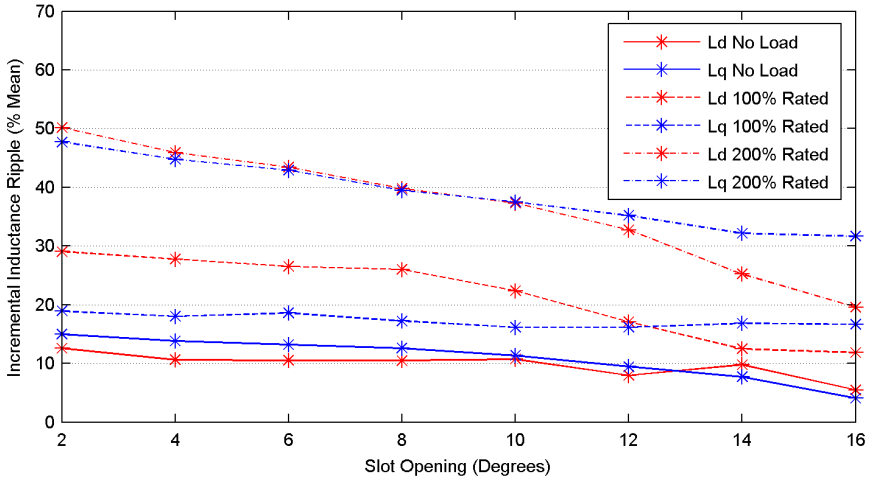

Figure 3.11: Influence of SO on incremental inductance ripple

The results in Figure 3.12 illustrate the effect the slot opening has on the overall

machine performance. Since the slot/pole combination is unchanged throughout the cogging torque always follows the same profile, formed from the Lowest Common Multiple (LCM). Despite this, it is clear how the cogging torque significantly increases as the topology approaches an open slot condition. This supports general machine theory that an open slot will increase the interaction between the stator slots and rotor poles. The lowest level of cogging torque occurs with a small 4° slot opening. The variation from $2-16°$, causes up to 6.5% change in the mean torque production within the machine. The most effective performance occurring in the middle of the slot opening range. Upon investigation this appeared to be caused by the tooth bridge and tooth stem itself combining to create the most effective flux path across the main airgap at 8°.

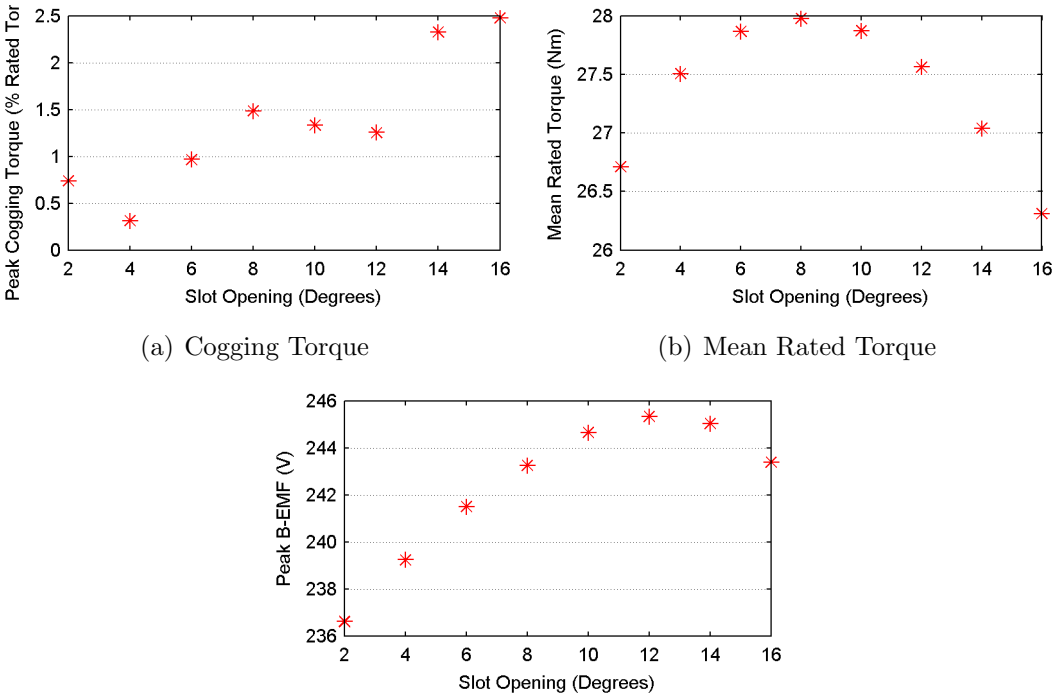

(a) Cogging Torque

(b) Mean Rated Torque

(c) No Load Back-EMF

Figure 3.12: Influence of SO on Machine Performance

The maximum supply voltage of the motor drive is an important limit during motor design, since this will theoretically impose the torque limit for a given speed of rotation based on the machine B-EMF production. It is therefore important to consider the machine design primarily at the operational rotational speed and generate the desired B-EMF at this point. The influence on B-EMF production is shown in Figure 3.12(c), obtained from simulating the machine rotating under no load at the 3000rpm operational point. There is a limited impact on the B-EMF

caused by the SO, the most significant parameter at play here is the effectiveness of the net PM flux. This translates to the maximum B-EMF at rated speed. THe shape of the PM poles and corresponding machine topology will influence the quality of the B-EMF.

The results show the varying extent to which the SO influences both the saliency characteristics and performance of the machine. The impact of the SO is clearly shown and means that with regard to self-sensing oriented design there are benefits to be obtained, although a compromise is required due to the conflicting advantages and disadvantages at various points.

3.6.2 Influence of Tooth Width

The tooth width was incrementally increased from the narrowest point of 6.5mm up to the widest point of 10.5mm. The aim was to investigate this extent of which the tooth width influences both the saliency characteristics of the machine and its fundamental performance.

Using the same analysis process as with varying the slot opening the results are presented below. As with the slot opening investigation, all other geometrical parameters where fixed during the whole process. During the analysis the SO was set to the median value of 8° so that the particular trends caused at either extremity were limited. The results in Figure 3.13 demonstrate the impact of varying the tooth width on the machine incremental inductances. There is a clear trend between increasing Tooth Width (TW) and increasing the magnitude of incremental inductance, this applies to both the D and Q-axis inductances.

As expected, L'_q still saturates significantly over the whole range of tooth widths analysed, the rate of saturation is independent of tooth width. This means with increasing load the initial saliency is lost as L'_q crosses L'_d and creates an inverse saliency condition. The data in Figure 3.13(g) indicates a zero saliency point occurs at under rated load. It suggests that a narrower tooth width could be implemented to improve this, moving the crossover point to a higher level of rated load. With a tooth width of 6.5mm the zero saliency point occurs at 99.52% rated load. If the trend of the plot continues then the crossover point would shift even higher, however, the impact this would have on the main flux path and overall torque production prevents using such narrow teeth.

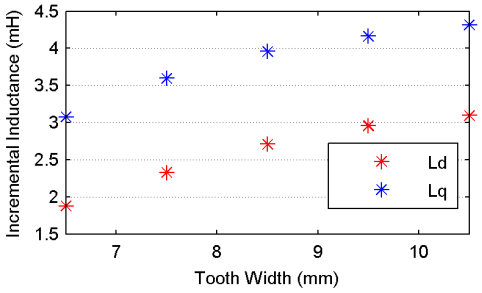

(a) No Load

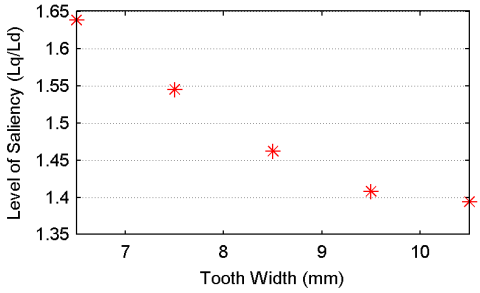

(b) No Load

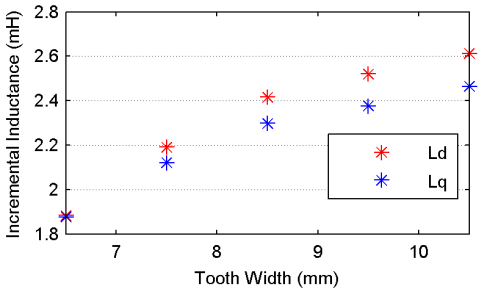

(c) 100% Rated Load

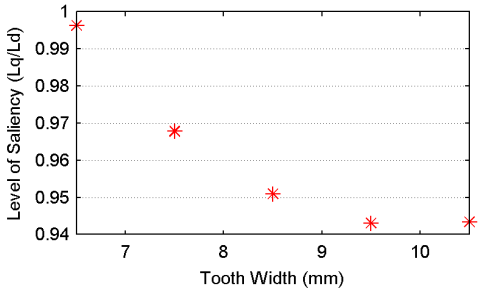

(d) 100% Rated Load

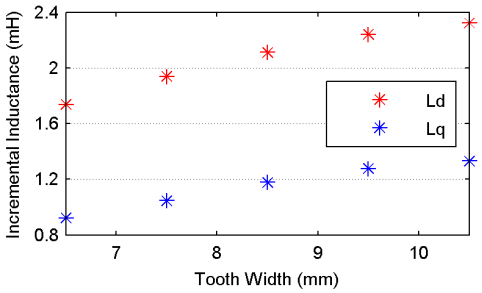

(e) 200% Rated Load

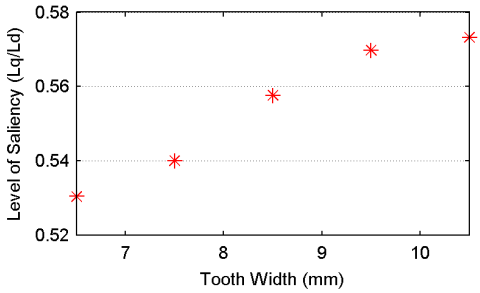

(f) 200% Rated Load

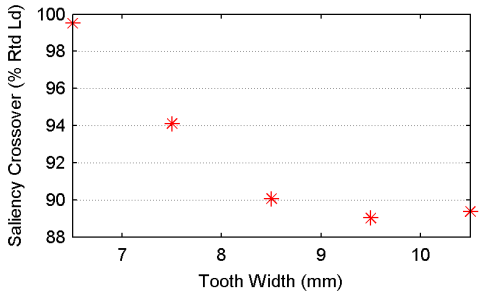

(g) Saliency Crossover Point

Figure 3.13: Influence of TW on Incremental Inductances

The impact of Q-axis saturation is shown once again in Figure 3.14 and the limited influence tooth width is clear. The tooth width appears not to fundamentally affect the incremental inductance profile.

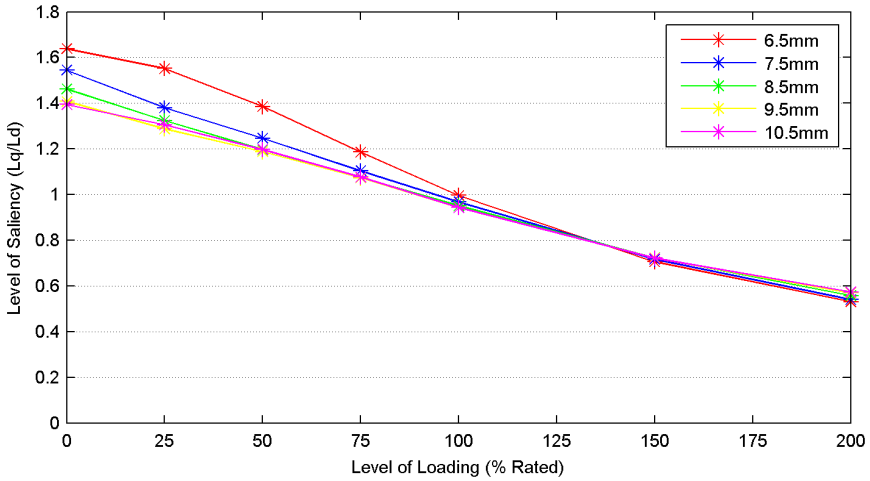

Figure 3.14: Variation of saliency due to loading and TW

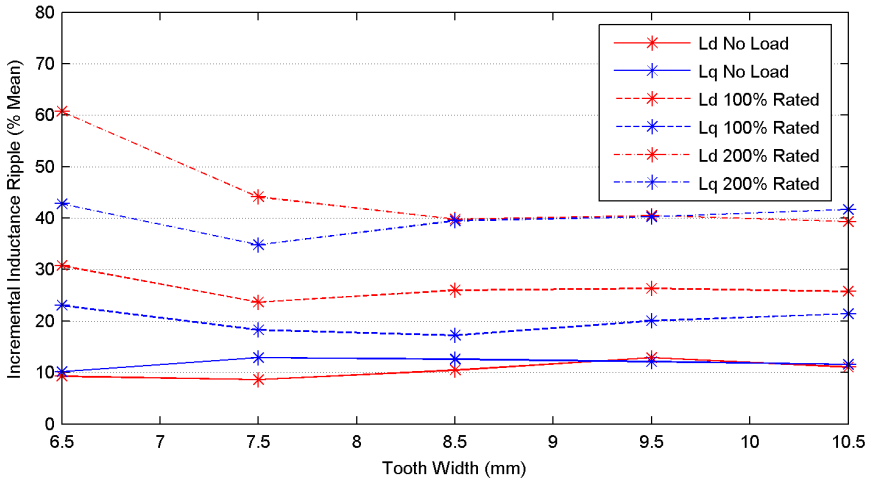

Figure 3.15: Influence of TW on incremental inductance ripple

The plots in Figure 3.15 are for the level of incremental inductance ripple, there is little variation caused by the change in tooth width. As with the data in the SO investigation previously, the level of inductance ripple increases greatly with load. At no load there is approximately 10% ripple, this is compared to a significant 40% ripple at 200% rated load.

The results analysing the relative impact TW has on overall machine performance are shown in Figure 3.16. The advantages gained in self-sensing capability must be put into context as ultimately a machine still needs to meet a design specification. The results agree with general machine design theory. The mean torque production is directly proportional to tooth width, up to the midpoint of 8.5mm. Beyond this width the level of electrical loading within the machine

begins to limit the torque production. Overall the mean torque production has an 8% variation across the range used for TW. There is a significant 25% variation in cogging torque caused by the TW, as shown in Figure 3.16(a). With this particular topology when $TW = 7.5$ there is a increased amount of interaction between the rotor poles and the stator slots. The level of no load B-EMF is directly proportional to tooth width, a 6% increase occurs from the narrowest to the widest tooth width.

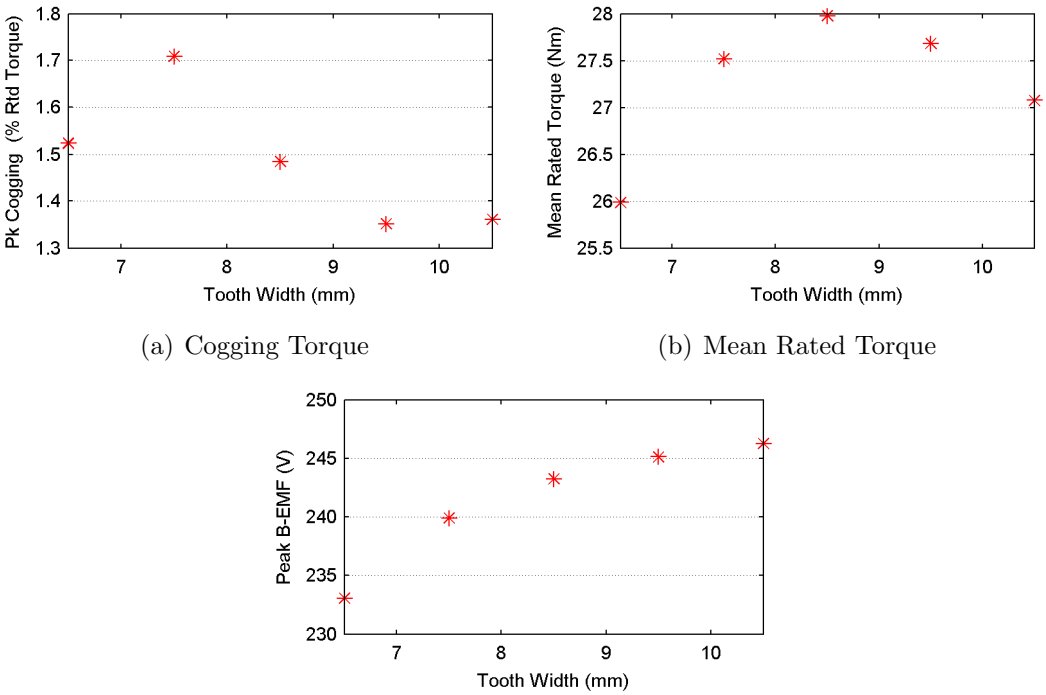

(a) Cogging Torque

(b) Mean Rated Torque

(c) No Load Back-EMF

Figure 3.16: Influence of TW on Machine Performance

The results from this investigation into the impact of TW are significant. It has been shown that the tooth width influences the saliency characteristics of a machine. Despite this observation, the tooth width is a fundamental parameter contributing to overall machine performance. In comparison to self-sensing capability the tooth width had far greater impact on fundamental performance that it should be optimized with this in mind.

3.6.3 Influence of Back Iron Thickness

The analytical process was repeated on the stator back-iron thickness. The back-iron was incrementally varied from the lower boundary of 3.0mm, up to 5.0mm.

The change was made with a fixed stator outer radius, therefore with increasing back-iron thickness the slot depth reduced.

The stator back-iron forms an integral part of the machine's main flux path. With this in mind the geometrical parameter should cause significant variation in the overall machine performance, however, the extent of impact on self-sensing characteristics is unknown. The collective results in Figure 3.17 illustrate the variation in incremental inductance caused by a changing back-iron thickness. As with the SO and Back-Iron (BI) results, L'_q suffers from significant saturation under increasing load. At all test loads it is evident that increasing BI contributes to an increase in the magnitude of the incremental inductances, most likely caused by and reduction in the reluctance along both the D and Q-axis paths. This relationship also causes the level of saturation on L'_q to be greater at the lower end of the BI range investigated.

The magnitude of L'_d reduces gradually from no load to 200% load when compared to L'_q and therefore there is a large variation in the saliency ratio. At no load there is a good level of saliency within the machine, particularly with a narrow back-iron path, as shown in Figure 3.17(b). With the large drop in L'_q the saliency condition quickly becomes inverse. The greater amount of saturation at the lower end of the BI range mentioned previous can be seen across Figures 3.17(b),(d),(f) and 3.18. At no load the level of saliency is greatest at $BI = 3.0$, however, once under load the condition is reversed as the impact of L'_q saturation is higher. The relative location of the saliency crossover point, in Figure 3.17(g), supports this as well since at $BI = 3.0$ the zero saliency condition occurs at 87.64% rated load, compared to 90.42% when $BI = 5.0$.

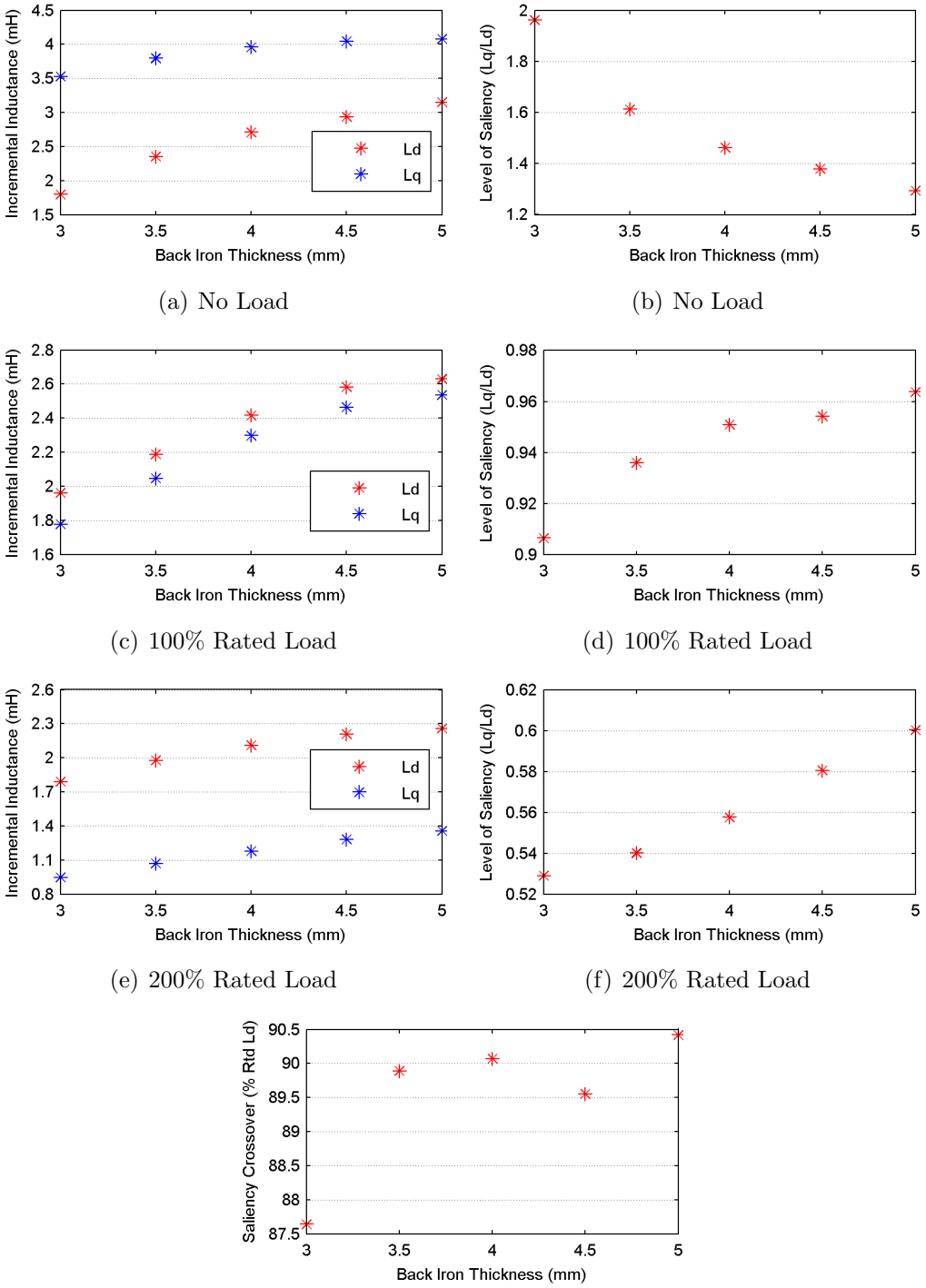

(a) No Load

(b) No Load

(c) 100% Rated Load

(d) 100% Rated Load

(e) 200% Rated Load

(f) 200% Rated Load

(g) Saliency Crossover Point

Figure 3.17: Influence of BI on Incremental Inductances

The level of ripple over the incremental inductance profiles is shown in Figure 3.19. As with previous results there is a large increase in the amount of ripple at high loads, while in general there is more ripple on the D-axis inductance. The

data shows a common trend over the whole loading range, with the percentage of ripple reducing as BI increases. This indirectly proportional relationship is once again caused by the impact on the main reluctance paths. A narrow back-iron can cause a bottle neck within the paths, this causes a greater variation between the high and low reluctance values when the D and Q-axis are aligned and completely out of line with the back-iron. The back-iron provides the primary

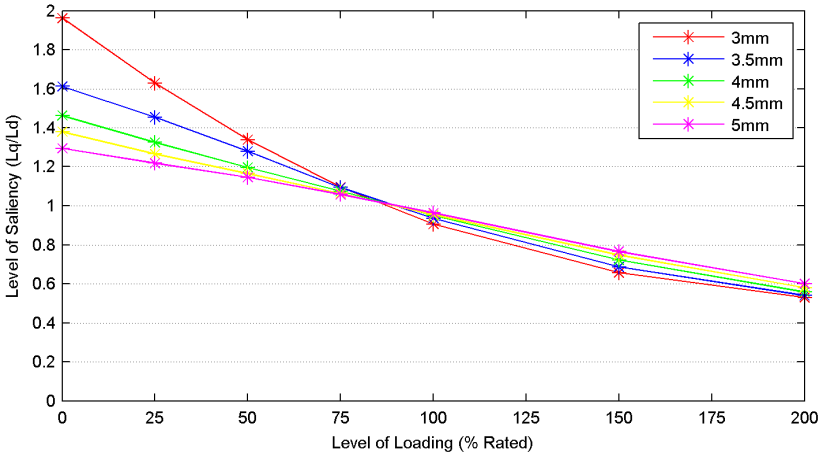

Figure 3.18: Variation of saliency due to loading and BI

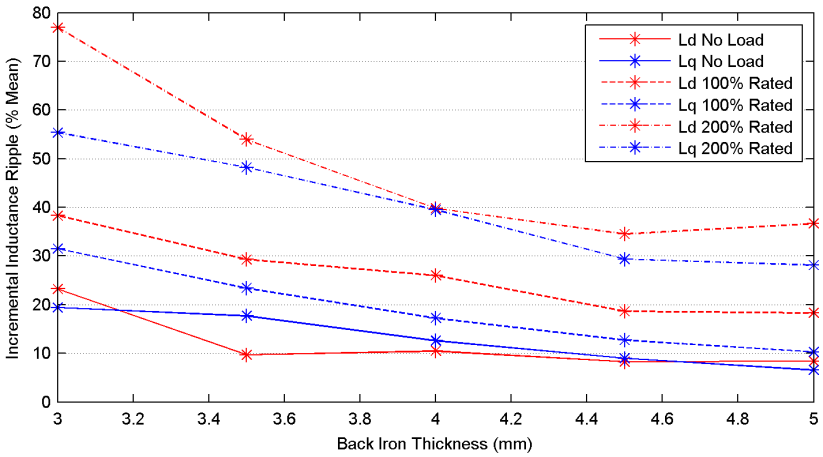

Figure 3.19: Influence of BI on incremental inductance ripple

link between stator teeth within the main flux path. This means it has a strong relationship with the overall machine performance as demonstrated in Figure 3.20. As expected a wider back-iron improves the main flux path connecting the rotor and stator. This causes the increase in mean torque production at the top end of the BI range seen in Figure 3.20(b). The back-iron thickness has an strong impact on the torque production under the proportional variation to current supply. This is not reflected in such a significant change in B-EMF, therefore a large majority

of the increase in torque is down to the current supply and not just the variation in geometry.

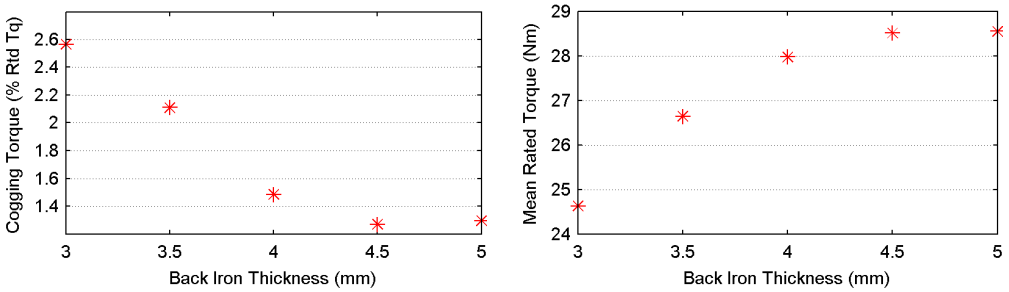

(a) Cogging Torque

(b) Mean Rated Torque

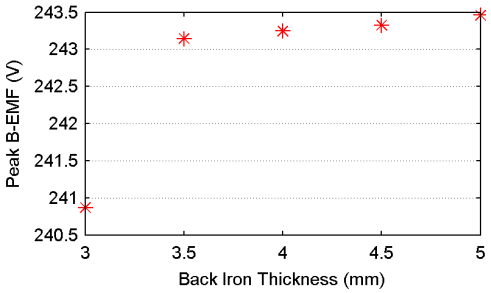

(c) No Load Back-EMF

Figure 3.20: Influence of BI on Machine Performance

There is a small increase caused by increasing BI from 3.0mm up to 5.0mm, although there is an interesting knee point at 3.5mm. Below this thickness the magnitude of no load B-EMF drops rapidly; suggesting that at such a thickness the back-iron is causing a significant bottle neck within the machine. The back-iron saturation occurring around this bottle neck also contributes to a large increase in cogging torque. This significant increase takes place when $BI < 4.0$ as shown in Figure 3.20(a).

The results analysed above validate the impact back-iron thickness has on the SPMSM topology. Variations in this geometrical parameter have an influence on both the self-sensing and performance characteristics of the machine. Much like the tooth width, the significant impact caused by varying BI is on overall machine performance. There is opportunity to use this parameter during design to improve sensorless capability, particular with regards to the feasibility region. However, the fundamental nature of BI within machine design for meeting performance requirements means that in general it should be optimized primarily with this in mind.

3.7 Influence Rotor Geometry

The work discussed in Section 3.6 was focused on the stator geometry and its relative impact on the main saliency characteristic. The impact on fundamental performance of the various geometrical changes were also noted. As stated at the beginning of Section 3.6 the rotor geometry has less impact on the HF saliency since the machine is dominated by the saturation saliency that occurs within the stator. In order to confirm this assumption the stator topology from Section 3.6 was used along with a generic variable rotor topology. To remove possibility of influence from the stator it was kept unchanged throughout, along with the level of loading. Instead the rotor geometry consisted of a 10p configuration with simple radial PM poles which had a constant inset equal to 20% of the PM thickness. An illustration of this topology is shown in Figure 3.21, in the rotor section the PM poles are highlighted in blue with the rotor lamination in grey.

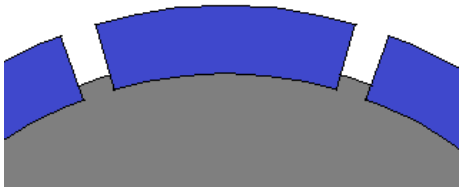

Figure 3.21: Illustration of rotor geometry

The influence of magnet span was the primary focus during this body of work. To enable the comparison of each variant a means of volume control was imposed on the magnet thickness. This meant that a constant PM volume was used and therefore the magnet thickness was set as a function of magnet span. Incremental stepped changes were made to the PMs and the relative impact on HF saliency was observed.

The collective results presented in Figure 3.22 illustrate the incremental inductance values and resulting levels of saliency at three loading levels. The plots demonstrate that there is negligible influence caused by changing the relative width and thickness of the PM poles. The impact of loading is still clearly visible with the saturation of L'_q. Since the volume of PM material was constant the overall magnetizing inductance within the machine remained unchanged. If the magnet span was varied with a fixed magnet thickness it would be expected to cause more of an impact since the level of magnetizing inductance would be changing.

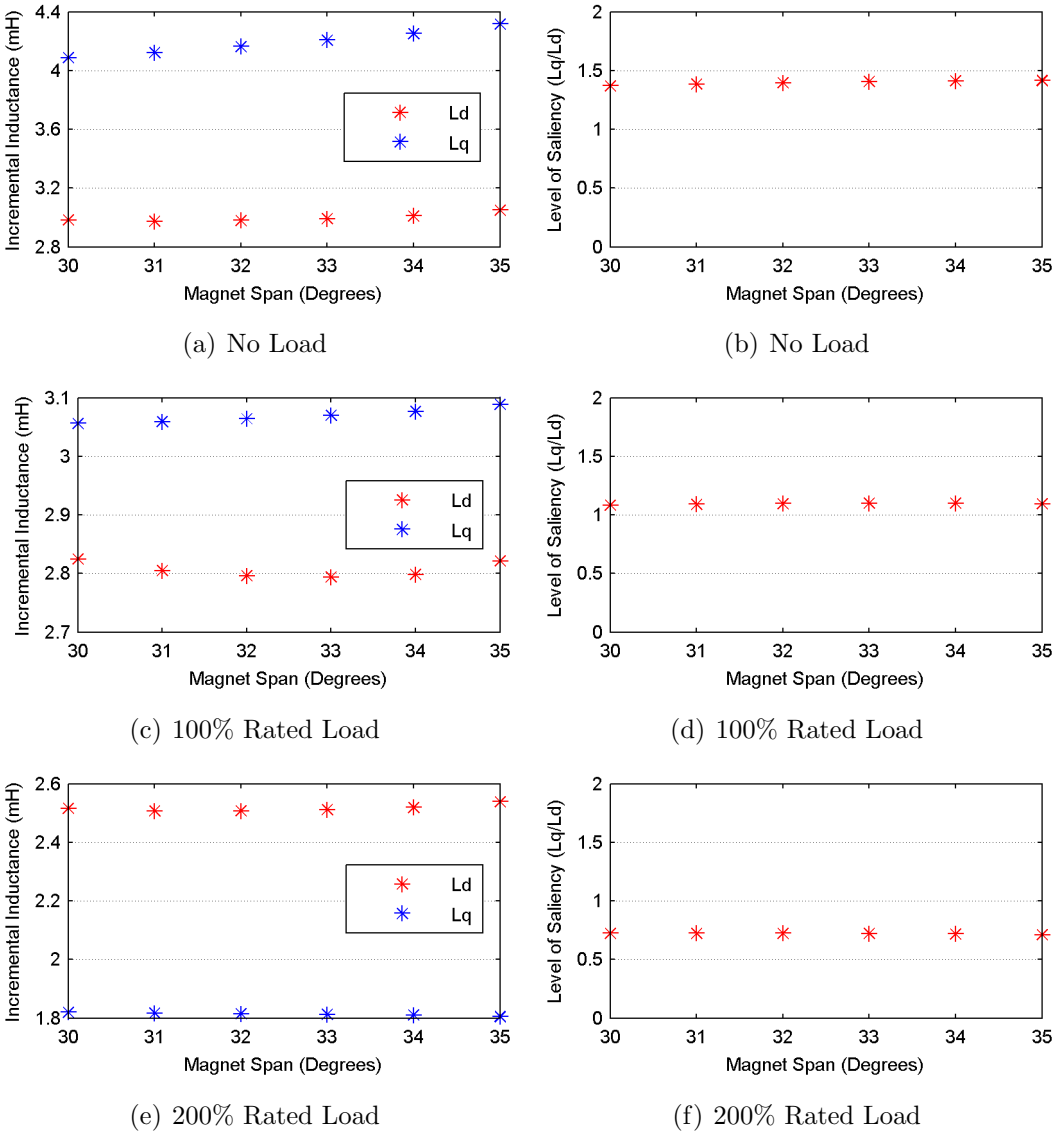

(a) No Load

(b) No Load

(c) 100% Rated Load

(d) 100% Rated Load

(e) 200% Rated Load

(f) 200% Rated Load

Figure 3.22: Influence of MS on Incremental Inductances

The results show that the stator geometry is far more significant in surface-mount and inset topologies due to the dominant saturation saliency. The rotor topology, with respect to the PM span, thickness and inset is more of a concern towards the fundamental performance of the machine. It has a significant factor as it determines the ability of the machine to generate a B-EMF and torque. While the shape and positioning directly impacts on the quality of B-EMF and torque.

3.8 Influence of Variable Stator Tooth Widths

The findings presented in 3.6.2 reveal that the tooth width within a SPMSM can influence the overall saliency characteristics of the machine. The level of impact was seen to be limited, especially in comparison to the impact on fundamental machine performance. As a continuation of the investigation the tooth width was again utilized to observe if saliency properties could be enhanced. Design variations to the existing topology using tooth width is advantageous since it is easily adapted within the stator lamination. The significant impact the tooth width has on fundamental performance means that there is only a limited range within which it could be varied to improve position detection. With this in mind various combinations of different tooth widths were analysed.

The investigation implemented only small variations of 0.5mm to the stator tooth widths. Instead of the overall change to tooth width, a sequence of tooth widths was used. These were simulated using FEA, then compared to the original 12s10p reference model. Two adaptations were analysed, a repeated 1-2-3-1-2-3 sequence and a modulated 1-2-3-2-1-2 sequence. The geometrical variation is shown in Table 3.3 and the sequences are illustrated in Figure 3.23. Only half of the stator teeth are shown, since the particular sequence is repeated over the second half the stator.

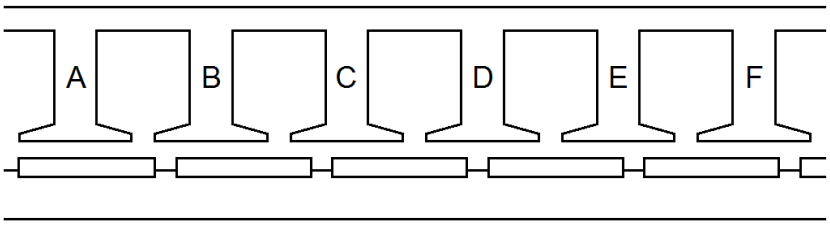

Figure 3.23: Stator tooth geometry reference

	A	B	C	D	E	F
Ref	8.5	8.5	8.5	8.5	8.5	8.5
Mod	8.0	8.5	9.0	8.5	8.0	8.5
Rep	8.0	8.5	9.0	8.0	8.5	9.0

Table 3.3: Variation to stator tooth width (dimensions in mm)

The simulation results were used to analyse both the fundamental and sensorless properties of each stator configuration. An overview of these results is shown in

Table 3.4. Since the average tooth width remains equal to the reference machine for both topologies, the overall magnetic loading of the machine is unchanged. For this reason the overall torque production of each machine remains the same as demonstrated in the results. This is advantageous since the design concepts cause no ill effects to torque production. The variation to tooth width is however expected to influence both the torque ripple and cogging torque. The changing tooth width likely causes additional interaction between the stator slots and rotor poles.

The repeated (Rep) sequence shows the greatest increase in the amount of cogging and ripple. The significant change in magnetic loading between the 9.0mm tooth and the adjacent 8.0mm tooth generates the disruption in torque quality. Whereas, the gradual ramping sequences of the second configuration does not suffer to the same extent. This results in similar torque characteristics to the reference machine.

Topology	Torque			Saliency
	Rated (Nm)	Ripple (%)	Cogging (%)	(Lq/Ld)
Ref	28.49	4.02	5.51	1.26
Mod	28.45	3.92	5.93	1.26
Rep	28.43	5.16	6.95	1.26

Table 3.4: Overview of performance analysis

There is no noticeable impact on the machine saliency ratio with either of the two stator configurations examined. Instead the effects of varying tooth width can be seen in the individual incremental inductances and the position dependent saliency profile. The incremental inductance and saliency profiles are illustrated in Figure 3.24. The data is plotted over 36° which, for the 12s10p topology, represents half an electrical period. The oscillatory characteristics shown are repeated over the second halve of the electrical period and therefore not shown. Figure 3.24(b) clearly shows that the variation in tooth width has little impact of the Q-axis reluctance path, as the position dependent profile is closely matched.

A significant impact can be seen across the D-axis reluctance path of the Rep configuration in Figure 3.24(a). The sequence of tooth widths represented by the repeated pattern causes a large change in L'_d when it is aligned with the peak inductance path. The sequential peaks in L'_d step in magnitude, matching the steps up in tooth width. Aside from this however, the inductance profile is very similar to the reference machine. Therefore with no change in the Q-axis, the

L'_d characteristic can be seen in the position dependent saliency profile. When the Rep topology is compared to the reference machine in Figure 3.24(c) there is a clear stepping pattern created in the saliency profile. This three step pattern repeats over a whole electrical and mechanical period and induces a position dependent characteristic that could improve position detection.

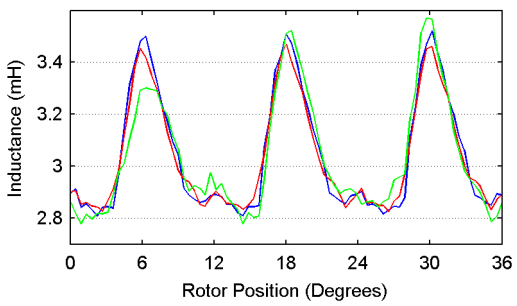

(a) D-axis Inductance

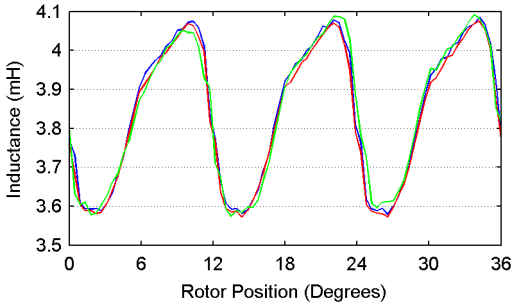

(b) Q-axis Inductance

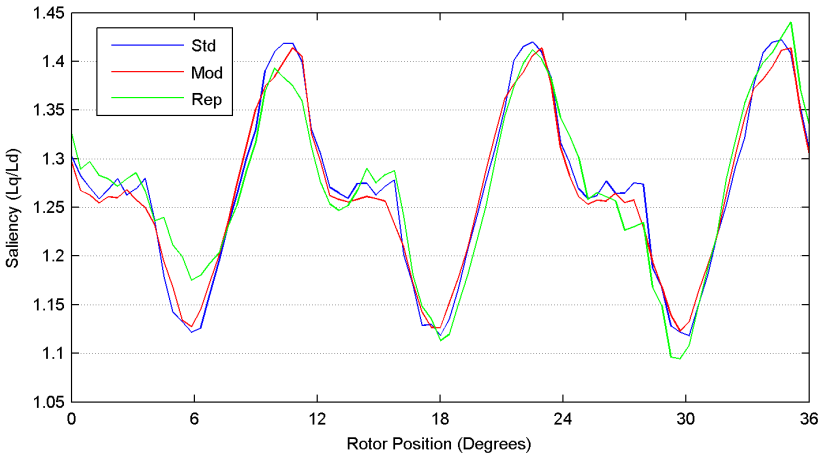

(c) Saliency Profile

Figure 3.24: Saliency characteristics of simulated models

The cause of the steps in L'_d is the variation in the flux density created by the various tooth widths involved in the stator. This creates variations in the D-axis reluctance paths which can be observed in the inductance profile. The flux density plots in Figure 3.25 show the reference model and repeated model at the identical point during the simulation. As can be seen the change in tooth width alters the level of flux density in the neighbouring teeth, changing the D-axis reluctance.

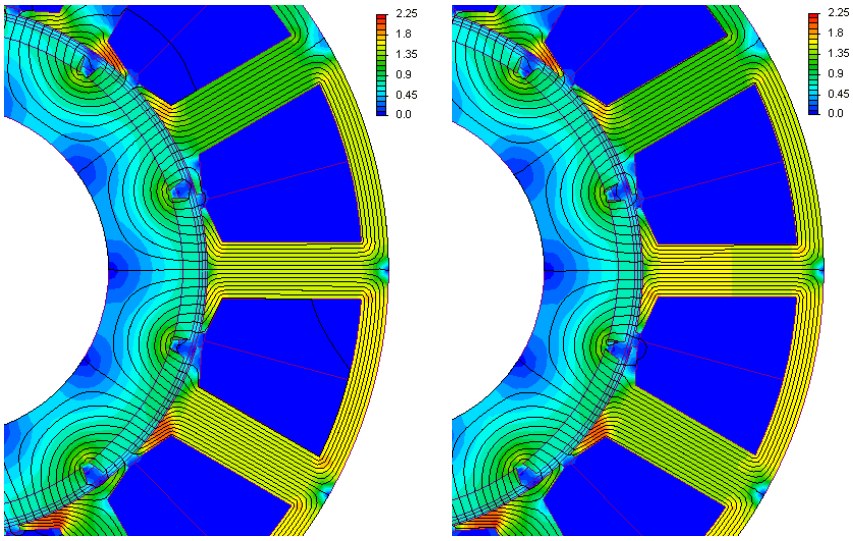

(a) Reference Model (b) Repeated Model

Figure 3.25: Flux density plot of simulated models

The analysis above has shown that incorporating a varying sequence of tooth widths can induce an additional position dependent characteristic in the saliency profile of a machine. The use of a repeated pattern causes stepped changes to both the peak and troughs in the profile which could be used in position detection. The standard saliency features of an SPMSM still apply to such a design, and therefore it will still suffer from L'_q saturation and saliency crossover (Figure 3.26).

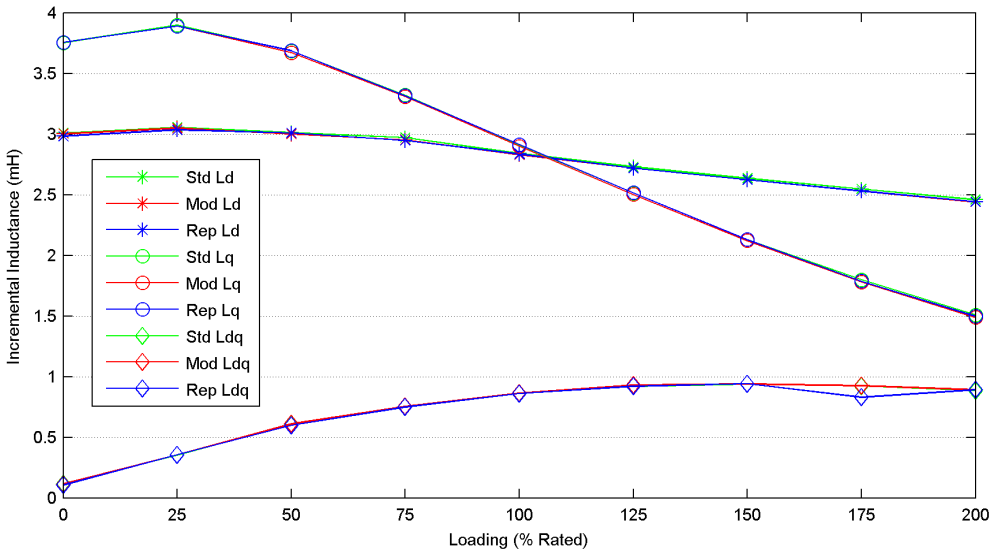

Figure 3.26: Incremental inductance variation with load

The adjustments to the stator teeth causes no variation with the influence of

load as seen in Figure 3.26. The deterioration of saliency with load is the major shortcoming of HF saliency tracking. This design approach has been ineffective at improving on this condition. Despite this it proposes and interesting option during the machine design, where introducing a position dependent saliency pattern can be advantageous. The main consideration with this design concept is the possible impact on the quality of torque production. The data presented shows that it has very limited impact on the level of torque production but it caused a dramatic reduction in torque quality due to cogging torque and torque ripple. These are important fundamental properties for a servo motor and the negative impacts that occur need to be considered when reviewing the suitability of the design method for a given purpose.

3.9 Feasibility of Zigzag Flux of Inducing Reverse Saliency

The inherent nature of the Q-axis incremental inductance to saturate, in many cases heavily, with increasing load is an important consideration for self-sensing properties. Since the D-axis incremental inductance does not tend to saturate and decrease, a saliency crossover point is likely to occur. With the use of HF injection for position tracking the crossover point is of great concern since the zero saliency condition prevents accurate control. The crossover point can be disregarded if it occurs outside of the loading range. Alternatively, it could be ignored if this occurs outside the specified low or zero speed operational envelope for the machine. When there is a more generic operational envelope this is not the case however.

Recent approaches to overcome this problem have proposed an interesting solution. In [33], the overall approach involved designing a SPMSM with an inverse saliency, even at no load. With L'_q always lower in magnitude to L'_d this prevents any form of zero saliency condition. Since for HF saliency tracking simply requires a distinguishable saliency L'_d and L'_q the inverse saliency does not present an issue. In addition to this, with increasing load L'_q will still saturate like a traditional machine. However, this will cause the level of inverse saliency which generally improves controllability and simplifies decoupling within the control.

The authors in [33] devise several design principles to induce an inverse saliency condition during machine design. The use of a similar number of poles and slots, in combination with concentrated windings is shown to produce good results. The inverse saliency is generated by introducing an addition reluctance term into

the magnetic equivalent circuit for the Q-axis. This new term is from a zigzag leakage effect caused around the airgap when aligned with the Q-axis. The increase in reluctance simultaneously causes an reduction in inductance; providing the reduction is sufficient to cause $L'_q < L'_d$ an inverse saliency occurs. The tooth bridges at the stator slot openings are designed relatively thin so that the zigzag flux can easily cause them to saturate. This saturation takes place when in line with the Q-axis and therefore reduces the magnitude of L'_q.

The principles of such an approach were used during the following tests to determine whether it could be used to create and inverse saliency on the 12s10p test topology used previously. Since this benefits from a similar number of poles and slots, as well as concentrated windings it could be suitable for this design approach. As a result, the machine dimensions were varied to investigate if a zigzag leakage flux could be induced. These variable dimensions were focused around the tooth bridges and rotor poles. An overview of the results obtained are shown in Table 3.5.

	Tooth		PM			Airgap	Saliency	Torque	
	Tip (mm)	Bridge (mm)	Length (mm)	Span (°)	Inset (mm)	Length (mm)	Ratio $\frac{L'_q}{L'_d}$	Rated (Nm)	Cogging (% Rtd)
Ref	0.85	3	3	34	1.5	1	1.13	31.0	0.14
1	1	2	3	34	1	1	1.06	32.3	0.21
2	0.8	4	3	34	1	1	1.17	31.9	0.10
3	0.8	2	3	34	1	1	1.12	31.0	0.39
4	0.8	1.6	3	34	1	1	1.05	31.5	1.16
5	0.5	0.75	3	34	1	1	0.98	29.1	4.56
6	0.5	0.75	3	30	1	1	0.99	28.3	1.76
7	0.5	0.75	3	26	1	1	0.94	26.8	2.10
8	0.5	0.5	4	26	1.5	1	0.94	28.1	1.65
9	0.5	0.5	4	26	1	1	0.93	27.6	1.11
10	0.5	0.75	3	26	1.5	0.5	1.09	29.8	3.39
11	0.5	0.5	3	26	1.5	0.5	1.08	29.2	2.38
12	0.5	0.75	3.5	26	1.5	1	0.95	27.5	2.01

Table 3.5: Overview of inverse saliency topologies

The data in the table features the geometrical parameters which were adjusted and various performance related results. The ultimate aim is to generate an inverse saliency over the entire loading range. For this investigation therefore the saliency ratio was calculated at no load, this would ensure that if an inverse saliency is achieved it will be present at all loads. Column eight shows the saliency

ratio for each test topology, in this case an inverse saliency is when $\frac{L'_q}{L'_d} < 1$. With several parameter adjustments by test topology five an inverse saliency is present within the machine. This is maintained for the remaining topologies, except type 10 and 11 which exhibited a traditional saliency ratio due to the airgap length being the same as the tooth tip. In addition to the saliency ratio each topology was simulated to establish the basic performance properties.

The rated torque and level of cogging torque were calculated from these simulations and can be seen in columns nine and ten. There were several topologies that supported the principles outlined in previous research, however inducing the zigzag leakage flux saturation did not come without a cost to the machine. Using the reference test machine it is clear that such a topology causes severe deterioration in both the torque capability of machine and quality of torque production.

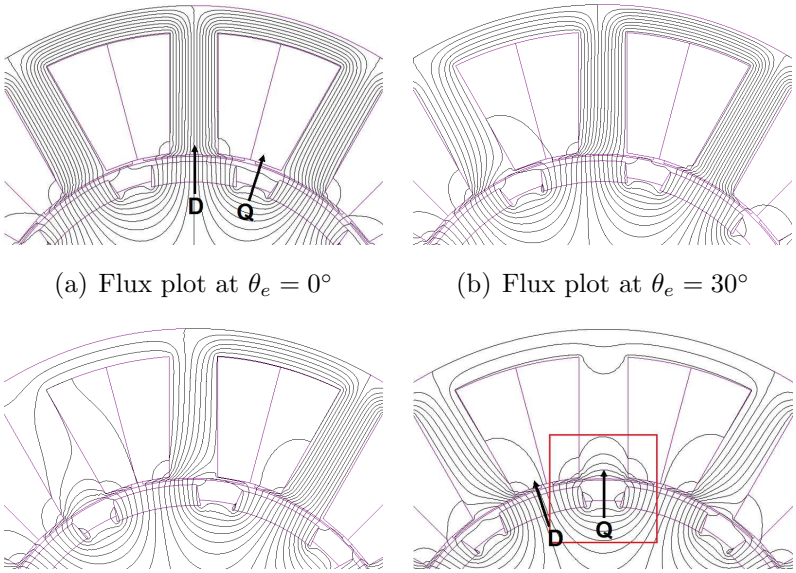

(a) Flux plot at $\theta_e = 0°$ (b) Flux plot at $\theta_e = 30°$

(c) Flux plot at $\theta_e = 60°$ (d) Flux plot at $\theta_e = 90°$

Figure 3.27: FEA simulation results demonstrating zigzag leakage flux

The best test design achieved was number nine, this topology had an inverse saliency at no load along with the lowest level of cogging torque. The flux plots in Figure 3.27 are from FEA simulations for version nine. They show the zigzag leakage flux fully induced when the Q-axis is perfectly aligned with the stator tooth at $\theta_e = 90°$. The level of zigzag flux changes with rotor position, a minimum occurs at $\theta_e = 0°$ corresponding to the D-axis alignment with the stator tooth. The peak occurs at $\theta_e = 90°$ when the Q-axis is aligned with the stator tooth. The red box in Figure 3.27(d) highlights the significant leakage flux occurring at

this point. This leakage causing additional saturation in the thin tooth bridges and causes the reduction to L'_q. After the peak at $\theta_e = 90°$ the level of zigzag leakage flux then decreases as the rotor continues rotating towards the following minimum.

The impact of the zigzag leakage flux on version nine can be seen clearly in Figure 3.28. Here in 3.28(a) the zigzag leakage flux is at its minimum value and therefore causes no noticeable influence. The magnetic flux plot in 3.28(b), where $\theta_e = 90°$, demonstrates the saturation in the tooth bridges caused by the peak value of zigzag leakage flux. The level of saturation is contributed to by the relative thickness of the tooth bridge which means it saturates easily.

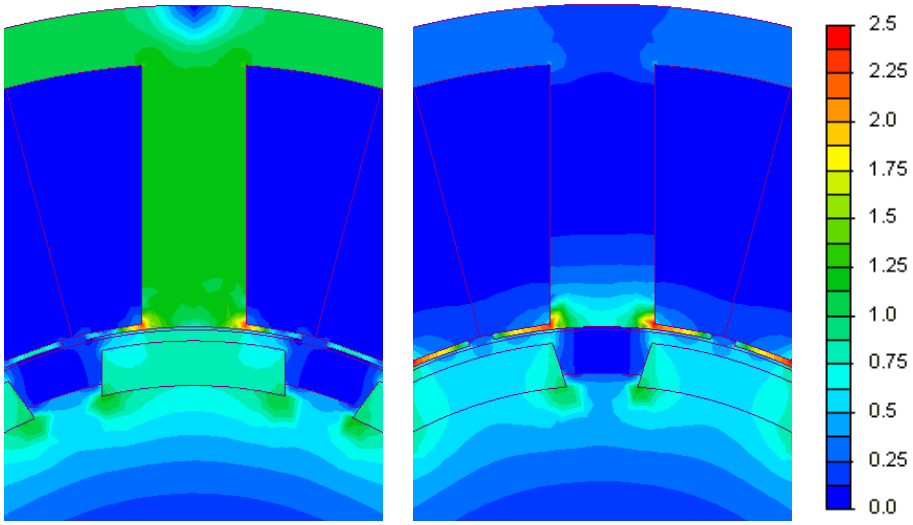

(a) B Plot at $\theta_e = 0°$ (b) B Plot at $\theta_e = 90°$

Figure 3.28: Magnetic flux density plots at two rotor positions

Despite this being the best test result the overall performance of the machine has reduced too much. In comparison to the reference machine there is an 11% drop in rated torque, while the level of cogging torque increases from a mere 0.14% up to 1.11%. As discussed above, the ability to design a machine with an inverse saliency is at desirable with regards to sensorless control. This approach unfortunately limits the machine performance to much to be a realistic design method, particularly associated with this form of 12s10p SPMSM topology.

3.10 Summary

The methodology to analyse self-sensing characteristics presented in this chapter enables them to be accounted for during initial design stages. The use of FE to calculate the HF inductance properties is faster and simpler than having to produce prototypes at each design iteration. There is also the added benefit of targeted saliency design, if a set machine topology is known to have certain negative saliency characteristics. This allows the FEA and design optimization to target specific aspects, such as saliency crossover point or the overall saliency ratio.

The various work presented in this chapter is focused on the impact of geometrical parameters have of machine properties. The research mostly investigated geometrical variations in the stator of an inset PMSM. The findings from the investigation into slot opening, tooth width and back iron thickness demonstrated how saliency characteristics can change. An important referencing point made throughout has been to consider the impact on fundamental machine performance whenever sensorless detection properties were enhanced. It was shown that although there is only a limited level of variation possible, without deteriorating fundamental performance, the sensorless detection properties can be positively changed. This suggests that a carefully selected combination of alterations to geometrical parameters can be used to optimized a machine topology for enhanced position detection capability.

It was demonstrated that the PM rotor poles do not influence the dominant saturation saliency within an inset PMSM topology. This was the case providing the amount of PM material was kept constant. This constant ensured that the amount of magnetizing flux created by the rotor poles was kept even. The level of saturation that takes place within the stator at set loads was therefore similar between the magnet span variations and instead the investigation reaffirmed the observation that it is the stator saturation saliency which is dominant in the HF saliency tracking.

The latter sections of this chapter looked at more novel approaches to improving sensorless position capability. Despite this they both followed traditional machine structures and wouldn't require major changes to production techniques. The two design approaches demonstrated promising improvements to saliency characteristics. The impact that each design had on fundamental machine performance was notable. The approach of an inherent reverse saliency proposed by the authors

of [33] is particularly interesting. Although the initial work to replicate the characteristic in a generic topology was not encouraging, the concept is ultimately the only guaranteed method to remove the danger of a zero saliency condition. For this reason targeting machine design to introduce an easily saturated Q-axis inductance path is a leading design option.

Chapter 4: Development of Variable Machine Topology

4.1 Introduction

This chapter provides the full details of the PMSM structural topology used for the optimization design routine. Throughout, all of the design decisions are justified based on one or several reasons. The design selections are based on cost, structural integrity, manufacturability and performance. The optimized design of the project is focused on surface-mount and inset rotor topologies. These are perceived as being poor selections for sensorless control due to their low natural saliency ratio.

The relatively small variation between the D and Q-axis flux paths is the primary cause of similar L'_d and L'_q values and therefore a small saliency ratio. Despite this inherent characteristic surface-mount and inset PMSMs are a popular choice for industrial servo machines. They offer a simpler rotor structure that is suited to mass production, high power density, lower rotor losses and improved PM utilization. The chapter describes the geometrical topology, material selection, slot/pole combinations and the thermal constraints used during optimization.

4.2 Automated Machine Design

A conventional approach to designing of electrical machines is illustrated by the flow diagram in Figure 4.1. The preliminary design specifications can be derived based on a specific objective such as an actuator or a more general operation from market research into various operational nodes. This will determine the significant performance requirements for the machine, with the operating conditions and duty also contributing factors. The second stage involves sizing the machine through traditional analytical equations based on electrical and magnetic loading [53]. During this stage additional machine parameters need to be considered such as slot/pole combination, rotor configuration, winding design, cooling method and construction materials.

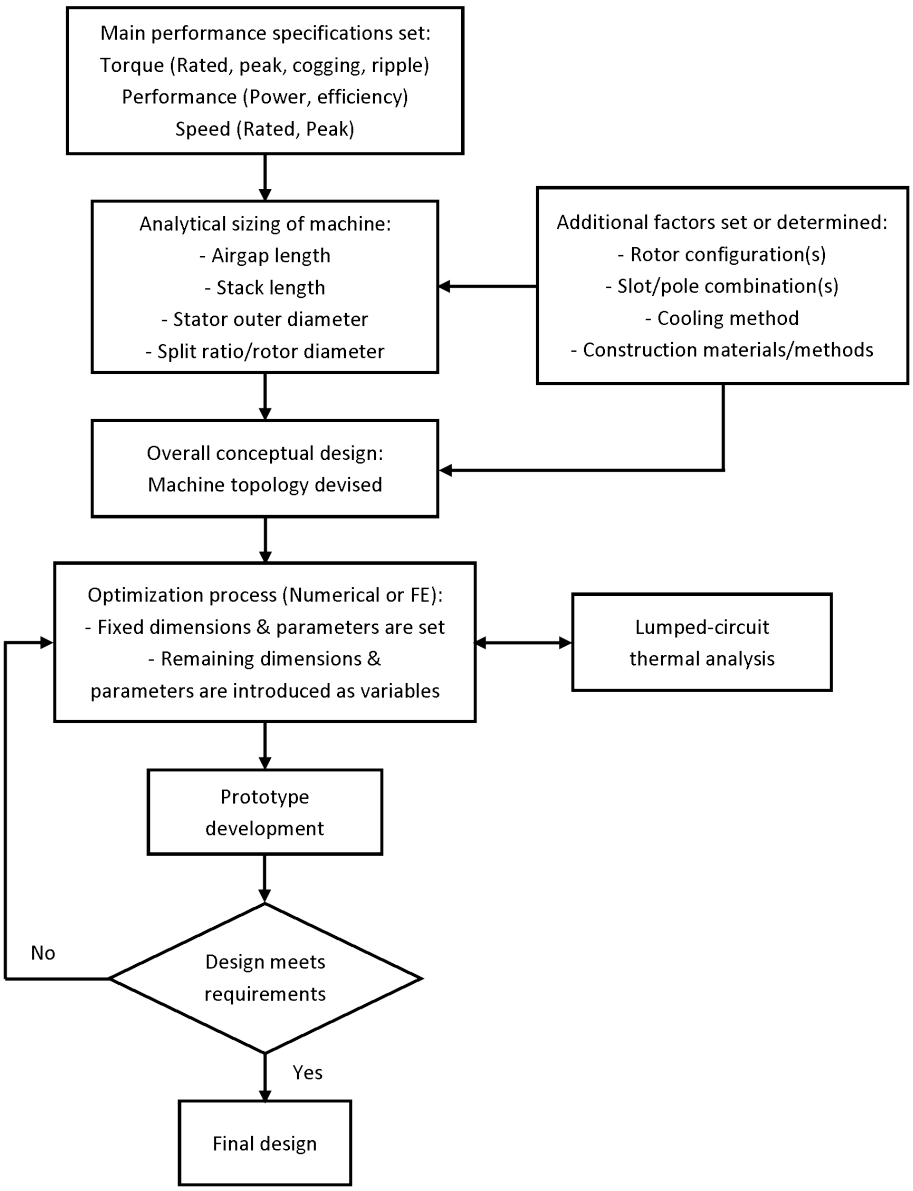

Figure 4.1: Conventional design process

With these factors in mind an overall conceptual design is devised where the main machine dimensions are taken into account when developing the machine topology, along with construction methods or restrictions. After completion of this stage the conceptual design is optimized based on the performance requirements, where thermal analysis plays a significant part. Prototype development follows, where experimental testing is used to feed changes back into the optimization process. This continues until a final design that meets the design specification is achieved.

The remainder of this chapter discusses the conceptual design of the machine

topology that will be optimized. The initial sizing of the machine was determined from existing commercial servo motor. The main focus of this project is centred on the optimization process within the overall design procedure illustrated in Figure 4.1. This firstly required a conceptual design to be used throughout the optimization and then to develop an appropriate optimization routine. During the development of the machine topology there was a emphasis on maintaining a generic design with conventional construction techniques.

4.3 Matlab Machine Script

The first stage of the optimization process involved developing a script in Matlab which allowed the machine topology to be remotely compiled in MagNet and enable parameters to be entered as variables. This script gradually evolved over time as further parameters were integrated into it to allow a more complete scripting process. The script was developed to consist of a traditional PMSM structure that enabled the slot/pole combination to be adjusted as well. The topology was adapted from the 12s10p machine used in Chapter 3 when investigating stator parameters. Due to the generic form of the topology great level of parametrization is possible, without altering the geometrical structure.

During the design process the majority of geometrical parameters were available as variables, excluding:

- Stack Length
- Airgap Length
- Stator Outer Diameter
- Shaft Diameter

These were fixed during the optimization so that the results could be easily compared with regards to size, weight and power density. The Airgap Length (AG), the distance from the outer rotor surface to the inner stator surface, was fixed to 0.75mm which is a practical value that ensures sufficient tolerance necessary for mass production.

The stator design was selected to use segmented teeth with double concentrated windings. This would mean a 50% packing factor (P_f) is easily achievable and the overall construction is simple to manufacture. The rotor topology consists of a

simple structure, ignoring any bore holes etc. that might be used to improve the inertia of the rotor. With this the basic topology was generated, incorporating numerous parameters within the script, as detailed in the ensuing sections.

4.3.1 Stator Design

The outer dimensions of the stator were fixed using a stack length and stator outer radius of 88mm and 67.5mm respectively. The stator inner radius is set based on the Split Ratio (SR) of the machine, which is a significant parameter in the overall script. This is calculated in the standard form as shown in 4.1, where SR = Split Ratio, SIR = Stator Inner Radius, SOR = Stator Outer Radius.

$$SR = \frac{SIR}{SOR} \tag{4.1}$$

The SR sets the inner boundary and therefore with this all external dimensions of the stator are established. Beyond this the tooth segment is parametrized to enable changes and optimization. The basic structure of an individual tooth segment is shown in Figure 4.2. It shows the inner and outer surfaces of the stator are defined using radial arcs, each set to their corresponding radial distance. The inner surface of the stator back iron is also defined in this way, with all arcs set using a variable radius from the centre of the shaft.

Flat edges are used for the ends of each tooth segment, defined with straight lines from the centre of the shaft separated by the slot span angle. The same principle is used to define the edge of each tooth bridge with the angle this time set as the deviation inside of the slot span. This therefore defines the degree of slot opening. The last feature of each tooth segment is the flat backed tooth bridge, set as a straight edge from the base of the tooth bridge to the tooth tip.

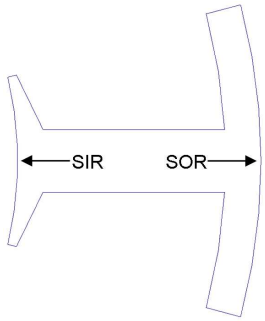

Figure 4.2: Segmented tooth design

The stator topology and segmented tooth design enables the following geometrical parameters to be scripted, and then be fixed or optimized depending on the requirement of the simulation.

- Slot Opening (SO) - defined in angular degrees, with the greater the angle, the larger the slot opening
- Tooth Width (TW) - defined in mm
- Tooth Tip (TT) thickness - defined in mm
- Tooth Bridge (TB) thickness - defined in mm
- Back Iron (BI) thickness - defined in mm

The nature of these variables mean that they all have upper and lower limits imposed upon them, whether it be due to structural demands, manufacturability or performance based.

The slot opening must be greater than 0 and less than the radial arc of the slot itself. The eventual upper limit is set so that there is sufficient tooth bridge available to support the nomex paper retention of the windings within the slot. The TW must be wide enough to offer structural integrity to the tooth construction, while from a performance point of view it also needs to be wide enough to prevent a high level of saturation. The same conditions also apply to the BI, Tooth Bridge (TB) and Tooth Tip (TT). Additionally, the TB must be greater than or equal to the TT due to tooth design. Previous work and standard machine design theory has shown that all of these dimensions impact on the overall machine performance, to varying extents. While they will also have varying levels of influence on the HF characteristics of the machine.

The stator parameters, along with the split ratio, completely define the tooth topology and consequently the stator slots. When formed into a complete stator they set the Slot Cross-sectional Area (A_{slot}). Assuming a constant packing factor of 50%, they also set the total Copper Cross-sectional Area (A_{cu}) of each slot. Since the double layer concentrated winding arrangement is also a constant throughout all the design iterations the level of electrical loading will change as the stator dimensions do. As with design processes there are many approaches considered with how to address setting the level of electrical loading.

- Keep constant current supply to windings and therefore current density in the slots varies.

- Adjust current supply depending on slot area to maintain constant current density.
- Adjust current supply to keep copper losses constant when copper area changes.
- Use a thermal equivalent circuit to determine a rated current; either at steady state or peak conditions.

The first two options offer the simplest solutions, however when making comparisons across various slot and pole combinations they are not advantageous. With the optimization process discussed later a constant current density and thermal equivalent model are both used.

The use of this segmented design allows the slot number to be easily changed when the script is compiled, meaning simulations can be performed on various slot combinations. The number of slots will set the slot span ($= 360/s$) and therefore the overall radial width of each tooth segment. This completely defines the stator dimensions and with that the rotor design can then be set.

4.3.2 Rotor Design

The overall dimensions of the rotor are set at the same point as the stator, firstly with an identical active stack length. The value of Slot Inner Radius (SIR) set by the SR is used to state the outer radius of the rotor, simply being $SIR - AG$. This is possible because of the fixed airgap length, characterized by the length from the inner most stator surface to the outer most rotor surface. As stated previously AG is a fixed at 0.75mm due to the tolerance required during mass production.

The rotor topology uses surface mount or inset PMs, where a variable parameter is used to define the amount the PMs are inset. Set from 0% which would signify a complete surface mount design to 100%, where the PM would be complete inset within the rotor lamination. This parameter could be a key driver in terms of saliency within the machine since it causes a geometrical variation between the D and Q-axis. This is why SPMSMs are generally regarded to have low natural saliency and considered poor from a sensorless control point of view. The rotor is designed such that the inset PMs will be self-retaining using the inter pole tooth segments.

The rotor back iron is designed as a single lamination for simplicity, while a generic

length of back iron is created between the outer surface of the rotor lamination and the shaft. With the fixed positioning of the DQ-axis on the rotor, removal of rotor back-iron to reduce inertia with bore holes could be done with minimal impact to performance during final design stages. When used in conjunction with the DL concentrated windings the stator flux does not interact with the rotor back-iron as much when compared to the distributed [54] and therefore becomes less significant.

The large back iron will remove any form of rotor back iron saturation in all slot/pole combinations. This structure therefore ignores the possibility of bore holes that are generally used to improve the inertia of the rotor. Traditionally these are positioned and sized so to have very little impact on the main rotor flux path. For the purpose of this optimization these are therefore ignored. In spite of this rotor bore holes offer the possibility of introducing a geometrical feature into the rotor for sensorless position detection [19].

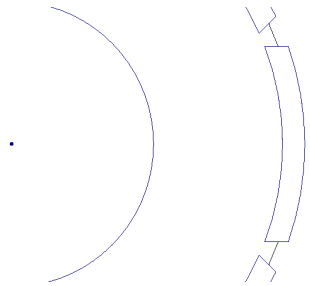

Figure 4.3: Section of rotor design

A small section of the rotor design is shown in Figure 4.3, it shows one rotor magnet with the ends of the two neighbouring magnets either side. The schematic demonstrates how the inner and outer surfaces of the PMs are defined using radial arcs defined as the radius from the centre of the shaft. While the edges are effectively machined flat off forming parallel edges; the inter-magnet segments of the rotor lamination are defined in the same way. This design is how if the rotor magnets are inset enough the rotor lamination is able to form the retention method. Finally the inner diameter of the rotor back iron is also shown, acting as the outer radius of the machine shaft.

The rotor topology presented above has been generated in a similar process to the stator to allow parametrization. This allows the following geometrical parameters to be scripted and then either fixed or variable depending on the needs of the optimization.

- Permanent Magnet Thickness (MT) - defined in mm
- MS - defined in angular degrees
- Permanent Magnet Inset (MI) - defined as percentage of MT from 0-100%

The last rotor variable required is the pole number that, as well as determining the number of poles, sets the upper boundary for the magnet span. This, with the stator dimensions and the above parameters defined the rotor can be compiled. At this point the complete machine topology is established. All of the variable stator and rotor parameters discussed are illustrated using the wire-frame model in Figure 4.4. The whole machine topology is then simply created with a repetitive pattern which depends on the number of slot for the stator and number of poles for the rotor. Finally, to reduce simulation time standard boundary conditions are imposed and to improve FEA the airgap is split up into four radial layers.

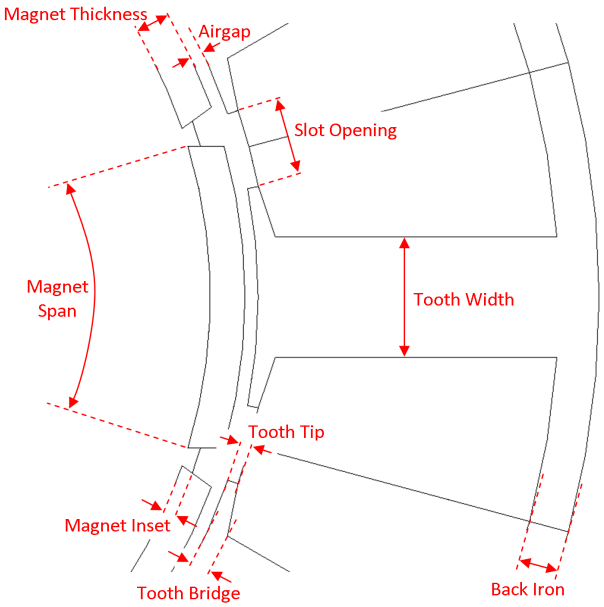

Figure 4.4: Variable geometrical parameters in Matlab machine script.

4.3.3 Material Selection

The various materials selected for the design process where used based on compromising between quality and cost. The choices were kept constant throughout all design topologies so that they wouldn't influence the results which are focused on the main geometrical and saturation saliencies in the machine. Non-oriented silicon steel (M330) is used for both the stator and rotor laminations due to its strong magnetic properties, low core losses and manufacturability.

The rotor uses rare earth PMs, in this case using a good grade of neodymium iron boron (N38). This choice allows for high power density and good protection against thermal degradation. The use of rare earth PM materials are a major cost driver within the machine and means the total PM volume needs to be considered during the optimization to limit elevated manufacturing costs. The stator windings are constructed using industrially standard copper windings and impregnation resin. The conductivity and thermal properties that this combination forms is the reason that it is the commercial standard.

During machine development there was a consideration of the HF characteristics that can contribute to losses and parasitic effects. Therefore the stator and rotor laminations were kept thin and the rotor poles are segmented to minimize any eddy currents induced.

4.3.4 Slot/Pole Combinations for Optimization

The machine scripting and development of the optimization routine was performed using a 12s10p topology as detailed previously. In order for the common trends to be investigated with regards to the impact of various geometrical parameters; the same machine script was adapted, along with the optimization routine. This meant a number of alternative slot/pole combinations could be investigated, all of which are standard selections for double layer concentrated windings. The number of combinations available were limited by general design rules that determine suitable ratios.

- Even number of poles
- Number of pole pairs (P), per section (F), must not be multiple of phase number. Where $F = gcd(s, P)$
- Number of poles cannot equal number of slots

It is also possible to determine a feasibility region for the number of slots per pole per phase (q), bounded by $0.25 < q < 0.5$. The fundamental winding factor (K_{w1}) for possible slot/pole combinations is shown in Table 4.1. The greyed out cells signify a slot/pole combination that does not satisfy the design rules. There are several winding factors that are poor in value compared to others and therefore have been discounted. In addition, several options suffer from unwanted magnetic pull due to the winding configurations used. The suitable design options selected are shown in the table in bold text.

s\p	8	10	12	14	16	18	20	22
9	**0.945**	0.945	0.866	q<0.25				
12	0.866	**0.933**		0.933	0.866	q<0.25		
15	q>0.5	0.866		0.951	0.951		0.866	q<0.25
18		q>0.5	0.866	0.902	**0.945**		**0.945**	0.902
21			q>0.5	0.866	0.89		0.953	0.953
24				q>0.5	0.866		**0.933**	**0.949**

Table 4.1: Winding Factor (K_{w1}) for DL Concentrated Windings

The fundamental winding factor is not the sole consideration when choosing suitable slot/pole combinations. There are a variety of other factors that can help determine suitability. A higher pole number requires a higher supply frequency and causes an increase in iron core losses. Meanwhile, a higher LCM for a given slot/pole combination results in a cogging torque of higher frequency and lower magnitude. The design options selected are in Table 4.2, along with their corresponding K_{w1} for DL concentrated windings and LCM.

s	p	LCM	K_{w1}
9	8	72	0.945
12	10	60	0.933
18	16	144	0.945
18	20	180	0.945
24	20	120	0.933

Table 4.2: Comparison of Slot/Pole Combinations

As with the 12s10p topology, the stack length, airgap length, stator outer diameter and rotor inner diameter were all fixed. This maintained some consistency between each machine and allowed for direct comparison.

4.3.5 Phase Windings

The three-phase DL concentrated winding configuration for the 12s10p machine is shown in Figure 4.5, this also clearly illustrates the whole topology. The decision to use double layer concentrated windings was made due to the numerous advantages they present over distributed and single-layer concentrated windings. This also follows a recent trend in industry to begin implementing them more often. When used in conjunction with the segmented stator design a high slot packing factor (P_f) of 50% is a practically achievable value for mass production

and exceeds that of distributed windings. The stator construction process is also simpler, since the phase windings can be wound using a bobbin machine onto individual teeth [54]. Then put together to form the overall stator with the necessary inter-phase nomex insulation in place.

There are additional benefits gained from using DL windings, they still achieve high winding factors and create a large reduction in end winding length. This typically leads to a drop in copper losses compared to distributed windings but also reduces the amount of copper required. The reduction in copper losses leads to increased efficiency and power density [55]. While a significant reduction in copper volume contributes to a reduction in cost compared to distributed windings.

The two forms of concentrated winding, single-layer and double-layer, can be characterized by the number of coils per slot. A single-layer winding involves a single coil wound around alternating stator teeth, this means that each side of a coil fills adjacent stator slots. In comparison, a double-layer winding has each tooth wound with a single coil, this results in two sides of neighbouring coils per stator slot. A DL concentrated winding configuration offers a great selection of suitable slot/pole combinations compared to single-layer options; broadening the application range. The configuration generates a more sinusoidal B-EMF with lower rotor losses and a further reduction in end-windings, [55, 27]. There has been research regarding concentrated windings and sensorless capability, which in general has demonstrated they are a good choice ([15],[27],[33]).

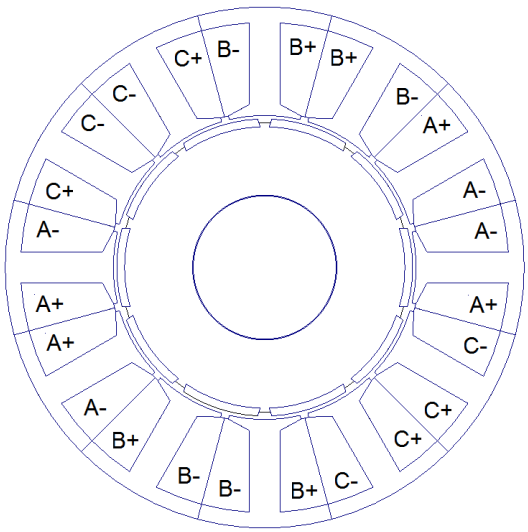

Figure 4.5: Double layer winding configuration for 12s10p configuration

The number of turns for the phase windings is set for each slot/pole combination. The reason for this is firstly to account for the large variation in slot area. Secondly, the number of turns varies to ensure a strong value for the no load B-EMF for each option. This means that the peak induced B-EMF is limited to account for the drive capabilities.

4.4 Equivalent Thermal Model

It was decided that all topologies would be simulated under steady state rated conditions. In order to calculate the rated load for each design iteration, under steady state conditions, an equivalent thermal model was developed for the machine topology as as part of the project. The equivalent thermal model is shown in Figure 4.6. This equivalent thermal model was integrated into the scripting process to calculate the rated load. Due to the symmetry of all the topologies investigated the thermal circuit was simplified and only half a tooth pitch section was modelled. As well as this, the circuit only accounts for the stator components of the machine, the model ignored the rotor and airgap due to the insignificant amounts of losses which occur here compared to copper and iron losses in the stator. Evaluating the equivalent model under steady state conditions means that the heat capacitances of each node do not need to be calculated.

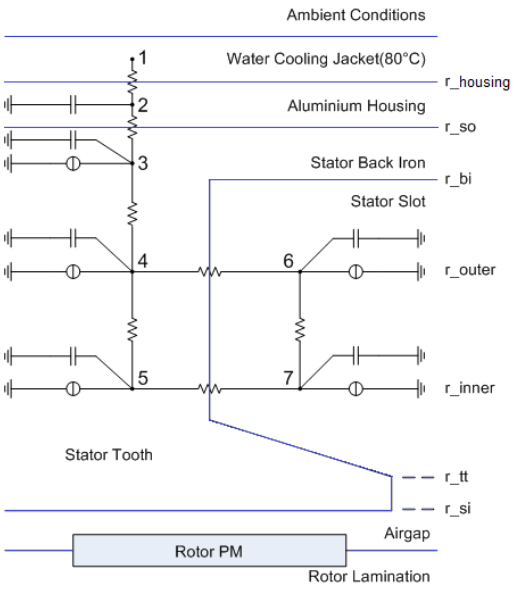

Figure 4.6: Equivalent thermal model of half slot/tooth sector.

The nodal circuit allows the steady state rated load to be estimated quickly during

the optimization routine. In order to resolve the equivalent thermal model the following assumptions were made.

- Machine is rotationally symmetrical and therefore only half a tooth pitch is modelled
- Steady state conditions, heat capacitances can be ignored
- Rotor losses insignificant do to SPMSM design
- Constant temperature boundary condition

All topologies are cooled using a water jacket around a standard aluminium housing. This water channel is assumed to be kept constant at $80°C$. With this assumption in place the heat transfer coefficient from the machine frame to the water jacket can be calculated. With a constant stack length of 87.6mm and assuming a velocity of $4ms^{-1}$ the heat transfer coefficient is calculated using Equation 4.2, this is a standard approximation obtained from [53]. This can then be converted into the equivalent thermal resistance for convection using Equation 4.3.

$$h_{conv} = 3.89\sqrt{\frac{\nu}{l}} = 26.29W/m^2/K \tag{4.2}$$

$$R_{th\_conv} = \frac{1}{h_{conv}A} \tag{4.3}$$

In order to use the equivalent thermal model, the uncertainty with the thermal properties of the slot windings has to be addressed. In this case the equivalent thermal conductivity of the slot windings, k_w, can be approximated by taking into account the thermal properties of both the copper winding and impregnation resin. Here a well devised approximation from [56] has been used as shown in Equation 4.4. The combination of copper and resin, within the slots, is equated to a uniform thermal conductivity. This is based on their respective thermal conductivities and the slot packing factor, P_f. P_f is fixed at 50% since this is a practical value for mass production of a machine with this form of construction.

$$k_w = \frac{k_{cu} \cdot k_r}{(P_f \cdot k_r) + (1 - P_f) \cdot k_{cu}} = \frac{386 \cdot 0.3}{(0.5 \cdot 0.3) + (1 - 0.5) \cdot 386} = 0.5995 \tag{4.4}$$

The nodal network formed in the equivalent thermal model (Figure 4.6) is used to calculate a steady state rated load. The thermal resistances are broken down from node to node before forming the conductance matrix, A. The equivalent thermal resistances that make up the whole nodal circuit are calculated using the

thermal resistance equation for conduction, Equation 4.5.

$$R_{th\_cond} = \frac{t}{hA} \tag{4.5}$$

The node to node thermal paths can be segmented into individual thermal resistances before summing the total in series. The thermal resistances for the seven node circuit are detailed below in Equations 4.6 - 4.12.

$$R_{12} = R_{12\_1} + R_{12\_2} \tag{4.6a}$$

$$R_{12\_1} = \frac{1}{h_{conv} \cdot A_{conv}} = \frac{1}{26.29 \cdot A_{conv}} \tag{4.6b}$$

$$R_{12\_2} = \frac{t_{housing}}{k_{housing} \cdot A_{housing}} = \frac{t_{housing}}{209 \cdot A_{housing}} \tag{4.6c}$$

$$R_{23} = R_{23\_1} + R_{23\_2} + R_{23\_3} \tag{4.7a}$$

$$R_{23\_1} = \frac{t_{housing}}{k_{housing} \cdot A_{housing}} = \frac{t_{housing}}{209 \cdot A_{housing}} \tag{4.7b}$$

$$R_{23\_2} = \frac{EIG_{Fe-Al}}{EIC_{Fe-Al} \cdot A_{so}} = \frac{0.000035}{760 \cdot A_{so}} \tag{4.7c}$$

$$R_{23\_3} = \frac{t_{bi}}{k_{stator} \cdot A_{so}} = \frac{t_{bi}}{28 \cdot A_{so}} \tag{4.7d}$$

$$R_{34} = \frac{t_{34}}{k_{stator} \cdot A_{34}} = \frac{t_{34}}{28 \cdot A_{34}} \tag{4.8}$$

$$R_{46} = R_{46\_1} + R_{46\_2} + R_{46\_3} \tag{4.9a}$$

$$R_{46\_1} = \frac{t_{tooth}}{k_{stator} \cdot A_{tooth}} = \frac{t_{tooth}}{209 \cdot A_{tooth}} \tag{4.9b}$$

$$R_{46\_2} = \frac{t_{liner}}{k_{liner} \cdot A_{liner}} = \frac{t_{liner}}{0.11 \cdot A_{liner}} \tag{4.9c}$$

$$R_{46\_3} = \frac{t_{slot}}{k_{w} \cdot A_{slot}} = \frac{t_{slot}}{0.5995 \cdot A_{so}} \tag{4.9d}$$

$$R_{45} = \frac{t_{45}}{k_{stator} \cdot A_{45}} = \frac{t_{45}}{28 \cdot A_{45}} \tag{4.10}$$

$$R_{57} = R_{57\_1} + R_{57\_2} + R_{57\_3} \tag{4.11a}$$

$$R_{57\_1} = \frac{t_{tooth}}{k_{stator} \cdot A_{tooth}} = \frac{t_{tooth}}{209 \cdot A_{tooth}} \tag{4.11b}$$

$$R_{57\_2} = \frac{t_{liner}}{k_{liner} \cdot A_{liner}} = \frac{t_{liner}}{0.11 \cdot A_{liner}} \tag{4.11c}$$

$$R_{57\_3} = \frac{t_{slot}}{k_w \cdot A_{slot}} = \frac{t_{slot}}{0.5995 \cdot A_{so}} \tag{4.11d}$$

$$R_{67} = \frac{t_{67}}{k_w \cdot A_{67}} = \frac{t_{67}}{0.5995 \cdot A_{67}} \tag{4.12}$$

The heat sources within the stator are calculated using the equations for both copper loss and iron loss. The copper loss is calculated with I^2R losses within the slots, where the rated I_{rms} is used along with resistivity for the steady state operating temperature of 120°. The P_f is used to account for the resin within the slot as shown in 4.13, along with assuming a solid conductor.

$$P_{cu} = I_{rms}^2 \cdot \left(\frac{\rho_{120}}{P_f} \cdot \frac{l_{stack}}{A_{slot}} \right) \tag{4.13}$$

The iron loss is estimated using calculations for both hysteresis and eddy current losses. The hysteresis losses are calculated using 4.14 where the result is in W/kg and therefore is multiplied by the amount of iron to obtain power loss. Equation 4.15 is used for estimating the eddy current losses; the result is in W/kg and so must be multiplied by the amount of iron involved. The first part of the equation estimates classical eddy current losses, while the second part is for excess eddy current loss. The two parts both assume that the flux density within the iron is varying sinusoidally. Finally, the total iron losses is calculated from equation 4.16 and is the total sum of all eddy current and hysteresis losses.

$$P_h = k_h f B_m^{\alpha} \tag{4.14}$$

$$P_e = \frac{d^2\pi^2}{6\rho\delta} f^2 B_m^2 + 8.67 k_e f^{1.5} B_m^{1.5} \tag{4.15}$$

$$P_{fe} = P_h + P_e \tag{4.16}$$

The thermal network is solved using the matrix relationship in Equation 4.17.

$$AX = B \tag{4.17}$$

Each of the matrices are defined in Equations 4.18 - 4.20. The conductance matrix (A) is created by the thermal conductances (G) associated with each node. Since conductance is the inverse of resistance each of the nodal thermal resistances are inverted before being put into the conductance matrix, therefore $G_2 = \frac{1}{R_2}$. The

heat source matrix (B) is created from all of the power losses associated with each node in the thermal circuit. These are known values calculated using estimated power losses. The relationship of the thermal matrix equation means that the temperature matrix (X) can be solve using A and B. The temperature matrix (X) is made up of each of the thermal temperatures at each node within the circuit. The design routine requires the steady state rated load to be calculated and is done so within a while loop. The loop incrementally increases the rated load until the peak steady state winding temperature is reached, where by the loop is exited and the last successful iteration is used. The servo motor design, using moderate quality materials means that a steady state winding temperature of 120° was set for all slot/pole combinations.

$$A = \begin{bmatrix} G_2 & -G_23 & 0 & 0 & 0 & 0 \\ -G_32 & G_3 & -G_34 & 0 & 0 & 0 \\ 0 & -G_43 & G_4 & -G_45 & -G_46 & 0 \\ 0 & 0 & -G_45 & G_5 & 0 & -G_57 \\ 0 & 0 & -G_46 & 0 & G_6 & -G_67 \\ 0 & 0 & 0 & -G_57 & -G_67 & G_7 \end{bmatrix} \tag{4.18}$$

$$X = \begin{bmatrix} \theta_2 \\ \theta_3 \\ \theta_4 \\ \theta_5 \\ \theta_6 \\ \theta_7 \end{bmatrix} \tag{4.19}$$

$$B = \begin{bmatrix} 0 \\ P_{BI} \\ P_{Tooth} \\ P_{Tooth} \\ P_{cu} \\ P_{cu} \end{bmatrix} \tag{4.20}$$

The use of this thermal equivalent circuit allows all of the topologies to be simulated at steady state rated load and means that comparisons can be formed across the various slot/pole combinations.

4.5 Design Constraints and Requirements

The specifications within Table 4.3 depict the various structural, material and operational requirements that need to be met by an optimized design. The aim is with the available machine topology and slot/pole combinations that these targets can be exceeded. The fundamental performance of the machine, must be able to satisfy the rated condition of 30Nm at 3000rpm and the peak condition of 45Nm at 2000rpm.

Structural and Material Constraints	Stator Outer Radius	67.5mm
	Active Stack Length	87.6mm
	Shaft Radius	$\leq$ 30mm
	Airgap Length	0.75mm
	Stator Lamination Steel	M330/50A
	Rotor Lamination Steel	M800/50A
	Permanent Magnet Type	NdFeB38
	Permanent Magnet Shape	Radial (Segmented)
	Permanent Magnet Volume	Fixed
	Slot Packing Factor	50 %
	Constant boundary temperature	80°
Performance Requirements	Rated & Max Torque	30 / 45 Nm
	Cogging Torque (Pk-to-Pk)	0.3 Nm (1 % Rtd)

Table 4.3: Machine Design Specifications

This forms the operational envelope for which sensorless control must be possible throughout. The specifications shown in the table are based on a standardized industrial servo motor.

4.6 Machine Scripting Flow Diagram

With the machine design finalized, the flow diagram in Figure 4.7 illustrates the scripting process that will be embedded within the GA optimization routine. The process begins with the GA assigned values to each of the design variables based on the population generated. With these values set the machine model is construction within MagNet and then simulated at a predetermined loading, speed and duration. The results are then called by Matlab for the fitness of iteration to be calculated before the process begins again for the next iteration.

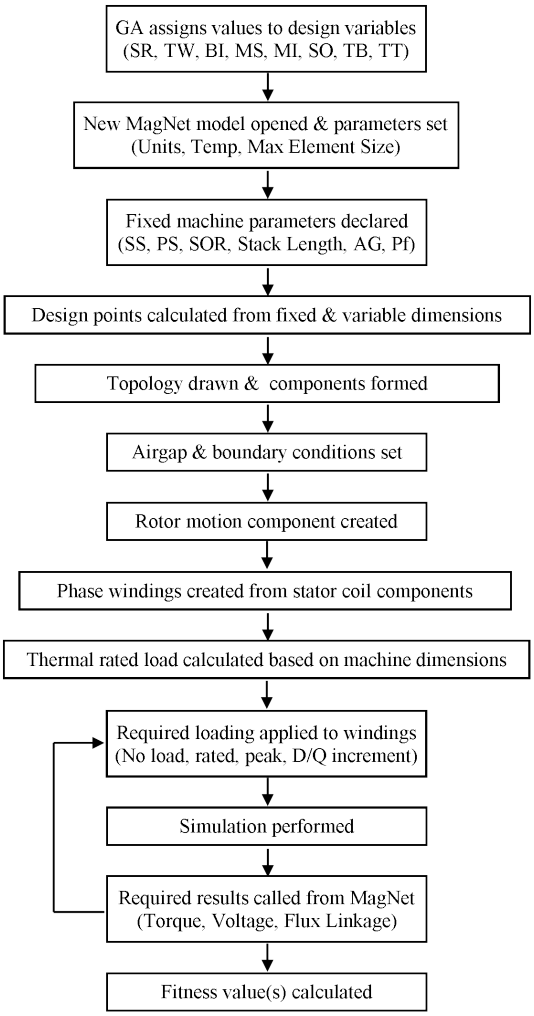

Figure 4.7: Flow diagram of machine scripting process

4.7 Summary

The complete PMSM topology presented during this chapter was formed into an automated script for each configuration, incorporating all of the discussed variables. In this form the structure can be manipulated easily within an optimization routine for all of the suggested slot/pole combinations. The common structural design, construction materials and thermal restraints are set across all available combinations. This ensures simple comparison of fundamental performance and optimization trends. In combination with the performance requirements all optimization results can be reviewed for suitability as well as analysed for design routine purposes.

Chapter 5: Development of Optimization Design Process

5.1 Introduction

This chapter presents the data and decisions used to develop the various optimization routines within the project. The routines were all based on GA optimization to find the global minimums (or maximums) through the design process. The decision to use GAs does not limit the range of options available for the design routine. They have the ability to optimize single or multi-objective problems, in single or multi-stage processes. In the following sections the structure of each optimization routine is generated and each reasoned decision is justified. Finally, a complete machine optimization is presented before the full results in the next chapter.

5.2 GA Optimization

GAs have been used for numerical optimization since their introduction in the 1970s, their popularity is based on the ability to find a global minimum (or maximum) based on natural selection and evolution. They benefit from exploring the whole search space for global optimums and do not narrow on a local optimum which can happen with alternative numerical methods.

5.2.1 GA Optimization Process

A GA mimics biological evolution by using natural selection to continuously modify a population of individuals. An individual is made up of a set of values for all the optimization variables (referred to as genes), with a population consisting of a set number of individuals. A fitness function is created for the GA process which is used to evaluate the fitness of each individual in the population. The fitness function is closely linked to, or is, the desired characteristics to be optimized, e.g. mean torque production. For the initial population the values assigned to each individual are done randomly and then the fitness of all individuals is calculated.

In order to generate the next (new) population for the following generation of the GA, three main processes are performed on the current population:

- Selection, here individuals are selected and carried over into the new population, this can be based on elitism and therefore a set number with the best fitness values are selected. Alternatively those with the worst fitness values can be discarded. Two popular forms of sampling are used here, stochastic, where the best individual(s) can be selected several times or deterministic, where the best and worst can only be selected once.
- Crossover, here two randomly selected individuals in the new population are mated together. Once again a random process is used to set a point along the individual, after this line the genes of each individual are swapped. This process is performed at a defined probability, known as the crossover rate (P_c), careful selection of this rate is required as a low crossover rate will create a constricted, ineffective search. Meanwhile a high crossover rate will cause greater disruption of good individuals, generally a crossover rate of 0.6-0.8 is used.
- Mutation, here a single parent is selected at random and changed. Similar to crossover, this is performed at a defined probability, known as the mutation rate (P_m). Generally this rate is relatively small (<0.1). Mutation helps the search process avoid loss of potentially useful genetic data and prevents a premature convergence.

After the population has been evaluated and selection, crossover and mutation have taken place a new population is created. This population is carried over to the following generation of the GA and then the whole process is repeated until the stopping criteria is met as shown in Figure 5.1. A detailed procedure for the third process in the routine where the fitness of all individuals is calculated is based on the flow diagram presented in Figure 4.7 of Chapter 4.

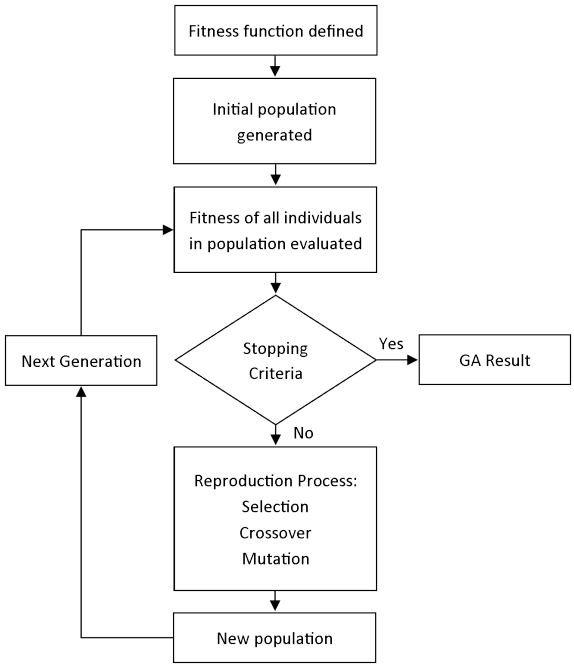

Figure 5.1: Flow chart of GA optimization process.

5.2.2 Selection of GA Operation Parameters

There are several parameters considered when refining a GA process. Each one influences the individuals selected for the next generation and the children these parents produce. The combination of values assigned to these variables will ultimately impact on the speed of convergence and quality of result. Sensitivity analysis of the following parameters is required.

- Fitness Function, this is set as the objective function that is to be minimized (or maximized). E.g. to maximize mean torque production, fit=1/mean(torque)
- Number of Variables, this is the number of variables in each individual and ultimately all the variables that are to be optimized. The machine script has eight available variables.
- Boundaries, this sets the upper and lower boundaries for each variable that makes up an individual. E.g. split ratio has a lower boundary of 0.55 and upper boundary of 0.65.
- Population Size, this selection has a major impact on the quality of GA result; a larger population of individuals will generally produce an improved result, however it will also greatly increase computation time. In the optimization process this is declared as the number of individuals (N_{ind}).

- Number of Generations, this is a stopping criteria which sets the maximum number of generations (G_{max}) the GA will perform, more generations will allow for greater convergence but increase computation time.
- Elitism/Generation Gap, this specifies the number of individuals with the best fitness that will be carried over to the next generation. The terms essentially cover the same process but can be implemented as an elitism fraction which dictates the amount of the population that survives the next cycle or as a generation gap (G_{gap}) which dictates the amount of the population that is replaced each cycle.
- Crossover Rate, this specifies the rate (P_c) at which the next generation are produced using crossover reproduction.
- Mutation Rate, this specifies the rate (P_m) at which the next generation are produced using mutation reproduction.

The fitness function, number of variables and their corresponding boundaries are predetermined by the focus of the GA; however, the remaining parameters need to be derived specifically for each optimization routine.

5.2.3 Single vs Multi-Stage Optimization

Optimiation can be performed in a number of forms, including the ability to use multiple stages of optimization during a single process. Single-stage optimization is the simplest form of optimization and is completed using a single routine. Here the GA optimizes a given set of variables (genes) to a global solution. Multi-stage optimization runs consecutive single-stage routines before outputting a final solution. Each stage requires a set of variables and an objective function. The multi-stage format presents various advantages, since each stage of optimization the variables can be targeted towards the objective before the following stage targets a new objective. The order of the stage objectives needs careful consideration, so too does the extent of which the variables can be optimized. After each of the stages the new variables should have smaller boundary conditions implemented upon them, this will go some way to limit the impact the next optimization will have on the previous stage outcome.

5.2.4 Single vs Multi-Objective Optimization

A GA optimization process searches and reproduces a given population in order to find a global minimum solution, while inverting the objective function allows the process to find a global maximum. The target objective can be a simple function (e.g. maximize torque) or a complex multi-objective function. The advantages of a single-objective optimization are that the process has a single target and is more likely to find a global solution, while using a relatively low amount of computational effort to do so. However, the process can only optimize for a single objective, which in many situations is insufficient. To overcome this a multi-stage approach can be introduced using single objectives, although this would increase computational time for the whole process. A multi-objective process will simultaneously optimize two or more objectives, that are often conflicting.

The nature of multi-objective optimization means that during the evolution of solutions as one objective is improved further, one or more other objective will suffer as a result. At the end, during the decision making process, the results are analysed on a 2D scatter plot (for two objectives) or a 3D surface plot (for three objectives). Here suitable solutions are selected based on a compromise for each objective function. The decision requires selecting the solution which satisfies all objectives or using predetermined weighting for set objectives. This form of GA optimization can be advantageous in situations where a target objective is required to be minimized (or maximized), while at the same time meeting certain design levels or limits. For example, optimizing for maximum torque production, while ensuring cogging torque stays below a threshold of 1% or the overall efficiency stays above a threshold of 95%.

5.3 Selection of GA Design Parameters

Although there are several variables available within the machine script for the GA process the number used during optimization needs to be refined so that a practical solution can be reached. An overall optimization routine must be assigned practical boundaries, constraints and objectives in order to work towards a global optimum both accurately and efficiently. The broad scope that has been designed into the overall machine script allows for a large amount of customization. The choice of fitness function, whether single or multiple, has to be prioritized so the main objectives are targeted. Despite this, even without be-

ing an optimization objective, additional factors or parameters can be accounted for through child based functions or manipulating constants. In this section the various objectives available for optimization are discussed, along with additional constraints that can and will be implemented.

5.3.1 Optimization Objectives

There are several options when considering which fundamental machine properties to use in the GAs fitness function. Generally the following can be considered as traditional, practical and clear performance indicators.

Overall Performance Drivers

- Efficiency
- Machine Losses
- Torque Production (Rated / Peak)
- Torque Quality (Ripple / Cogging)
- B-EMF (Peak and/or Quality)
- Size and Weight
- Cost

The list above provides a broad range of options, several of which are suitable for this projects purpose. The main concern within this project is to enhance self-sensing characteristics with limited impact on fundamental performance. Torque production and quality are considered to be the most essential performance drivers to fundamental performance. The machine script developed has a defined structural limit and therefore size can easily be disregarded. Taking this into account and the fact that all geometrical variables used will have practical boundaries imposed it can be assumed that both weight and cost will be similar across all design iterations. This means that they can also be disregarded as design objectives. The optimization is focused on self-sensing characteristics and the FEA simulations target this, due to this efficiency and losses are ignored since it would increase computation time and possibly require additional simulations. The B-EMF presents an additional option to torque and is an important factor

within machine design. In order to analyse fundamental performance it was decided that torque production would be used during a single objective approach. A multi-objective approach would optimize for torque ripple and cogging torque as well since this could be obtained easily from the same, or similar, simulations.

The sensorless capability of a machine topology can be summarized with three main saliency characteristics. This is when concerned solely with estimated position detection using HF injection methods.

Self-Sensing Performance Drivers

- Saliency Ratio
- Saliency Crossover Point
- Saliency Ripple

The saliency ratio is the most practical choice for an optimization objective, since it is the fundamental requirement for HF injection methods, while it impacts on the speed and accuracy of control. This saliency ratio of a machine can be calculated at various loading points but in order to reduce the computation time of optimization it is best to select the most significant loading point, i.e. when it is at it's lowest in the loading range. For this two approaches can be used. The first is to optimize for an inverse saliency calculate the saliency ratio at no load as it is the worst case operating point and the saliency ratio theoretically increases with load.The second option is to maximize the saliency ratio at peak loading. For this design approach, peak loading represents the worst case loading point where the saliency ratio will be at its lowest having suffered from Q-axis saturation. The level of ripple can influence the accuracy of the control scheme and can also determine the amount of signal processing required for position estimation. This means it is a good choice for an objective within a multi-objective approach but would not be used as a single objective.

Optimization Constants

The nature of the design optimization requires controls in place to ensure consistency throughout the process. Constants across iterations allow control over essential performance targets or cost drivers. Instead of optimizing this condition

the design is implemented so that the constant is guaranteed. The following offer sensible design constants, with the design process using one or all of the them.

- Copper Loss (I^2R Losses) - Not used during the optimization routine
- Current Density / Electrical Loading - Not used during the optimization routine
- Maximum Winding Temperature - Implemented for the optimization routine
- PM Volume - Implemented for the optimization routine
- Construction materials and methods - Implemented for the optimization routine

5.4 Two Stage, Single-Objective Optimization Routine

The following sections outline the procedure that was undertaken to create a two stage, single objective optimization routine. The two stage approach was devised for the overall optimization of the machine. During the first stage, the main geometrical topology is defined by optimizing with regards to overall performance. Following this the resultant dimensions are fixed and the remaining variables are used during a secondary optimization process to improve self-sensing characteristics.

5.4.1 Stage One

The first stage focuses on optimizing the overall machine topology with regards to general machine performance. Torque production would be the main parameter used for stage one optimization, this meant the fitness function was selected as $FF = \frac{1}{\overline{T}_r}$, to maximize mean torque production. The initial selection of variables for stage one was therefore based on those that significantly impact on overall torque production, SR, TW, MT, MS. The GA routine was carried out under a variety of conditions and produced some clear results. As expected when optimizing for greater torque production the best objective values were obtained at the upper boundaries of MT and MS. Higher values for these variables resulted in increased PM volume (as well as cost) and consequently greater torque production. This meant the natural selection of GA eventually only selected

values on the upper boundary of both of these variables. This is clearly indicated in Figure 5.2, where the data is from one of the initial GA tests carried out. Once selection has taken place over approximately ten generations the GA only produces children using values for MT and MS very close to their respective upper boundaries.

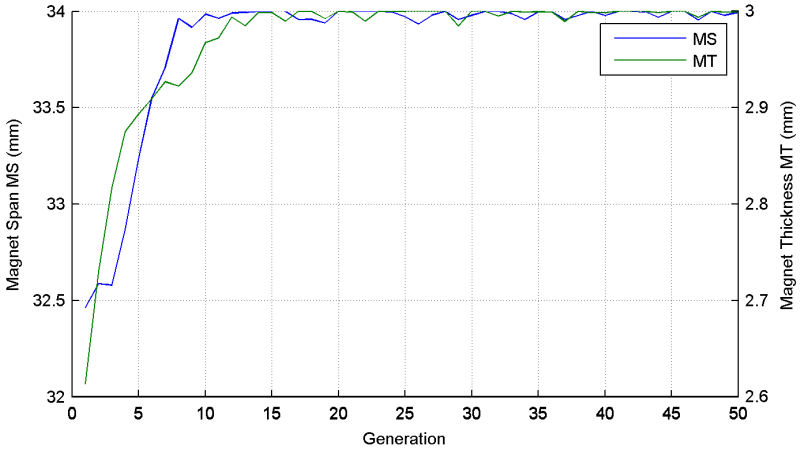

Figure 5.2: Average value for selected individuals per generation

Using these findings the machine script was adjusted so that the variable dimension, MT, was a function of MS. The function was created using a constant PM cross-sectional area as shown in Equation 5.1. From this, since all of the available topologies had the same active stack length, a constant total volume of rotor PM material would be set for all topologies. This would result in fair comparison between topologies since the amount of PM material used contributes a significant cost of the overall machine. Given that MT was changed to be a function of MS it was removed as a variable for stage one, leaving MS as the single rotor based variable.

$$MT = r_o - r_i = r_o - \sqrt{r_o^2 - \frac{360 \cdot A_{PM}}{MS \cdot \pi}} \tag{5.1}$$

$$r_o = SIR - AG \tag{5.2}$$

With the removal of MT, the variable for stator back iron, BI was set as the fourth variable for the first stage of optimization. This decision was due to the influence back iron thickness has on the main flux path in the stator. This point in the flux path can often cause a bottleneck condition, which would have a detrimental impact on the overall machine performance.

With the number and type of variables set for stage one of the optimization routine the upper and lower boundaries were set. The values assigned for each

boundary, shown in Table 5.1, were based on realistic selections influenced by electromagnetic principles, structural integrity and manufacturability. All initial testing and consequent refinement of the GA routine was carried out on the 12s10p topology.

Variable	Lower	Upper
SR	0.55	0.65
TW	6.0mm	11.0mm
MS	26.0°	34.0°
BI	3.0mm	6.0mm

Table 5.1: Boundary conditions for stage one variables

The main structure of the GA process is set with the initial decision to use a single objective optimization for overall torque production at rated load. With these in place the GA routine was performed repeatedly under various changing parameters to test the effectiveness of the optimization. The influence on the quality of result was investigated for the N_{ind}, P_c and P_m. Throughout this testing phase the GA was set to complete 50 generations, this enabled the best quality results to be examined further to determine if suitable convergence took place at a point below 50. In addition a fixed G_{gap} of 0.9 was used to ensure an adequate number of best individuals survived future generations without limiting evolution through crossover and mutation.

A summary of the results is shown in Table 5.2, where the best objective, using minimum based optimization is calculated as the inverse of mean torque production. An overview of the results in Table 5.2 shows how an increase in N_{ind} improves the quality of the GA result marginally, although as discussed previously the duration of the optimization greatly increases. The influence of the P_c and P_m can been seen in the table, but it is clearer when analysing the evolution of the best objective through generations.

N_{ind}	P_c	P_m	Best Objective ($\frac{1}{T_r}$)	Ref
25	0.6	0.05	0.0338	A
		0.1	0.0337	B
	0.75	0.05	0.0337	C
		0.1	0.0337	D
	0.9	0.05	0.0337	E
		0.1	0.0338	F
50	0.6	0.05	0.0337	G
		0.1	0.0337	H
	0.75	0.05	0.0337	I
		0.1	0.0337	J
	0.9	0.05	0.0337	K
		0.1	0.0337	L
75	0.6	0.05	0.0337	M
		0.1	0.0337	N
	0.75	0.05	0.0337	O
		0.1	0.0337	P
	0.9	0.05	0.0337	Q
		0.1	0.0337	R

Table 5.2: Best objective value obtained with given N_{ind}, P_c and P_m

The progression of the best objective value over the 50 generations is shown in Figures 5.3, 5.4 and 5.5 and is a better illustration of the influence of P_c and P_m. The quality of result from half of those with 25 individuals are not sufficient, Figure 5.3 shows that the variants A and F converge to a poor result, while B is particularly slow to converge before reaching a competitive objective value. The best objective value is achieved by D, which uses $P_c = 0.75$ and $P_m = 0.1$, although interestingly it converges to this value relatively late at generation 43. Therefore another important result to note from this group is E, which uses $P_c = 0.9$ and $P_m = 0.05$ to converge well and after only 33 generations.

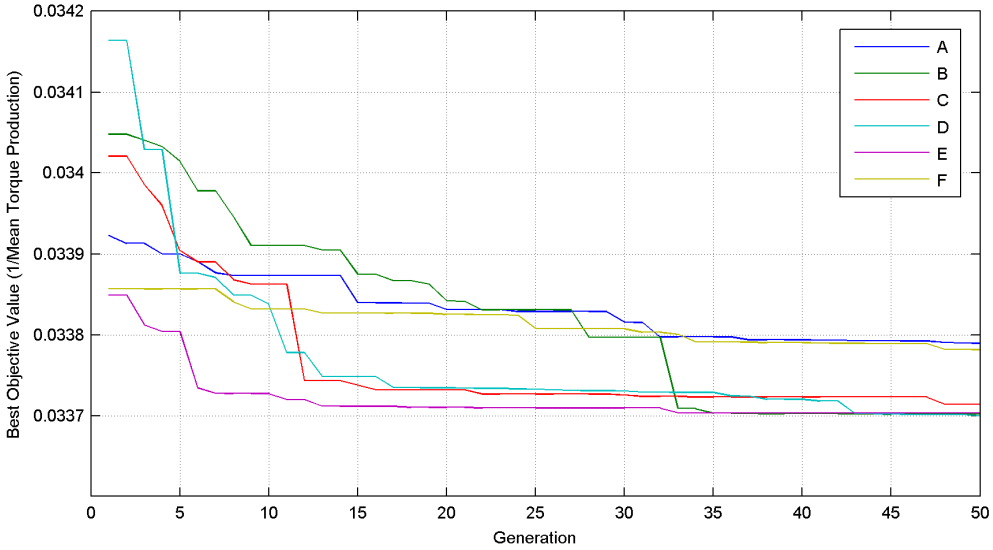

Figure 5.3: Evolution of best objective for N_{ind}=25

The testing carried out using 50 individuals per generations produces a higher quality of result across the board, compared to 25 individuals, as expected. Figure 5.4 indicates how there is good convergence with all the tests, having settled within 30 generations, baring the parameters used for H. The best objective value was generated by test L, which uses $P_c = 0.9$ and $P_m = 0.1$, despite this all of the final objective values are within a very small range. So much so that, J which uses identical GA parameters to D in Figure 5.3 optimizes to 0.03370.

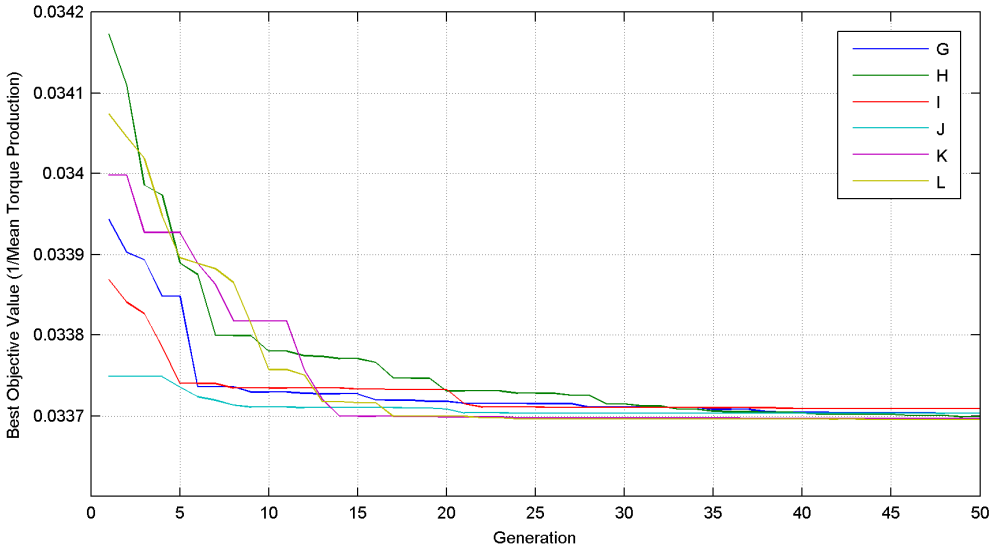

Figure 5.4: Evolution of best objective for N_{ind}=50

Finally, the benefit of 75 individuals per generation on the quality of result was investigated. The results from this stage of testing are shown in Figure 5.5. Due

to the greater amount of individuals, the speed of convergence is very good for all of the tests carried out. The best objective value has settled and very little improvement in the quality of results occurs beyond generation 25. Once again the GA parameters that generate the best objective value are $P_c = 0.75$ and $P_m = 0.1$, which were set for test P. The final objective value for P after 50 generations is 0.03369, and interestingly there is little improvement after generation 25 since here the best objective is 0.03367.

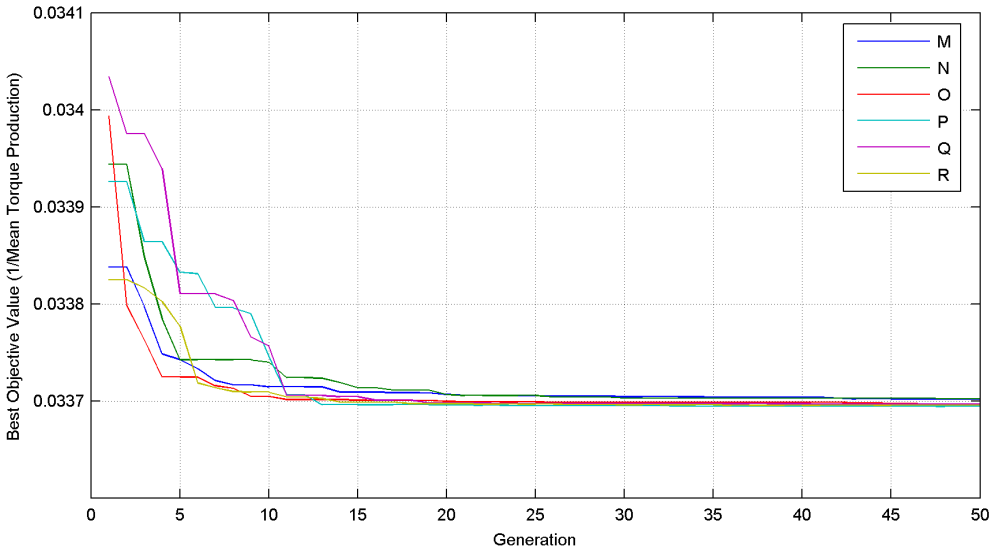

Figure 5.5: Evolution of best objective for N_{ind}=75

The outcomes from the strategic testing carried out using various constants for GA parameters have provided solid evidence for the final selection of parameters for single objective optimization. The combination of a crossover rate, $P_c = 0.75$ and mutation rate, $P_m = 0.1$ has provided the most encouraging results. Although with a large population the testing results have shown that the selection of these values is not critically sensitive for the optimization problem.

The main compromise that needed to be overcome is the conflict of optimization duration and quality of result. The most suitable option would be to use a larger population of 75 individuals, while only allowing the GA to reproduce for up to 25 generations. However due to the limited improvement of the final result 50 individuals are used. The impact on the best objective with a maximum of 25 generations is demonstrated in Table 5.3 where the best objective values for 25 and 50 generations are compared. The data in the table shows how with effective selections for P_c and P_m the GA can reach a high quality result within a low amount of generations, greatly reducing computational time and effort. The final

parameters selected for the single objective stage one process are as follows:

- $N_{ind} = 50$
- $P_c = 0.75$
- $P_m = 0.1$
- $G_{gap} = 0.9$
- $G_{max} = 25$

These values will be set for the GA parameter across all the topologies that have been selected as part of the optimization process. The boundaries assigned for each stage one variable can change between topologies, since the structural integrity will vary between them.

N_{ind}	P_c	P_m	Best Objective at 25	Best Objective at 50	Ref
25	0.6	0.05	0.0338	0.0338	A
		0.1	0.0338	0.0337	B
	0.75	0.05	0.0337	0.0337	C
		0.1	0.0337	0.0337	D
	0.9	0.05	0.0337	0.0337	E
		0.1	0.0338	0.0338	F
50	0.6	0.05	0.0337	0.0337	G
		0.1	0.0337	0.0337	H
	0.75	0.05	0.0337	0.0337	I
		0.1	0.0337	0.0337	J
	0.9	0.05	0.0337	0.0337	K
		0.1	0.0337	0.0337	L
75	0.6	0.05	0.0337	0.0337	M
		0.1	0.0337	0.0337	N
	0.75	0.05	0.0337	0.0337	O
		0.1	0.0337	0.0337	P
	0.9	0.05	0.0337	0.0337	Q
		0.1	0.0337	0.0337	R

Table 5.3: Best objective value obtained with given N_{ind}, P_c and P_m

The FEA used to calculate the torque characteristics of each machine model determines the simulation requirements. In order to calculate the mean torque production the model has to be simulated over sufficient duration to account for the torque ripple involved. With these simulations a significant contribution to the torque ripple is cogging torque. This oscillates at a frequency related to the LCM of the slot and pole combination. Consequently, the minimum simulation

duration is set as the period of cogging torque fluctuation, which is simply the duration of a mechanical revolution divided by the LCM for the topology.

5.4.2 Stage Two

The second stage of optimization takes place after stage one, fixing the variables involved to their values that contributed to the best objective. The focus of stage two is on improving the self-sensing characteristics of the initial design output from stage one. As detailed previously, the most important aspects of self-sensing properties are the overall level of saliency, the amount of saliency ripple and the saliency crossover point. The maximization of the level of saliency (L'_q/L'_d) was set as the initial objective function within a single-objective process. The machine variables SR, TW, MS and BI are fixed after stage one, as well as MT since it is defined as a function of MS. Therefore the following machine variables are included in the second optimization stage; SO, TB, TT and MI.

The multi-stage process requires strict boundary constraints to be placed on the variables in order for their variation to have limited impact on the stage one optimization. Following on from the testing results at stage one the 12s10p topology was again used during the initial testing of stage two. The variables were fixed at the centre point of the upper and lower boundaries during stage one, in theory this means the final solution will have overall performance characteristics close to the stage one solution. Once again, the values assigned for each boundary, shown in Table 5.4, were based on realistic selections influenced by electromagnetic principles, structural integrity and manufacturability. For example, TT has a minimum thickness in order to be structurally sound, while due to the stator topology it also has to be less than or equal to TB.

Variable	Lower	Upper
SO	2°	8°
TB	2mm	5mm
TT	0.75mm	2mm
MI	0	1

Table 5.4: Boundary conditions for stage two variables

The GA parameters assigned during stage one were used again for stage two as they have been shown to work effectively with the GA routine involved. In order to analyse the saliency characteristics the simulation settings for stage two differ

from those required in stage one. Firstly, for each iteration the machine model has to be simulated three times to calculate the incremental inductances, as outlined in Chapter 3. Secondly, unlike the torque characteristics which can be obtained from a relatively short simulation duration, the saliency requires longer. There is a strong 6^{th} harmonic in the incremental inductances and therefore to accurately calculate the saliency the machine model must be simulated for at least $\frac{1}{6^{th}}$ of an electrical period. The second optimization stage was tested on the stage one design result of the 12s10p topology. The results are presented in Figure 5.6.

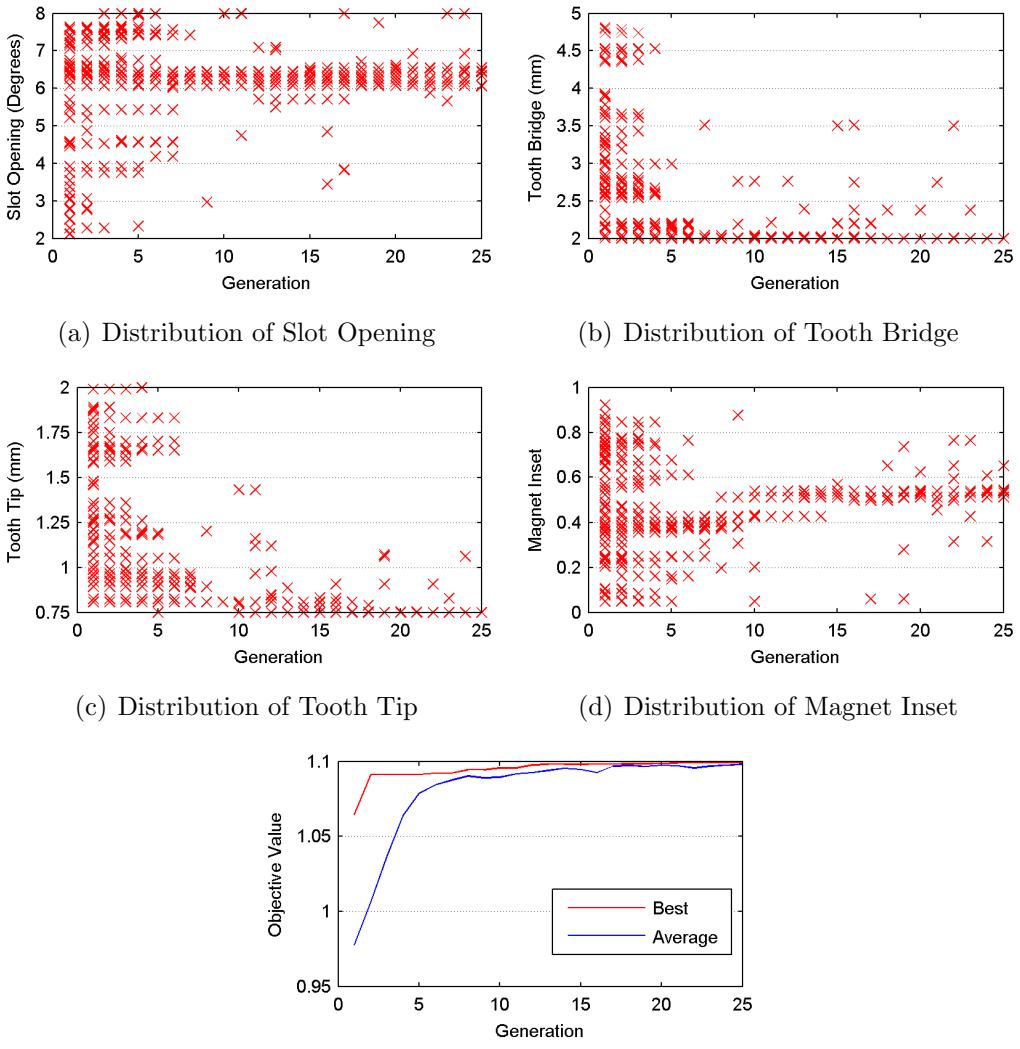

(a) Distribution of Slot Opening

(b) Distribution of Tooth Bridge

(c) Distribution of Tooth Tip

(d) Distribution of Magnet Inset

(e) Evolution of Best Objective

Figure 5.6: Stage two GA optimization of 12s10p topology

The results in the scatter plots 5.6(a)-(d) show the values selected for the given variable in each progressive generation. The distribution for all four design variables used reduces during the optimization and ultimately the optimum range

for each narrows significantly by the 25^{th} generation. The evolution of the best objective, here being the level of saliency (L'_q/L'_d), is plotted in Figure 5.6(e). The optimization improves the saliency in the machine at rated load, a similar average value at the end of the routine suggests the design had converged. The test shows good evolution throughout the GA routine and lead to an improved saliency design. These parameters are therefore suitable to be used for the whole design process as they are identical to stage one.

With level of saliency as the stage objective, it is important to assess the objective at the appropriate loading. To ensure complete controllability throughout the whole operational envelope, the level of saliency needs to be calculated at peak loading (providing maximum torque). At this point it is essential that there is a positive saliency, $\frac{L'_q}{L'_d} > 1$. This guarantees that there is no zero saliency condition within the whole loading range. In addition to this, the level of saliency will be at its worst, or lowest, at peak conditions. Therefore, increasing saliency at this point will improve the overall quality of the HF tracking signal. This then contributes to increased accuracy and simpler signal processing. This is why optimizing for saliency at peak torque is the primary objective of stage two.

The discussion in Chapter 3 outlines the various advantages of an inverse saliency machine. With this in mind the stage two optimization can be repeated using a second approach; optimizing for inverse saliency, $\frac{L'_q}{L'_d} < 1$. The promise that an inverse saliency machine presents for sensorless control meant that is was investigated as alternative objective. Under this condition the level of saliency must be calculated and minimized under no load. If it is possible to optimize a machine that has inverse saliency at no load then this ensures the condition will be constant throughout. Once again, the greater the level of saliency (in this case, inverse), the better the quality of sensorless tracking is. With Q-axis saturation taking place, the saliency signal will continue to improve under load. With the two stage process refined it is then performed on all of the available topologies, not only to optimize each individual but to determine the best overall.

5.5 Single Stage, Multi-Objective Optimization Routine

The following section introduces a second optimization routine for the project. In a differing approach to the first proposed routine this uses multi-objective optimization. Optimizing primarily for fundamental performance the GA will determine suitable results for two or more objectives. The nature of the process

means that the use of evolutionary selection will improve one objective while there is the possibility the others will suffer. A truly multi-objective optimization routine will treat each objective function with equal importance. The use of a weighted objective function to achieve a multi-objective process requires in depth analysis to determine an appropriate weighting scale. The approach is more complex to develop and returns a global optimum instead of a population of feasible results.

The incorporation of saliency characteristics and sensorless controllability into the optimization routine can be done in two forms. The first is to have level of saliency, or saliency crossover point, as a primary objective, similar to the second stage of the single-objective process. Alternatively the optimization process can run in alignment with a penalty function to ensure sensorless controllability. This second method would simply check to confirm if a zero saliency condition exists in the operational envelope. As discussed previously, this would involve either $\frac{L'_q}{L'_d} > 1$ at peak loading for traditional saliency or $\frac{L'_q}{L'_d} < 1$ at no load for inverse saliency. A benefit is that another parameter could be optimized in its place, possibly improving fundamental performance.

The GA would then perform machine design optimization in a traditional form, focusing on generic performance characteristics. The downsides to this approach are that calculating saliency is the largest time component of the optimization process and since it is still present in both, to maximize its effectiveness it is logical to be a primary objective. Secondly, although a form of saliency is all that it required for sensorless position control, accuracy and simplicity of control is correlated to the level of saliency. The two optimization approaches will be performed, with their respective result analysed and compared.

With the level of saliency at peak loading as one on the objectives it is important to select the others to help meet additional design specifications. The level of torque production within the machine is always a primary goal in machine design and can also have a direct impact on sensorless control characteristics. If a machine can produce torque efficiently at a lower level of loading then it is possible less Q-axis saturation takes place to produce maximum torque output. The lower Q-axis saturation will improve saliency under load. Selecting mean torque production as an objective is a sensible choice since it is a major performance driver.

The third and final objective selected will assess the quality of torque production.

The simplest approach to analyse this involves minimizing cogging torque as an objective function, under no load conditions as standard. Alternatively the percentage of torque ripple can be taken into account.

With these selections, the multi-objective approach is complete. The optimization routine will have three target objectives:

- Maximize mean rated torque ($FF = \frac{1}{\bar{T}_R}$)
- Maximize saliency ratio at peak loading ($FF = \frac{1}{\Delta L}$)
- Minimize no load cogging torque ($FF = T_c$)

There are eight geometrical parameters available for optimization, all of which are used during the optimization process. The pareto fraction will be set at a practical value of 0.4 for the multi-objective routine. This fraction is the main Multi-Objective Genetic Algorithm (MGA) parameter used in multi-objective optimization, unlike the large number of parameters used in single-objective methods. This fraction sets the limit for the number of individuals in the current population that are positioned on the pareto front.

The penalty function multi-objective routine, removes saliency as a optimization objective. Instead the MGA firstly confirms if the individual meets or exceeds the threshold. Here, the threshold is set at $\frac{L'_q}{L'_d} \geq 1.05$ within an if statement. If the individual satisfies this requirement then the objective functions are calculated as normal. While the 'else if' term is set with the penalty function. Commonly an additive penalty term is applied, although multiplicative terms can be used. If the individual does not exhibit the required saliency, after calculating the objective functions a penalty value is added to each to diminish the final value of that individual and cause the GA to select future individuals away from that chromosome. The magnitude of the penalty term needs to be selected carefully as to not completely remove the genes that make up an infeasible result from future selections.

A death penalty term is also a possibility, this rejects all infeasible results from the search population. This is generally a negative approach in complex optimization problems since the MGA will expend too much time on too few appropriate results. The penalty function multi objective optimization will therefore use an additive penalty applied to all objectives. The results for the optimization method are shown and analysed in Chapter 6.

5.6 Optimization Design Routine Flow Diagram

With the machine scripts and optimization routines developed the implementation of these is illustrated in the flow diagram in Figure 5.7. The diagram illustrates the scripting flow that takes place within the GA routine in order to evaluate the fitness value of each individual of the population.

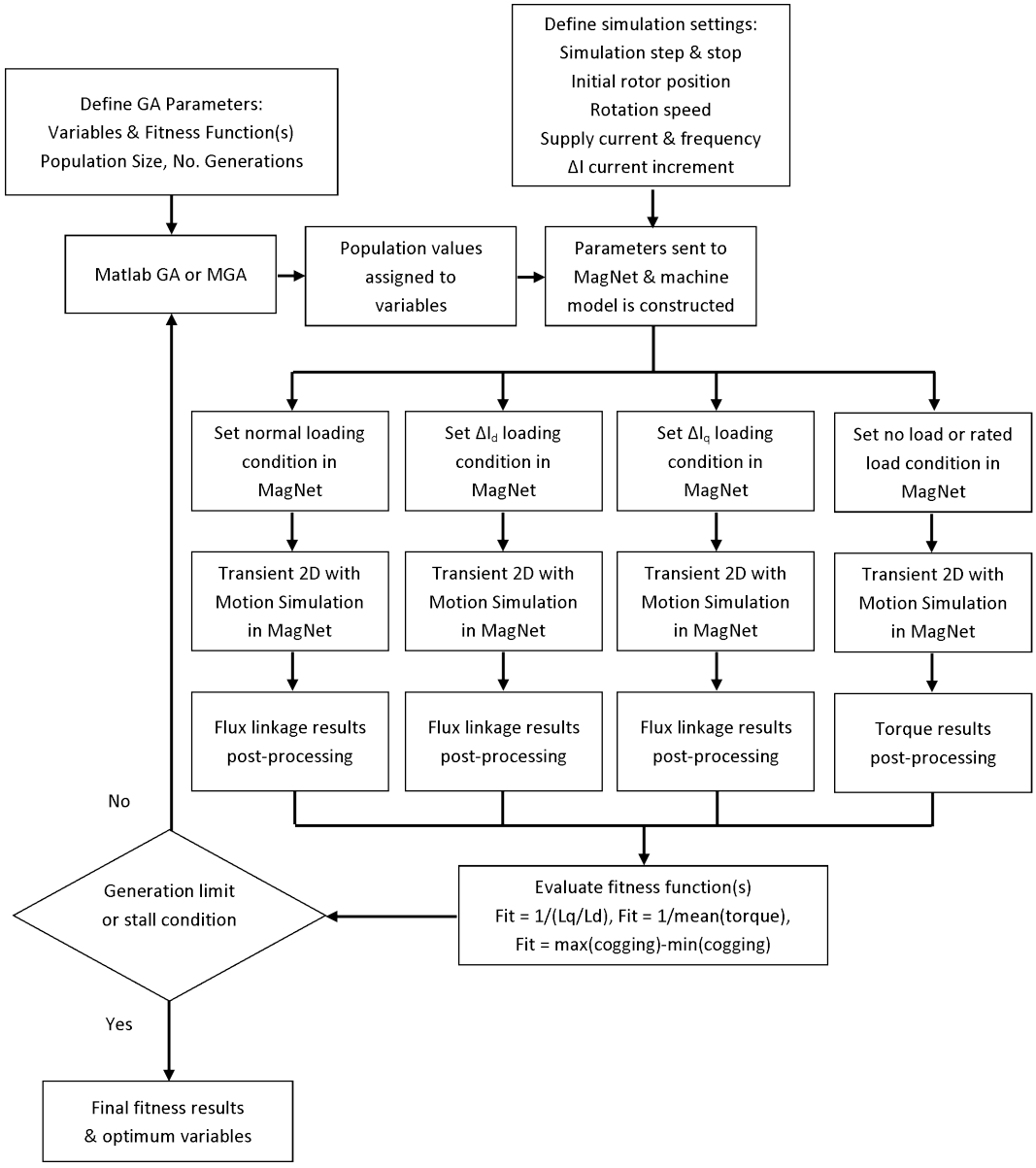

Figure 5.7: Flow diagram of fitness evaluation process

Each of the fitness objectives can be used in a single-objective routine or performed during a multi-objective routine. The flow diagram depicts the overarching GA control with the stopping condition after each iteration. In the routines

used the stopping criteria is the generation limit determined earlier in the chapter. It is flexible and additional stopping functions could be implemented such as a stall condition once a certain value to achieved.

5.7 Summary

The three main performance indicators that will be utilized during the optimization process are rated torque production, no load cogging torque and saliency ratio at the most significant loading point. Two design approaches have been devised, the first is a two stage, single-objective routine. The dominant machine parameters are optimized in the first stage for rated torque production. This optimized design is then manipulated during the second stage with the remaining variables optimized to enhance the machine saliency. This is examined at either peak load when concerned with a conventional ($L'_q > L'_d$) saliency or no load when concerned with an inverse ($L'_q < L'_q$) saliency. The second design approach uses all machine variables in an un-weighted multi-objective routine that optimizes for cogging torque, rated torque production and saliency.

The first approach uses an efficient single-objective optimization and can be stopped early if convergence takes place. Particularly, the first stage is computationally efficient as the large search space provided for the dominant variables are used with a relatively fast, single FE simulation. The second stage analyses the saliency characteristic and therefore requires three simulations, however due to the narrow search space provided that limits the impact on the stage one outcome the GA remains reasonably fast and can be stopped early is convergence takes place.

The multi-objective approach by contrast cannot be stopped early as convergence cannot be guaranteed. Due to the very large search space generated by all the variables involved the MGA must be provided with sufficient population size and generations to perform well. This increases the total computation time. The main argument that needs to be answered is; will the time efficient single-objective approach be able to successfully develop a suitable machine topology.

Additional results will also be obtained for special cases to investigate their suitability. The special cases are summarized below and will be referred to during the results section. The same optimization routine will be performed for the special cases, but only on a the slot/pole combinations that demonstrate the most

promise from previous results.

- Removing MI as a variable and fixing it at pre-determined value
- Limiting the number of variables available for the multi-objective process
- Using a penalty function approach for the multi-objective process

Chapter 6: Optimization Results

6.1 Introduction

The following chapter reviews and analyses the optimization results gathered from the two routines during the project. The previous chapter detailed each of the optimization routines and how they were devised to this point. Successful and unsuccessful optimization results are shown and contribute to the comparison of both optimization routines and optimum topologies.

6.2 Machine Design Specifications

Table 6.1 shows the specification requirements for the optimized machine. The design specifications can be used to analyse the suitability of each optimized design.

Structural and Material Constraints	Stator Outer Radius	67.5mm
	Active Stack Length	87.6mm
	Shaft Radius	$\leq$ 30mm
	Airgap Length	0.75mm
	Stator Lamination Steel	M330/50A
	Rotor Lamination Steel	M800/50A
	Permanent Magnet Type	NdFeB38
	Permanent Magnet Shape	Radial (Segmented)
	Permanent Magnet Volume	Fixed
	Slot Packing Factor	50 %
	Constant boundary temperature	80°
Performance Requirements	Rated & Max Torque	30 / 45 Nm
	Cogging Torque (Pk-to-Pk)	0.3 Nm (1 % Rtd)

Table 6.1: Machine Design Specifications

As well as the overall constraints set in Table 6.1 for the optimization routine, each variable must be assigned upper and lower boundary limits. Each of the selected slot/pole combinations is based on the same SPMSM geometrical construction and operated under the same performance conditions. However, the dimensional constraints must vary to account for the change in slot and/or pole number.

The boundary conditions implemented for the stage one variables are presented in Table 6.2. The split ratio was kept constant for all configurations since the external dimensions are unchanged. Tooth width was kept constant between the options by setting the boundaries based on the a proportion of the slot pitch ($\tau_u = \frac{\pi \cdot D}{s}$). Back iron thickness was then set proportionally from the respective boundaries for TW. The boundary limits of MS were determined by a percentage of the pole span ($PS = \frac{360}{p}$), which is dependent on the number of poles.

Topology	SR	TW		MS		BI	
		mm	% τ_u	Degrees	% PS	mm	% TW
9s8p	0.55-0.65	8-16	29-56	34.5-43.5	77-97	4.5-10	56-63
12s10p	0.55-0.65	6-12	29-56	28-34.5	78-96	3.5-7.5	58-63
18s16p	0.55-0.65	4.5-8.5	32-59	17.5-21.5	78-96	2.5-5.5	56-64
18s20p	0.55-0.65	4.5-8.5	32-59	14-17	78-95	2.5-5.5	56-64
24s20p	0.55-0.65	3.5-6.5	33-61	14-17	78-95	2-4	57-62

Table 6.2: Boundary conditions for stage one variables based on topology

The stage two boundary conditions for the stage two variables are shown in Table 6.3. SO boundaries were determined from a percentage of the slot span ($SS = \frac{360}{s}$). The magnet inset is set as a percentage of the magnet thickness, and kept constant across all configurations. The boundaries for TT were predetermined by the minimum of 0.75mm for structural integrity and maximum equal to the lower boundary of TB. The limits for TB were based on practical selections relating to the back-iron thickness and the slot number. As stated during the testing process, the stage two variables are fixed at their respective median values for the stage one process. This will ensure that the design result from stage one will suffer minimal disruption during stage two if the GA gravitates to either boundary limit. Aside from these geometrical variations the topologies are simulated and optimized for the same outputs and under the same restraints.

Topology	SO		TB	TT	MI
	Degrees	% SS	mm	mm	
9s8p	4-10	8-25	2-5	0.75-2	0.1-0.9
12s10p	2-8	7-26	2-5	0.75-2	0.1-0.9
18s16p	1.5-5	8-25	1.5-3.5	0.75-1.5	0.1-0.9
18s20p	1.5-5	8-25	1.5-3.5	0.75-1.5	0.1-0.9
24s20p	1-4	7-26	1.2-3	0.75-1.2	0.1-0.9

Table 6.3: Boundary conditions for stage two variables based on topology

All of the upper and lower limits stated have been selected based on either theoretical limitations imposed by the topology or practical design choices. For example, the upper limit of MS is determined by the maximum angular span per pole ($MS \leq \frac{360}{p}$). The design dictates that the limit is marginally lower than this to account for insetting the PMs into the rotor back iron. In contrast, the lower limits of TW and BI were selected so that the minimum value would still provide sufficient structural integrity and form the main flux path.

6.3 Two Stage, Single-Objective GA Optimization Results

The stage by stage results for each slot/pole combination will be presented and analysed to determine both positive and negative design trends. Particularly those in stage two which enhance the main saturation saliency characteristic. The single objective GA routine allows the population distributions for each variable and generation to be plotted. This is used for the trend analysis and allows insight into causes of poor optimization results.

6.3.1 9s8p Optimization

The data in Figure 6.1 shows the distribution of populations for each of the stage one variables. The plots indicate the values selected by the GA through each generation of the optimization and the evolution of the best objective. Analysing the distribution of each variable allows their significance to be assessed and whether there is an optimum value for the given objective. The optimization result from stage one is shown in Figure 6.1, where the GA is maximizing the mean torque production at steady state rated load. The population distribution plots clearly demonstrate that as expected all four variables strongly influence the level of torque production within the machine. The SR quickly moves to the median value of the available range. Beyond the tenth generation the GA selects only a value from a very narrow range around 0.59. Although a true optimum is not found by the end of the process, it clearly demonstrates the significance of the variable. The values outwith the optimum value towards the 25^{th} generation occur due to the mutation and crossover functions in the GA.

The TW also gravitates to a very small range, in this case towards the top end of the range allowing an increase in the level of magnetic loading. So too does the

back iron thickness, which appears to match tooth width proportionally to provide an adequate main flux path to equal the desired magnetic loading. Within this application there is a limited consideration towards iron losses due to the thermal model used, this is likely to encourage the optimization will naturally move towards high magnetic loading. The GA has found near optimums for both of these variables (Figures 6.1(b) & 6.1(c)) at the top end of their respective dimensional range. However, since they both impact on the slot area, and therefore electrical loading, the optimums are not necessarily found at the extreme of their boundaries. This is caused by the compromise between increasing magnetic loading and maintaining electrical loading.

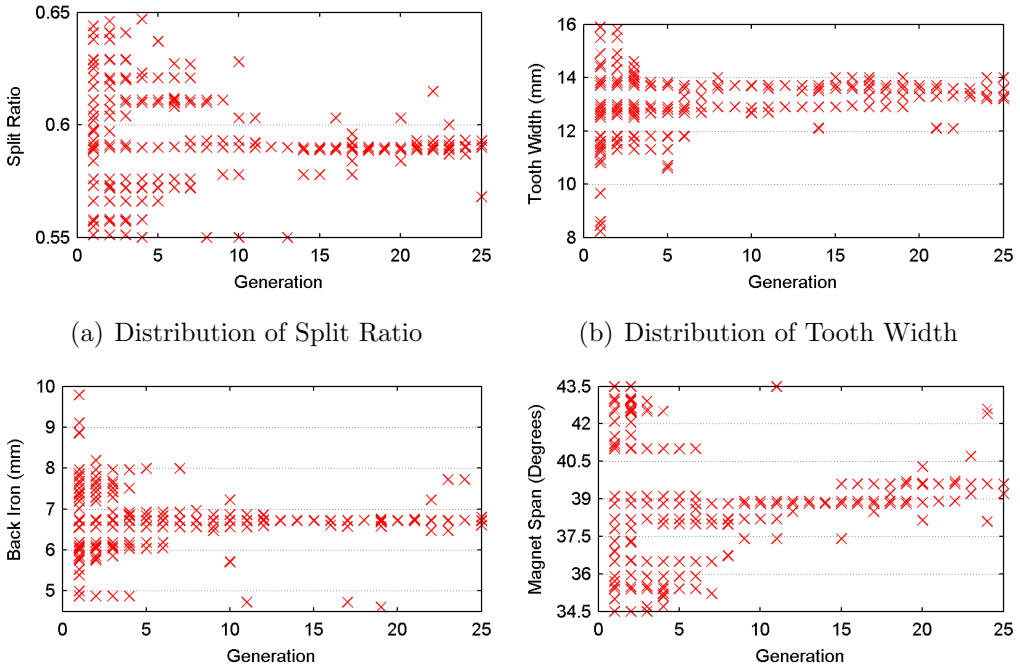

(a) Distribution of Split Ratio

(b) Distribution of Tooth Width

(c) Distribution of Back Iron

(d) Distribution of Magnet Span

Figure 6.1: Stage one GA optimization of 9s8p topology

The final variable utilized in the optimization is MS. This is, by definition, a parent of MT and so directly influences it to maintain overall PM volume. With this topology, an optimum value is found resulting in a relatively elongated radial pole shape. However, at 39.2° the optimum is near the median value of the optimization range. The complete routine after 25 generations demonstrates improved mean torque generation. This is generated by a topology with the following dimensions, SR = 0.593, TW = 13.6mm, BI = 6.72mm, MS = 39.2°. These dimensions are then set for the second stage of optimization.

The second stage of optimization evolves the machine topology further to enhance the HF saliency characteristic. This is approached in two ways, by targeting the largest level of saliency both normal and inverse. Each optimization routine is performed at their respective worst case loading level. This is equal to no load for inverse saliency calculation and peak load for calculating a traditional saliency. The results of this optimization are shown in Figure 6.2. The population distribution plots show both objectives, with normal saliency represented in red and inverse saliency in blue. In a general overview there is a clear difference in the distribution of population for all variables.

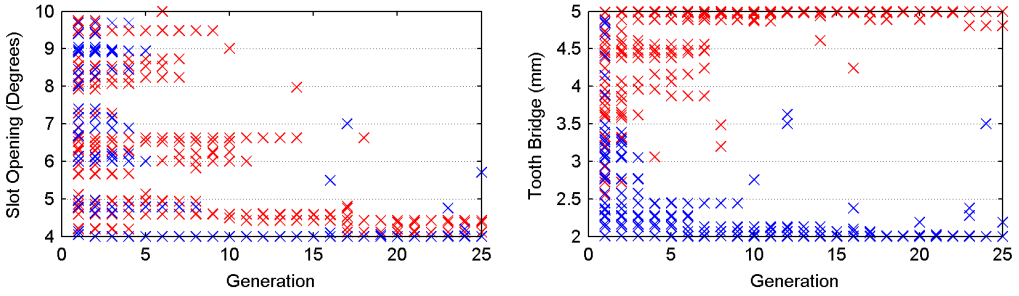

(a) Distribution of Slot Opening

(b) Distribution of Tooth Bridge

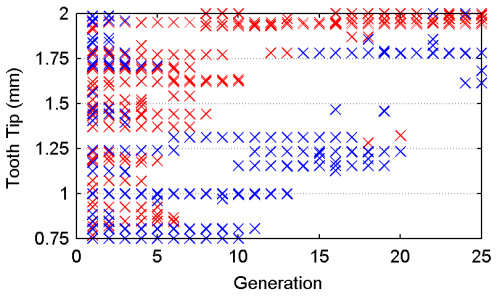

(c) Distribution of Tooth Tip

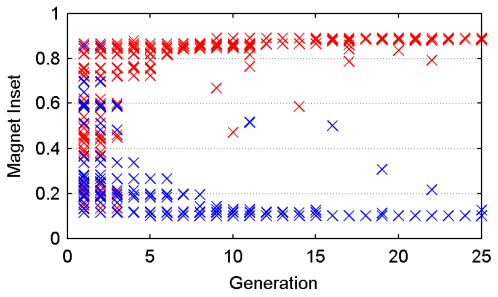

(d) Distribution of Magnet Inset

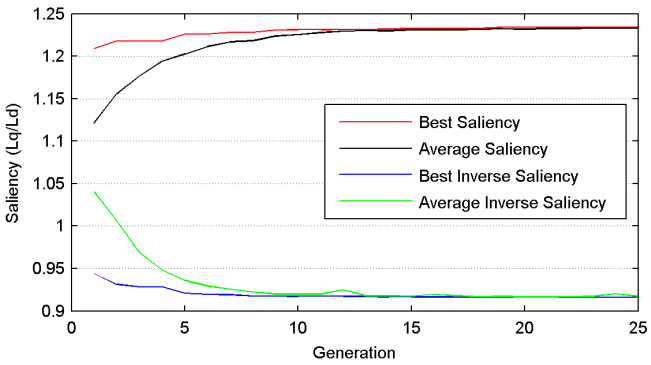

(e) Evolution of Best Objectives

Figure 6.2: Stage two GA optimization of 9s8p topology

The tooth bridge thickness and tooth tip thickness have a strong correlation, with each moving to either the upper of lower boundaries. They combine together to have a strong influence on the D-axis and Q-axis incremental inductances and therefore the saliency of the machine. The data in Figures 6.2(b) & 6.2(c) shows how a thinner overall tooth bridge contributes to a machine with a strong inverse saliency. The opposite condition leads to a more traditional saliency. The slot opening works in collaboration with the tooth bridge since it determines its length. The evolution of the design routine leads towards a stator topology with contrasting tooth bridges. A long and thick tooth bridge is formed to produce the best traditional saliency, that will not easily saturate under load. During the evolution of the GA the large search spaces for SO, TB and TT narrow towards their respective optimum values after eight to ten generations.

The correlation between the tooth tip and bridge thickness is clear, the higher values demonstrate improved results. This forms a significant section of the stator iron to improve upon the main flux path, as well as the level of saliency. This is largely contrasting to the inverse saliency optimization, demonstrating that these variables have significant impact on the objective function. A large and thin tooth bridge is shown to be advantageous since it encourages saturation even at low loading. This is a desirable characteristic for inducing inverse saliency. The tooth tip starts with a wide search space and initially starts to target values in the lower half of the dimensional range. Late in the process the optimum value is in fact higher than expected at 1.78mm.

The result for magnet inset in Figure 6.2(d) displays a rugged trend for the stage two objectives. A large inset for the PM rotor poles clearly helps increase HF saliency within the machine. This is a well known characteristic and has been presented in recent research, some of which is covered in Chapter 2. The inset naturally creates a difference in the D and Q-axis reluctance paths, since the rotor back-iron has a far greater permeability than the air gap and PM material (which is treated as air). This theory is confirmed by the inverse saliency result. A small inset produces the largest inverse saliency at no load, since it reduces the inherent condition that makes $L'_q > L'_d$. The inverse condition is only possible by reducing the magnitude of the Q-axis inductance at no load or encouraging saturation even at no load.

The stage one result can be optimized to achieve both a traditional saliency and an inverse saliency. Both of the stage two results are good and indicate they would form machines that are controllable throughout the operational envelope.

A saliency ratio of 1.23 at peak torque is achieved by the routine, produced from SO = 4.11°, TB = 5.00mm, TT = 2.00mm, MI = 0.883. Meanwhile, an inverse saliency ratio of 0.92 is achieved at no load, produced with the following values. SO = 4.00°, TB = 2.00mm, TT = 1.78mm, MI = 0.100.

6.3.2 12s10p Optimization

The results of the stage one optimization for the 12s10p topology are shown in Figure 6.3. The best objective, here mean rated torque production, has a strong convergence and therefore has reached an optimum value during the process. All four variables show convergence to to optimum values, reaffirming the notion that they all strongly influence torque production. Through the evolutionary selection the range of values narrows significantly from the initial design boundaries. The SR begins with the standard wide distribution and maintains a wide search space through the first seven generations. It evolves to a very narrow range by the end of the optimization but indicates there is not a true optimum. Instead a split ratio around 0.585 contributes to the highest rated torque production.

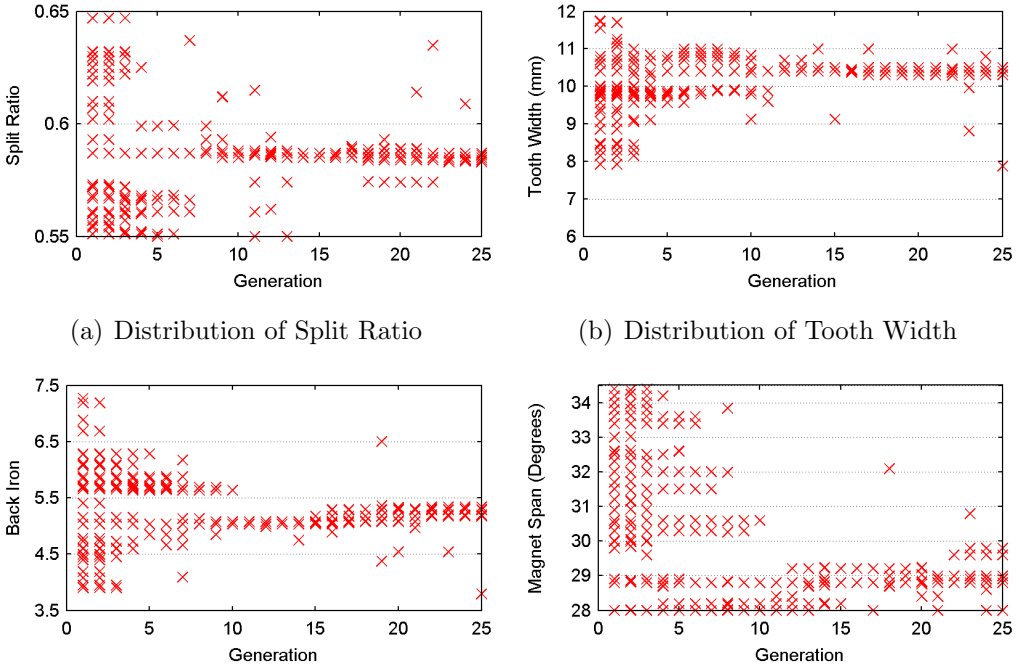

(a) Distribution of Split Ratio

(b) Distribution of Tooth Width

(c) Distribution of Back Iron

(d) Distribution of Magnet Span

Figure 6.3: Stage one GA optimization of 12s10p topology

Figure 6.3(b) shows that the TW quickly tends towards the upper end of its dimensional range. This contributes to a greater level of magnetic loading, while

not impacting on electrical loading too much. The trend is repeated with back iron thickness, which needs to provide an adequate flux path to match the tooth width. The tendency for the GA to select high values for TW and BI is expected for all topologies. The compromise here is to maximize the magnetic loading within the machine, while maintaining suffient electrical loading to fully utilize the main flux paths. The GA utilizes the final variable by analysing a broad selection of magnet spans, through this it finds the best objectives at the lower end of the range. This forms relatively thick poles that help produce good levels of torque. With this PM form there could be a strong cogging torque produced by the interaction between the poles and stator slots. This will be investigated when the optimum topology is analysed.

The analysis of the GA optimization demonstrates a good convergence to a high level of torque production, that comfortable meets the performance specification. The best objective is formed from assigning the following values, SR = 0.584, TW = 10.5mm, BI = 5.3mm, MS = 29.0°.

The second stage of the optimization process was performed using the above values and the routine run for each objective. The results of both are displayed in Figure 6.4. The best objectives of each routine achieve their primary aims, firstly a positive saliency at peak torque and secondly an inverse saliency at no load. Although they are both successful from this fundamental point of view, the respective levels of saliency represent poor values.

An optimum tooth bridge shape is found for both design objectives. A long and thin tooth bridge which creates a small slot opening forms a reluctance path that reduces the Q-axis inductance enough to induce an inverse saliency, even at no load. Instead, a thin and much shorter tooth bridge produces a machine with a distinct traditional saliency, that is still present at peak load. The population distributions for the tooth bridge and tooth tip thickness indicate a poor performance under the GA optimization. Both quickly narrow their search space to the lower end of their respective ranges. They fail to maintain a wide population of values that is possibly detrimental to the final result. This is particularly the case for the TB variable in Figure 6.4(b), which reduces the search space to under 30% by only the fourth generation. Given the previous result for the 9s8p topology, where a thick tooth bridge is advantageous for traditional saliency, this could have a big impact on the best objective.

The final values and evolutionary trends for MI are strong and follow a practical

route. A small inset, near to surface mount configuration is a clear optimum for inverse saliency. As expected, when optimizing for a traditional saliency a significant amount of inset is desirable since it creates a physical variation in the D and Q-axis inductance pathways. In the end an inset of around 40% is found as the optimum, as with all optimization routines this result might be erroneous due to the influence of the poor values for TB and TT. Given these values 0.4 is the best value, however, with more robust values for the other variables the level of inset could have been much larger.

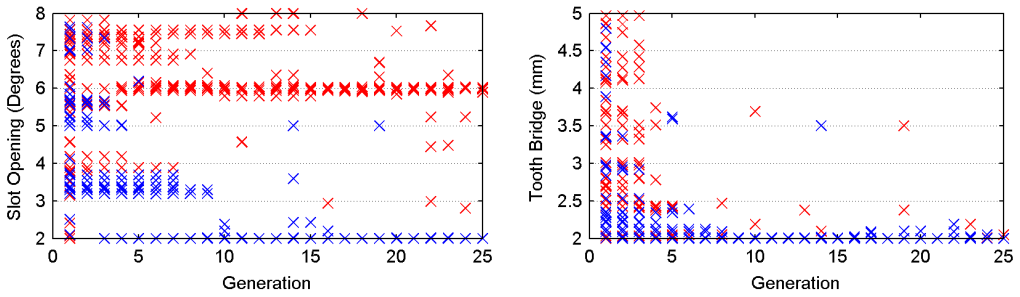

(a) Distribution of Slot Opening

(b) Distribution of Tooth Bridge

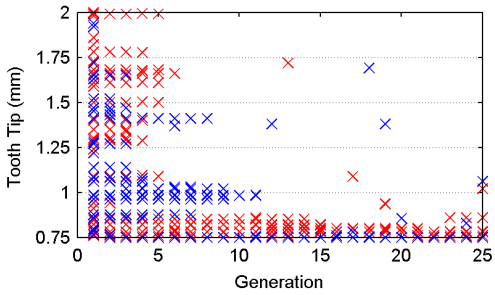

(c) Distribution of Tooth Tip

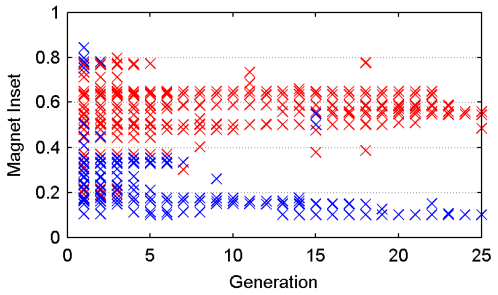

(d) Distribution of Magnet Inset

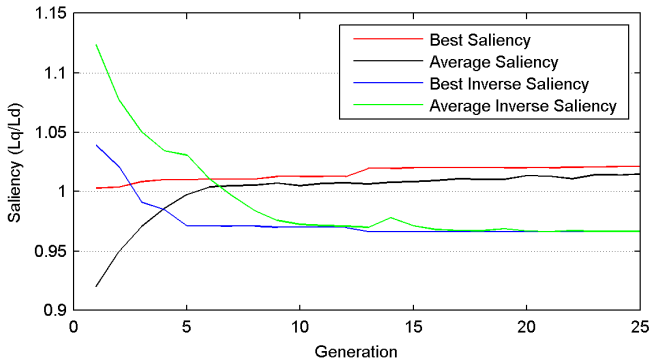

(e) Evolution of Best Objectives

Figure 6.4: Stage two GA optimization of 12s10p topology

The evolution of both objective functions is plotted in Figure 6.4(e). A best ob-

jective of 1.01 is found at peak load by the completion of the routine. This just about achieves the design aim of no zero saliency crossover point within the operational envelope. The differential between L'_d and L'_q at this point is far too small to provide a saliency that can be accurately controlled. The early convergence suggests that no improvement would be found through further generations. It is also further evidence that the GA population selection for selected variables was not broad enough during the early generations. The second optimization generates a best objective of 0.97, achieving the primary design target of an inverse saliency at no load. This objective value does not offer a strong saliency signal at the worst case operating point to make a sensible choice. The more gradual convergence means that the optimization was rugged and successful and provides additional results for comparison.

6.3.3 18s16p Optimization

The population distributions for the first stage optimization routine are shown in Figure 6.5. The four variables, optimized for torque production, all evolved to optimum values by the the end of the 25 generation process. A relatively high value was the result for the split ratio within the machine. Beyond the tenth generation the GA rarely selected a value away from 0.624 and therefore clearly contributes the greatest level of torque production at rated load. The amount of magnetic loading within the machine is strongly influenced by the tooth width and back iron thickness. The tooth width has an optimum value at the higher end of the available range helping create a substantial flux path between the rotor and the stator. Given this, the GA finds that a low value for BI that adequately supports this amount of magnetic loading.

The optimum magnet span that results from the process is very close to the upper boundary provided. This value produces elongated rotor poles, which are relatively thin. This is unlike the 9s8p and 12s10p topologies. This form of rotor pole clearly produces a good level of torque, but also should generate a good quality torque with limited cogging. This thin profile could be susceptible to demagnetization however, so this requires consideration when analysing performance at peak loading conditions.

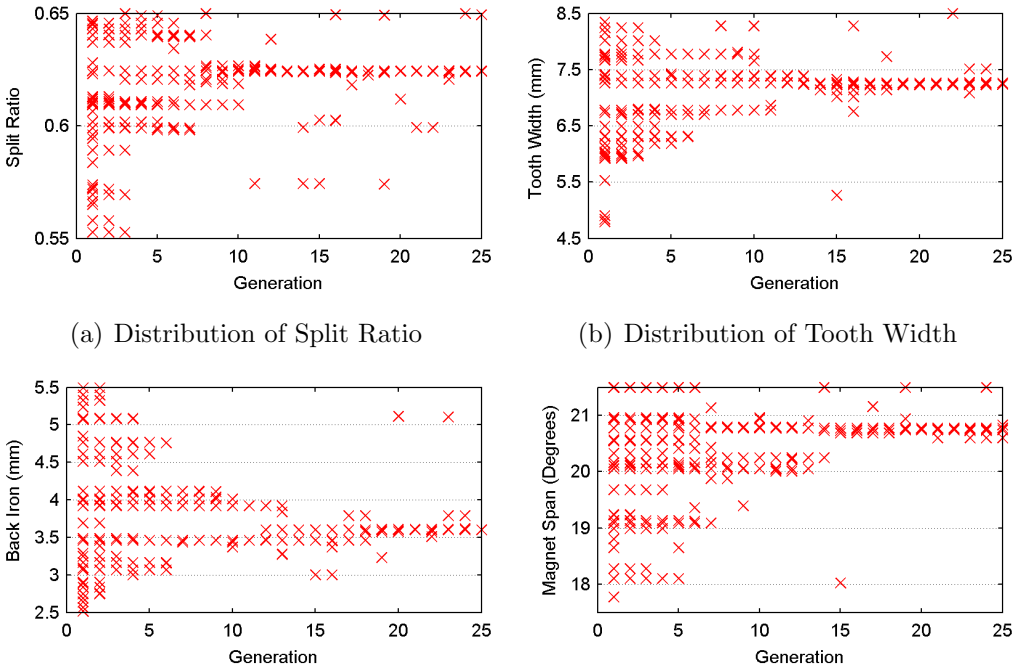

(a) Distribution of Split Ratio

(b) Distribution of Tooth Width

(c) Distribution of Back Iron

(d) Distribution of Magnet Span

Figure 6.5: Stage one GA optimization of 18s16p topology

The values for the stage one variables all demonstrate their impact on torque production due to convergence during the GA process. The best objective for stage one is obtained using the following values within the 18s16p topology. SR = 0.624, TW = 7.26mm, BI = 3.60mm, MS = 20.74°.

The two forms of stage two results are shown in Figure 6.6, with the population distributions and the evolution of best objectives. The initial conclusion of the results is that a suitable topology can be optimized for traditional saliency, meanwhile a topology with inherent inverse saliency is not possible with the design constraints.

The tooth bridge shape gradually evolves throughout the optimization design process. Upon completion, a thin and relatively short tooth bridge is created to generate the greatest traditional saliency ratio at peak torque. A median value for SO proves to be advantageous, although a complete optimum is not found. The TB and TT both quickly gravitate to the bottom of the respective boundaries. This thin format is contrasting to the thick format that is optimized in the 9s8p topology. With this machine it suggest that the slot opening and magnet inset are the more significant in determining the incremental inductances within the machine and therefore the HF saliency. During the optimization for inverse

saliency, TB and TT again evolve towards the lower boundary. A narrow slot opening contributes to reducing the traditional saliency ratio and consequently the optimized machine has a long and thin tooth bridge format.

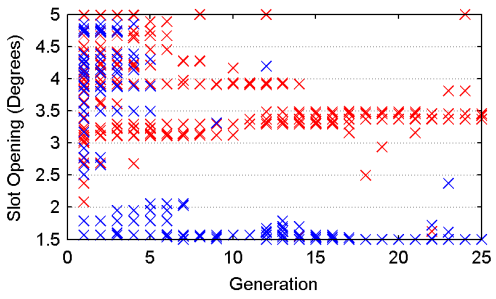

(a) Distribution of Slot Opening

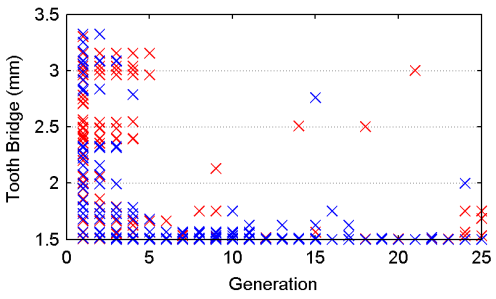

(b) Distribution of Tooth Bridge

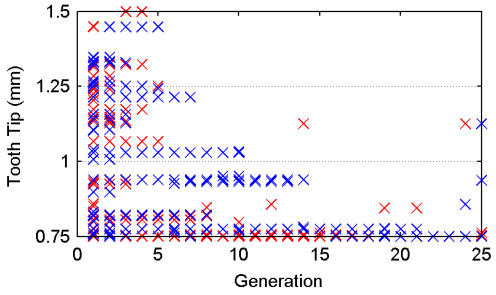

(c) Distribution of Tooth Tip

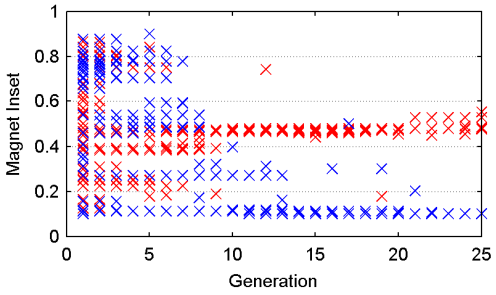

(d) Distribution of Magnet Inset

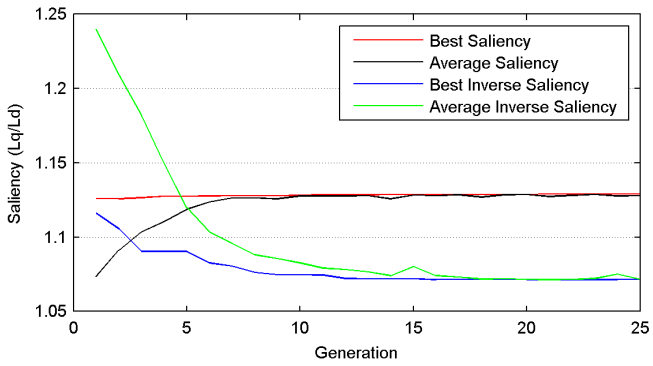

(e) Evolution of Best Objectives

Figure 6.6: Stage two GA optimization of 18s16p topology

The data plot in Figure 6.6(d) illustrates the population pathways that lead to the optimum stage two topologies. A surface mount configuration is a clear optimum for the inverse saliency result. Despite traditional theory a fully inset rotor is not the optimized result for a traditional saliency. Instead an optimum value for MI is found in a narrow range around 0.5, this still helps create a natural variation between the D and Q-axis reluctance paths and produces an improved saliency

ratio at peak torque.

The best objective results for both routines show good convergence before the end of each routine, suggesting optimums have been found. A best objective of 1.07 is found at no load and consequently an inverse saliency machine is not successful as a design objective. At peak torque production a best objective of 1.13 is found, this produces a topology that can be sensorlessly controlled throughout the whole operational envelope. This best objective is achieved with the following values, SO = 3.45°, TB = 1.50mm, TT = 0.75mm, MI = 0.528.

6.3.4 18s20p Optimization

The first stage optimization uses the same 18 slot stator format that applied to the previous 18s16p selection, with the exception of the winding configuration. The population distributions for all four stage one variables are shown in Figure 6.7. A high split ratio is quickly discovered to contribute to the greatest torque production. After only five generations the GA has gravitated to the top end of the search space. This forms a machine with a relatively narrow band for the stator and large rotor.

As expected, the tooth width and back iron thickness both have optimum values due to their strong influence on the objective function. A median value for TW is best for torque production, while this is paired with a low value for BI to create a suitable level of magnetic loading within the stator. These values demonstrate a slight correlation to the 18s16p result, however the variation in pole number and stator winding clearly causes differences. An optimum magnet span is not achieved by the end of the stage one process. The GA maintains a wide search space through several generations and in the end is still selecting from a narrow range around 15°. By not utilizing the full angular span available, the rotor poles are thicker.

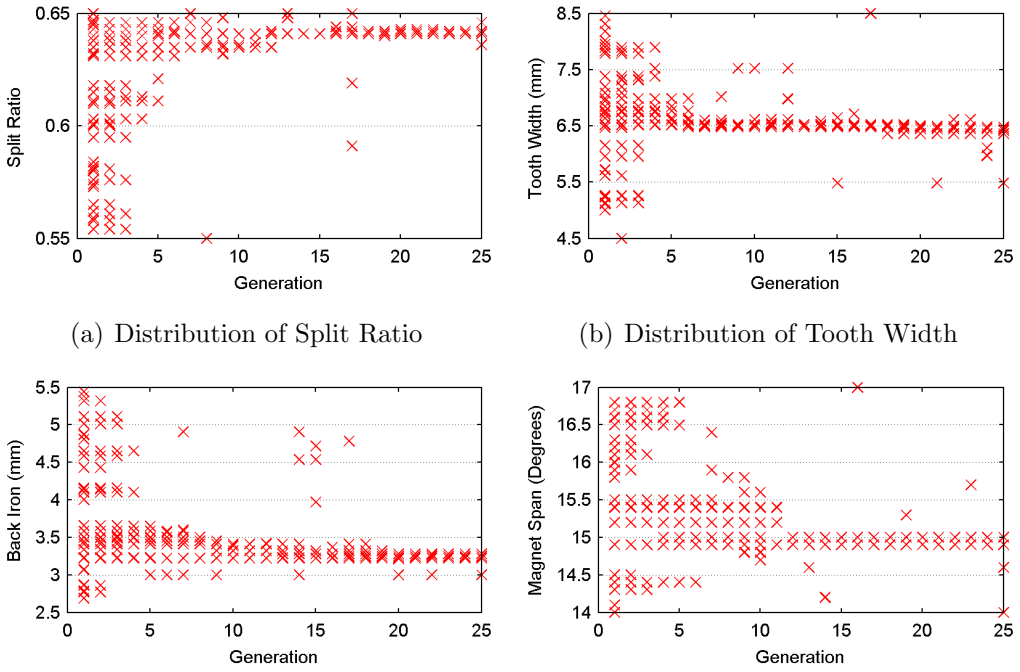

(a) Distribution of Split Ratio

(b) Distribution of Tooth Width

(c) Distribution of Back Iron

(d) Distribution of Magnet Span

Figure 6.7: Stage one GA optimization of 18s20p topology

The stage one process shows strong convergence towards an optimum value for rated torque production. The best objective achieved after the 25^{th} generation was with the follow values. SR = 0.643, TW = 6.49mm, BI = 3.29mm, MS = 14.95°.

The second stage of optimization is performed once for each of the two objective functions, with the stage one variables fixed at their optimum values. The complete results for both optimizations are shown in Figure 6.8. The best objective found through the completed routine for a primary objective of traditional saliency at peak torque is a poor result and far from achieving the design target. The 18s20p topology demonstrates a more encouraging result for the secondary objective of inverse saliency at no load. Both of the optimization results display convergence before the routines were completed and therefore the GA has found optimum results for both. The individual stage two variables will now be analysed for their values and significance.

From an overall perspective the population plots displayed in Figure 6.8(a-d) do not show a clear difference between each objective that would be expected. This suggests that one of the overall GA results is poor and erroneous, most likely caused by poor population selection early in the routine. Based on the results,

the primary objective routine (displayed in red) has performed poorly. Taking this into account the overall result and evolutionary trends for that routine offer very little importance, other than demonstrating poor values for the objective.

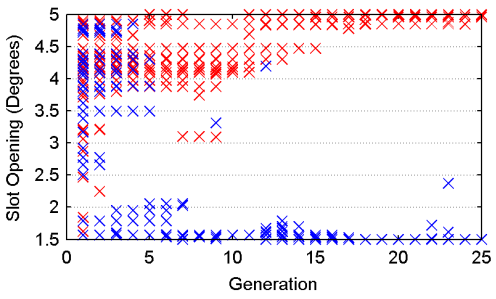

(a) Distribution of Slot Opening

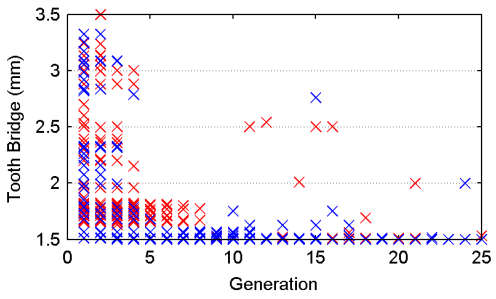

(b) Distribution of Tooth Bridge

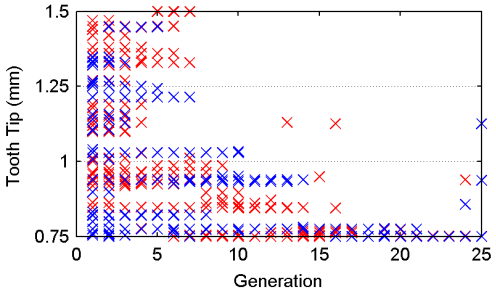

(c) Distribution of Tooth Tip

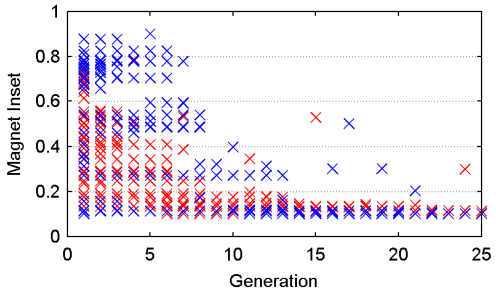

(d) Distribution of Magnet Inset

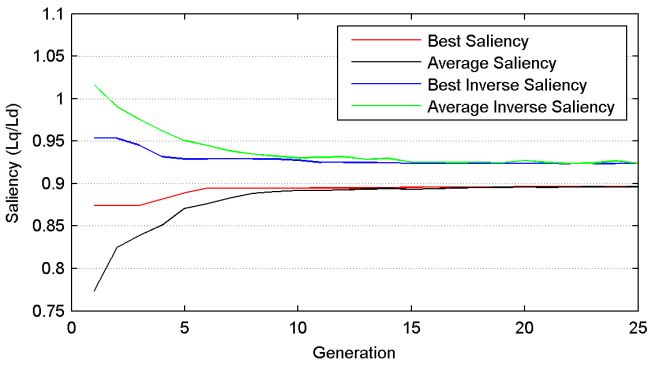

(e) Evolution of Best Objectives

Figure 6.8: Stage two GA optimization of 18s20p topology

A small slot opening, on the boundary is the optimum value for the inverse saliency machine. The tooth bridge and tooth tip variables also gravitate to the lower end of their dimensional ranges, with both optimum values on the boundary. These three variables combine together to form the overall tooth bridge shape and size. A long and thin tooth bridge is the optimum format and since this will easily saturate it has a significant impact on generating an inverse saliency,

even at no load. This works in combination with the magnet inset during the optimization. The minimum amount of inset is the optimum value, reducing the physical geometrical difference between the D and Q-axis. Apart from the SO variable, the alternative optimization objective has the same optimum values for all of the variables. Analysing the population distributions this appears to have been caused by the poor selections of TB and TT values during the initial generations of the routine. Once the GA narrows its search space onto a poor section of these variables it has the knock-on effect of causing poor selections for the the other variables.

A best objective of 0.92 is achieved for an inverse saliency at no load, representing a strong value at the worst case operating point. This allows for an accurate form of sensorless control to tracking the HF inverse saliency. The best individuals for this result are SO = 1.5°, TB = 1.50mm, TT = 0.75mm, MI = 0.11.

6.3.5 24s20p Optimization

The data plots in Figure 6.9 illustrate the population distribution for the four GA variables. The 24s20p topology has the same format as the 12s10p with double the number of slots and poles. This means it could demonstrate similar trends to the stage one result. The split ratio result in Figure 6.9(a) gravities to a very narrow range close to the upper boundary of 0.65. This shows no correlation to the 12s10p topology. With regards to the tooth width variable, after the large search space begins to narrow the GA evolves along two trend lines, indicating two possible values that produce strong torque production. Beyond the fifteenth generation the optimum value then narrows to a single result around 6mm. As with the previous slot/pole combinations, the back iron thickness needs to match the tooth width in order to provide a substantial flux path around the stator slots. A relatively narrow back iron is found to be optimum since it achieves this aim. The GA is drawn away from just selecting a high value for BI since it significantly impacts on the slot area and consequently the level of electrical loading in the machine.

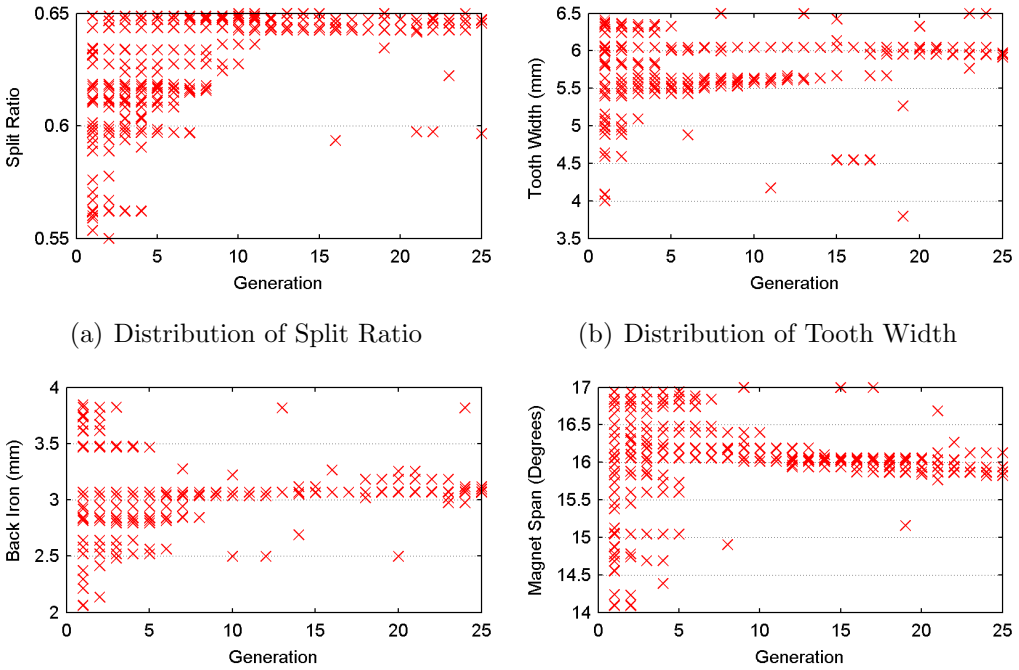

(a) Distribution of Split Ratio

(b) Distribution of Tooth Width

(c) Distribution of Back Iron

(d) Distribution of Magnet Span

Figure 6.9: Stage one GA optimization of 24s20p topology

There is no clear optimum found for the magnet span during the process. Instead a small range around 16° generates the highest level of rated torque. This value is towards the top end of the variable range and forms rotor poles that are wide and thin in shape. At the completion of the 25^{th} generation process the highest level of rated torque is achieved in a topology with the following values. SR = 0.646, TW = 5.95mm, BI = 3.12mm, MS = 15.87°.

These results for stage one were fixed within the machine script and the second optimization process was performed. The stage two results are displayed in Figure 6.10, with the traditional saliency objective in red and inverse saliency in blue. Each of the variables demonstrate distinct differences between targeting a traditional saliency and an inverse saliency. On reviewing the overall objective result in Figure 6.10(e) at peak torque the machine can be optimized to exhibit a saliency of 1.20. Optimizing for inverse saliency, at the no load worst case, does not prove successful with a best objective of 1.11. Both objectives indicate sufficient convergence by the end of the process to determine that there would be limited benefit to further generations.

In combination, SO, TB and TT form the overall tooth bridge size and shape. The three variables each evolve towards optimums that creates a thick and short

tooth bridge to improve saliency. In contrast, when targeting inverse saliency a thin, long tooth bridge exhibits desirable characteristics. With these results it indicates that limiting the level of saturation within the tooth bridge improves the traditional saliency ratio. Since the saturation saliency component is in general the most dominant within a SPMSM design. This reasoning is justified by the thin form that will easily saturate, even at low load, for inverse saliency. Despite this statement, the optimizaed machine does not have an inverse saliency at no load. The level of Q-axis saturation is not sufficient to induce an inverse saliency and consequently the design objective is not successful.

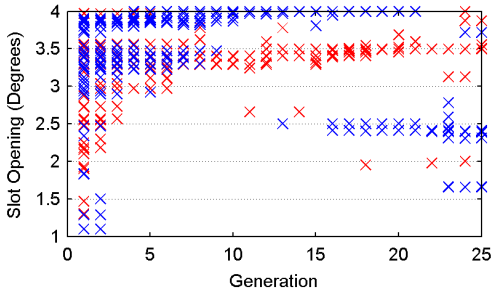

(a) Distribution of Slot Opening

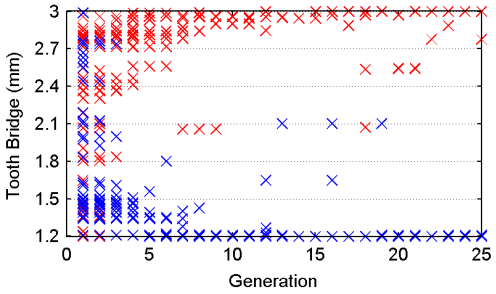

(b) Distribution of Tooth Bridge

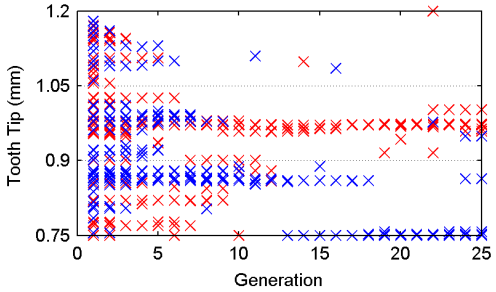

(c) Distribution of Tooth Tip

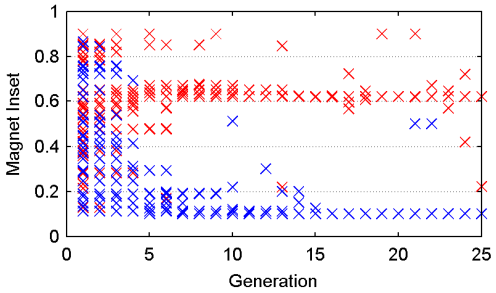

(d) Distribution of Magnet Inset

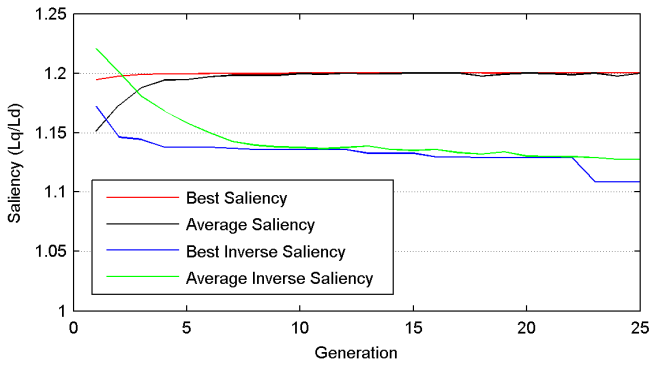

(e) Evolution of Best Objectives

Figure 6.10: Stage two GA optimization of 24s20p topology

The proportion of insertion that the PM poles have into the rotor back iron is certain to influence the main saliency component of the machine. With the axis alignment with the centre of the rotor pole and the inter-pole region, the variation in reluctance is caused the the effective airgap created by the near air permeability of the PM material. The population distribution for MI shown in Figure 6.10(d) reveals the favourable level of inset to be around 60% for a large saliency and 10% for an inverse saliency. The very small inset for inverse saliency will ensure the main reluctance is close to equal for the D and Q-axis paths. This would suggest that a fully inset machine creates the best saliency ratio, however, the result for this 24s20p topology is best using a 60% inset.

The inverse saliency topology results are benificial for trend analysis but unfortunately a suitable machine for the performance specification is not possible. A traditional saliency approach clearly has a strong saliency ratio even at peak torque and therefore indicates a suitable design choice. This saliency ratio of 1.2 was achieved by selecting the follows values. SO = 3.5°, TB = 3.00mm, TT =1.00mm, MI = 0.621.

6.4 Feasibility & Trend Analysis of Optimum Topologies

The two stage, single-objective optimization results in the preceding sections were performed over a broad range of slot/pole combinations, under identical constraints and requirements. This provides a large data set to not only select a suitable topology for the design specifications, but to investigate the geometrical influences on the main HF saliency characteristics. The initial analysis of each optimization result has determined whether the best objective represents a suitable value for the design specification. The routines that proved unsuccessful could have been caused by the overall topology being unsuitable or by a poor and ineffective GA process. The comparison of all these results together allows the cause to be investigated. In addition to this, an analytical comparison of all the results, good and bad, will determine design trends that enhance the fundamental and saliency performance of the machine.

The first optimization stage, focused on maximizing the thermal rated torque performance for each slot/pole combination. The best individuals for each variable and their respective topology is presented in Table 6.4, each under the opt (optimum) column. With the variation in the number of slots and poles as discussed before the dimensional boundaries change for each topology proportionally. The

lower (LB) and upper (UB) boundaries are therefore displayed in the table as well to demonstrated the location of each optimum relative to its limits. With respect to the stage one variables, all of the boundaries have significant variations apart from the split ratio which is constant throughout. Since the external dimension is also constant across all topologies, SR maintains consistent boundaries. The optimum split ratio covers a good range for all of the combinations, this range is significantly smaller than the overall GA search space. A mid to high split ratio appears best, creating a machine with a relatively large rotor diameter.

It has been observed with each of the individual results that there is a correlation between TW and BI. A wider tooth will naturally increase the main flux path coupling the stator and rotor. However, with this increase the thickness of the back iron must be able to efficiently accommodate the greater amount of magnetic loading. This creates a robust correlation between the two variables, an individual with only one of these dimensions at a high value will perform poorly. The poor performance is caused by two factors, the first being a the large amount of stator iron will be effectively wasted. Secondly the wasted iron is there in place of slot area, reducing the electrical loading of the machine. This trend is made increasingly significant since the individuals are simulated at their theoretical thermal steady state rated load. With a fixed supply or loading some erroneous result could appear to perform well despite poor utilization of either electrical or magnetic loading capability.

	SR			TW			BI			MS		
	LB	Opt	UB	LB	Opt	UB	LB	Opt	UB	LB	Opt	UB
9s8p	0.55	0.593	0.65	8	13.60	14	4	6.72	8	32	39.19	43.5
12s10p	0.55	0.584	0.65	6	10.45	11	3.5	5.29	6.5	28	29.03	34.5
18s16p	0.55	0.624	0.65	4.5	7.26	8.5	3	3.60	6	16	20.74	21.5
18s20p	0.55	0.643	0.65	4.5	6.49	8.5	3	3.29	6	14	14.95	17
24s20p	0.55	0.646	0.65	3.5	5.95	6.5	2.5	3.12	5.5	14	15.87	17

Table 6.4: Overview of stage one torque optimization results

The optimum value for MS shows significant variation across each slot/pole combination within its respective limits. This variable acts a functional parent to the PM thickness in order to maintain a constant volume and therefore material cost. There is no particular trend evident from the results, instead the selection of this value is primarily influenced by the slot and pole numbers. In this case each appears to have a optimum, but its proportional value within the limits has no correlation.

The optimum values obtained from stage one were fixed for the second stage with a new set of variables introduced to improve the overall saliency ratio at its worst case operating point. This is at peak torque during the primary objective optimization of traditional saliency, meanwhile at no load for the repeated optimization targeting inverse saliency. The stage two results are presented in tabular form similar to stage one, with an additional table displaying the saliency characteristics of each best objective result.

Table 6.5 shows the optimum values for a traditional saliency objective, within their respective boundaries. The corresponding saliency characteristics at significant operating points are shown in Table 6.6. The comparison between each topology in combination with the best objective saliency characteristics will allow for common trends to be observed and determine the probable cause behind poor results. Of the six slot/pole combinations optimized, three were found to achieve the design objective and offer suitable choices. The 24 slot topology exhibits a significant saliency over the whole loading range. The best objectives are obtained from very similar values to those expected for the stage variables. With this result a tooth bridge with a broad profile is evident, along with a considerable slot opening that consequently shortens the length of the tooth bridge. This combination will be shown to be significant when compared to poor results, as well as the inverse saliency results. The 24 slot configuration also has a moderate magnet inset, at around the half inset value of 0.5.

	SO			TB			TT			MI		
	LB	Opt	UB	LB	Opt	UB	LB	Opt	UB	LB	Opt	UB
9s8p	4	4.11	10	2	5.00	5	0.75	2.00	2	0	0.883	1
12s10p	2	5.98	8	2	**2.00**	5	**0.75**	0.75	2	0	0.559	1
18s16p	1.5	3.45	5	1.5	1.50	3.5	0.75	0.75	1.5	0	0.528	1
18s20p	1.5	4.96	5	1.5	**1.50**	3.5	0.75	**0.75**	1.5	0	**0.100**	1
24s20p	1	3.50	4	1.2	3.00	3	0.75	1.00	1.2	0	0.621	1

Table 6.5: Overview of stage two saliency optimization results

The 18s16p is the third topology which exhibits a strong worst case saliency and therefore offers a suitable final choice. There is a common trend between this configuration and the 24s20p option. Once again a notable slot opening that creates a short tooth bridge is advantageous. So too is a moderate level of magnet inset, once again close to a half inset value of 0.5. There is no correlation however when analysing the tooth bridge profile, which in the case is thin and the variable that define the profile are both at their lower boundaries. This

goes against the convention observed and discussed previously that a broad tooth bridge profile limits the level of Q-axis saturation. The reason that these optimum values combine to produce a suitable machine is evident when the incremental inductances are considered as opposed to just the saliency ratio. Compared to the 24 slot combination where L'_q saturates by over 20% from no load to peak torque, here it only suffers from 9% saturation. This is almost equal to the rate at which the D-axis inductance saturates and why saliency ratio remains fairly even over the whole loading range. This indicates that the thin profile has a certain level of saturation caused by the no load magnet flux and despite the level of loading applied this area of the machine no longer impacts on the main saturation saliency observed in the HF saliency ratio.

	No Load			Rated			Peak		
	$\bar{L}'_d$	$\bar{L}'_q$	$\frac{\bar{L}'_q}{\bar{L}'_d}$	$\bar{L}'_d$	$\bar{L}'_q$	$\frac{\bar{L}'_q}{\bar{L}'_d}$	$\bar{L}'_d$	$\bar{L}'_q$	$\frac{\bar{L}'_q}{\bar{L}'_d}$
9s8p	17.3	21.0	1.22	13.19	11.76	0.89	11.69	8.48	0.73
12s10p	5.79	6.22	1.07	5.02	5.29	1.05	4.84	4.67	0.96
18s16p	3.05	3.43	1.12	2.89	3.31	1.15	2.81	3.12	1.11
18s20p	3.05	2.95	0.97	2.96	2.69	0.91	2.85	2.55	0.89
24s20p	2.60	3.21	1.23	2.28	2.87	1.25	2.18	2.58	1.19

Table 6.6: Overview of stage two best objective saliency characteristics

The three remaining optimization results do not equate to suitable design choices as they all have zero saliency conditions located within the loading range proposed in the specifications. With each of these best objectives the reason they are unsuccessful is down to two fundamental causes. The first is with that particular slot/pole combination and its associated design constraints it is not possible to avoid a zero saliency condition up to peak loading. This could be due to too severe level of Q-axis saturation or too small a natural saliency to begin with. The secondary cause is poor performance by the genetic algorithm. If during the initial populations a few erroneous or abnormal results are found this could influence the evolutionary path followed during the rest of the routine, possibly moving the variables away from their global optimums. This is a shortcoming of many numerical optimization methods and can be a particular issue is the initial population is poor.

The 18s20p result has been caused by a poor optimization performance, the final values selected represent very poor selections based on findings to this point. The thin tooth bridge profile will experience a considerable amount of saturation even

at no load. A magnet inset of 0.1 means there will be a small natural saliency within the machine, in combination with the Q-axis saturation at no load created by the tooth bridge shape means the saliency will be minimal or even inverse. In this case as can be seen in Table 6.6 the machine exhibits an small inverse saliency throughout the loading range. The 12s10p topology proves unsuccessful for the design specifications. This result once again looks have been significantly impacted by poor population selection of TB and TT, this has caused the no load saliency to drop to a low level of 1.07. When load is applied up towards peak, the saliency ratio suffers further due to L'_q saturation causing the zero saliency condition. The final topology that failed to meet requirements is the 9s8p option. Here the optimum values that form the best objective are robust selections and suggest a good result. This is evident as the is a strong saliency ratio of 1.22 at no load. Despite this, the configuration has a saliency crossover point below rated torque. The individual incremental inductance values demonstrates the severe level of saturation that takes place under load and the cause of the poor optimization result.

Topology	$\bar{T}$ (Nm)	T_c (% Rtd)	T_r (% Rtd)	T_r (% Pk)	k_t	B-EMF	
						$\hat{f}_1$	THD
9s8p	32.1	1.1 %	5.4 %	5.2 %	1.91	414 V	6.89 %
12s10p	33.9	1.2 %	7.2 %	6.8 %	1.72	396 V	6.48 %
18s16p	33.1	0.34 %	4.3 %	4.7 %	1.89	410 V	10.2 %
18s20p	32.3	0.51 %	9.7 %	11 %	1.53	346 V	15.8 %
24s20p	32.5	1.1 %	4.2 %	3.6 %	1.86	411 V	5.34 %

Table 6.7: Fundamental performance of traditional saliency topologies

Fundamentally all that is necessary for sensorless rotor position tracking is a constant form of HF saliency. Although this is the case, a machine with a greater level of saliency will perform better under sensorless control due to the improved SNR of the position tracking signal. This can be used as a contributing factor when selecting the best objective topology. The two stage, single-objective process has produced two feasible machine designs. The 24s20p configuration represents the best choice based on the superior saliency ratio compared to the18s16p configuration. However, the fundamental performance of each machine must be considered as well before making a final selection.

The stage two results where no load inverse saliency was the objective are displayed in Tables 6.8, 6.9 and 6.10. This form of design objective is not conventional and by no means a possible objective in most cases. It is worthwhile

exploring this design approach however since it offers a genuine method to completely remove the possibility of the a zero saliency condition. The results also offer further insight into designing for traditional saliency since they theoretically should produce an inverse trend. The optimum values for each stage variable demonstrate a clear trend across all of the optimized slot/pole combinations. The first three variables, SO, TB and TT combine to form the tooth bridge profile. It is clear that a long and thin tooth bridge is the optimum, all of the optimums are close to their respective lower boundaries. Based on the work in Chapter 3 this is expected since the thin profile will easily saturate when aligned with the Q-axis.

	SO			TB			TT			MI		
	LB	Opt	UB	LB	Opt	UB	LB	Opt	UB	LB	Opt	UB
9s8p	4	4.00	10	2	2.00	5	0.75	1.79	2	0	0.100	1
12s10p	2	2.00	8	2	2.00	5	0.75	0.75	2	0	0.100	1
18s16p	1.5	1.50	5	1.5	1.50	3.5	0.75	0.75	1.5	0	0.100	1
18s20p	1.5	1.50	5	1.5	1.50	3.5	0.75	0.75	1.5	0	0.112	1
24s20p	1	1.66	4	1.2	1.20	3	0.75	0.75	1.2	0	0.100	1

Table 6.8: Overview of stage two inverse saliency optimization results

	No Load			Rated			Peak		
	$\bar{L}'_d$	$\bar{L}'_q$	$\frac{\bar{L}'_q}{\bar{L}'_d}$	$\bar{L}'_d$	$\bar{L}'_q$	$\frac{\bar{L}'_q}{\bar{L}'_d}$	$\bar{L}'_d$	$\bar{L}'_q$	$\frac{\bar{L}'_q}{\bar{L}'_d}$
9s8p	10.2	9.23	0.91	9.90	10.1	1.02	9.65	9.57	0.99
12s10p	6.13	5.70	0.93	5.25	5.15	0.98	5.09	4.60	0.90
18s16p	3.27	3.44	1.05	3.12	3.41	1.09	3.04	3.20	1.05
18s20p	3.53	3.24	0.92	3.45	2.98	0.86	3.29	2.76	0.84
24s20p	2.45	2.69	1.10	2.25	2.54	1.13	2.16	2.36	1.09

Table 6.9: Overview of stage two best objective inverse saliency characteristics

Topology	$\bar{T}$ (Nm)	T_c (% Rtd)	T_r (% Rtd)	T_r (% Pk)	k_t	B-EMF	
						$\hat{f}_1$	THD
9s8p	32.4	0.36 %	5.3 %	5.2 %	1.93	414 V	13.5 %
12s10p	34.5	2.2 %	8.0 %	7.1 %	1.76	398 V	10.2 %
18s16p	32.9	0.37 %	4.2 %	4.9 %	1.88	407 V	11.9 %
18s20p	31.3	0.24 %	11 %	12 %	1.48	337 V	21.6 %
24s20p	32.6	1.9 %	5.1 %	5.1 %	1.86	411 V	9.83 %

Table 6.10: Fundamental performance of inverse saliency topologies

All of the optimized topologies have the minimal level of PM inset that will limit

the geometrical variation between the D and Q-axis HF inductance paths. This works in conjunction with the tooth bridge profile and increased Q-axis reluctance to produce an inverse saliency machine. The matched results for all of the stage variables only works effectively on one of the optimized topologies. The 18s20p configuration has a no load saliency ratio of 0.92 and peak saliency ratio of 0.84. This follows the theoretical benefit of an inverse saliency by improving with load, hence the worst case operating point being no load. The best objective results for the five remaining slot/pole combinations do not have a no load inverse saliency, or those that do are unable to form a significant saliency characteristic that is present across the whole loading range. This is the case with the 9s8p and 12s10p configurations. The 18s20p topology is the only suitable design choice from this two stage, single-objective routine and will be analysed in more detail.

6.4.1 18s20p Inverse Saliency Machine

The rated torque, optimized 18s20p topology provided an appropriate configuration to create a machine which has an inherent inverse saliency. This form of high frequency saliency means as the Q-axis inductance saturates at a greater rate than the D-axis under load the fundamental saliency characteristic improves. In order to induce the inverse characteristic, even at no load, in general it is necessary to reduce L'_q enough to less than its D-axis equivalent. The thin and long tooth bridge profile that was optimized becomes saturated easily due to the zig zag leakage flux that occurs when aligned with the Q-axis. This leakage flux can be increased or encouraged to occur with the selection of similar slot and pole numbers, which is the case with this 18s20p topology. The presence of this leakage flux is illustrated in the flux plots in Figure 6.11, where 6.11(a) is in alignment with the D-axis with minimal leakage flux and 6.11(b) is in alignment with the Q-axis and causing saturation within the tooth bridge.

The optimization routine has successfully achieved an objective value that creates in saliency ratio of 0.92 at no load, down to 0.84 at peak torque. Although this is the desirable outcome, previous work in Chapter 3 revealed that a machine design like this has several detrimental effects on the fundamental performance of the machine. A more detailed analysis of the HF saliency profile also reveals an interesting characteristic. The machine topology has been optimized to induce an inverse saliency, achieved by saturating the Q-axis inductance. This objective is successful since at no load $L'_q < L'_d$. However, this topology appears to cause a secondary effect on the D-axis reluctance path. The plot in Figure 6.12 illustrates

how the D and Q-axis inductances change with respect to load. The solid line represents the mean value at that torque output, while the dashed lines represent the peak and trough values over a whole rotation, indicating the inductance ripple.

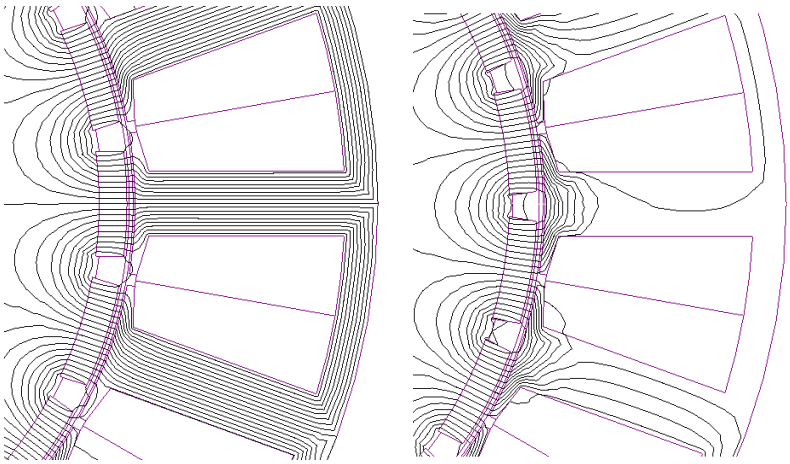

(a) Flux plot at $\theta_e = 0°$ (b) Flux plot at $\theta_e = 90°$

Figure 6.11: No load zigzag leakage flux in 18s20p topology

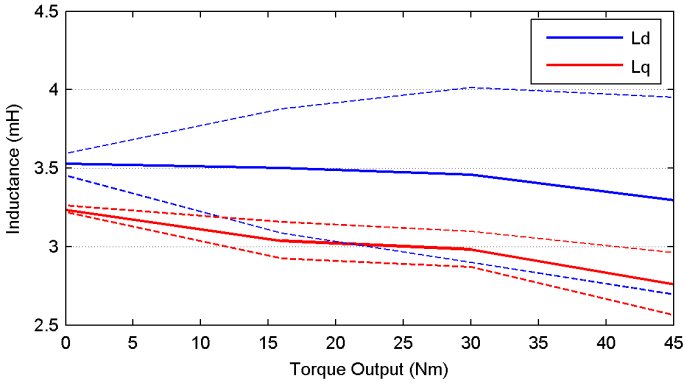

Figure 6.12: HF saliency profile against torque output

The data shows how both incremental inductances are decreasing at a similar rate with respect to increasing load. It also demonstrates how the level of ripple, caused by a changing rotor position creating fluctuations in the respective D and Q-axis reluctance paths. The incremental inductance ripple has the a repetitive pattern over a whole revolution, with a frequency equal to six times the electrical frequency of the machine ($f_{L'} = 6 \times f_e$). It is an expected result that the level of ripple increases with load, with the proportional increase in L'_q ripple in Figure 6.12 typical. The data shows how the machine topology that is advantageous

to producing an inverse saliency creates a significant ripple on L'_d. This level of ripple causes issues with the signal processing within the sensorless control scheme. Most notably though is that the ripple is large enough to cause multiple zero saliency points within a single rotation. The ripple created by large fluctuations in L'_d is caused by the saturation occurring in the stator under operation. Heavily saturated stator iron effects the reluctance properties of the iron. As the rotor position changes the flux density of the various stator back iron sections varies. The large ripple on L'_d occurs because the D-axis reluctance path passes through the stator iron at points of peak saturation and low saturation at regular intervals. In contrast, the Q-axis reluctance path remains far more consistent due to the leakage inductance that is encouraged to occur due to the tooth bridge profile.

The fundamental performance of an inverse saliency machine has been shown to as poor in previous work. In general the tooth bridge profile can contribute to no load cogging torque and significantly to the torque ripple under load. The machine analysis confirms this observation, the machine generates a low cogging torque but when under load there is a significant torque ripple. At the rated torque operating point this torque ripple is 11.5%. In addition to this the secondary optimization has reduced the quality of the induced B-EMF present at no load. This has introduced significant 3^{rd} and 5^{th} harmonics as shown by the Fast Fourier Transform (FFT) result in Figure 6.13. The 21.56 % Total Harmonic Distortion (THD) is clearly evident in the B-EMF waveform.

The performance analysis of this topology has demonstrated that despite successfully meeting the design objective it is inadequate as a machine design. The large D-axis incremental inductance ripple causes zero saliency points at high load that limits the sensorless control ability. The geometrical design generates a very poor quality torque output and the previous conclusion on targeting an inverse saliency characteristic in Section 3.9 remains the same. Although the design approach is encouraging in theory, it has not been possible to implement it in practice within a strong performing PMSM.

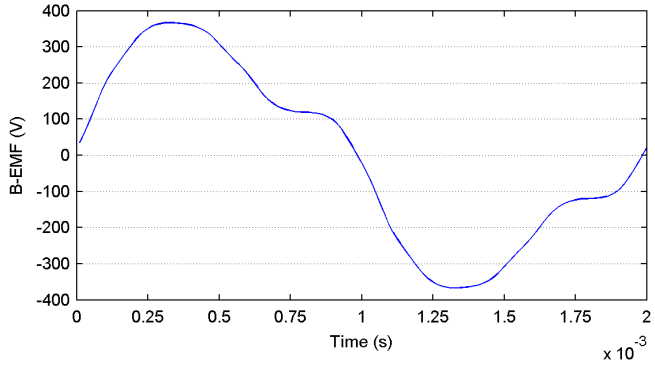

(a) No load B-EMF waveform

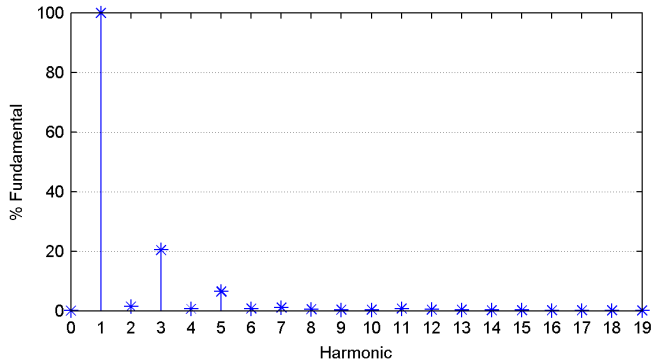

(b) Harmonic content of no load B-EMF

Figure 6.13: FFT analysis of no load B-EMF

6.4.2 24s20p Traditional Saliency Machine

The two stage, single-objective optimization process, revealed the 24s20p topology as the best choice based on the HF saliency characteristic it produces. The machine topology produces a strong saliency ratio of 1.23 at no load. This is a good starting point for sensorless controllability since it allows a significant margin for which the Q-axis inductance can saturate under load. As expected with increasing load L'_q reduces to a greater extent than L'_d. Up towards rated torque output the saliency ratio remains consistent before the level of saturation begins to effect L'_q more. This leads to a saliency ratio of 1.19 at peak loading. The saliency profile with respect to torque output is shown in Figure 6.14. The data shows the mean value over a complete revolution, with the highest and lowest inductance values represented by the dashed lines. The plot illustrates that there is a strong saliency throughout the whole operational range.

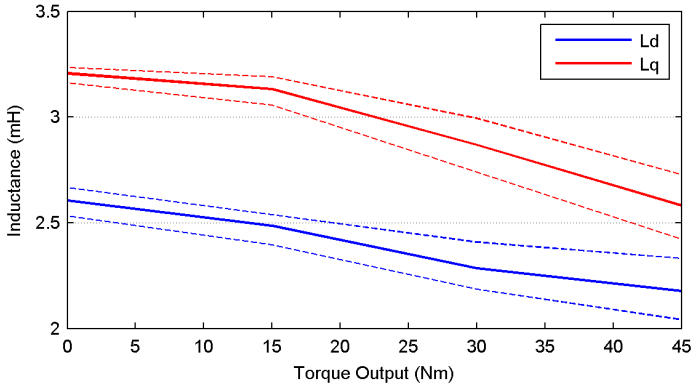

Figure 6.14: HF saliency profile against torque output

The load dependent ripple is clearly evident, however up to peak loading it is not too big to create controllability issues. The overall saliency characteristic is formed by the main machine flux paths across the rotor and stator. This means the main saturation saliency formed with the topology is strong and not impacted upon by saliencies created by individual geometrical features. Consequently, this has contributed well towards the fundamental performance of the machine since it is largely unaffected and followed a traditional topological design. The machine produces a relatively high amount of no load cogging torque, since this was not taken into account during the optimization process it could be expected. The cogging torque contributes to the level of torque ripple when operating under load, however this 4% torque ripple is acceptable.

The plot in Figure 6.15 shows a FFT analysis of the no load B-EMF. There is a small harmonic content to the B-EMF, with $THD = 5.34\%$. This is encouraging and has been helped by the machine topology and radial shaped PM poles.

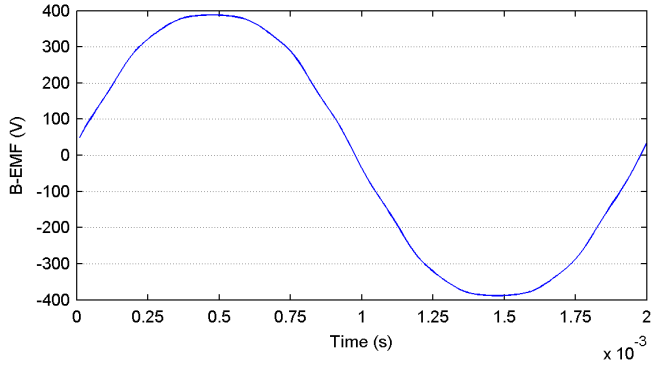

(a) No load B-EMF waveform

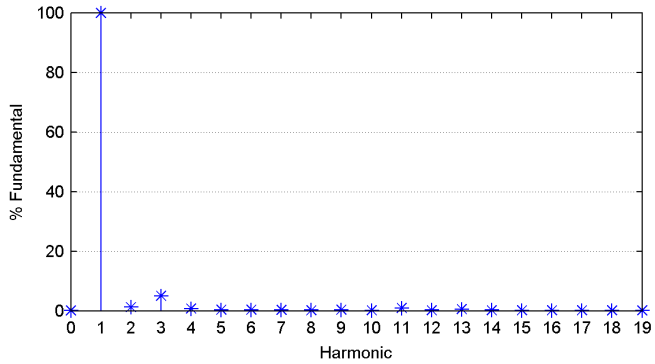

(b) Harmonic content of no load B-EMF

Figure 6.15: FFT analysis of no load B-EMF

The 24s20p topology demonstrates excellent HF saliency levels over the operating range that enables accurate sensorless control. This means the machine design could be sensorlessly controlled beyond the defined operational envelope. In terms of fundamental performance, the machine generates a strong torque with a low level of torque ripple. The level of cogging torque is a concern and provides further evidence as to why it should be considered as a optimization objective. The two stage, single-objective design routine produced a slot/pole combination and geometrical topology that meets the performance requirements. Despite this, following an in depth examination of the fundamental performance there are clear improvements that can be made to the machine by considering torque quality during a multi-objective optimization routine.

6.5 Single Stage, Multi-Objective Genetic Algorithm Results

The optimization results from the two stage, single-objective routine have revealed design trends that enhance the saliency characteristics of a PMSM. This leads to improved accuracy for HF injection based position tracking, while removing zero saliency conditions that can cause major issues. The 24s20p topology as shown to be the best selection during the two stage, single-objective routine, due to good saliency and high torque production. The MGA approach discussed in Chapter 5 will be carried out on this slot/pole combination. Focusing on fundamental performance and a traditional HF saliency. Based on all findings to this point an inverse saliency machine was no longer considered as a design option.

A number of multi-objective routines were performed to provide a large data set that could be used to determine a suitable design routine and best topological design. These were all performed on the 24s20p topology, since this has been shown to be the most feasible design option up to this point. There are eight geometrical parameters available for optimization; this could prove to be too large of a search space for the GA to sufficiently converge. To combat this several MGA routines were carried out with a reduced number of variables. When a variable is removed and set as a constant, a strong performing value was selected based on previous results.

The boundary conditions fr each design parameter were refined to improve the efficiency of the optimization routine. The adjustments were made based on the observations made with the population distribution plots presented in Section 6.3.5. The updated boundaries are presented in Table 6.11.

Variable	LB	UB
Split Ratio	0.60	0.65
Tooth Width	3.5mm	6.5mm
Back Iron Thickness	2mm	4mm
Magnet Span	14.5°	17.5°
Slot Opening	1.5°	4°
Tooth Bridge Thickness	1.2mm	3mm
Tooth Tip Thickness	0.8mm	1.2mm
Magnet Inset	10%	90%

Table 6.11: Boundary conditions for 24s20p MGA routine

The MGA objective functions used for the routine are rated torque production, no load cogging torque and HF saliency ratio at peak loading. The latter of which

is implemented as either an overall objective function, or as minimum threshold based penalty term as discussed in the previous chapter.

6.5.1 MGA Routine with Eight Design Variables

This routine uses all eight variable geometrical parameters within the machine script. It was performed on several occasions to examine the possible outcomes when adjusting the objective functions. The optimization variants are as follows:

- 3 objectives, saliency at peak load, rated torque production and no load cogging torque.
- 2 objectives, rated torque production and no load cogging torque. Multiplicative penalty term for $\frac{L'_q}{L'_d} < 1.10$ at peak load.
- 2 objectives, rated torque production and no load cogging torque. Death penalty term for $\frac{L'_q}{L'_d} < 1.10$ at peak load.

The multi-objective approach generate a data set of best objectives (feasible solutions). As opposed to an optimum result the data set incorporates those individuals that produce the best values for one or many objective functions. It is then down to a compromised solution to select single or multiple results that reflect the best choices.

The final solution results from the first optimization routine is shown in Table 6.12. Each solution has their associated objective value for the three objective functions. The values highlighted in bold typeface are immediately discounted as they are outside of the design range, making that solution unsuitable. In the case of saliency this is below the 1.10 threshold, for rated torque production this is below the 30Nm threshold. Finally, for cogging torque this is above the 0.3Nm peak to peak threshold. The best solutions remaining are then weighed up based on their individual benefits before the final solutions are selected (highlighted in red typeface). Once the threshold values are met for each objective it is more advantageous for a machine to exhibit a higher saliency, lower cogging torque and higher rated torque. The optimization routine runs simulations at three different loadings in order to gather all the required data for optimization.

Of the final solutions produced by the eight variable routine in Table 6.12 there are two solutions that display superior objective values, solutions seven and 15. These two solutions have a strong saliency ratio at peak loading, produce a strong

rated torque and have low no load cogging torque. Based on the data available at this point, solution seven appears to be the best choice based on the torque characteristics. However, both topologies are analysed in more detail and with increased accuracy to ensure this remains the case.

Soln	Saliency	Cogging	Torque	Soln	Saliency	Cogging	Torque
1	**1.07**	0.124	36.9	11	1.18	**0.333**	34.9
2	1.10	**0.911**	35.9	12	**0.99**	**0.866**	37.2
3	1.23	**0.447**	33.4	13	1.29	0.234	32.2
4	1.19	**0.569**	34.7	14	1.05	**0.677**	36.7
5	1.18	**0.312**	34.8	15	1.24	0.145	33.0
6	1.31	**0.971**	32.4	16	**1.01**	**0.549**	36.5
7	1.17	0.083	33.8	17	1.28	0.288	33.1
8	1.13	**0.603**	35.6	18	1.14	**0.786**	35.1
9	1.20	**0.422**	34.5	19	1.12	**0.455**	35.2
10	1.16	0.259	35.0	20	**1.07**	**0.341**	35.6

Table 6.12: 24s20p MGA result with three objectives and eight variables

The two best solutions have their respective advantages and disadvantages and are not necessarily closely matched. The optimum values that form the best solutions are displayed in Table 6.13. Relative to the initial boundary conditions the two topologies are similar. The difference in the geometrical parameters reveals where the cause of variation in performance is. The greater level of cogging torque in solution 15 originates from the larger slot opening combined with a thin tooth bridge. This formulation has created a greater amount of interaction between the stator slots and rotor poles. The disparity in the magnet inset between the two solutions is a contributing factor of the superior saliency characteristic in solution 15, contributing to a larger effective airgap in the D-axis reluctance path.

Soln	SR	TW	BI	MS	MI	SO	TB	TT
7	0.628	5.59	3.97	16.73	0.391	2.78	2.56	1.22
15	0.632	5.19	3.13	17.05	0.438	3.53	2.21	0.82

Table 6.13: Optimum dimensions of best solutions for MGA variables

The topologies for solution seven and 15 were simulated accurately and analysed for their fundamental and sensorless performance. The data presented in Table 6.14 is an overview of the HF saliency properties at significant loading points. Both of the solutions maintain a strong saliency ratio over the whole loading range. It is evident that L'_q saturates significantly within both topologies. Due

to the high no load saliency characteristic there is no zero saliency condition for either. The two solutions are controllable. Solution 15 represents a better choice in terms of SNR and signal processing of the HF saliency tracking signal.

Soln	No Load			Rated			Peak		
	$\bar{L}'_d$	$\bar{L}'_q$	$\frac{L'_q}{L'_d}$	$\bar{L}'_d$	$\bar{L}'_q$	$\frac{L'_q}{L'_d}$	$\bar{L}'_d$	$\bar{L}'_q$	$\frac{L'_q}{L'_d}$
7	2.52	3.35	1.33	2.31	2.97	1.28	2.21	2.57	1.16
15	1.97	2.83	1.44	1.84	2.49	1.36	1.77	2.13	1.21

Table 6.14: Saliency characteristics for best solution topologies

The fundamental performance analysis results are presented in Table 6.15. Here the quality can be compared using the level of no load cogging torque and torque ripple under load. Once again, both topologies perform well and their respective cogging torque are well within the design specifications.

Soln	T_c (% Rtd)	T_r (% Rtd)	T_r (% Pk)	k_t	B-EMF	
					$\hat{f}_1$	THD
7	0.295	2.85	2.47	1.83	404 V	7.28 %
15	0.491	3.66	2.43	1.81	395 V	4.86 %

Table 6.15: Fundamental performance of best solution topologies

An FFT analysis was performed on the B-EMF waveforms for each topology. The peak fundamental value and THD of the respective waveforms are indicated in Table 6.15. Each waveform is shown in Figure 6.16, along with the harmonic content obtain using the FFT. The two solutions represent good machine design choices with a good compromise between performance indicators; here solution 15 is the best available topology obtained from the optimization process. The machine exhibits excellent saliency characteristics that ensure accurate sensorless control. In addition to this, despite having greater cogging torque it is well within the limits of the design specification and the quality of the B-EMF means the overall machine is an excellent choice.

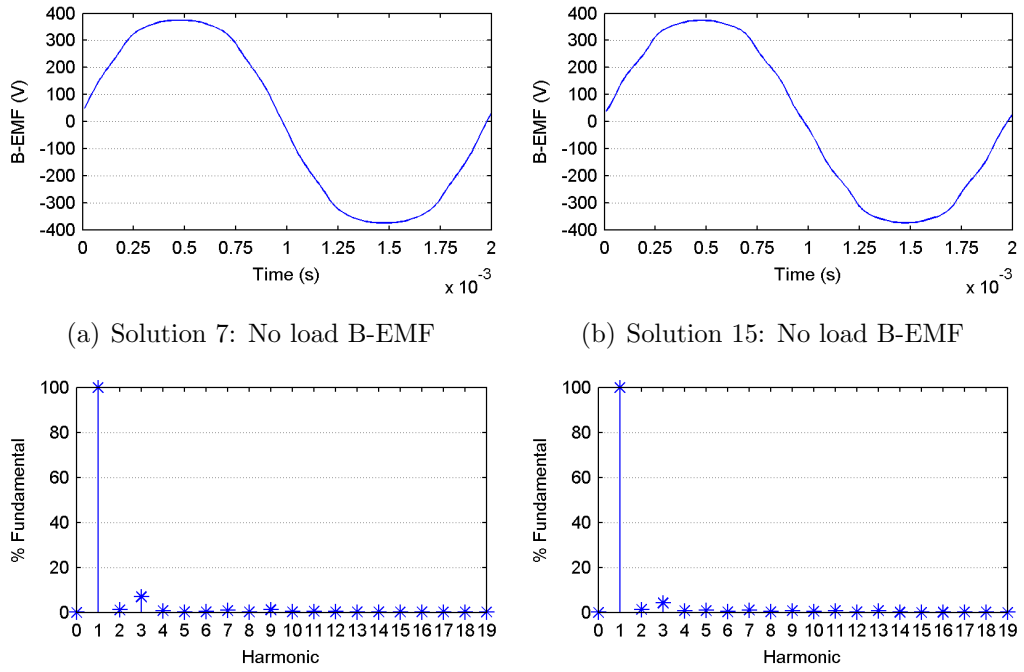

(a) Solution 7: No load B-EMF

(b) Solution 15: No load B-EMF

(c) Solution 7: B-EMF harmonic content

(d) Solution 15: B-EMF harmonic content

Figure 6.16: FFT analysis of B-EMF for best solution topologies

6.5.2 Penalty Function Approach

The identical parameters were used in repeated MGA routines following this eight variable examination. The significant variation was that the HF saliency ratio was removed as a objective function. Instead a penalty function method was implemented, with the saliency threshold set as $\frac{L'_q}{L'_d} \geq 1.10$. Any individual created by the GA that had a saliency ratio below this threshold had a penalty function applied to the remaining objective values (no load cogging torque and rated torque production). Those individuals that successfully exceeded the threshold limit would have their objective scores unchanged. The optimization routine was carried out repeatedly with initially an additive penalty and then a multiplicative penalty. After unsuccessful routines, the magnitude of the penalty was adjusted and then the optimization was repeated.

In principal, all that is required to control a machine using HF injection position tracking is a distinguishable saliency. It is not necessary to maximize it during the optimization, although a higher level of saliency can simplify the control scheme and accuracy. By having it as an objective function it could be causing excessive deterioration to the fundamental performance during the optimization

by 'pulling' future individuals away from strong performing values. This is the reason a penalty function method was tested. The threshold value of $\frac{L'_q}{L'_d} \geq 1.10$ was set so that any individual that met this condition could be sensorlessly controlled.

Calculating the saliency at peak loading means it is at it's lowest value in the loading range. It has been discussed previously that under high load the incremental inductance ripple, caused by varying rotor position, is significant. The saliency value calculated by the GA fitness function is based on mean values. Therefore, a threshold value of 1.10 takes into account the possibility that in real terms it is lower at given rotor positions and ensures that controllability is still possible at these points. This method of saliency calculation reduces the simulation accuracy required during the FEA and therefore total optimization duration.

In order for the optimization to be effective the level of penalty function needs to be considered, [57]. Several attempts were performed using incremental changes in both Additive Penalty Function (APF) and Multiplicative Penalty Function (MPF) methods. In the end a moderate MPF produced feasible solutions with the highest quality of result. With the initial unsuccessful routines the results revealed that during the initial populations there were no individuals that exceeded the saliency threshold. This caused the MGA to assume that the objective scores with penalties applied to be good fitness values instead of moving away from or discarding them.

An alternative penalty function approach is a Death Penalty Function (DPF); this uses the same process but has a severe penalty for unsuccessful individuals. When an individual does not meet or exceed the penalty threshold it is in theory rejected completely from being a feasible solution as the penalty applied is ∞. The main drawback with this is that the MGA may not revisit the particular variable values that contribute to an unsuccessful individual. The DPF method was carried out in addition to the traditional penalty function approach.

The penalty function method represented an inviting approach to the machine design challenge. It provided the opportunity to remove the saliency characteristic as a primary optimization objective. This meant it would not dictate the geometrical changes during the routine. Instead the optimization routine would be solely focused on fundamental machine performance. The main drawback with this approach is that without the pull of the saliency characteristic the GA can spend a large amount of time moving towards poor individuals.

Multiplicative Penalty Function

The same GA parameters were implemented with a 1.5 multiplicative penalty on each objective function and a saliency penalty function threshold of 1.10. The results from this successful optimization routine are shown in Table 6.16. Without the direct pull of a saliency objective the GA progresses through the initial generations and narrows in on feasible solutions. The data in the table shows that with the final solutions there is very little variation in the thermal rated load capability, except for solution two. With the saliency characteristic removed the design choice comes down to a simple compromise between torque production and cogging torque. This means that solution three represents the best choice. The superior torque production, compared to solution two, will benefit the peak torque saliency characteristic. The peak torque output can be achieved with lower electrical loading and therefore limit the amount of Q-axis saturation.

Soln	Cogging	Torque
1	0.099	37.6
2	0.036	35.9
3	0.039	37.6
4	0.069	37.6
5	0.217	37.7
6	0.159	37.6
7	0.099	37.6

Table 6.16: 24s20p MGA result with multiplicative penalty function

Death Penalty Function

Following the successful implementation of a MPF the design routine was repeated using a death penalty function. The DPF aims to immediately reject infeasible solutions from subsequent generations. It can lead to a more efficient optimization routine but due to the high rate of rejected individuals the GA can be pushed away possible optimum results. The results from the successful routine are presented in Table 6.17.

Soln	Cogging	Torque
1	0.073	37.2
2	0.099	35.4
3	0.141	37.6
4	0.245	37.7
5	0.275	37.7
6	0.175	37.7
7	0.077	37.3

Table 6.17: 24s20p MGA result with death penalty function

With the same parameters the MGA has also produced seven feasible results, all of a similar standard to the multiplicative penalty. Solution one is the best choice, marginally better than solution seven based on the data set. The final solutions from the penalty function approach were analysed in greater detail. An overview of the saliency characteristic is presented in Table 6.18 and the fundamental performance in Table 6.19. An interesting point that immediately arises is the peak saliency ratio. The two best solutions have a ratio of just above the 1.10 threshold. This indicates that enhancing saliency as an objective does cause detrimental effects to the torque quality in the machine. If they were mutually exclusive there is every chance that even without it as an objective the best topology would have a ratio comfortably above the threshold. As discussed during the decision making of the threshold value, since it is not an objective the value must be low and achievable as the GA cannot directly influence the saliency ratio when it is not incorporated as an objective function.

Soln	No Load			Rated			Peak		
	$\bar{L}'_d$	$\bar{L}'_q$	$\frac{L'_q}{L'_d}$	$\bar{L}'_d$	$\bar{L}'_q$	$\frac{L'_q}{L'_d}$	$\bar{L}'_d$	$\bar{L}'_q$	$\frac{L'_q}{L'_d}$
MPF	2.31	3.06	1.32	2.08	2.62	1.26	1.98	2.24	1.13
DPF	2.58	3.44	1.33	2.28	2.88	1.26	2.16	2.36	1.10

Table 6.18: Saliency characteristics for best solution topologies

The increased emphasis on no load cogging torque within the design routine is evident with both the MPF and DPF results, Table 6.19. This specific focus is particularly important with regards to servo motors, where as with alternative applications another torque characteristic might be deemed more significant. There is a clear improvement in the quality of this objective in comparison to the three objective routines. Without the direct influence of saliency as an objective this is expected. The primary focus of the MGA on torque production and cogging

torque has caused a drop in the quality of B-EMF waveforms. With both forms of penalty function there is a noticeable increase in THD which will contribute to increased loses during operation.

Soln	T_c (% Rtd)	T_r (% Rtd)	T_r (% Pk)	k_t	B-EMF	
					$\hat{f}_1$	THD
MPF	0.137	3.39	2.95	1.85	403 V	7.28 %
DPF	0.125	3.06	2.57	1.84	404 V	7.79 %

Table 6.19: Fundamental performance of best solution topologies

The no load B-EMF waveforms generated by the two solutions are plotted in Figure 6.17. The harmonic content of each waveform is displayed below their respective waveforms. Using the data from an FFT analysis.

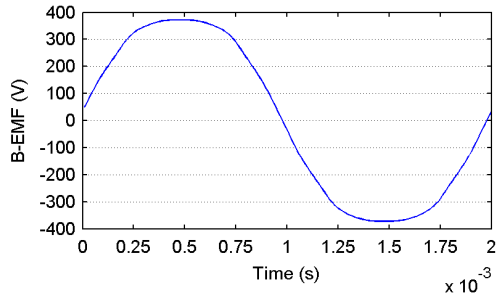

(a) MPF Solution: No load B-EMF

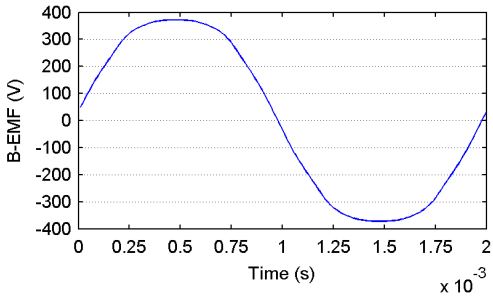

(b) DPF Solution: No load B-EMF

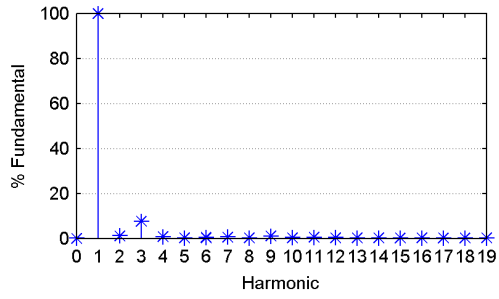

(c) MPF Solution: B-EMF harmonic content

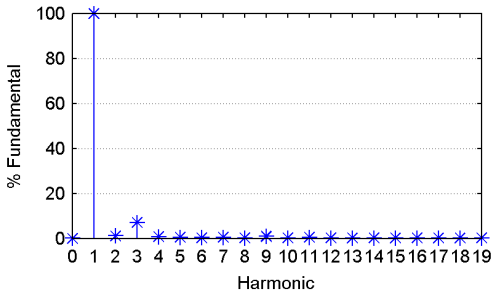

(d) DPF Solution: B-EMF harmonic content

Figure 6.17: FFT analysis of B-EMF for best solution topologies

The geometrical values for these two best solutions are shown in Table 6.20. The performance characteristics are closely matched since both topologies are similar in their make up. The only significant difference between the two configurations is the degree of slot opening. The MPF solution has a larger slot opening, which creates a shorter tooth bridge. This appears to cause the marginal improvement

in peak torque saliency ratio. Once again, this tooth bridge format demonstrates the characteristic of a lower no load saliency ratio that has a lower rate of Q-axis saturation. This reduced saturation rate means that the traditional saliency characteristic is still present further up the loading range.

Soln	SR	TW	BI	MS	MI	SO	TB	TT
MPF	0.626	5.57	2.97	16.90	0.257	3.51	1.76	0.84
DPF	0.633	5.60	3.00	16.79	0.284	2.70	1.84	0.80

Table 6.20: Optimum dimensions of best solutions for MGA variables

The penalty function approach has demonstrated that although the main saliency characteristic is an important design factor it is not necessary as a direct objective. With the threshold set at 1.10 the MGA was given a relatively low penalty based threshold that could be met reasonable well by the topology. It was aimed at just ensuring controllability. The geometrical topology works in combination to produce an effective machine design, while also forming the main HF reluctance paths. This approach has therefore shown that the main saliency characteristic can still be exploited through a penalty function. With the saliency threshold set at a low value it has ensured the routine had more chance of a success. If a design specification requires a strong saliency at peak load then the penalty function approach is not the best choice as without the direct pull of a saliency objective the MGA is likely to fail.

With the penalty function method used to this point the removal of saliency as an objective has resulted in a dual objective process. There is the option of introducing a third objective with the possibility of further improving the properties of the final solution. With the FE intensive optimization routine, rather than introducing an objective that requires additional simulations it is possible to analyse rated torque ripple using the data set already available. A MPF optimization routine was performed with these three objective functions. The final solutions obtained from the routine are presented in Table 6.21, with infeasible objective values highlighted in bold typeface. The cogging torque data is represented in peak-to-peak Nm, while the torque ripple is quantified as the peak-to-peak ripple as a percentage of rated torque.

Soln	Cogging	Torque	% Ripple	Soln	Cogging	Torque	% Ripple
1	0.250	37.3	3.17	8	0.125	36.5	2.82
2	0.191	37.4	3.27	9	0.152	36.0	1.95
3	**0.557**	35.8	0.96	10	0.171	37.1	3.35
4	**0.372**	36.5	1.61	11	0.110	36.9	3.01
5	**0.348**	36.2	1.34	12	0.211	36.5	2.36
6	**0.594**	36.5	1.84	13	0.126	36.5	2.66
7	**0.619**	36.8	2.02	14	**0.508**	35.8	1.14

Table 6.21: 24s20p MGA result with MPF, three objectives and eight variables

The MGA solutions show a large variation in cogging torque and torque ripple while exceeding the saliency threshold. Several of the solutions are deemed unrealistic due to a significant cogging torque characteristic. The best solution is determined as number 11, since the machine exhibits both a low cogging torque and rated torque ripple. When the topology was optimized in more detail the suitability of the final design was analysed. The variable results that produce the topology are shown in Table 6.22.

Soln	SR	TW	BI	MS	MI	SO	TB	TT
11	0.644	5.87	3.26	16.63	0.303	2.44	2.48	0.88

Table 6.22: Optimum dimensions of best solution for MGA variables

The additional focus of the GA upon torque characteristics is evident. The machine has a no load cogging torque of 0.306%, a rated torque ripple of 2.88% and peak torque ripple of 2.83%. The expected improvement in torque ripple has taken place but there has been a trade-off, with an increase in no load cogging torque. The machine also produced a smooth no load B-EMF, with a fundamental voltage of 417V and 8.08% THD. This distortion is largely due to the 3^{rd} harmonic.

In comparison to the results presented previously the revised MGA routine was able to improve the torque ripple characteristic. This was at the expense of increasing the no load cogging torque, although it remained well below the maximum threshold. This routine explored the possibility of obtaining additional gains when using a penalty function approach. In this instance the torque ripple was introduced since the required data was easily gathered within the existing FE simulations. The marked improvement demonstrates that while ensuring sensorless capability the machine design routine can continue to successfully optimize

for three objectives. The level of torque ripple is not a fundamental property that is largely significant to the servo machine specifications and therefore not justifiable when it reduces the quality of machine cogging torque. This does however demonstrate that if an additional machine specification was important it could be incorporated. The decision would have to be made as to whether the possible increase in individual simulation time required for an objective, which greatly increases overall duration, is necessary.

6.5.3 MGA Routine with Seven Design Variables

The eight geometrical variables within the machine topology ensured there was a high amount of parametrization available. The eight variable MGA routine produced good quality results with a strong final solution. The eight variables had their respective boundaries reduced prior to the MGA routine, taking advantage of the previous findings from the single objective routines. This contributed to the quality of the results as it narrowed the search space for the GA. It allowed the GA to spend all the optimization time on more feasible solutions. Taking this into consideration, reducing the number of variables can go a long way to improving the efficiency of the MGA and ultimately the quality of results.

To this point in time the level of PM inset in the rotor (MI) has been a variable with a significantly large search space. This has allowed its relative impact upon sensorless properties to be examined and help improve the optimization results. However, particularly in a numerical optimization problem such as this, it improves the quality of result if variables have equal weight. The MI variable has significant influence upon all outcome objectives and greatly impacts on how its fellow variables interact. In machine design the level of inset is often predetermined by the a rotor design decision or production limitations. The seven variable routine removes MI as a design variable and instead sets it as a constant practical value. Taking into account the manufacturing processes that were factored in during the development of the topology the level of inset is set as 0.3. This value means the topology benefits from the characteristics and simpler construction of a SPMSM while the PM poles are inset enough to be self-retaining within the rotor lamination.

The results of the optimization routine are shown in Table 6.23. The data clearly demonstrates that the quality of result has improved compared to the eight variable routine. Fixing the level of magnet inset has removed a dominant variable

that arguably prevented the GA from spending more time on strong performing solutions. The overall quality of result is dependent on a sensible choice for MI and with a value of 0.3 it can be seen that all of the best solutions are suitable design choices. The optimum solutions from the previous MGA results were all found to have a value for MI in the region of 0.3. All of the 20 final solutions meet the design specification since they are all above/below their respective thresholds. Based on the values presented the two solutions that were investigated further are solutions one and two. This decision was made with the knowledge that once the torque production and saliency ratio characteristic are satisfied, cogging torque becomes the single most important determinant.

Soln	Saliency	Cogging	Torque	Soln	Saliency	Cogging	Torque
1	1.23	0.104	37.5	11	1.18	0.117	36.8
2	1.24	0.078	37.5	12	1.28	0.197	37.1
3	1.21	0.138	37.6	13	1.21	0.147	37.6
4	1.12	0.120	37.2	14	1.17	0.131	37.3
5	1.14	0.114	37.2	15	1.20	0.128	37.2
6	1.23	0.158	37.5	16	1.27	0.112	35.8
7	1.28	0.256	37.1	17	1.27	0.158	37.1
8	1.27	0.185	37.1	18	1.22	0.144	37.3
9	1.21	0.113	37.6	19	1.17	0.114	36.7
10	1.28	0.256	37.1	20	1.26	0.164	37.5

Table 6.23: 24s20p MGA result with three objectives and seven variables

These best two solutions have very similar objective results, with the most significant difference being no load cogging torque. The closely matched results occur since the overall topologies are comparable. The dimensions that form these two best solutions are present in Table 6.24. The near equal optimal performance is confirmed by the two topologies being very similar in their configuration. With the magnet inset fixed at 0.3 the GA determines that a tooth bridge which is short and thin, with respect to the boundary limits, is beneficial.

Soln	MI	SR	TW	BI	MS	SO	TB	TT
1	0.30	0.640	5.21	2.87	17.11	3.12	1.26	0.94
2	0.30	0.639	5.12	2.85	17.29	3.51	1.30	0.93

Table 6.24: Optimum dimensions of best solutions for MGA variables

The two solutions were analysed in depth with a focus of the three most significant operating points within the loading range. The saliency characteristic was

calculated at the three operating points, with the incremental inductance values at each presented in Table 6.25. Both solutions maintain a strong saliency up to and beyond the peak torque requirements. From the values of L'_q it is clear that saturation has taken place under increasing load. The rate of saturation is significantly greater than that seen in L'_d, however the strong saliency ratio present at no load helps combat this up to, and beyond, peak loading. The large differential between L'_d and L'_q means that with HF injection, accurate rotor position tracking is possible. Since the saliency characteristics are closely matched for both topologies the same conclusion can be drawn on both.

Soln	No Load			Rated			Peak		
	$\bar{L}'_d$	$\bar{L}'_q$	$\frac{\bar{L}'_q}{\bar{L}'_d}$	$\bar{L}'_d$	$\bar{L}'_q$	$\frac{\bar{L}'_q}{\bar{L}'_d}$	$\bar{L}'_d$	$\bar{L}'_q$	$\frac{\bar{L}'_q}{\bar{L}'_d}$
1	1.79	2.38	1.33	1.70	2.24	1.32	1.66	2.04	1.23
2	1.73	2.36	1.37	1.64	2.18	1.33	1.61	1.98	1.23

Table 6.25: Saliency characteristics for best solution topologies

The similarity between these two solutions continues with their fundamental properties. These are summarized in Table 6.26. The two best solutions continue to represent suitable design choices. Their torque properties are good, with solution two demonstrating marginally improved no load cogging torque.

Soln	T_c (% Rtd)	T_r (% Rtd)	T_r (% Pk)	k_t	B-EMF	
					$\hat{f}_1$	THD
1	0.466	4.47	3.86	1.81	393 V	6.9 %
2	0.411	4.49	3.47	1.80	391 V	6.0 %

Table 6.26: Fundamental performance of best solution topologies

As with all of the feasible solutions in Table 6.23, a constant level of PM inset has removed a significant variant within the machine topology. The inset has a particularly strong influence on the saliency characteristic within the machine since it directly impacts on the difference in back iron paths from the pole and inter-pole regions. There is limited variation in the torque quality throughout the final results. This allows the fundamental quality of the machine topology to be analysed from the additional point of view of no load induced B-EMF. The two solutions have a strong fundamental at a high voltage level. The radially shaped rotor poles generate a smooth sinusoidal waveform as expected, with limited harmonic content. As well as the fundamental values in the table, the FFT analysis of both waveforms is illustrated in Figure 6.18. The graphics once

again illustrate the limited variation in performance between the two solutions, with both topologies producing a 3^{rd} harmonic.

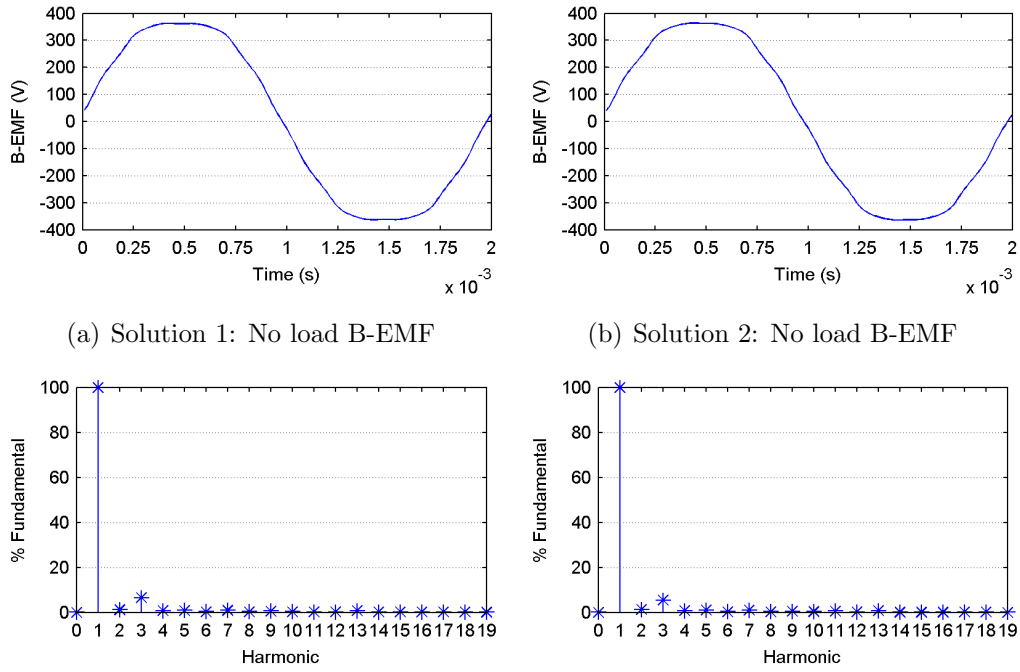

(a) Solution 1: No load B-EMF

(b) Solution 2: No load B-EMF

(c) Solution 1: B-EMF harmonic content

(d) Solution 2: B-EMF harmonic content

Figure 6.18: FFT analysis of B-EMF for best solution topologies

When comparing the two best solutions, they both comfortably meet the design specifications. Of the two choices, solution two is marginally superior across the broad selection of performance characteristics. The machine topology analysis has demonstrated excellent fundamental performance. In addition to this, the strong saliency ratio over the whole operational envelope ensures that the fundamental performance can be extracted through sensorless control using HF injection.

6.5.4 MGA Routine with Six Design Variables

The continued evolution of the optimization routine lead to a six variable method. This routine follows on in the identical format to those described previously. In this case though the split ratio is removed as a design variable along with MI, using the same reasoning as before. SR is a significant parameter within the machine script, and has a top down impact on all other variables. It is also a design factor that is often predetermined during the initial design decisions either through preference or a specification dictating the external dimensions of

the stator and/or rotor. The top down impact that SR has on all other machine variables means that by setting it as a constant considerably reduces the overall search space for the GA. Providing a strong performing value is set as the constant then the feasible solutions from this optimization routine should be of a high quality once again. In this running of the six variable routine SR was fixed at 0.635 and MI at 0.3.

The final solutions obtained from the optimization routine are presented in Table 6.27. Those solutions that fail to meet a threshold performance objective are highlighted in bold typeface. With the remaining solutions the two best choices were selected based on the their respective objective values. Solution two and 17 represented the best machine topologies, both have a good saliency characteristic, low cogging torque and high torque production.

Soln	Saliency	Cogging	Torque	Soln	Saliency	Cogging	Torque
1	1.26	**0.536**	37.1	11	1.20	0.194	37.7
2	1.23	0.103	36.8	12	1.25	**0.362**	37.2
3	1.28	0.203	34.9	13	1.26	**0.482**	37.1
4	1.29	**0.842**	36.6	14	1.30	**0.603**	35.7
5	1.20	0.062	37.6	15	1.27	**0.639**	37.1
6	1.28	**0.768**	36.7	16	1.21	0.182	37.6
7	1.20	0.213	37.7	17	1.24	0.118	37.5
8	1.22	0.291	37.5	18	1.24	**0.415**	37.5
9	1.21	0.162	37.6	19	1.30	**0.749**	35.5
10	1.31	**0.638**	35.1	20	1.23	**0.320**	37.5

Table 6.27: 24s20p MGA result with three objectives and six variables

The quality of the optimization results in Table 6.27 is strong but based on the average it is inferior to the seven variable routine. A constant magnet inset and split ratio allows the GA to spend more time optimizing the remaining variables, in theory improving the quality of results. With this approach however, the values applied to MI and SR will limit the final quality of optimum topologies. Since these are the two most dominant variables and can often override the influence of others during the routine. A practical selection for the two constants can be based on manufacturing requirements and in this design case they were selected based on findings to this point.

The optimum values that produce the two best solutions are shown in Table 6.28. The influence of the saliency objective is evident in these values, particularly since

as discovered already the short, relatively thick tooth bridge helps combat the amount of Q-axis saturation.

Soln	MI	SR	TW	BI	MS	SO	TB	TT
2	0.30	0.635	5.16	3.22	17.18	3.50	2.75	0.95
17	0.30	0.635	5.28	2.87	17.30	3.71	2.23	0.89

Table 6.28: Optimum dimensions of best solutions for MGA variables

The HF saliency characteristics of solutions two and 17 are in Table 6.29. The expected drop in fundamental saliency occurs under increasing load. This is anticipated and the focus of the objective function is to ensure that the positive saliency ratio is still present at peak loading. Taking this into account, both of the solutions comfortably achieve this. With a saliency above 1.2 even in a worst case scenario the two solutions not only have complete sensorless capability, they also will be able to be controlled accurately without the need for overly complex signal processing.

Soln	No Load			Rated			Peak		
	$\bar{L}'_d$	$\bar{L}'_q$	$\frac{L'_q}{L'_d}$	$\bar{L}'_d$	$\bar{L}'_q$	$\frac{L'_q}{L'_d}$	$\bar{L}'_d$	$\bar{L}'_q$	$\frac{L'_q}{L'_d}$
2	1.98	2.87	1.45	1.86	2.55	1.37	1.79	2.22	1.24
17	1.94	2.78	1.43	1.80	2.45	1.36	1.74	2.12	1.22

Table 6.29: Saliency characteristics for best solution topologies

These two solutions were selected due to their torque characteristics. These are confirmed with further analysis using FEA. A more detailed simulation has discovered that the no load cogging torque value for solution 17 was underestimated. The data presented in Table 6.30 demonstrates the superior torque quality of solution two. Although this topology has a marginally lower rated torque production it comfortably meets the rated torque requirement. The torque quality therefore becomes the more important property, making solution two the more suitable choice.

Soln	T_c (% Rtd)	T_r (% Rtd)	T_r (% Pk)	k_t	B-EMF	
					$\hat{f}_1$	THD
2	0.174	3.82	2.45	1.81	396 V	5.0 %
17	0.365	4.22	2.76	1.81	397 V	5.1 %

Table 6.30: Fundamental performance of best solution topologies

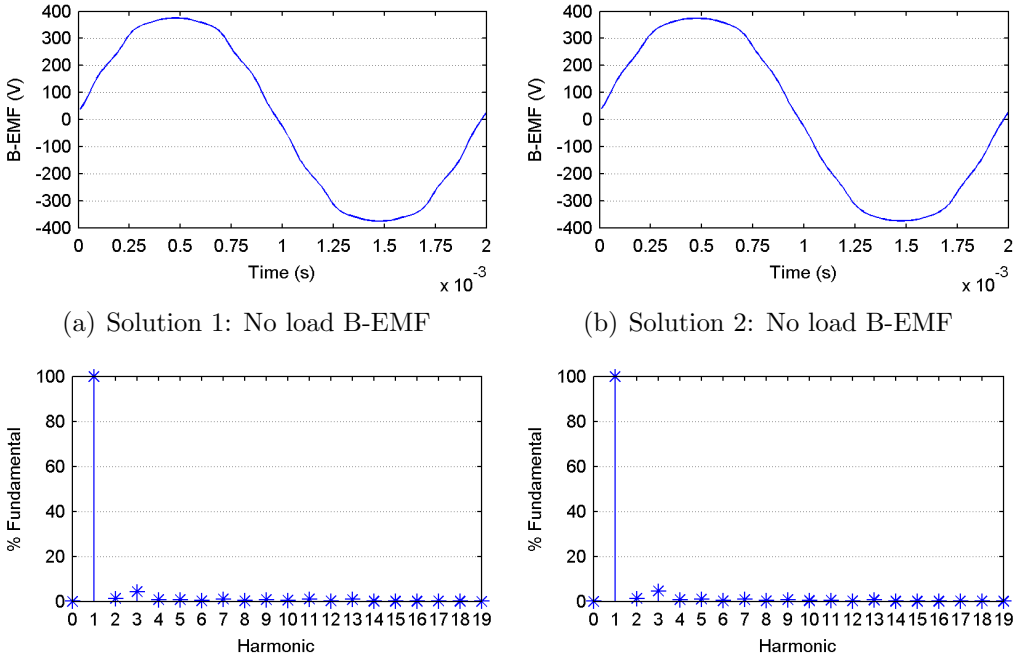

(a) Solution 1: No load B-EMF

(b) Solution 2: No load B-EMF

(c) Solution 1: B-EMF harmonic content

(d) Solution 2: B-EMF harmonic content

Figure 6.19: FFT analysis of B-EMF for best solution topologies

The B-EMF of each solution was compared, with the data shown in Table 6.30 and Figure 6.19. There is very little to choose between the two topologies on this basis and so either would represent an appropriate selection. With the complete performance analysis of these optimized solutions it is clear that solution two is the best choice from the six variable routine. It performs strongly on the three main optimization objectives and with more in depth analysis has demonstrated superior fundamental performance.

6.6 Trend Analysis

The progression of the MGA approach, where the number of design variables available was reduced, has improved the quality of the final solution. Removing the dominant geometrical parameters and fixing them at strong performing values enabled the optimization routine to focus on the remaining individuals in greater detail. The six variable routine, where the split ratio and magnet inset were fixed, has produced a very high quality machine that successfully meets the three distinct design specifications.

With all of the final designs the major dimensions are closely matched, with limited deviation. These dimensions are the three that have a strong influence

on the fundamental torque characteristic within the machine. The tooth width, back iron thickness and magnet width (and therefore thickness) of the four final designs are near to their mean values of 5.26mm, 3.04mm and 17.11° respectively. The most significant variation comes in the tooth bridge profiles of each of the design. This geometrical feature within the topology has a detectable influence on both saliency characteristic and cogging torque. Since this point with the main machine flux path is the most susceptible to saturation, especially at lower loads, it contributes to the main saliency within the machine and can go a long way to shifting the zero saliency point. The tooth bridge profile is also a significant variant in the cogging torque characteristic as it directly affects the interaction between the stator slots and rotor poles when they pass during rotation.

A wireframe illustration of each topology is presented in Figure 6.20. With this visual representation the limitation variation in TW, BI and MS can be seen. The sub-figures also graphically demonstrate the similarity in the tooth bridge profile between the two eight variable solutions. While the seven variable solution has a tooth bridge profile on the low end extreme and the six variable at the high end extreme. The thicker tooth profile that covers a large amount of the slot opening (Figure 6.20(d)) contributes to the low cogging torque value observed with the six variable solution. This profile also produces a strong no load saliency ratio of 1.45 that can withstand the 15% reduction due to Q-axis saturation.

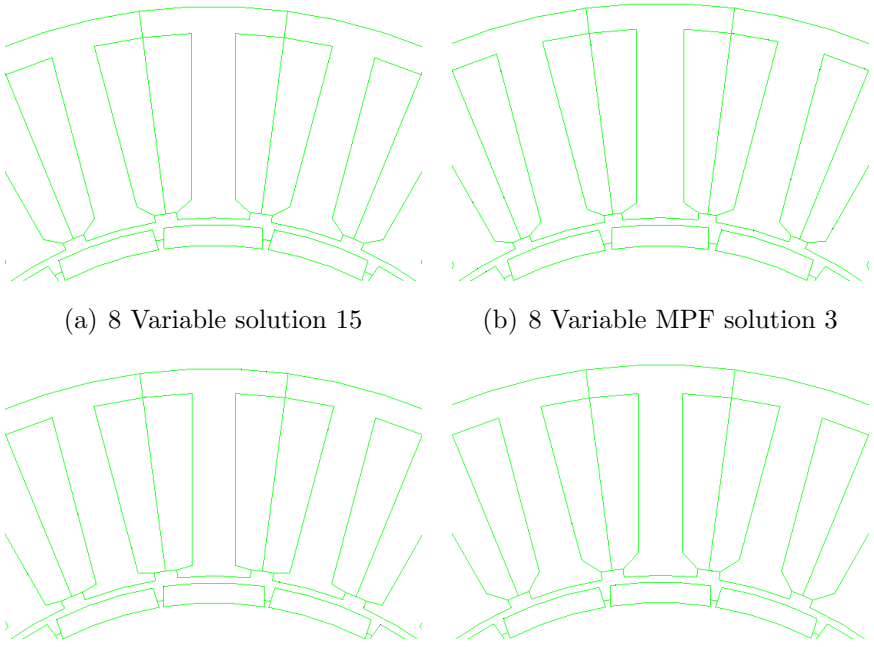

(a) 8 Variable solution 15

(b) 8 Variable MPF solution 3

(c) 7 Variable solution 2

(d) 6 Variable solution 2

Figure 6.20: Wireframe schematic of geometrical topologies

The rate of saturation that occurs from no load to peak load is similar in the eight variable and six variable routines. Both of these are more severe than the routine with seven variables. The former shows a average reduction in saliency of 15% from no load to peak load. This is significantly higher than the 9% drop in the latter routine. This is largely due to only a 16 % drop in L'_q from no load to peak load, compared to around 24% for the other optimum machines. When analysing the four solutions (two best from each routine) they all closely match on the dimensional values. The exception to this is the tooth bridge profiles. With the seven variable routine the tooth bridge and tooth tip values are closer in value with respect to the other solutions. The tendency here is that with a thinner tooth bridge the overall topology has a lower no load saliency. This is because the residual magnetic flux created solely by the PMs causes a higher flux density within the tooth bridge. Although this means a lower no load saliency ratio it limits the rate of Q-axis under load. Overall this leads to a more consistent level of saliency across the whole loading range for solutions one and two in the seven variable routine.

6.7 Summary

This section has collated all of the optimization results obtained during the project. The two distinct approaches to the design problem have their respective advantages and disadvantages which have been discussed throughout. The speed of the single objective routine can be a strong benefit during preliminary design stages where fundamental decisions are made regarding slot/pole combination and external dimensions. Even with a multi-stage approach as used in this project the quality of result will be limited to solely the primary objective. This is not the case during machine design and instead a machine design process is the continuous compromise between a number of specifications. Another advantage of the single objective routine is that it enables the designer to go into more in depth trend analysis. With the GA focusing on the sole objective it enables clear geometrical trends to be established that improve on it and even those that are detrimental.

The outcome of the multi stage, single-objective optimization routines have shown the slot/pole combination has a significant impact on the main saliency characteristic. The D and Q-axis orientation is predetermined by the rotor pole number. With the fixed orientation, if the stator slot number is changed there will be a di-

rect impact on the HF inductance paths, stator flux leakage and saturation. This means that the interaction of the slot/pole combination has a strong influence on the fundamental saliency characteristic.

During the second optimization stage none of the four variables were found to be fundamental to enhancing saliency properties. Of the four, the level of magnet inset was the dominant stage two variable. It directly impacts on the D-axis reluctance paths and consequently the relative difference in magnitude between L'_d and L'_q. It is in combination with the MGA optimization results that these generic trends could be analysed further. The conclusions obtained from the single-objective approach can be categorized in two forms, effectiveness of optimization routine and optimized topology results.

The multi stage, single-objective routine is insufficient for a machine design process. Even though the stage variables were carefully selected to maximize the effectiveness of each stage. The overall routine is faster than a comparable multi-objective routine but the relative reduction in optimization time is not beneficial enough to warrant its selection. Instead, as mentioned previously, the single-objective approach could be utilized in preliminary design selections, either to compare slot/pole combinations, external dimensions or to determine strong values for dominant geometrical parameters like the split ratio and magnet inset. The latter of which could be advantageous for narrowing the overall search space prior to a MGA routine. This approach takes advantage of the speed of optimization and can improve the efficiency of the MGA routine used later.

The results obtained from the optimization process revealed firstly that with this geometrical topology in place a 24s20p configuration produced the most suitable result. The machine maintained a good saliency characteristic across the whole loading range but fell short on the torque characteristics. In addition the results targeting inverse saliency confirmed that this approach is inappropriate given this SPMSM topology as it causes too much deterioration to fundamental machine performance.

The MGA has been shown to effectively optimize a complete machine topology that exceeds the design specifications. The objective functions used were a direct reflection on the design specifications and could ultimately be adjusted for differing specifications. While, the routine approached sensorless capability in two forms, directly enhancing the main saliency characteristic as an objective function and applying a penalty function that ensures the saliency is above a

defined threshold. The efficiency of the MGA routine and its respective results were improved further when the total number of variables was reduced. In both instances, the six and seven variable routines, final solutions were limited by the constant values applied to the fixed variables. Despite this the average quality of the final solutions was greatly improved.

The format with which the penalty function was applied showed that the remaining optimization objectives could be further improved without the 'pull' of saliency as an objective. In this instance, the outcome was a particular reduction in the no load cogging torque within the final solutions. The improvement with this individual objective was good but on the whole the reduced emphasis on saliency is not worthwhile. The removal of saliency as an objective creates the opportunity for an alternative third objective to be optimized. This was tested with the example of rated torque ripple. In further optimization routines there is the possibility of incorporating alternative properties such as B-EMF quality and losses. However, in an optimization routine that is already dominated by FE simulation time it was decided that this avenue would not be investigated due to the labour intense analysis required for these calculations in an iterative process.

	24s20p Single-Objective Solution	24s20p Multi-Objective 6 Variables, Solution 2
$\bar{T}$ (Nm)	32.5	36.8
T_c (% Rated)	1.1	0.17
T_r (% Rated)	4.2	3.82
T_r (% Peak)	3.6	2.45
B-EMF $\hat{V}_1$ (V)	411	396
B-EMF THD (%)	5.34	5.0
No load saliency ($\frac{L'_q}{L'_d}$)	1.23	1.45
Rated load saliency ($\frac{L'_q}{L'_d}$)	1.25	1.37
Peak load saliency ($\frac{L'_q}{L'_d}$)	1.19	1.24
Optimization time (h)	32	50

Table 6.31: Comparison of machines resulting from optimization approaches

The two final machine design results that were obtained from each design approach are presented in Table 6.31 for comparison. It demonstrates the superior quality of result gathered from the single stage, multi-objective design routine. The last row of the table shows the total computation time for each of the optimizations. The two stage, single-objective result in the first data column is

significantly faster to completion. Although this is an important factor the quality of the MGA result demonstrates that the greater duration is worthwhile.

Chapter 7: Case Study of Existing PMSM

The following chapter implements the sensorless oriented design methods developed in a case study for an existing traction machine. The machine topology and performance specification will be analysed first, along with the HF saliency characteristics. The topology will then undergo optimization to enhance the sensorless controllability of the machine, specifically in the areas of weakness.

7.1 24s16p Traction Machine

The case study is focused on a traction machine that uses an IPMSM topology with a 24s16p configuration. A wireframe diagram in Figure 7.1 illustrates the basic topology of the machine, showing a sector of the stator and rotor together.

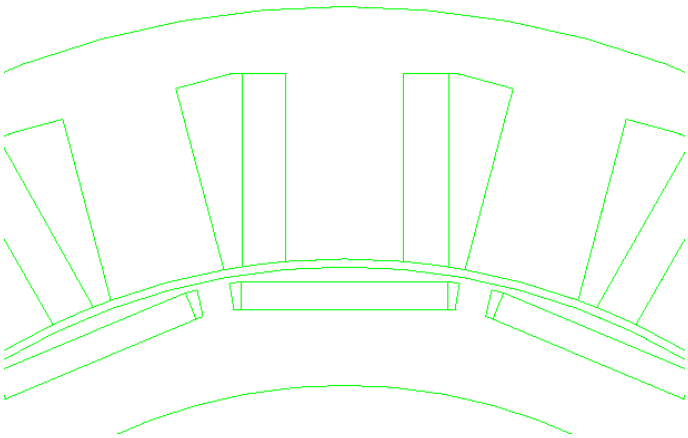

Figure 7.1: Wireframe sector of case study machine

The stator uses open slots with DL concentrated windings. The open slot allows for each winding to be bobbin wound and placed onto their respective teeth easily. Also a unique approach involves two forms of coil, trapezoidal and uniformly wound. The trapezoidal coils are inserted first over alternate teeth, followed by the uniformly wound coils on the remaining teeth. This design allows the slots to be filled effectively, while keeping construction simple. Although it creates differing coil shapes, the net average for each phase and the stator as a whole evens out, greatly reducing any impact. The stator lamination is in a traditional form and due the open slot design is a simple design. The winding configuration

is in a delta formation with each of the coils connected in parallel. This creates eight parallel paths in each phase.

In addition to the external dimensions of the stator outer radius (SOR) and stator inner radius (SIR) there are three distinctive geometrical parameters that generate the stator. The first is the tooth width (TW), which with this machine is 25mm. The second is the slot depth (SD), this is defined as the straight radial distance from the stator inner radius to the top of the slot. The machine has a slot depth of 39.5mm which in combination with the stator outer radius defines the back iron thickness. The final parameter defines the angular offset from the slot side to the slot back, the slot vector (SV) is 90°. All of the geometrical parameters that define the stator are illustrated in Figure 7.2.

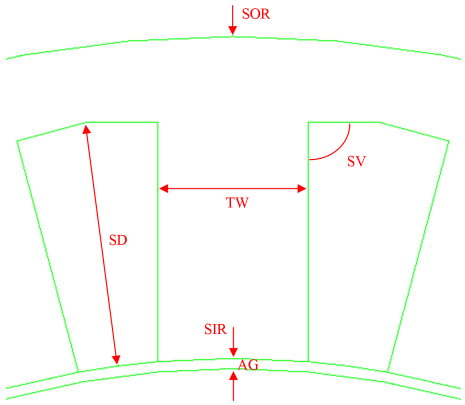

Figure 7.2: Stator geometrical parameters

The IPM rotor has a uniform external and internal cylindrical surface. The PM poles are inserted into lamination slots that have air bridges either side, largely designed to allow the excess bonding agent to overflow. The poles are segmented in a uniform rectangular shape, making them easy to manufacture. The segmented design helps reduce eddy current loses within the PMs but is also largely due the skewed rotor. The slot/pole combination and open slot design means the machine will suffer from a significant cogging torque. The rotor combats this through a skewed stack design. There are five equal sections across the active length of the rotor, each skewed 1.25° from the previous.

The geometrical parameters that make up the rotor definition are as follows. The external surfaces are defined with the rotor outer radius (ROR) and inner radius (RIR). The PMs are defined as a magnet width (MW) and magnet thickness (MT). The degree of embedding is dictated by the magnet bridge (MB) which is

the straight line radial distance from the rotor outer radius to the outermost point of the PM. Finally, the size of the air bridges either side of the poles is defined by the amount of web separation (WS) between it neighbouring air bridge. All of these parameters that generate the overall rotor topology are illustrated in Figure 7.3.

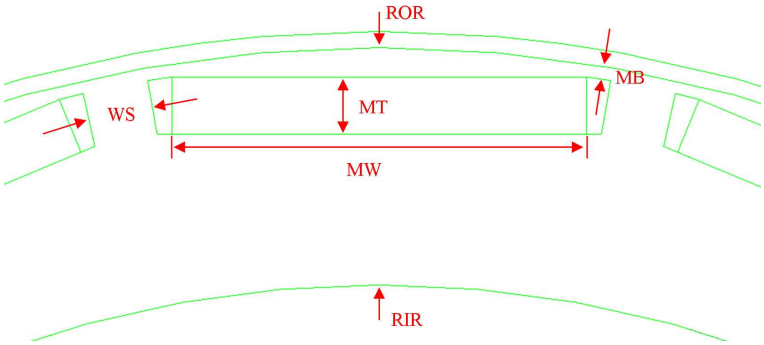

Figure 7.3: Rotor geometrical parameters

The data in Table 7.1 provides a summary of the machine specifications.

Slots	24	Poles	16
Steel	M235	PM	N42SH
Stack Length	85mm	AG	1.7mm
SOR	200mm	ROR	145mm
SIR	146.7mm	RIR	120mm
SD	39.5mm	MW	44mm
SV	90°	MT	6mm
TW	25mm	MB	1.4mm
Connection	Delta	WS	7mm
Coil Turns	72	Coil Paths	8 Parallel
Rated	220Nm @ 1300rpm	Peak	660Nm @ 868rpm

Table 7.1: Test machine specifications

7.2 Performance Analysis of Traction Machine

The machine is designed to be embedded within a hybrid system and therefore during operation will generally spin idly at around 1000rpm. The rated performance of the traction machine is 220 Nm at 1300 rpm. The peak torque requirement is three times the rated performance and is generally employed during a hard start up. It is also during peak torque output that low speed sensorless control is at its most challenging. Since the machine rotates idly when the engine

is running and not necessarily under load, B-EMF tracking control schemes can be employed. The fundamental performance of the machine is analysed in the following section. After this the HF saliency characteristics of the machine are investigated to assess the low speed rotor position tracking capability.

The machine produces a strong fundamental torque with a reasonable cogging torque. The level of cogging torque is greatly reduced by the skewed rotor, which is stepped in five incremental stages. The peak to peak cogging torque is 14.4 Nm, which is 6.5 % rated torque. When operating at rated load the machine exhibits a 4.1 % torque ripple and then 1.9 % at the peak overload torque output. The traction machine has been designed to be able to provide a high quality rated torque, with the ability to overload heavily in order to generate the required high torque output.

The rotor configuration has smoothed out the no load induced B-EMF. The staggered PM poles produce a near sinusoidal B-EMF with very little harmonic content as shown by the FFT analysis in Figure 7.4. This analysis was carried out at the rated speed of 1300 rpm.

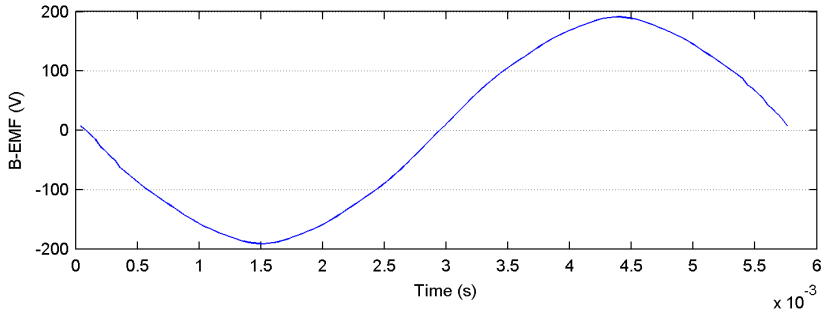

(a) No load B-EMF

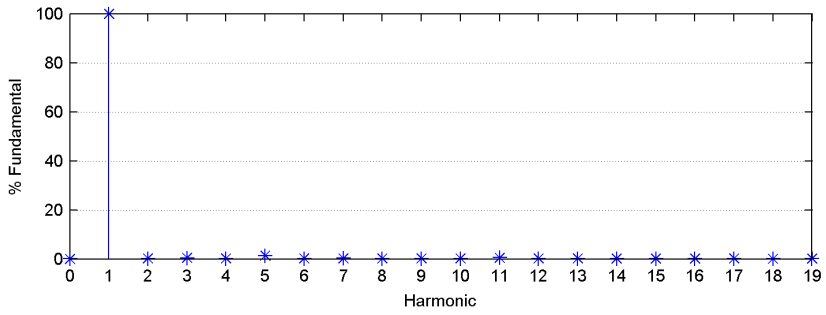

(b) Harmonic content of no load B-EMF

Figure 7.4: FFT analysis of test machine B-EMF

The HF saliency characteristic of the test machine was analysed to determine

its sensorless capability. This involved FEA at significant loading points within the operational envelope. An overview of the main saliency characteristic is illustrated in Figure 7.5. The large no load saliency ratio is expected due to the buried PM rotor configuration. This forms a significant variation in D and Q-axis reluctance paths. Despite a no load saliency of 1.57, under increasing load L'_q saturation becomes an issue within the required loading range. The machine has a high overload capability of 300% rated load. At this level of loading the Q-axis reluctance path is heavily saturated, to the extent that $L'_q < L'_d$. The dashed lines in the figure represent the peak and trough values of the incremental inductances created by the position dependent fluctuations. Taking the incremental inductance ripple into account there is a zero saliency region at 236% rated load.

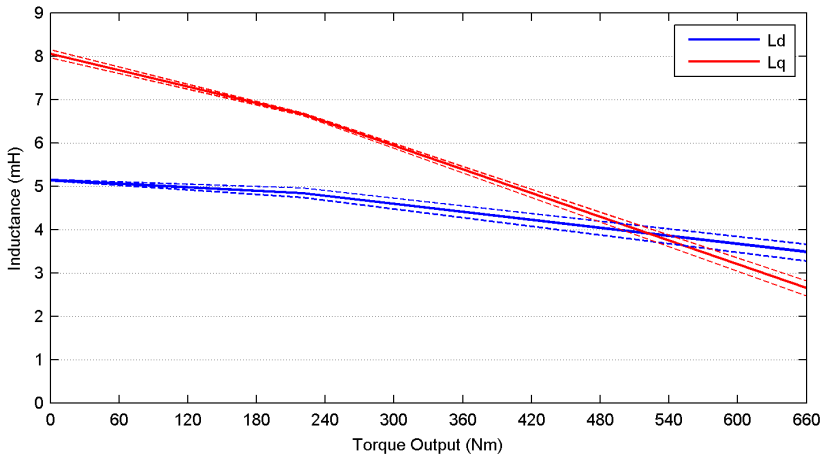

Figure 7.5: HF saliency profile against torque output

A summary of the test machine fundamental and sensorless properties is given in Table 7.2. The traction machine has a unique and refined geometrical design that performs strongly. The zero saliency condition means that the machine is not capable of HF saliency tracking control across the whole operational envelope. During a hard start, when the machine is required to generate up to peak torque from zero speed, the machine will fail under sensorless control. Using the GA optimization strategies developed during this project, it was investigated whether the existing topology could be optimized further to improve sensorless capability with limited impact on the existing fundamental performance.

Cogging Torque (% Rated)	6.5	No Load Saliency	1.57
Rated Torque Ripple (% Rated)	4.7	Rated Load Saliency	1.38
Peak Torque Ripple (% Peak)	2.2	Peak Load Saliency	0.76
B-EMF (Peak)	191 V	B-EMF (THD)	1.57 %

Table 7.2: Summary of test machine performance analysis

7.3 Self-Sensing Optimization of Traction Machine

A single objective approach was used to explore the possibility of shifting the zero saliency condition beyond peak loading. This format is more time efficient that using the MGA approach and initially just examines whether the zero saliency condition can be removed from the loading range. The main external dimensions of the topology were fixed since the machine has been designed with a specific application in mind. The stator and rotor configuration was therefore parametrized while keeping the inner and outer diameters of the stator and rotor constant, along with the stack length. The geometrical design features were parametrized with their respective upper and lower boundary limits dictated by structural constraints and practical selections. Their relative impact on fundamental performance was not a primary concern initially until the degree of sensorless capability enhancement was understood. The topological design naturally creates five geometrical parameters.

- Tooth Width (TW), in the standard format of parallel edged tooth with the width defined in mm. The default is 25mm, with 22mm and 28mm applied as the boundary limits.
- Slot Depth (SD), defines the straight line length from the inner diameter of the stator to the base on the slot. By definition, with a fixed stator outer diameter, it also sets the back iron thickness. The default is 39.5mm, with 37mm and 42mm set as boundary limits.
- Magnet Width (MW), defines the width of the uniform rectangular PM rotor poles. To maintain a constraint on PM volume it was fixed with the magnet thickness set as a function of width. The default value is 44mm, with 40mm and 44mm set as the boundary limits. The default magnet width is already at its upper boundary limit since each pole must have an air bridge either side and an adequate web separation to ensure structural integrity.

- Web Separation (WS), defines the straight line distance between the two adjacent magnet air bridges. This means is defines the size of the air bridges and width of the inter-pole back iron. The default is 7mm, with 3mm and 7mm applied as boundary limits. In combination with the maximum magnet width the maximum web separation must be theoretically possibly to guarantee the GA does not fail.
- Magnet Bridge (MB), this defines the straight line distance that the outer-most point of the rotor poles is embedded within the rotor lamination. The default is 1.4mm, with 1mm and 4mm applied as boundary limits.

All five of these geometrical parameters were implemented into the machine script within a single-objective GA routine. The machine was then optimized to ensure a distinguishable saliency characteristic over the whole loading range. The current saliency loading profile in Figure 7.5 shows how the overall saliency needs to be increased or amount of Q-axis saturation that takes place reduced. The single-objective optimization routine was performed at peak loading with the objective function set to maximize saliency at this point.

The results of the optimization routine are show in Figure 7.6. The peak loading saliency ratio has been increased from 0.76 to 0.93. This is still a long way short of the desired result, even more so when the incremental inductance ripple is taken into account. The position dependent ripple means that when the saliency value over a complete rotation can vary significantly compared to the average that is calculated. The GA data plots in the figure demonstrate that the optimization has converged with the optimum topology created differing greatly from the original. Particular interest is drawn on the rotor parameters as they are fixed in relation to the D and Q-axis so an inherent difference in their reluctance paths can be induced. The buried magnet design means that there will be a significant no load saliency, while a small magnet bridge is advantageous since it brings the PM poles close to the rotor surface.

The saliency profile with respect to loading is illustrated in Figure 7.7. The comparison with Figure 7.5 demonstrates the shift of the zero saliency condition. The GA enhancement shifts the crossover to a point nearer the edge of the loading range, approximately 255% rated load. This is still short of the desired 300% and based on the strong convergence by the GA there is little improvement to be gained from adjusting these geometrical parameters further.

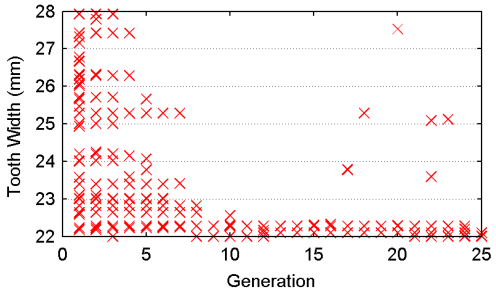

(a) Distribution of Tooth Width

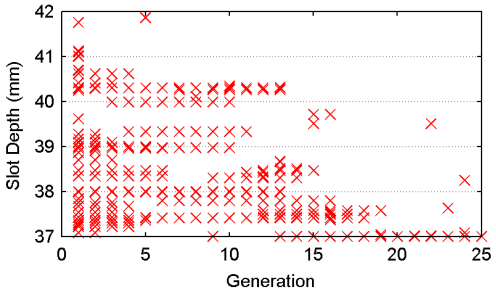

(b) Distribution of Slot Depth

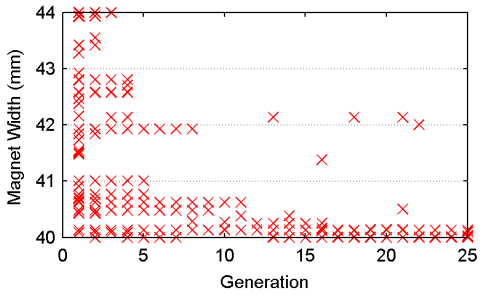

(c) Distribution of Magnet Width

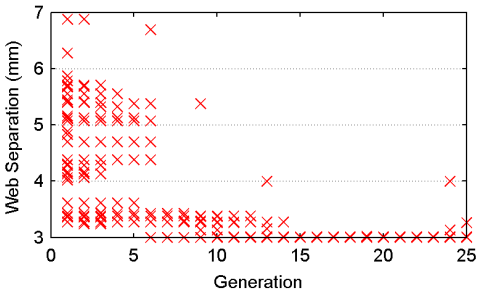

(d) Distribution of Magnet Separation

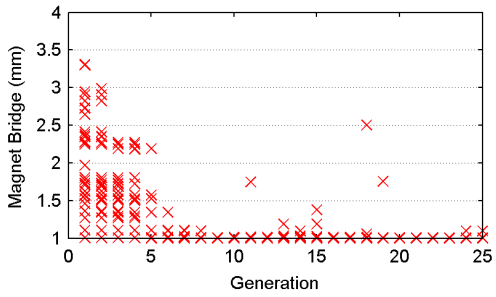

(e) Distribution of Magnet Bridge

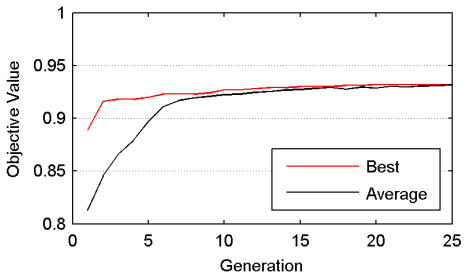

(f) Evolution of Best Objective

Figure 7.6: GA result of rotor variables and best objective

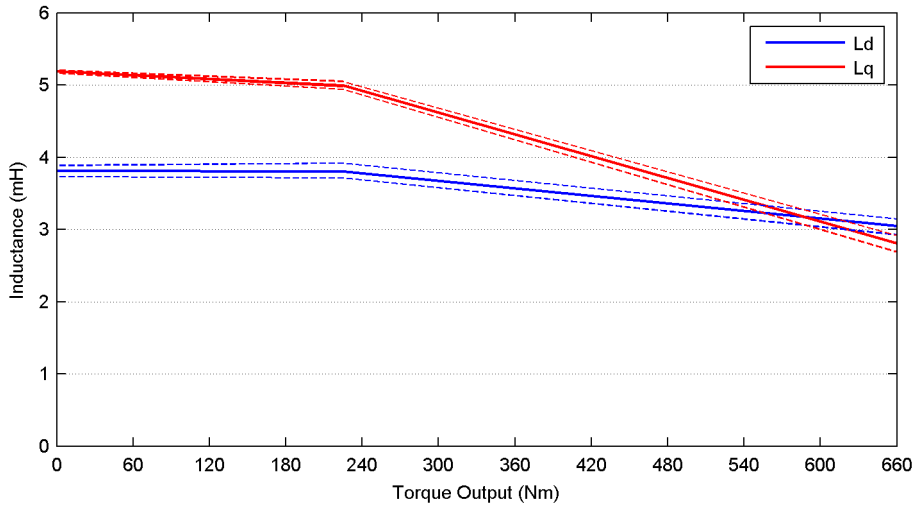

Figure 7.7: HF saliency profile against torque output

The impact of this optimization on fundamental performance is summarized in Table 7.3. The single-objective routine was not concerned with impacting on the fundamental performance, however, the constraint applied to the variables boundaries was intended to limit any possible impact. As can be seen there has been a reduction in no load cogging torque but this has not resulted in a drop in torque ripple. A slight deterioration has also occurred with the B-EMF.

Cogging Torque (% Rated)	5.43	No Load Saliency	1.37
Rated Torque Ripple (% Rated)	3.22	Rated Load Saliency	1.31
Peak Torque Ripple (% Peak)	3.47	Peak Load Saliency	0.93
B-EMF (Peak)	190 V	B-EMF (THD)	2.07 %

Table 7.3: Summary of optimized test machine performance analysis

The constraint on the existing dimensions of the machine limit the ability to optimized the machine further within the established routines. An alternative approach is to broaden the routine to investigate to strong performing slot/pole combinations. The two formats were selected as a 48s16p distributed winding configuration and a 24s20p concentrated winding configuration. These two configurations were selected based on the strong characteristics that come from the combinations and resulting electrical design. The rotor and stator topology was unchanged with the two new machine formats, only adjusting the dimensional boundaries based on the proportional change to the number of slots and poles.

7.4 24s20p & 48s16p Machine Alternatives

The 48s16p configuration uses a traditional distributed winding layout in combination with the existing stepped rotor. The rotor topology was completely unchanged, along with the limits for the GA variables. The stator design was maintained while taking into account the increase in slot number when selecting the new boundary limits. The 24s20p configuration keeps the same stator design and limits, however, with a revised DL concentrated winding design. The rotor format was again kept constant, with the boundary limits adjusted to account for the increased pole number. The slot and pole combination ensures a small cogging torque characteristic and removes the need for the original stepped rotor design.

The two new machine topologies were parametrized to enable the same optimization process to be performed. In both cases all external dimensions were kept

constant, along with all of the prior material selections. A single-objective approach was performed with the five variables. The best objective results from the two GA routines are presented in Figure 7.8, along with the resulting saliency profile of the best objectives. The data shown in these two plots demonstrates

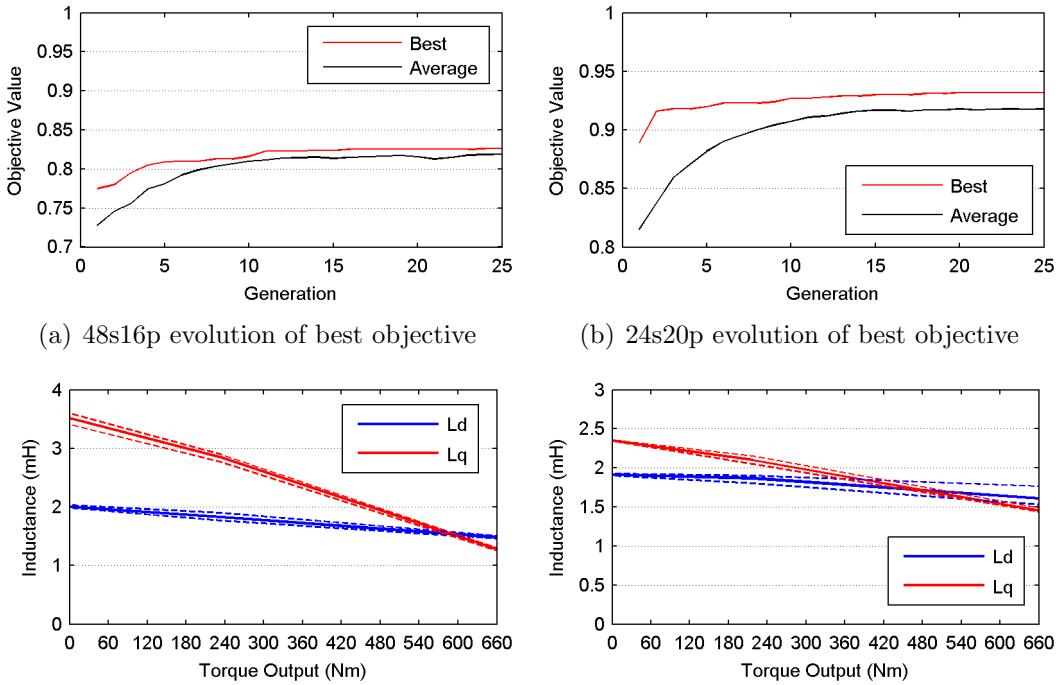

(a) 48s16p evolution of best objective

(b) 24s20p evolution of best objective

(c) Saliency profile vs torque output

(d) Saliency profile vs torque output

Figure 7.8: GA result for alternative machine configurations

that once again the optimization routine has successfully influenced the main saliency characteristics. Despite this it was not able to increase the peak loading saliency ratio sufficiently to ensure a positive saliency over the whole loading range. Instead with the 24s20p configuration there is still a zero saliency condition due to the L'_q saturation. The GA maximized the saliency ratio at peak loading. In this instance this has lead to a machine that exhibits a peak saliency ratio of 0.93. Despite this the GA has achieved this with a machine that has a low no load saliency ratio and instead has a less significant drop in L'_q. This gradual drop in L'_q means the crossover of L'_d and L'_q takes place at a lower level of load, approximately 200% rated load, depending on the exact rotor position. This is still within the 300% loading range and therefore the change in slot/pole combination has not been successful.

The 48s16p approach produces a more encouraging result, although the peak loading saliency ratio is only 0.83. The distributed winding causes the machine

to have a significantly improved no load saliency ratio of 1.75. This configuration also suffers from a dramatic, linear reduction of L'_q with respect to load. The steepness of this gradient, combined with the high no load saliency means a zero saliency condition occurs at 260% rated load. The incremental inductances have a smaller position dependent ripple, compared to the concentrated winding topologies. The evenly distributed single phase windings limits the fluctuation between peak and trough incremental inductance values with rotor position. This contributes to a higher crossover point since L'_d and L'_q deviated less from their respective mean values.

The single-objective routine ignored any impact on the fundamental performance of the machine. A summary of the fundamental performance of these two optimized machine designs are shown in Table 7.5 and 7.4. The 24s20p configuration demonstrates the strong characteristic of this slot/pole combination. Without the need of a stepped rotor geometry the machine still exhibits a lower cogging torque and similar torque ripple to the original test machine. In comparison, the 48s16p distributed winding machine has poor torque quality, even with the stepped rotor geometry. The 48s16p has advantageous saliency characteristics and with a more in-depth MGA analysis could be improved further, particularly with regards to fundamental performance.

Cogging Torque (% Rated)	5.78	No Load Saliency	1.76
Rated Torque Ripple (% Rated)	7.16	Rated Load Saliency	1.55
Peak Torque Ripple (% Peak)	5.69	Peak Load Saliency	0.86
B-EMF (Peak)	196 V	B-EMF (THD)	2.57 %

Table 7.4: Summary of 48s16p optimized machine performance analysis

Cogging Torque (% Rated)	2.10	No Load Saliency	1.23
Rated Torque Ripple (% Rated)	4.52	Rated Load Saliency	1.12
Peak Torque Ripple (% Peak)	2.74	Peak Load Saliency	0.91
B-EMF (Peak)	192 V	B-EMF (THD)	1.47 %

Table 7.5: Summary of 24s20p optimized machine performance analysis

7.5 Summary

The considerable overload characteristic of the machine means that large amounts of Q-axis saturation are inevitable. The IPM rotor creates a strong no load

saliency, as high as 1.57 in the original machine. Even taking this into consideration it will always be a challenge to augment the topology is such a way that a zero saliency point does not occur.

Marginal improvement was possible through optimizing the existing topology, enlarging the sensorless capability loading range. While the experimentation with additional slot/pole combinations revealed no superior options. The 48s16p machine demonstrated how the distributed windings reduces the level of incremental inductance ripple, even under increasing load. The 24s20p represents an excellent slot/pole combination for fundamental performance, despite this with the geometrical topology unchanged the GA was unable to achieve a design with complete sensorless capability.

In order to investigate the possibility of complete sensorless capability over the whole 300% loading range in more detail the topology would have to be parametrized further. This would cause excessive impact on the fundamental performance of the machine, so much so that it may no longer meet the design specifications. In order to produce a machine able to meet these specifications under sensorless control the initial design would have to be repeated while taking account of the main saliency characteristic.

Chapter 8: Conclusion

The PMSM is considered the industrial standard for servo applications. The high power density, accurate control and modular structure make them excellent choices for a wide range of operations and environments. In order to be accurately controlled the machine requires an active feedback system for rotor position. This is traditionally achieved with a shaft mounted encoder or resolver. The rotor position is essential to the drive system which has meant the relative disadvantages associated with an encoder or resolver have been overlooked. Integrating a position sensor significantly increases the size, weight and cost of each individual motor. While they can also reduce the reliability and prevent use in extreme environments.

The detrimental impact of shaft mounted position sensors has generated considerable motivation towards sensorless control schemes and self-sensing machines. Numerous sensorless control approaches have been developed and become well established. The two distinct control schemes can be categorized as B-EMF tracking schemes and HF injection position tracking schemes. The former offers a simple approach that works under medium to high speed operation but fails at low to zero speed. The latter offers the ability to control a machine accurately across the whole speed range. In order to achieve this the machine must exhibit a distinguishable saliency between the D and Q-axis incremental inductances.

These incremental inductances in the DQ rotor reference frame are formed by the reluctance paths created in alignment with each axis. The incremental inductances, L'_d and L'_q, are both load and position dependent. In general, PMSMs have a traditional saliency where $L'_d < L'_q$ and particularly with IPMs the rotor topology contributes to a larger saliency. Taking advantage of the main saturation saliency characteristic has a significant downside. Under load, due to the Q-axis alignment with the fundamental B-EMF, saturation significantly reduces the magnitude of L'_q. This causes a zero saliency condition at high load where $L'_d = L'_q$. Creating a loading point, or range, where the machine is uncontrollable. A major concern therefore with self-sensing PMSMs is ensuring this zero saliency condition, that is inevitable, occurs outside of the operation envelope.

The D and Q-axis incremental inductance paths are formed through their respec-

tive paths, aligned with that rotor position. The values for L'_d and L'_q are dependent on the materials they pass through and their respective distance through each material. In addition to this the load dependent characteristic is caused by the variation to material properties under increasing flux density. With this in mind the HF saliency, created by the main saturation characteristic could be manipulated to enhance the level of saliency. A larger saliency ratio would improve the signal processing and accuracy of the sensorless control, while removing zero saliency points can ensure complete controllability.

Chapter 3 presented the methodology used to calculate incremental inductances using FEA. Through experimental verification it was demonstrated that the values obtained from this method reflect experimental magnitudes and characteristics. This means that the main HF saliency characteristic can be assessed using a 2D FE simulation process. The conclusion can therefore be drawn that the self-sensing saliency characteristic of a PMSM can be calculated and therefore targeted for enhancement during a design process.

The approach of the project firstly focused on if it is possible to enhance self-sensing properties through the manipulation standard geometrical parameters within a SPMSM topology. Then progressing onto incorporating the enhancement of self-sensing properties into a PMSM optimization design routine. How the saliency characteristic was calculated and at which loading point, or points, was integral to the success of the design routine. Beyond this the work investigated the most feasible approach to accommodating the self-sensing characteristics into a machine design routine. Where the focus should be and is still primarily on fundamental performance. The decision was made to use a genetic algorithm based optimization design tool. With this in place numerous GA routine formats were analysed and compared for their advantages and disadvantages in Chapters 5 and 6.

The aim of the design process was to ensure that a cost effective machine was the result. Utilizing design techniques that allowed for a mass production process. This acted as a strong decision maker as the geometrical topology was developed in Chapter 4. The variable machine design used a traditional topology that would perform strongly when considering fundamental properties. The design routine targeted a final design with excellent fundamental performance that could be extracted over the whole loading range through sensorless control.

The final design routine involved a MGA with three optimization objectives.

The main saliency characteristic at peak loading, along with the two main design specifications, rated torque and cogging torque. It was demonstrated that the efficiency of optimization results was improved when dominant machine variables were removed and instead fixed as strong performing constants. The six variable routine produced the best result but it was reliant on appropriate values being applied to the split ratio and magnet inset. Single-objective optimization proved insufficient on several levels but when used appropriately it was demonstrated to be a useful precursor to determining boundary limits and quickly comparing numerous topologies.

The 24s20p finalized design successfully exceeded the design specifications. The complete analysis of the topology demonstrated that beyond these three requirements the machine exhibited excellent performance qualities. The optimized geometrical values created a machine that used a simplistic construction that could be successfully implemented into large scale production.

8.1 Limitations and further development

The self-sensing oriented design routine requires a significant amount of FE simulation time to sufficiently analyse the HF saliency characteristic of a machine. When this is built into a optimization routine that analyses each individual it creates a slow optimization approach. At present there is not a more efficient method to determine the HF saliency characteristics of a machine. This makes the optimization process slow and it encourages limitation to the accuracy of the FE simulations. It also means it is advantageous to only assess the saliency at certain loading points rather than producing a saliency profile for each individual. The development of a complex numerical model has be shown to accurately calculate the torque performance of SPMSMs in [58] and [59]. With the rigid geometrical topology used during the project this approach could be incorporated to analyse the torque characteristic of each individual and contribute to a reduction in the FEA requirements.

The geometrical topology that was developed for the optimization routine drew on a few key design objectives that determined certain outcomes. Particularly the requirement of traditional construction methods. This lead to a single, rigid topology that was carried through the remainder of the project, although there was flexibility in terms of slot/pole combination. To further develop this the best approach would be to create a more encompassing machine script. This would

firstly build the slot/pole combination selection into the GA routine, rather than separate routines at present that are compared post-process. Secondly, the GA routine would be given more flexibility in terms of distributed, single-layer and double-layer winding selections. Finally, the machine design could evolve so that the topology is less constrained and there is a material selection option.

These developments would lead to a more complex and complete optimization tool. However, the variety of outcomes would be greatly increased and comparison would be more complex. Feasible machine designs could be vastly different in terms of cost and ease of construction. Using the present design routine the outcomes all fall into a narrow window in terms of cost and manufacturability, which was intentional. It means comparisons are simple and final selection can come down to performance characteristics.

Bibliography

[1] M. Degner and R. Lorenz, "Using multiple saliencies for the estimation of flux, position, and velocity in ac machines," *Industry Applications, IEEE Transactions on*, vol. 34, no. 5, pp. 1097 –1104, 1998.

[2] P. Acarnley and J. Watson, "Review of position-sensorless operation of brushless permanent-magnet machines," *Industrial Electronics, IEEE Transactions on*, vol. 53, no. 2, pp. 352–362, 2006.

[3] F. Briz and M. Degner, "Rotor position estimation," *Industrial Electronics Magazine, IEEE*, vol. 5, no. 2, pp. 24–36, 2011.

[4] R. Bojoi, M. Pastorelli, J. Bottomley, P. Giangrande, and C. Gerada, "Sensorless control of pm motor drives; a technology status review," in *Electrical Machines Design Control and Diagnosis (WEMDCD), 2013 IEEE Workshop on*, pp. 168–182, 2013.

[5] M. Tursini, R. Petrella, and F. Parasiliti, "Initial rotor position estimation method for pm motors," *Industry Applications, IEEE Transactions on*, vol. 39, no. 6, pp. 1630–1640, 2003.

[6] Y. Yan, J. Zhu, and Y. Guo, "Initial rotor position estimation and sensorless direct torque control of surface-mounted permanent magnet synchronous motors considering saturation saliency," *Electric Power Applications, IET*, vol. 2, no. 1, pp. 42–48, 2008.

[7] J. Arellano-Padilla, C. Gerada, G. Asher, and M. Sumner, "Inductance characteristics of pmsms and their impact on saliency-based sensorless control," in *Power Electronics and Motion Control Conference (EPE/PEMC), 2010 14th International*, pp. S1–1–S1–9, 2010.

[8] T. Frenzke, "Impacts of cross-saturation on sensorless control of surface permanent magnet synchronous motors," in *Power Electronics and Applications, 2005 European Conference on*, pp. 10 pp. –P.10, 0-0 2005.

[9] M. Caner, C. Gerada, and G. Asher, "Permanent magnet motor design optimisation for sensorless control," in *Electrical Machines and Power Electron-*

ics and 2011 Electromotion Joint Conference (ACEMP), 2011 International Aegean Conference on, pp. 670–675, 2011.

[10] A. Faggion, N. Bianchi, and S. Bolognani, "Ringed-pole permanent-magnet synchronous motor for position sensorless drives," *Industry Applications, IEEE Transactions on*, vol. 47, no. 4, pp. 1759–1766, 2011.

[11] K. J. Binns, K. Al-Aubidy, and D. W. Shimmin, "Implicit rotor position sensing using search coils for a self-commutating permanent magnet drive system," *Electric Power Applications, IEE Proceedings B*, vol. 137, no. 4, pp. 253–258, 1990.

[12] D. Montesinos, S. Galceran, F. Blaabjerg, A. Sudria, and O. Gomis, "Sensorless control of pm synchronous motors and brushless dc motors - an overview and evaluation," in *Power Electronics and Applications, 2005 European Conference on*, 0 2005.

[13] W. Limei, G. Qingding, and R. Lorenz, "Sensorless control of permanent magnet synchronous motor," in *Power Electronics and Motion Control Conference, 2000. Proceedings. IPEMC 2000. The Third International*, 2000.

[14] X. Xiang and Y. He, "Sensorless operation of pmsm based on hybrid rotor position self-sensing scheme," in *Electrical Machines and Systems, 2007. ICEMS. International Conference on*, pp. 714 –718, oct. 2007.

[15] N. Bianchi, S. Bolognani, A. Faggion, E. Fornasiero, and A. Sartorello, "Zero-speed sensorless drive capability of fractional-slot inset pm machine," in *Power Electronics, Machines and Drives (PEMD 2012), 6th IET International Conference on*, pp. 1 –6, march 2012.

[16] A. Faggion, E. Fornasiero, N. Bianchi, and S. Bolognani, "Sensorless capability of fractional-slot surface-mounted pm motors," in *Electric Machines Drives Conference (IEMDC), 2011 IEEE International*, pp. 593 –598, may 2011.

[17] A. Eilenberger, E. Schmidt, and M. Schro anddl, "Sensorless capability of permanent magnet synchronous machines due to saturation- and reluctance-based coupling effects," in *Sensorless Control for Electrical Drives (SLED), 2010 First Symposium on*, pp. 14 –17, july 2010.

[18] H. de Kock, M. Kamper, and R. Kennel, "Anisotropy comparison of reluctance and pm synchronous machines for position sensorless control us-

ing hf carrier injection," *Power Electronics, IEEE Transactions on*, vol. 24, pp. 1905 –1913, aug. 2009.

[19] M. Leksell, L. Harnesfors, and H. P. Nee, "Machine design considerations for sensorless control of pm motors," in *in Proceedings of the International Conference on Electrical Machines*, vol. 1, pp. 619 –624, 1998.

[20] S.-C. Yang and R. Lorenz, "Surface permanent magnet synchronous machine self-sensing position estimation at low speed using eddy current reflected asymmetric resistance," in *Power Electronics and Applications (EPE 2011), Proceedings of the 2011-14th European Conference on*, pp. 1 –10, 30 2011-sept. 1 2011.

[21] P. Garcia, D. Reigosa, F. Briz, C. Blanco, and J. Guerrero, "Sensorless control of surface permanent magnet synchronous machines using the high frequency resistance," in *Energy Conversion Congress and Exposition (ECCE), 2011 IEEE*, pp. 2709 –2716, sept. 2011.

[22] N. Bianchi, S. Bolognani, J.-H. Jang, and S.-K. Sul, "Advantages of inset pm machines for zero-speed sensorless position detection," in *Industry Applications Conference, 2006. 41st IAS Annual Meeting. Conference Record of the 2006 IEEE*, vol. 1, pp. 495 –502, 2006.

[23] N. Bianchi and S. Bolognani, "Sensorless-oriented design of pm motors," *Industry Applications, IEEE Transactions on*, vol. 45, pp. 1249 –1257, july-aug. 2009.

[24] R. Wrobel, A. Budded, D. Holliday, P. Mellor, and P. Sangha, "Design considerations for permanent magnet brushless machines for zero-speed sensorless position estimation," in *Industry Applications Conference, 2006. 41st IAS Annual Meeting. Conference Record of the 2006 IEEE*, vol. 3, pp. 1494 –1500, 8-12 2006.

[25] K. Akatsu, M. Harke, and R. Lorenz, "Spmsm design considerations for initial position and magnet polarity estimation using carrier signal injection," in *Industry Applications Conference, 2007. 42nd IAS Annual Meeting. Conference Record of the 2007 IEEE*, pp. 2393 –2398, 23-27 2007.

[26] S. Wu, D. Reigosa, Y. Shibukawa, M. Leetmaa, R. Lorenz, and Y. Li, "Interior permanent magnet synchronous motor design for improving self-sensing performance at very low speed," in *Electrical Machines and Systems, 2008. ICEMS 2008. International Conference on*, pp. 3278 –3283, 2008.

[27] D. Reigosa, K. Akatsu, N. Limsuwan, Y. Shibukawa, and R. Lorenz, "Self-sensing comparison of fractional slot pitch winding vs. distributed winding for fw- and fi-ipmsms based on carrier signal injection at very low speed," in *Energy Conversion Congress and Exposition, 2009. ECCE 2009. IEEE*, pp. 3806 –3813, 2009.

[28] A. Budden, R. Wrobel, D. Holliday, P. Mellor, A. Dinu, P. Sangha, and M. Holme, "Impact of rotor design on sensorless position estimation," in *IEEE Industrial Electronics, IECON 2006 - 32nd Annual Conference on*, pp. 787 –792, 6-10 2006.

[29] Y. Kano, T. Kosaka, N. Matsui, and T. Nakanishi, "Sensorless-oriented design of ipm motors for general industrial applications," in *Electrical Machines, 2008. ICEM 2008. 18th International Conference on*, pp. 1 –6, 6-9 2008.

[30] Y. Kano, T. Kosaka, N. Matsui, and T. Nakanishi, "Rotor geometry design of interior pmsms with and without flux barriers for more accurate sensorless control," *Industrial Electronics, IEEE Transactions on*, vol. PP, no. 99, p. 1, 2011.

[31] Y. Kano, T. Kosaka, N. Matsui, T. Takahashi, and M. Fujistuna, "Design of saliency-based sensorless drive ipm motors for hybrid electric vehicles," in *Energy Conversion Congress and Exposition (ECCE), 2012 IEEE*, pp. 4362 –4369, sept. 2012.

[32] P. Sergeant, F. De Belie, and J. Melkebeek, "Rotor geometry design of interior pmsms with and without flux barriers for more accurate sensorless control," *Industrial Electronics, IEEE Transactions on*, vol. PP, no. 99, p. 1, 2011.

[33] S.-C. Yang, T. Suzuki, R. Lorenz, and T. Jahns, "Surface permanent magnet synchronous machine design for saliency-tracking self-sensing position estimation at zero and low speeds," in *Energy Conversion Congress and Exposition (ECCE), 2010 IEEE*, pp. 3493 –3500, 2010.

[34] A. Faggion, E. Fornasiero, N. Bianchi, and S. Bolognani, "Sensorless capability of fractional-slot surface-mounted pm motors," *Industry Applications, IEEE Transactions on*, vol. 49, no. 3, pp. 1325–1332, 2013.

[35] N. Bianchi and S. Bolognani, "Design optimisation of electric motors by genetic algorithms," *Electric Power Applications, IEE Proceedings* -, vol. 145,

pp. 475 –483, sep 1998.

[36] N. Bianchi, D. Durello, and E. Fornasiero, "Multi-objective optimization of a pm assisted synchronous reluctance machine, including torque and sensorless detection capability," in *Power Electronics, Machines and Drives (PEMD 2012), 6th IET International Conference on*, pp. 1 –6, march 2012.

[37] N. Bianchi, D. Durello, and E. Fornasiero, "Multi-objective optimization of an interior pm motor for a high-performance drive," in *Electrical Machines (ICEM 2012), 20th IEEE International Conference on*, pp. 376–382, sept 2012.

[38] G. Pellegrino and F. Cupertino, "Ipm motor rotor design by means of fea-based multi-objective optimization," in *Industrial Electronics (ISIE), 2010 IEEE International Symposium on*, pp. 1340 –1346, july 2010.

[39] G. Pellegrino and F. Cupertino, "Fea-based multi-objective optimization of ipm motor design including rotor losses," in *Energy Conversion Congress and Exposition (ECCE), 2010 IEEE*, pp. 3659 –3666, sept. 2010.

[40] J.-F. T. Ming-Hua Lin and C.-S. Yu, "A review of deterministic optimization methods in engineering and management," in *Mathematical Problems in Engineering, vol. 2012*, 2012.

[41] Y. Duan and D. Ionel, "A review of recent developments in electrical machine design optimization methods with a permanent magnet synchronous motor benchmark study," in *Energy Conversion Congress and Exposition (ECCE), 2011 IEEE*, pp. 3694 –3701, sept. 2011.

[42] R. Wrobel and P. Mellor, "Design considerations of a direct drive brushless machine with concentrated windings," *Energy Conversion, IEEE Transactions on*, vol. 23, no. 1, pp. 1–8, 2008.

[43] H. Hasanien, A. Abd-Rabou, and S. Sakr, "Design optimization of transverse flux linear motor for weight reduction and performance improvement using response surface methodology and genetic algorithms," *Energy Conversion, IEEE Transactions on*, vol. 25, pp. 598 –605, sept. 2010.

[44] S. Semidey, Y. Duan, J. Mayor, and R. Harley, "Optimal electromagnetic-thermo-mechanical integrated design for surface mount permanent magnet machines considering load profiles," in *Energy Conversion Congress and Exposition (ECCE), 2010 IEEE*, pp. 3646 –3653, sept. 2010.

[45] W. Ouyang, D. Zarko, and T. Lipo, "Permanent magnet machine design practice and optimization," in *Industry Applications Conference, 2006. 41st IAS Annual Meeting. Conference Record of the 2006 IEEE*, vol. 4, pp. 1905 –1911, oct. 2006.

[46] X. Meng, S. Wang, J. Qiu, J. G. Zhu, Y. Wang, Y. Guo, D. Liu, and W. Xu, "Dynamic multilevel optimization of machine design and control parameters based on correlation analysis," *Magnetics, IEEE Transactions on*, vol. 46, pp. 2779 –2782, aug. 2010.

[47] S. Vaez-Zadeh and A. Ghasemi, "Design optimization of permanent magnet synchronous motors for high torque capability and low magnet volume," *Electric Power Systems Research*, vol. 74, no. 2, pp. 307 – 313, 2005.

[48] G. Sizov, D. Ionel, and N. Demerdash, "A review of efficient fe modeling techniques with applications to pm ac machines," in *Power and Energy Society General Meeting, 2011 IEEE*, pp. 1 –6, july 2011.

[49] M. Yilmaz and P. Krein, "Capabilities of finite element analysis and magnetic equivalent circuits for electrical machine analysis and design," in *Power Electronics Specialists Conference, 2008. PESC 2008. IEEE*, pp. 4027 –4033, june 2008.

[50] Infolytica, "Magnet software environment." `http://www.infolytica.com/en/products/magnet`, August 2013.

[51] J. Nakatsugawa, Y. Notohara, D. Li, and Y. Iwaji, "Inductance measurement method for permanent magnet synchronous motors using ac with dc bias," pp. 1 –4, sep. 2008.

[52] D. Li, Y. Iwaji, T. Endo, and Y. Notohara, "An auto-tuning method of inductances for permanent magnet synchronous motors," in *Proceedings of the 2005 Japan Industry Applications Society Conference*, pp. 385–388, August 2005.

[53] J. Pyrhonen, T. Jokinen, and Hrabovcova, *Design of Rotating Electrical Machines*. Wiley, 2008.

[54] S.-O. Kwon, S.-I. Kim, P. Zhang, and J.-P. Hong, "Performance comparison of ipmsm with distributed and concentrated windings," in *Industry Applications Conference, 2006. 41st IAS Annual Meeting. Conference Record of the 2006 IEEE*, vol. 4, pp. 1984–1988, 2006.

[55] A. EL-Refaie, "Fractional-slot concentrated-windings synchronous permanent magnet machines: Opportunities and challenges," *Industrial Electronics, IEEE Transactions on*, vol. 57, no. 1, pp. 107–121, 2010.

[56] M. Galea, C. Gerada, T. Raminosoa, and P. Wheeler, "A thermal improvement technique for the phase windings of electrical machines," *Industry Applications, IEEE Transactions on*, vol. 48, pp. 79 –87, jan.-feb. 2012.

[57] O. Yeniay, "Penalty function methods for constrained optimization with genetic algorithms," *Mathematical and Computational Applications*, vol. 10, pp. 45–56, 2005.

[58] T. Lubin, S. Mezani, and A. Rezzoug, "Two-dimensional analytical calculation of magnetic field and electromagnetic torque for surface-inset permanent-magnet motors," *Magnetics, IEEE Transactions on*, vol. 48, no. 6, pp. 2080–2091, 2012.

[59] T. Lubin, S. Mezani, and A. Rezzoug, "2-d exact analytical model for surface-mounted permanent-magnet motors with semi-closed slots," *Magnetics, IEEE Transactions on*, vol. 47, no. 2, pp. 479–492, 2011.

Acronyms

AG . . . . . Airgap Length

APF . . . . . Additive Penalty Function

B-EMF . . . . . Back Electromotive Force

BI . . . . . Back-Iron

D-axis . . . . . Direct Axis

DL . . . . . Double-Layer

DPF . . . . . Death Penalty Function

FE . . . . . Finite Elements

FEA . . . . . Finite Element Analysis

FFT . . . . . Fast Fourier Transform

GA . . . . . Genetic Algorithm

HF . . . . . High Frequency

IPM . . . . . Interior Permanent Magnet

IPMSM . . . . . Interior Permanent Magnet Synchronous Machine

LCM . . . . . Lowest Common Multiple

MGA . . . . . Multi-Objective Genetic Algorithm

MI . . . . . Permanent Magnet Inset

MPF . . . . . Multiplicative Penalty Function

MS . . . . . Permanent Magnet Span

MT . . . . . Permanent Magnet Thickness

MTPA . . . . . Maximum Torque Per Ampere

PM . . . . . Permanent Magnet

PMSM . . . . . Permanent Magnet Synchronous Machine

Q-axis . . . . . Quadrature Axis

SIR . . . . . Slot Inner Radius

SNR . . . . . Signal-to-Noise Ratio

SO . . . . . Slot Opening

SPMSM . . . . . Surface Mount Permanent Magnet Synchronous Machine

Spp . . . . . Slots/Pole/Phase

SR . . . . . Split Ratio

TB . . . . . Tooth Bridge

THD . . . . . Total Harmonic Distortion

TT . . . . . Tooth Tip

TW . . . . . Tooth Width

VB . . . . . Visual Basic

Glossary

A_{cu} . . . . . Copper Winding Cross-sectional Area

A_{slot} . . . . . Slot Cross-sectional Area

G_{gap} . . . . . Generation Gap

G_{max} . . . . . Generation Gap

h . . . . . Heat Transfer Coefficient

i_i . . . . . Current Increment

K_w . . . . . Winding Factor

L'_d . . . . . Direct-Axis Inductance

L'_{dq} . . . . . Mutual Inductance

L'_q . . . . . Quadrature-Axis Inductance

L'_{qd} . . . . . Mutual Inductance

N_{ind} . . . . . Number of Indiviuals

P . . . . . Number of Pole Pairs

p . . . . . Number of Poles

P_c . . . . . Crossover Rate

P_f . . . . . Packing Factor

P_m . . . . . Mutation Rate

s . . . . . Number of Slots

List of Figures

1.1 Sensorless control strategies and classification 3
1.2 DQ-axis reference frame for 3s2p & 12s10p topology 4
1.3 Incremental inductance variation with Rotor Position 6
1.4 Incremental inductance variation with load 7

2.1 Saliency Analysis Results for [15] 14
2.2 PM motors with (a) inset rotor and (b) IPM rotor [22] 16
2.3 Layout of a Single Stator Slot [24] 16
2.4 L'_{dq} & ΔL vs load current for FW- & FI-IPM designs [27] 17
2.5 PM parameters with 14 suitable selections [28] 18
2.6 Parametrization of test IPM Motor [29] 19
2.7 Effect of rotor tooth opening on $\Delta\varepsilon_f$ and ΔS [31] 19
2.8 FEA magnetic flux density plots from two rotor positions 21
2.9 Data analysis of first optimization [36] 24
2.10 Definition of design variables and GA optimization results [37] . . 25

3.1 Supply circuit diagram for FE inductance measurement 30
3.2 Block diagram of experimental setup 32
3.3 Phasor alignment for rotor position & loading configuration . . . 33
3.4 Illustration of measured voltage and current waveforms 33
3.5 Experimental vs. FEA measurement of incremental inductances . 34
3.6 Incremental inductance variation with rotor position 35
3.7 Incremental inductance variation with loading 36
3.8 Variable geometrical parameters under investigation 37
3.9 Influence of SO on Incremental Inductances 39
3.10 Variation of saliency due to loading and SO 40
3.11 Influence of SO on incremental inductance ripple 40
3.12 Influence of SO on Machine Performance 41
3.13 Influence of TW on Incremental Inductances 43
3.14 Variation of saliency due to loading and TW 44
3.15 Influence of TW on incremental inductance ripple 44
3.16 Influence of TW on Machine Performance 45
3.17 Influence of BI on Incremental Inductances 47

3.18 Variation of saliency due to loading and BI 48
3.19 Influence of BI on incremental inductance ripple 48
3.20 Influence of BI on Machine Performance 49
3.21 Illustration of rotor geometry 50
3.22 Influence of MS on Incremental Inductances 51
3.23 Stator tooth geometry reference 52
3.24 Saliency characteristics of simulated models 54
3.25 Flux density plot of simulated models 55
3.26 Incremental inductance variation with load 55
3.27 FEA simulation results demonstrating zigzag leakage flux 58
3.28 Magnetic flux density plots at two rotor positions 59

4.1 Conventional design process 64
4.2 Segmented tooth design 66
4.3 Section of rotor design 69
4.4 Variable geometrical parameters in Matlab machine script. 70
4.5 Double layer winding configuration for 12s10p configuration . . . 73
4.6 Equivalent thermal model of half slot/tooth sector. 74
4.7 Flow diagram of machine scripting process 80

5.1 Flow chart of GA optimization process. 83
5.2 Average value for selected individuals per generation 89
5.3 Evolution of best objective for N_{ind}=25 92
5.4 Evolution of best objective for N_{ind}=50 92
5.5 Evolution of best objective for N_{ind}=75 93
5.6 Stage two GA optimization of 12s10p topology 96
5.7 Flow diagram of fitness evaluation process 100

6.1 Stage one GA optimization of 9s8p topology 106
6.2 Stage two GA optimization of 9s8p topology 107
6.3 Stage one GA optimization of 12s10p topology 109
6.4 Stage two GA optimization of 12s10p topology 111
6.5 Stage one GA optimization of 18s16p topology 113
6.6 Stage two GA optimization of 18s16p topology 114
6.7 Stage one GA optimization of 18s20p topology 116
6.8 Stage two GA optimization of 18s20p topology 117
6.9 Stage one GA optimization of 24s20p topology 119
6.10 Stage two GA optimization of 24s20p topology 120
6.11 No load zigzag leakage flux in 18s20p topology 128

6.12 HF saliency profile against torque output 128
6.13 FFT analysis of no load B-EMF 130
6.14 HF saliency profile against torque output 131
6.15 FFT analysis of no load B-EMF 132
6.16 FFT analysis of B-EMF for best solution topologies 137
6.17 FFT analysis of B-EMF for best solution topologies 141
6.18 FFT analysis of B-EMF for best solution topologies 147
6.19 FFT analysis of B-EMF for best solution topologies 150
6.20 Wireframe schematic of geometrical topologies 151

7.1 Wireframe sector of case study machine 157
7.2 Stator geometrical parameters 158
7.3 Rotor geometrical parameters 159
7.4 FFT analysis of test machine B-EMF 160
7.5 HF saliency profile against torque output 161
7.6 GA result of rotor variables and best objective 164
7.7 HF saliency profile against torque output 164
7.8 GA result for alternative machine configurations 166

List of Tables

3.1 Experimental Test Machine 32
3.2 Test Machine Parameters 38
3.3 Variation to stator tooth width (dimensions in mm) 52
3.4 Overview of performance analysis 53
3.5 Overview of inverse saliency topologies 57

4.1 Winding Factor (K_{w1}) for DL Concentrated Windings 72
4.2 Comparison of Slot/Pole Combinations 72
4.3 Machine Design Specifications 79

5.1 Boundary conditions for stage one variables 90
5.2 Best objective value obtained with given N_{ind}, P_c and P_m 91
5.3 Best objective value obtained with given N_{ind}, P_c and P_m 94
5.4 Boundary conditions for stage two variables 95

6.1 Machine Design Specifications 103
6.2 Boundary conditions for stage one variables based on topology . . 104
6.3 Boundary conditions for stage two variables based on topology . . 104
6.4 Overview of stage one torque optimization results 122
6.5 Overview of stage two saliency optimization results 123
6.6 Overview of stage two best objective saliency characteristics . . . 124
6.7 Fundamental performance of traditional saliency topologies 125
6.8 Overview of stage two inverse saliency optimization results 126
6.9 Overview of stage two best objective inverse saliency characteristics 126
6.10 Fundamental performance of inverse saliency topologies 126
6.11 Boundary conditions for 24s20p MGA routine 133
6.12 24s20p MGA result with three objectives and eight variables . . . 135
6.13 Optimum dimensions of best solutions for MGA variables 135
6.14 Saliency characteristics for best solution topologies 136
6.15 Fundamental performance of best solution topologies 136
6.16 24s20p MGA result with multiplicative penalty function 139
6.17 24s20p MGA result with death penalty function 140
6.18 Saliency characteristics for best solution topologies 140
6.19 Fundamental performance of best solution topologies 141

6.20 Optimum dimensions of best solutions for MGA variables 142
6.21 24s20p MGA result with MPF, three objectives and eight variables 143
6.22 Optimum dimensions of best solution for MGA variables 143
6.23 24s20p MGA result with three objectives and seven variables . . . 145
6.24 Optimum dimensions of best solutions for MGA variables 145
6.25 Saliency characteristics for best solution topologies 146
6.26 Fundamental performance of best solution topologies 146
6.27 24s20p MGA result with three objectives and six variables 148
6.28 Optimum dimensions of best solutions for MGA variables 149
6.29 Saliency characteristics for best solution topologies 149
6.30 Fundamental performance of best solution topologies 149
6.31 Comparison of machines resulting from optimization approaches . 154

7.1 Test machine specifications 159
7.2 Summary of test machine performance analysis 162
7.3 Summary of optimized test machine performance analysis 165
7.4 Summary of 48s16p optimized machine performance analysis . . . 167
7.5 Summary of 24s20p optimized machine performance analysis . . . 167

Appendix A: Matlab Scripts

A.1 Single-Objective GA Master Script

```
% Clears and closes all Matlab data
clear all ;
clear global;
close all;
clc;

% Declares MagNet application
global MN6
MN6 = actxserver('MagNet.Application');
set(MN6, 'Visible', 1);
MN6 = evalin('base','MN6');

% Declares global variables
global SR TW MS BI b_Exit gen func_count SimFunction GetParamFunct
b_Exit = 0;

% load GA_Temp;          % Load data from previous generation if GA fails

%%% Runs at the beginning of the GA process %%%
if size(gen,1)==0
    SimFunction = 'FF_Torque_24s20p_St1';
    GetParamFunct = 'getParam_St1';
    FileLog = '24s20pSt1Torque.txt';
    CapSel = 1;                 % Compatibility with dofunc

    % Confirm upper and lower boundaries
    Params='SR_TW_MS_BI';       % Names for Variables
    FieldD=[0.55  3.5  14  2.5;    % Lower Boundaries for Each Variable
            0.65  6.5  17  5.5];   % Upper Boundaries for Each Variable

    % Define GA parameters
    NVAR=size(FieldD,2);        % Number of Variables
    GGAP=0.9;                   % Generation Gap
    XOVR=0.75;                  % Crossover Rate
    MUTR=0.1;                   % Mutation Rate depending on NVAR
    MAXGEN=25;                  % Maximum Number of Generations
    INSR=0.8;                   % Insertion Rate
    Nind=75;                    % Number of Individuals

    % Specify other routines as strings
    SEL_F = 'sus';          % Name of selection function
    XOV_F = 'recdis';       % Name of recombination funcion for individuals
    MUT_F = 'mutbga';       % Name of mutation function
    OBJ_F = 'fitness';      % Name of function for objective value

    Chrom = crtrp(Nind,FieldD); % Generates chromosones for whole population
```

```
    gen = 0;                        % Generational counter
    func_count = 0;                 % Function counter
    tGlobal = tic;                  % Timer
    % Calculate objective function for population
    [ObjVal,Chrom] = feval(OBJ_F,Chrom);

    tTotal = toc(tGlobal);          % Time for Generation
    TimeLeft = tTotal*MAXGEN;       % Estimation of remaining Time based on first
        Generation
    fprintf('Time for first generation: = %0.3fs, end of the whole process in
        %0.0fh %0.0fm %0.1fs (%s)\n',tTotal,floor(TimeLeft/3600),floor((TimeLeft
        -floor(TimeLeft/3600)*3600)/60),rem(TimeLeft,60),datestr(now+TimeLeft
        /86400));      % display counter
end

%%% Generational loop %%%
while gen < MAXGEN && b_Exit == 0
    tStart=tic;                     % Timer
    fprintf('GA_Script: Current generation = %0.0f/%0.0f, %0.0f to go\n',gen,
        MAXGEN,MAXGEN-gen);

    % Fitness assignment to whole population
    FitnV=ranking(ObjVal);
    % Select individuals from population
    SelCh=select(SEL_F,Chrom,FitnV,GGAP);
    % Recombine selected individuals
    SelCh=recombin(XOV_F,SelCh,XOVR);
    % Mutate offsprings
    SelCh=mutate(MUT_F,SelCh,FieldD,[MUTR]);
    % Calculate objective function for offsprings
    [ObjVoff,SelCh]=feval(OBJ_F,SelCh);
    % Insert best offspring in population replacing worst parents
    [Chrom,ObjVal]=reins(Chrom,SelCh,1,1,ObjVal,ObjVoff);

    gen=gen+1;          % Generational counter

    [best_objv(gen) ii]=min(ObjVal);
    best_ind(gen,:)=Chrom(ii,:);

    feval(GetParamFunct,Chrom(ii,:));
    Fit = feval(SimFunction,2);

    func_counter(gen,:) = func_count;

    % Plots the best objective value from each generation
    figure(1);
    plot((best_objv),'ro'); xlabel('Generation'); ylabel('Best Value');
    text(0.5,0.95,['Best=',num2str(best_objv(gen))],'Units','normalized');
    drawnow

    tElapsed=toc(tStart);                       % Stops Timer
    tTotal = tTotal + tElapsed;                 % Calculates total elapsed time
    TimeLeft = tTotal/(gen+1)*(MAXGEN-gen);     % Calculates time remaining
    fprintf('Time for the generation: = %0.3fs, end of the whole process in
        %0.0fh %0.0fm %0.1fs (%s)\n',tElapsed,floor(TimeLeft/3600),floor((
        TimeLeft-floor(TimeLeft/3600)*3600)/60),rem(TimeLeft,60),datestr(now+
        TimeLeft/86400));      % display counter
```

```
    % displays best objective value so far
    fprintf('Current best objective value = %0.5f\n',best_objv(gen));

    % Saves iterative GA data to textfile
    fileID = fopen(FileLog, 'a');
    fprintf(fileID,'Generation %d',gen);
    fprintf(fileID,'\r\n');
    fprintf(fileID,'%10.5e;',Chrom(:,1));
    fprintf(fileID,'\r\n');
    fprintf(fileID,'%10.5e;',Chrom(:,2));
    fprintf(fileID,'\r\n');
    fprintf(fileID,'%10.5e;',Chrom(:,3));
    fprintf(fileID,'\r\n');
    fprintf(fileID,'%10.5e;',Chrom(:,4));
    fprintf(fileID,'\r\n');
    fprintf(fileID,'%10.5e;',ObjVal);
    fprintf(fileID,'\r\n');
    fclose(fileID);

    save GA_Temp;   % Saves GA data so can be resumed from most recent
        generation
end

tTotal = toc(tGlobal);                  % Total time for GA routine
fprintf('Total time of the process: %0.0fh %0.0fm %0.1fs\n',floor(tTotal/3600),
    floor((tTotal-floor(tTotal/3600)*3600)/60),rem(tTotal,60));

% Select the best individual from the overall generations
if exist('best_objv','var')
    [bob_objv ii]=min(best_objv);
    feval(GetParamFunct,best_ind(ii,:));
    fprintf('Bob objv = %e, generation: %0.0f (%0.0f ind., %0.0f gen)\n',
        bob_objv,ii,Nind,MAXGEN);
    fprintf('Params Min/Max:%s\n','Params');
    fprintf('%10.2e ',FieldD(1,:));
    fprintf('\n');
    fprintf('%10.2e ',FieldD(2,:));
    fprintf('\n');
    fprintf('SR = %e; TW = %e; MS = %e; BI = %e;\n\n',SR,TW,MS,BI);
end
```

A.2 Multi-Objective GA Master Script

```
clear all;
clear global;
close all;
clc;

global MN6
MN6 = actxserver('MagNet.Application');
Consts = invoke(MN6, 'getConstants');
set(MN6, 'Visible', 1);
MN6 = evalin ('base','MN6');

FitnessFunction = @MGA_24s20p_8;    % Function handle to the fitness function
```

```
numberOfVariables = 7;                  % Number of decision variables
lb = [0.6 4.5 14.5 2.5 1.5 0.75 1.5 0.1]; % Lower bound
ub = [0.65 7 17.5 4.5 4 1.5 3.5 0.9];     % Upper bound
A = []; b = [];                         % No linear inequality constraints
Aeq = []; beq = [];                     % No linear equality constraints
options = gaoptimset('PlotFcns',@gaplotpareto,'PopulationSize',50,'Generations'
    ,20,'PopulationType','doubleVector','ParetoFraction',0.4);

[x,Fval,exitFlag,Output] = gamultiobj(FitnessFunction,numberOfVariables,A,b,Aeq,
    beq,lb,ub,options);
```

A.3 Single-Objective Fitness Function

```
function Fit = FF_Torque_24s20p_St1(Torque)

% Defines global variables that are passed throughout optimization scripts
global Torq Value SR TW MS BI

% Simulation settings
p = 10;                                 % Pole pairs
initpos = -1;                           % Initial rotor position (degrees)
speed_rpm = 3000;                       % Simulation speed (rpm)
simul_step = 0.01;                      % Simulation time step
simul_stop = 0.05;                      % Simulation duration

speed_degps = speed_rpm*360/60;         % Calculates speed in deg per sec
freq_meca = speed_rpm/60;               % Calculates mechanical frequency
freq_elec = p*freq_meca;                % Calculates electrical frequency
period = 1e3/freq_elec;                 % Period (ms)
timemillisec = 0:simul_step:simul_stop; % Defines timemillisec

GA24s20p_St1                            % Calls machine subscript

% Loading settings
Id = 0;
Iq = RatedLoad_Peak;
Idelta = 0.5;
Phase = 0;

% Imports variant into MagNet
invoke(MN6, 'processCommand', ['Call setvariant(101,',num2str(initpos),')']);
invoke(MN6, 'processCommand', ['Call setvariant(102,',num2str(speed_degps),')'])
    ;
invoke(MN6, 'processCommand', ['Call setvariant(103,',num2str(freq_elec),')']);
invoke(MN6, 'processCommand', ['Call setvariant(104,',num2str(simul_step),')']);
invoke(MN6, 'processCommand', ['Call setvariant(105,',num2str(simul_stop),')']);
invoke(MN6, 'processCommand', ['Call setvariant(106,',num2str(Id),')']);
invoke(MN6, 'processCommand', ['Call setvariant(107,',num2str(Iq),')']);
invoke(MN6, 'processCommand', ['Call setvariant(108,',num2str(Idelta),')']);
invoke(MN6, 'processCommand', ['Call setvariant(109,',num2str(Phase),')']);
invoke(MN6, 'processCommand', 'initpos = getVariant(101)');
invoke(MN6, 'processCommand', 'speed_degps = getVariant(102)');
invoke(MN6, 'processCommand', 'freq_elec = getVariant(103)');
invoke(MN6, 'processCommand', 'simul_step = getVariant(104)');
invoke(MN6, 'processCommand', 'simul_stop = getVariant(105)');
```

```
invoke(MN6, 'processCommand', 'Id = getVariant(106)');
invoke(MN6, 'processCommand', 'Iq = getVariant(107)');
invoke(MN6, 'processCommand', 'Idelta = getVariant(108)');
invoke(MN6, 'processCommand', 'Phase = getVariant(109)');

% Sets solver settings within MagNet
invoke(MN6, 'processCommand', 'Call getDocument().beginUndoGroup("Set Solver
    Options", true)');
invoke(MN6, 'processCommand', 'Call getDocument().setSolverMaterialType(
    infoNonlinearMaterial)');
invoke(MN6, 'processCommand', 'Call getDocument().setSourceFrequency(freq_elec)'
    );
invoke(MN6, 'processCommand', 'Call getDocument().setPolynomialOrder("", 2)');
invoke(MN6, 'processCommand', 'Call getDocument().endUndoGroup()');

% Sets transient settings within MagNet
invoke(MN6, 'processCommand', 'Call getDocument().beginUndoGroup("Set Transient
    Options", true)');
invoke(MN6, 'processCommand', 'Call getDocument().setFixedIntervalTimeSteps(0,
    simul_stop, simul_step)');
invoke(MN6, 'processCommand', 'Call getDocument().deleteTimeStepMaximumDelta()')
    ;
invoke(MN6, 'processCommand', 'Call getDocument().setTimeStepStorageStartTime(
    start_store)');
invoke(MN6, 'processCommand', 'Call getDocument().endUndoGroup()');
invoke(MN6, 'processCommand','Call getDocument().beginUndoGroup("Set Properties
    ", true)');
invoke(MN6, 'processCommand','Call getDocument().setParameter("", "
    SourcesOnAtTransientStart", "Yes", infoStringParameter)');
invoke(MN6, 'processCommand','Call getDocument().endUndoGroup()');

% Sets motion settings within MagNet
invoke(MN6, 'processCommand','Call getDocument().getView().selectObject("Moving
    Rotor", infoSetSelection)');
invoke(MN6, 'processCommand','Call getDocument().beginUndoGroup("Set Moving
    Rotor Properties", true)');
invoke(MN6, 'processCommand','Call getDocument().setMotionPositionAtStartup("
    Moving Rotor", initpos)');
invoke(MN6, 'processCommand','REDIM ArrayOfValues1(1)');
invoke(MN6, 'processCommand','ArrayOfValues1(0)= 0');
invoke(MN6, 'processCommand','ArrayOfValues1(1)= 5');
invoke(MN6, 'processCommand','REDIM ArrayOfValues2(1)');
invoke(MN6, 'processCommand','ArrayOfValues2(0)= speed_degps');
invoke(MN6, 'processCommand','ArrayOfValues2(1)= speed_degps');
invoke(MN6, 'processCommand','Call getDocument().setMotionSpeedVsTime("Moving
    Rotor", ArrayOfValues1, ArrayOfValues2)');
invoke(MN6, 'processCommand','Call getDocument().endUndoGroup()');

% Apply Normal Loading Conditions to Current Sources using subscript
SetLoading_Normal
% Saves MagNet model
invoke(MN6, 'saveDocument', ('C:\Users\eexjb2\Desktop\model.mn') );
% Begin FEA Simulation in MagNet
invoke(MN6, 'processCommand', 'Call getDocument().solveTransient2dWithMotion()')
    ;
% Post-process subscript, calls torque result from MagNet
PostProcess_Torque
```

```
% Saves MagNet result
invoke(MN6, 'saveDocument', ('C:\Users\eexjb2\Desktop\result.mn') );
% Fitness function set to minimize torque
Value = 1/mean(Torq);

Fit = Value;
```

A.4 Multi-Objective Fitness Function

```
function Fit = MGA_24s20p_8(x)
% Defines GA Variables
SR=x(1);
TW=x(2);
MS=x(3);
BI=x(4);
SO=x(5);
TT=x(6);
TB=x(7);
IN=x(8);

% Defines global variables that are passed throughout optimization scripts
global Saliency Cogging Torq

% Simulation settings
p = 10;                                % Pole pairs
initpos = -1;                          % Initial rotor position (degrees)
speed_rpm = 3000;                      % Simulation speed (rpm)
simul_step = 0.01;                     % Simulation time step
simul_stop = 0.05;                     % Simulation duration

speed_degps = speed_rpm*360/60;          % Calculates speed in deg per sec
freq_meca = speed_rpm/60;                % Calculates mechanical frequency
freq_elec = p*freq_meca;                 % Calculates electrical frequency
period = 1e3/freq_elec;                  % Period (ms)
timemillisec = 0:simul_step:simul_stop; % Defines timemillisec

MGA24s20p                          % Calls machine subscript

% Loading settings
Id = 0;
Iq = RatedLoad_Peak;
Idelta = 0.5;
Phase = 0;

% Imports variant into MagNet
invoke(MN6, 'processCommand', ['Call setvariant(101,',num2str(initpos),')']);
invoke(MN6, 'processCommand', ['Call setvariant(102,',num2str(speed_degps),')'])
    ;
invoke(MN6, 'processCommand', ['Call setvariant(103,',num2str(freq_elec),')']);
invoke(MN6, 'processCommand', ['Call setvariant(104,',num2str(simul_step),')']);
invoke(MN6, 'processCommand', ['Call setvariant(105,',num2str(simul_stop),')']);
invoke(MN6, 'processCommand', ['Call setvariant(106,',num2str(Id),')']);
invoke(MN6, 'processCommand', ['Call setvariant(107,',num2str(Iq),')']);
invoke(MN6, 'processCommand', ['Call setvariant(108,',num2str(Idelta),')']);
invoke(MN6, 'processCommand', ['Call setvariant(109,',num2str(Phase),')']);
```

```
invoke(MN6, 'processCommand', 'initpos = getVariant(101)');
invoke(MN6, 'processCommand', 'speed_degps = getVariant(102)');
invoke(MN6, 'processCommand', 'freq_elec = getVariant(103)');
invoke(MN6, 'processCommand', 'simul_step = getVariant(104)');
invoke(MN6, 'processCommand', 'simul_stop = getVariant(105)');
invoke(MN6, 'processCommand', 'Id = getVariant(106)');
invoke(MN6, 'processCommand', 'Iq = getVariant(107)');
invoke(MN6, 'processCommand', 'Idelta = getVariant(108)');
invoke(MN6, 'processCommand', 'Phase = getVariant(109)');

% Sets solver settings within MagNet
invoke(MN6, 'processCommand', 'Call getDocument().beginUndoGroup("Set Solver
    Options", true)');
invoke(MN6, 'processCommand', 'Call getDocument().setSolverMaterialType(
    infoNonlinearMaterial)');
invoke(MN6, 'processCommand', 'Call getDocument().setSourceFrequency(freq_elec)'
    );
invoke(MN6, 'processCommand', 'Call getDocument().setPolynomialOrder("", 2)');
invoke(MN6, 'processCommand', 'Call getDocument().endUndoGroup()');

% Sets transient settings within MagNet
invoke(MN6, 'processCommand', 'Call getDocument().beginUndoGroup("Set Transient
    Options", true)');
invoke(MN6, 'processCommand', 'Call getDocument().setFixedIntervalTimeSteps(0,
    simul_stop, simul_step)');
invoke(MN6, 'processCommand', 'Call getDocument().deleteTimeStepMaximumDelta()'
    );
invoke(MN6, 'processCommand', 'Call getDocument().setTimeStepStorageStartTime(
    start_store)');
invoke(MN6, 'processCommand', 'Call getDocument().endUndoGroup()');
invoke(MN6, 'processCommand','Call getDocument().beginUndoGroup("Set Properties
    ", true)');
invoke(MN6, 'processCommand','Call getDocument().setParameter("", "
    SourcesOnAtTransientStart", "Yes", infoStringParameter)');
invoke(MN6, 'processCommand','Call getDocument().endUndoGroup()');

% Sets motion settings within MagNet
invoke(MN6, 'processCommand','Call getDocument().getView().selectObject("Moving
    Rotor", infoSetSelection)');
invoke(MN6, 'processCommand','Call getDocument().beginUndoGroup("Set Moving
    Rotor Properties", true)');
invoke(MN6, 'processCommand','Call getDocument().setMotionPositionAtStartup("
    Moving Rotor", initpos)');
invoke(MN6, 'processCommand','REDIM ArrayOfValues1(1)');
invoke(MN6, 'processCommand','ArrayOfValues1(0)= 0');
invoke(MN6, 'processCommand','ArrayOfValues1(1)= 5');
invoke(MN6, 'processCommand','REDIM ArrayOfValues2(1)');
invoke(MN6, 'processCommand','ArrayOfValues2(0)= speed_degps');
invoke(MN6, 'processCommand','ArrayOfValues2(1)= speed_degps');
invoke(MN6, 'processCommand','Call getDocument().setMotionSpeedVsTime("Moving
    Rotor", ArrayOfValues1, ArrayOfValues2)');
invoke(MN6, 'processCommand','Call getDocument().endUndoGroup()');

% Apply, Simulate and Process No Load Normal Loading Conditions to Current
    Sources
SetLoading_Normal
% Starts FEA simulation in MagNet
```

```
invoke(MN6, 'processCommand', 'Call.getDocument().solveTransient2dWithMotion()')
    ;
% Post-process subscript, calls torque result from MagNet
PostProcess_Torque

% Calculates peak torque loading and imports to MagNet
Iq = 45*(RatedLoad_Peak/mean(Torq));
invoke(MN6, 'processCommand', ['Call.setvariant(107,',num2str(Iq),')']);
invoke(MN6, 'processCommand', 'Iq.=..getVariant(107)');

% Apply, Simulate and Process Normal Loading Conditions to Current Sources
SetLoading_Normal
% Saves model
invoke(MN6, 'saveDocument', ('C:\Users\eexjb2\Documents\Magnet\MGA\24s20p\
    MGA_Model.mn'));
% Starts FEA simulation in MagNet
invoke(MN6, 'processCommand', 'Call.getDocument().solveTransient2dWithMotion()')
    ;
% Post-process subscript, calls results from MagNet
PostProcess_Normal

% Apply, Simulate and Process DeltaD Loading Conditions to Current Sources
SetLoading_DeltaD
% Starts FEA simulation in MagNet
invoke(MN6, 'processCommand', 'Call.getDocument().solveTransient2dWithMotion()')
    ;
% Post-process subscript, calls results from MagNet
PostProcess_DeltaD

% Apply, Simulate and Process DeltaQ Loading Conditions to Current Sources
SetLoading_DeltaQ
% Starts FEA simulation in MagNet
invoke(MN6, 'processCommand', 'Call.getDocument().solveTransient2dWithMotion()')
    ;
% Post-process subscript, calls results from MagNet
PostProcess_DeltaQ
% Post-process subscript, calculates saliency from MagNet results
PostProcess_Ldq

% Apply, Simulate and Process No Load Normal Loading Conditions to Current
    Sources
SetLoading_NoLoad_Normal
% Starts FEA simulation in MagNet
invoke(MN6, 'processCommand', 'Call.getDocument().solveTransient2dWithMotion()')
    ;
% Post-process subscript, calls cogging torque results from MagNet
PostProcess_Cogging

% Saves MagNet model
invoke(MN6, 'saveDocument', ('C:\Users\eexjb2\Desktop\MGA_Result.mn'));

Fit(1) = 1/Saliency;
Fit(2) = (max(Cogging)-min(Cogging));
Fit(3) = 1/mean(Torq);
```

A.5 Machine Script

```
% Variable Stator Script for 24s20p SPMSM
%************************************************

% Open New MagNet Document
invoke(MN6, 'processCommand', 'Call newDocument()');

% Set Model Units to Millimeters
invoke(MN6, 'processCommand', 'Call getDocument().beginUndoGroup("Set Default
    Units", true)');
invoke(MN6, 'processCommand', 'Call getDocument().setDefaultLengthUnit("
    Millimeters")');
invoke(MN6, 'processCommand', 'Call getDocument().endUndoGroup()');

%************************************************************************
% Conversion constant for degrees - radians
Pi = 3.14159265358979323846;
Rad = (Pi)/(180);

% Define Slot/Pole Combination
Ns = 24;          % Number of Slots
Np = 10;          % Number of Pole Pairs
SS = 360/Ns;      % Slot Span
PS = 360/(2*Np);% Pole Span

% Fixed Dimensions
Lstack = 120;     % Stack Length (mm)
SOR = 67.5;       % Stator Outer Radius (mm)
AG = 0.75;        % Airgap Length (mm)
HT = 4;           % Aluminium Housing Thickness (mm)

% Winding properties
Zq = 16;          % Number of Conductors per Slot
Pf = 0.5;         % Slot Packing Factor

% Variable Dimensions
SR = 0.63;        % Split Ratio
TW = 5.9;         % Tooth Width (mm)
BI = 3.5;         % Back Iron Thickness (mm)
MS = 16.5;        % Magnet Span (Degress)
SO = 2.5;         % Slot Opening (Degrees)
TB = 2.0;         % Tooth Base Thickness (mm)
TT = 1.0;         % Tooth Tip Thickness (mm)
IN = 0.30;        % Magnet Inset Ratio

% Defines remaining dimnesions
SIR = SR * SOR;           % Convert Split Ratio into SIR
% Magnet Thickness as a function of MS
Area_PM = 600/(2*Np);     % Cross sectional area of PM pole
Mor = SIR-AG;
Mir = sqrt( (Mor^2)-((Area_PM*360) / (MS*Pi)) );
MT = Mor - Mir;           % Magnet Thickness (mm)

% Calculate Stator Design Points
Ax = sqrt((SIR+TB)^2-(TW/2)^2);
```

```
Ay = TW/2;
Bx = sqrt((SOR-BI)^2-(TW/2)^2);
By = TW/2;
Cx = cos(((SS+0.1)/2)*Rad)*(SOR-BI);
Cy = sin(((SS+0.1)/2)*Rad)*(SOR-BI);
Dx = cos((SS/2)*Rad)*(SOR);
Dy = sin((SS/2)*Rad)*(SOR);
Ex = cos((SS/1.98)*Rad)*(SIR+TT);
Ey = sin((SS/1.98)*Rad)*(SIR+TT);
Fx = cos(((SS/2)-(SO/2))*Rad)*(SIR);
Fy = sin(((SS/2)-(SO/2))*Rad)*(SIR);
Gx = cos(((SS/2)-(SO/2))*Rad)*(SIR+TT);
Gy = sin(((SS/2)-(SO/2))*Rad)*(SIR+TT);

% Calculate Rotor Design Points
Nx = cos(((MS/2)+(PS-MS+3))*Rad)*(SIR-AG-MT+(IN*MT));
Ny = sin(((MS/2)+(PS-MS+3))*Rad)*(SIR-AG-MT+(IN*MT));
Ox = cos((MS/2)*Rad)*(SIR-AG-MT);
Oy = sin((MS/2)*Rad)*(SIR-AG-MT);
Px = cos(((MS-3)/2)*Rad)*(SIR-AG-MT+(IN*MT));
Py = sin(((MS-3)/2)*Rad)*(SIR-AG-MT+(IN*MT));
Qx = cos((MS/2)*Rad)*(SIR-AG);
Qy = sin((MS/2)*Rad)*(SIR-AG-MT);
Shaft = 0.65*(SIR-AG-MT+(IN*MT));

% Calculate airgap devision points
AG1 = SIR-((3*AG)/4);
AG2 = SIR-(AG/2);
AG3 = SIR-(AG/4);
InnerAir = Shaft-0.2;

% Coordinate points for MagNet selection tool
SelectMagnetN = SIR-AG-(MT/2);
SelectMagnetSx = cos(PS*Rad)*(SIR-AG-(MT/2));
SelectMagnetSy = sin(PS*Rad)*(SIR-AG-(MT/2));
SelectEdges4x = cos((PS/2)*Rad)*(SIR-AG-MT+(IN*MT));
SelectEdges4y = sin((PS/2)*Rad)*(SIR-AG-MT+(IN*MT));
SelectRotorLam = ((SIR-AG-MT)+Shaft)/2;
SelectAG1 = SIR-((7*AG)/8);
SelectAG2 = SIR-((5*AG)/8);
SelectAG3 = SIR-((3*AG)/8);
SelectAG4 = SIR-(AG/8);
SelectInnerAir = Shaft-0.1;

% Sending Parameters to Variant and importing into MagNet
invoke(MN6, 'processCommand', ['Call setvariant(1,',num2str(SO),')']);
invoke(MN6, 'processCommand', 'SO = getVariant(1)');
% """ Repeated for all parameters """ %
invoke(MN6, 'processCommand', ['Call setvariant(63,',num2str(SelectInnerAir),')'
    ]);
invoke(MN6, 'processCommand', 'SelectInnerAir = getVariant(63)');

%%%% Create Stator %%%%
% Draw lines and arcs for stator
invoke(MN6, 'processCommand','Call getDocument().getView().newLine(Ax, Ay, Bx,
    By)');
```

```
invoke(MN6, 'processCommand','Call getDocument().getView().newArc(0,0,Cx,-Cy,
    Bx,-By)');
invoke(MN6, 'processCommand','Call getDocument().getView().newLine(Fx,Fy,Gx,
    Gy)');
invoke(MN6, 'processCommand','Call getDocument().getView().newLine(Gx,Gy,Ax,
    Ay)');
invoke(MN6, 'processCommand','Call getDocument().getView().newLine(Ax,-Ay,Bx,
    -By)');
invoke(MN6, 'processCommand','Call getDocument().getView().newLine(Fx,-Fy,Gx,
    -Gy)');
invoke(MN6, 'processCommand','Call getDocument().getView().newLine(Gx,-Gy,Ax,
    -Ay)');
invoke(MN6, 'processCommand','Call getDocument().getView().newArc(0,0,Fx,-Fy,
    Fx,Fy)');
invoke(MN6, 'processCommand','Call getDocument().getView().newArc(0,0,Bx,By,
    Cx,Cy)');
invoke(MN6, 'processCommand', 'Call getDocument().getView().newCircle(0,0,SOR)
    ');

% Condition dependent on tooth bridge dimensions
if TB==TT
    invoke(MN6, 'processCommand','Call getDocument().getView().newArc(0,0,Gx,
        Gy,Ex,Ey)');
    invoke(MN6, 'processCommand','Call getDocument().getView().newArc(0,0,Ex,-
        Ey,Gx,-Gy)');
else
    invoke(MN6, 'processCommand','Call getDocument().getView().newLine(Ex,Ey,Gx
        ,Gy)');
    invoke(MN6, 'processCommand','Call getDocument().getView().newLine(Ex,-Ey,
        Gx,-Gy)');
end

% Select and Rotate Tooth, Coil R, Coil L Edges
invoke(MN6, 'processCommand', 'Call getDocument().getView().selectIn(30,10,
    -30,90,infoSetSelection,Array(infoSliceLine,infoSliceArc))');
for i = 1:Ns-1
    j = SS*i;
    invoke(MN6, 'processCommand', ['Call setvariant(1,',num2str(j),')']);
    invoke(MN6, 'processCommand', 'j = getVariant(1)');
    invoke(MN6, 'processCommand', 'Call getDocument().getView().
        rotateSelectedEdges(0,0,j,True)');
end

ToothLines              % Subscript that creates segmented stator teeth
MakeStatorComponents    % Subscript that makes tooth & slot components
Extract_StatorEdges     % Subscript extracts edges of all stator components

%%%% Create Rotor %%%%
% Draw lines and arcs for Rotor
invoke(MN6, 'processCommand', 'Call getDocument().getView().newArc(0,0,Px,Py,
    Nx,Ny)');
invoke(MN6, 'processCommand', 'Call getDocument().getView().newLine(Ox,Oy,Qx,
    Qy)');
invoke(MN6, 'processCommand', 'Call getDocument().getView().newLine(Ox,-Oy,Qx,
    -Qy)');
invoke(MN6, 'processCommand', 'Call getDocument().getView().newArc(0,0,Ox,-Oy
    ,Ox,Oy)');
```

```
invoke(MN6, 'processCommand', 'Call getDocument().getView().newArc(0,0,Qx,-Qy
    ,Qx,Qy)');
invoke(MN6, 'processCommand', 'Call getDocument().getView().newCircle(0,0,
    Shaft)');

% Creates South PM Component
invoke(MN6, 'processCommand', 'Call getDocument().getView().selectAt(
    SelectMagnetN,0,infoSetSelection,Array(infoSliceSurface))');
invoke(MN6, 'processCommand', 'REDIM ArrayOfValues(0)');
invoke(MN6, 'processCommand', 'ArrayOfValues(0)="South"');
invoke(MN6, 'processCommand', 'Call getDocument().getView().makeComponentInALine
    (Lstack,ArrayOfValues,"Name=Neodymium Iron Boron:38/15;Type=Uniform;
    Direction=[-1,0,0]",infoMakeComponentUnionSurfaces Or
    infoMakeComponentRemoveVertices)');
invoke(MN6, 'processCommand', 'Call getDocument().getView().selectObject("South
    ",infoSetSelection)');
invoke(MN6, 'processCommand', 'Call getDocument().rotateComponent(Array("South")
    ,0,0,0,0,0,1,18,1)');
invoke(MN6, 'processCommand', 'Call getDocument().beginUndoGroup("Set South
    Properties",true)');
invoke(MN6, 'processCommand', 'Call getDocument().setMaxElementSize("South",
    PMMesh)');
invoke(MN6, 'processCommand', 'Call getDocument().endUndoGroup()');
% Creates North PM Component
invoke(MN6, 'processCommand', 'Call getDocument().getView().selectAt(
    SelectMagnetN,0,infoSetSelection,Array(infoSliceSurface))');
invoke(MN6, 'processCommand', 'REDIM ArrayOfValues(0)');
invoke(MN6, 'processCommand', 'ArrayOfValues(0)="North"');
invoke(MN6, 'processCommand', 'Call getDocument().getView().makeComponentInALine
    (Lstack,ArrayOfValues,"Name=Neodymium Iron Boron:38/15;Type=Uniform;
    Direction=[1,0,0]",infoMakeComponentUnionSurfaces Or
    infoMakeComponentRemoveVertices)');
invoke(MN6, 'processCommand', 'Call getDocument().beginUndoGroup("Set North
    Properties",true)');
invoke(MN6, 'processCommand', 'Call getDocument().setMaxElementSize("North",
    PMMesh)');
invoke(MN6, 'processCommand', 'Call getDocument().endUndoGroup()');

% Select & Rotate Rotor Edges
invoke(MN6, 'processCommand', 'Call getDocument().getView().selectAt(
    SelectEdges4x,SelectEdges4y,infoToggleInSelection,Array(infoSliceLine,
    infoSliceArc))');
for i = 1:(2*Np)-1
    j = PS*i;
    invoke(MN6, 'processCommand', ['Call setvariant(1,',num2str(j),')']);
    invoke(MN6, 'processCommand', 'j = getVariant(1)');
    invoke(MN6, 'processCommand', 'Call getDocument().getView().
        rotateSelectedEdges(0,0,j,True)');
end
% Copy and Rotate Magnets
for i = 1:(Np)-1
    j = (2*PS)*i;
    invoke(MN6, 'processCommand', ['Call setvariant(1,',num2str(j),')']);
    invoke(MN6, 'processCommand', 'j = getVariant(1)');
    comm1 = 'Call getDocument().beginUndoGroup("Transform Component")';
    comm2 = 'Call getDocument().rotateComponent(getDocument().copyComponent(
        Array("North","South"),1),0,0,0,0,0,1,j,1)';
```

```
    comm3 = 'Call getDocument().endUndoGroup()';
    invoke(MN6, 'processCommand', comm1);
    invoke(MN6, 'processCommand', comm2);
    invoke(MN6, 'processCommand', comm3);
end
Extract MagnetEdges      % Subscript extracts edges from copied components

% Make Rotor Lam Component
invoke(MN6, 'processCommand', 'Call getDocument().getView().selectAt(
    SelectRotorLam, 0, infoSetSelection, Array(infoSliceSurface))');
invoke(MN6, 'processCommand', 'REDIM ArrayOfValues(0)');
invoke(MN6, 'processCommand', 'ArrayOfValues(0)= "Rotor Lam"');
invoke(MN6, 'processCommand', 'Call getDocument().getView().makeComponentInALine
    (Lstack, ArrayOfValues, "Name=M800-50A", infoMakeComponentUnionSurfaces Or
    infoMakeComponentRemoveVertices)');
invoke(MN6, 'processCommand', 'Call getDocument().getView().selectObject("Rotor
    Lam", infoSetSelection)');
invoke(MN6, 'processCommand', 'Call getDocument().beginUndoGroup("Set Rotor Lam
    Properties", true)');
invoke(MN6, 'processCommand', 'Call getDocument().setMaxElementSize("Rotor Lam",
    FeMesh)');
invoke(MN6, 'processCommand', 'Call getDocument().endUndoGroup()');

% Draw airgap divisions and shaft inner air
invoke(MN6, 'processCommand', 'Call getDocument().getView().newCircle(0, 0, AG1)
    ');
invoke(MN6, 'processCommand', 'Call getDocument().getView().newCircle(0, 0, AG2)
    ');
invoke(MN6, 'processCommand', 'Call getDocument().getView().newCircle(0, 0, AG3)
    ');
invoke(MN6, 'processCommand', 'Call getDocument().getView().newCircle(0, 0,
    InnerAir)');
% Create airgap components
invoke(MN6, 'processCommand', 'Call getDocument().getView().selectAt(SelectAG1,
    0, infoSetSelection, Array(infoSliceSurface))');
invoke(MN6, 'processCommand', 'REDIM ArrayOfValues(0)');
invoke(MN6, 'processCommand', 'ArrayOfValues(0)= "Airgap 1"');
invoke(MN6, 'processCommand', 'Call getDocument().getView().makeComponentInALine
    (Lstack, ArrayOfValues, "Name=Virtual Air", infoMakeComponentUnionSurfaces
    Or infoMakeComponentRemoveVertices)');
% """ Repeated for all four airgap components and shaft inner air """ %

% Create Inner Shaft Boundary Condition
invoke(MN6, 'processCommand', 'Call getDocument().beginUndoGroup("Assign
    Boundary Condition")');
invoke(MN6, 'processCommand', 'REDIM ArrayOfValues(1)');
invoke(MN6, 'processCommand', 'ArrayOfValues(0)= "Inner Air, Face#5"');
invoke(MN6, 'processCommand', 'ArrayOfValues(1)= "Inner Air, Face#6"');
invoke(MN6, 'processCommand', 'Call getDocument().createBoundaryCondition(
    ArrayOfValues, "BoundaryCondition#1")');
invoke(MN6, 'processCommand', 'Call getDocument().setMagneticFluxTangential("
    BoundaryCondition#1")');
invoke(MN6, 'processCommand', 'Call getDocument().endUndoGroup()');

% Selects rotor components and creates Motion Component for Rotor
invoke(MN6, 'processCommand', 'Call getDocument().getView().selectObject("North
    ", infoSetSelection)');
```

```
invoke(MN6, 'processCommand', 'Call getDocument().getView().selectObject("South
    ",infoAddToSelection)');
invoke(MN6, 'processCommand', 'Call getDocument().getView().selectObject("Copy
    of North #1",infoAddToSelection)');
invoke(MN6, 'processCommand', 'Call getDocument().getView().selectObject("Copy
    of South #1",infoAddToSelection)');
invoke(MN6, 'processCommand', 'Call getDocument().getView().selectObject("Copy
    of North #2",infoAddToSelection)');
invoke(MN6, 'processCommand', 'Call getDocument().getView().selectObject("Copy
    of South #2",infoAddToSelection)');
invoke(MN6, 'processCommand', 'Call getDocument().getView().selectObject("Copy
    of North #3",infoAddToSelection)');
invoke(MN6, 'processCommand', 'Call getDocument().getView().selectObject("Copy
    of South #3",infoAddToSelection)');
invoke(MN6, 'processCommand', 'Call getDocument().getView().selectObject("Copy
    of North #4",infoAddToSelection)');
invoke(MN6, 'processCommand', 'Call getDocument().getView().selectObject("Copy
    of South #4",infoAddToSelection)');
invoke(MN6, 'processCommand', 'Call getDocument().getView().selectObject("Copy
    of North #5",infoAddToSelection)');
invoke(MN6, 'processCommand', 'Call getDocument().getView().selectObject("Copy
    of South #5",infoAddToSelection)');
invoke(MN6, 'processCommand', 'Call getDocument().getView().selectObject("Copy
    of North #6",infoAddToSelection)');
invoke(MN6, 'processCommand', 'Call getDocument().getView().selectObject("Copy
    of South #6",infoAddToSelection)');
invoke(MN6, 'processCommand', 'Call getDocument().getView().selectObject("Copy
    of North #7",infoAddToSelection)');
invoke(MN6, 'processCommand', 'Call getDocument().getView().selectObject("Copy
    of South #7",infoAddToSelection)');
invoke(MN6, 'processCommand', 'Call getDocument().getView().selectObject("Copy
    of North #8",infoAddToSelection)');
invoke(MN6, 'processCommand', 'Call getDocument().getView().selectObject("Copy
    of South #8",infoAddToSelection)');
invoke(MN6, 'processCommand', 'Call getDocument().getView().selectObject("Copy
    of North #9",infoAddToSelection)');
invoke(MN6, 'processCommand', 'Call getDocument().getView().selectObject("Copy
    of South #9",infoAddToSelection)');
invoke(MN6, 'processCommand', 'Call getDocument().getView().selectObject("Rotor
    Lam",infoAddToSelection)');
invoke(MN6, 'processCommand', 'Call getDocument().getView().selectObject("Airgap
    1",infoAddToSelection)');
invoke(MN6, 'processCommand', 'Call getDocument().getView().selectObject("Airgap
    2",infoAddToSelection)');
invoke(MN6, 'processCommand', 'REDIM ArrayOfValues(22)');
invoke(MN6, 'processCommand', 'ArrayOfValues(0)= "North"');
invoke(MN6, 'processCommand', 'ArrayOfValues(1)= "South"');
invoke(MN6, 'processCommand', 'ArrayOfValues(2)= "Copy of North #1"');
invoke(MN6, 'processCommand', 'ArrayOfValues(3)= "Copy of South #1"');
invoke(MN6, 'processCommand', 'ArrayOfValues(4)= "Copy of North #2"');
invoke(MN6, 'processCommand', 'ArrayOfValues(5)= "Copy of South #2"');
invoke(MN6, 'processCommand', 'ArrayOfValues(6)= "Copy of North #3"');
invoke(MN6, 'processCommand', 'ArrayOfValues(7)= "Copy of South #3"');
invoke(MN6, 'processCommand', 'ArrayOfValues(8)= "Copy of North #4"');
invoke(MN6, 'processCommand', 'ArrayOfValues(9)= "Copy of South #4"');
invoke(MN6, 'processCommand', 'ArrayOfValues(10)= "Copy of North #5"');
invoke(MN6, 'processCommand', 'ArrayOfValues(11)= "Copy of South #5"');
```

```
invoke(MN6, 'processCommand', 'ArrayOfValues(12)=" Copy of North #6" ');
invoke(MN6, 'processCommand', 'ArrayOfValues(13)=" Copy of South #6" ');
invoke(MN6, 'processCommand', 'ArrayOfValues(14)=" Copy of North #7" ');
invoke(MN6, 'processCommand', 'ArrayOfValues(15)=" Copy of South #7" ');
invoke(MN6, 'processCommand', 'ArrayOfValues(16)=" Copy of North #8" ');
invoke(MN6, 'processCommand', 'ArrayOfValues(17)=" Copy of South #8" ');
invoke(MN6, 'processCommand', 'ArrayOfValues(18)=" Copy of North #9" ');
invoke(MN6, 'processCommand', 'ArrayOfValues(19)=" Copy of South #9" ');
invoke(MN6, 'processCommand', 'ArrayOfValues(20)=" Rotor Lam" ');
invoke(MN6, 'processCommand', 'ArrayOfValues(21)=" Airgap 1" ');
invoke(MN6, 'processCommand', 'ArrayOfValues(22)=" Airgap 2" ');
invoke(MN6, 'processCommand', 'Call getDocument().makeMotionComponent(
    ArrayOfValues)');
invoke(MN6, 'processCommand', 'Call getDocument().setMotionSourceType("Motion
    #1", infoVelocityDriven)');
invoke(MN6, 'processCommand', 'Call getDocument().beginUndoGroup("Set Motion
    Component", true)');
invoke(MN6, 'processCommand', 'Call getDocument().setMotionSpeedAtStartup("
    Motion#1", 0)');
invoke(MN6, 'processCommand', 'REDIM ArrayOfValues1(1)');
invoke(MN6, 'processCommand', 'ArrayOfValues1(0)= 0');
invoke(MN6, 'processCommand', 'ArrayOfValues1(1)= 5');
invoke(MN6, 'processCommand', 'REDIM ArrayOfValues2(1)');
invoke(MN6, 'processCommand', 'ArrayOfValues2(0)= 18000');
invoke(MN6, 'processCommand', 'ArrayOfValues2(1)= 18000');
invoke(MN6, 'processCommand', 'Call getDocument().setMotionSpeedVsTime("Motion
    #1", ArrayOfValues1, ArrayOfValues2)');
invoke(MN6, 'processCommand', 'Call getDocument().setMotionRotaryCenter("Motion
    #1", Array(0, 0, 0))');
invoke(MN6, 'processCommand', 'Call getDocument().setMotionRotaryAxis("Motion
    #1", Array(0, 0, 1))');
invoke(MN6, 'processCommand', 'Call getDocument().renameObject("Motion#1", "
    Moving Rotor")');
invoke(MN6, 'processCommand', 'Call getDocument().endUndoGroup()');

MakeWindings          % Subscript that creates windings from coil components
Calculate_SlotArea    % Subscript that calculates the slot cross-sectional area

% Defines coil properties using Zq & wire gauge using Pf with Zq & SlotArea
invoke(MN6, 'processCommand', 'Call getDocument().getView().selectObject("Coil
    #1", infoSetSelection)');
invoke(MN6, 'processCommand', 'Call getDocument().beginUndoGroup("Set Coil#1
    Properties", true)');
invoke(MN6, 'processCommand', 'Call getDocument().setCoilNumberOfTurns("Coil#1",
    Zq)');
invoke(MN6, 'processCommand', 'Call getDocument().setParameter("Coil#1", "
    StrandArea", StrandArea, infoNumberParameter)');
invoke(MN6, 'processCommand', 'Call getDocument().renameObject("Coil#1", "Coil A
    ")');
invoke(MN6, 'processCommand', 'Call getDocument().endUndoGroup()');
% """ Repeated for Coil B and Coil C """ %

SetCircuit_Ldq        % Subscript that creates the supply circuit
Thermal_RatedLoad     % Subscript of equivalent thermal model for rated load
```

A.6 Machine Subscripts

A.6.1 Toothlines

```
% Uses design points to draw each individual stator tooth
D1x = cos((SS/2)*Rad)*(SOR+1);
D1y = sin((SS/2)*Rad)*(SOR+1);
E1x = cos((SS/2)*Rad)*(SIR);
E1y = sin((SS/2)*Rad)*(SIR);
% Imports design points into MagNet
invoke(MN6, 'processCommand', ['Call setvariant(1,',num2str(D1x),')']);
invoke(MN6, 'processCommand', 'D1x = getVariant(1)');
invoke(MN6, 'processCommand', ['Call setvariant(1,',num2str(D1y),')']);
invoke(MN6, 'processCommand', 'D1y = getVariant(1)');
invoke(MN6, 'processCommand', ['Call setvariant(1,',num2str(E1x),')']);
invoke(MN6, 'processCommand', 'E1x = getVariant(1)');
invoke(MN6, 'processCommand', ['Call setvariant(1,',num2str(E1y),')']);
invoke(MN6, 'processCommand', 'E1y = getVariant(1)');
% Uses design points to draw line that segments stator teeth
invoke(MN6, 'processCommand','Call getDocument().getView().newLine(E1x, E1y, D1x
    , D1y)');
% """ Repeated to define all stator teeth """ %
```

A.6.2 MakeStatorComponents

```
% Uses DPs and Toothlines to create stator components
SelectToothx = cos((1*SS)*Rad)*((SIR+SOR)/2);
SelectToothy = sin((1*SS)*Rad)*((SIR+SOR)/2);
SelectCoilRx = cos(((SS*1)+((SS)/3))*Rad)*((SIR+SOR)/2);
SelectCoilRy = sin(((SS*1)+((SS)/3))*Rad)*((SIR+SOR)/2);
SelectCoilLx = cos(((SS*1)+((-SS)/3))*Rad)*((SIR+SOR)/2);
SelectCoilLy = sin(((SS*1)+((-SS)/3))*Rad)*((SIR+SOR)/2);

% Imports variants into MagNet
invoke(MN6, 'processCommand', ['Call setvariant(1,',num2str(SelectToothx),')']);
invoke(MN6, 'processCommand', ['Call setvariant(2,',num2str(SelectToothy),')']);
invoke(MN6, 'processCommand', ['Call setvariant(3,',num2str(SelectCoilRx),')']);
invoke(MN6, 'processCommand', ['Call setvariant(4,',num2str(SelectCoilRy),')']);
invoke(MN6, 'processCommand', ['Call setvariant(5,',num2str(SelectCoilLx),')']);
invoke(MN6, 'processCommand', ['Call setvariant(6,',num2str(SelectCoilLy),')']);
invoke(MN6, 'processCommand', 'SelectToothx = getVariant(1)');
invoke(MN6, 'processCommand', 'SelectToothy = getVariant(2)');
invoke(MN6, 'processCommand', 'SelectCoilRx = getVariant(3)');
invoke(MN6, 'processCommand', 'SelectCoilRy = getVariant(4)');
invoke(MN6, 'processCommand', 'SelectCoilLx = getVariant(5)');
invoke(MN6, 'processCommand', 'SelectCoilLy = getVariant(6)');

% Make Stator Components
% Tooth Component
invoke(MN6, 'processCommand','Call getDocument().getView().selectAt(SelectToothx
    , SelectToothy, infoSetSelection, Array(infoSliceSurface))');
invoke(MN6, 'processCommand','REDIM ArrayOfValues(0)');
invoke(MN6, 'processCommand','ArrayOfValues(0)= "Tooth 2"');
invoke(MN6, 'processCommand','Call getDocument().getView().makeComponentInALine(
    Lstack, ArrayOfValues, "Name=M330-50A", infoMakeComponentUnionSurfaces Or
```

```
    infoMakeComponentRemoveVertices)');
% Coil R Component
invoke(MN6, 'processCommand', 'Call getDocument().getView().selectAt(SelectCoilRx
    , SelectCoilRy , infoSetSelection , Array(infoSliceSurface))');
invoke(MN6, 'processCommand', 'REDIM ArrayOfValues(0)');
invoke(MN6, 'processCommand', 'ArrayOfValues(0)= "Coil R 2"');
invoke(MN6, 'processCommand', 'Call getDocument().getView().makeComponentInALine(
    Lstack , ArrayOfValues , "Name=Copper: 100% IACS" ,
    infoMakeComponentUnionSurfaces Or infoMakeComponentRemoveVertices)');
% Coil L Component
invoke(MN6, 'processCommand', 'Call getDocument().getView().selectAt(SelectCoilLx
    , SelectCoilLy , infoSetSelection , Array(infoSliceSurface))');
invoke(MN6, 'processCommand', 'REDIM ArrayOfValues(0)');
invoke(MN6, 'processCommand', 'ArrayOfValues(0)= "Coil L 2"');
invoke(MN6, 'processCommand', 'Call getDocument().getView().makeComponentInALine(
    Lstack , ArrayOfValues , "Name=Copper: 100% IACS" ,
    infoMakeComponentUnionSurfaces Or infoMakeComponentRemoveVertices)');
% """ Repeated for all remaining tooth and coil components """ %
```

A.6.3 ExtractStatorEdges

```
% Selects and extracts edge of stator components for 12s10p scripts
invoke(MN6, 'processCommand', 'Call getDocument().getView().selectObject("Tooth
    1", infoSetSelection)');
invoke(MN6, 'processCommand', 'REDIM ArrayOfValues(0)');
invoke(MN6, 'processCommand', 'ArrayOfValues(0)= "Tooth 1"');
invoke(MN6, 'processCommand', 'Call getDocument().getView().extractEdges(
    ArrayOfValues)');

invoke(MN6, 'processCommand', 'Call getDocument().getView().selectObject("Coil R
    1", infoSetSelection)');
invoke(MN6, 'processCommand', 'REDIM ArrayOfValues(0)');
invoke(MN6, 'processCommand', 'ArrayOfValues(0)= "Coil R 1"');
invoke(MN6, 'processCommand', 'Call getDocument().getView().extractEdges(
    ArrayOfValues)');

invoke(MN6, 'processCommand', 'Call getDocument().getView().selectObject("Coil L
    1", infoSetSelection)');
invoke(MN6, 'processCommand', 'REDIM ArrayOfValues(0)');
invoke(MN6, 'processCommand', 'ArrayOfValues(0)= "Coil L 1"');
invoke(MN6, 'processCommand', 'Call getDocument().getView().extractEdges(
    ArrayOfValues)');
% """ Repeated for all teeth and coil components """ %
```

A.6.4 ExtractMagnetEdges

```
% Selects the magnet components and extracts them
invoke(MN6, 'processCommand', 'Call getDocument().getView().selectObject("North
    ", infoSetSelection)');
invoke(MN6, 'processCommand', 'REDIM ArrayOfValues(0)');
invoke(MN6, 'processCommand', 'ArrayOfValues(0)= "North"');
invoke(MN6, 'processCommand', 'Call getDocument().getView().extractEdges(
    ArrayOfValues)');

invoke(MN6, 'processCommand', 'Call getDocument().getView().selectObject("South
    ", infoSetSelection)');
```

```
invoke(MN6, 'processCommand', 'REDIM ArrayOfValues(0)');
invoke(MN6, 'processCommand', 'ArrayOfValues(0)= "South"');
invoke(MN6, 'processCommand', 'Call getDocument().getView().extractEdges(
    ArrayOfValues)');
% """ Repeated for all rotor poles """ %
```

A.6.5 MakeWindings

```
% Phase A
invoke(MN6, 'processCommand', 'REDIM ArrayOfValues(15)');
invoke(MN6, 'processCommand', 'ArrayOfValues(0)= "Coil L 1"');
invoke(MN6, 'processCommand', 'ArrayOfValues(1)= "Coil R 1"');
invoke(MN6, 'processCommand', 'ArrayOfValues(2)= "Coil R 2"');
invoke(MN6, 'processCommand', 'ArrayOfValues(3)= "Coil L 2"');
invoke(MN6, 'processCommand', 'ArrayOfValues(4)= "Coil R 7"');
invoke(MN6, 'processCommand', 'ArrayOfValues(5)= "Coil L 7"');
invoke(MN6, 'processCommand', 'ArrayOfValues(6)= "Coil L 8"');
invoke(MN6, 'processCommand', 'ArrayOfValues(7)= "Coil R 8"');
invoke(MN6, 'processCommand', 'ArrayOfValues(8)= "Coil L 13"');
invoke(MN6, 'processCommand', 'ArrayOfValues(9)= "Coil R 13"');
invoke(MN6, 'processCommand', 'ArrayOfValues(10)= "Coil R 14"');
invoke(MN6, 'processCommand', 'ArrayOfValues(11)= "Coil L 14"');
invoke(MN6, 'processCommand', 'ArrayOfValues(12)= "Coil R 19"');
invoke(MN6, 'processCommand', 'ArrayOfValues(13)= "Coil L 19"');
invoke(MN6, 'processCommand', 'ArrayOfValues(14)= "Coil L 20"');
invoke(MN6, 'processCommand', 'ArrayOfValues(15)= "Coil R 20"');
invoke(MN6, 'processCommand', 'Call getDocument().makeSimpleCoil(1,
    ArrayOfValues)');
% Phase B
invoke(MN6, 'processCommand', 'REDIM ArrayOfValues(15)');
invoke(MN6, 'processCommand', 'ArrayOfValues(0)= "Coil R 3"');
invoke(MN6, 'processCommand', 'ArrayOfValues(1)= "Coil L 3"');
invoke(MN6, 'processCommand', 'ArrayOfValues(2)= "Coil L 4"');
invoke(MN6, 'processCommand', 'ArrayOfValues(3)= "Coil R 4"');
invoke(MN6, 'processCommand', 'ArrayOfValues(4)= "Coil L 9"');
invoke(MN6, 'processCommand', 'ArrayOfValues(5)= "Coil R 9"');
invoke(MN6, 'processCommand', 'ArrayOfValues(6)= "Coil R 10"');
invoke(MN6, 'processCommand', 'ArrayOfValues(7)= "Coil L 10"');
invoke(MN6, 'processCommand', 'ArrayOfValues(8)= "Coil R 15"');
invoke(MN6, 'processCommand', 'ArrayOfValues(9)= "Coil L 15"');
invoke(MN6, 'processCommand', 'ArrayOfValues(10)= "Coil L 16"');
invoke(MN6, 'processCommand', 'ArrayOfValues(11)= "Coil R 16"');
invoke(MN6, 'processCommand', 'ArrayOfValues(12)= "Coil L 21"');
invoke(MN6, 'processCommand', 'ArrayOfValues(13)= "Coil R 21"');
invoke(MN6, 'processCommand', 'ArrayOfValues(14)= "Coil R 22"');
invoke(MN6, 'processCommand', 'ArrayOfValues(15)= "Coil L 22"');
invoke(MN6, 'processCommand', 'Call getDocument().makeSimpleCoil(1,
    ArrayOfValues)');
% Phase C
invoke(MN6, 'processCommand', 'REDIM ArrayOfValues(15)');
invoke(MN6, 'processCommand', 'ArrayOfValues(0)= "Coil L 5"');
invoke(MN6, 'processCommand', 'ArrayOfValues(1)= "Coil R 5"');
invoke(MN6, 'processCommand', 'ArrayOfValues(2)= "Coil R 6"');
invoke(MN6, 'processCommand', 'ArrayOfValues(3)= "Coil L 6"');
invoke(MN6, 'processCommand', 'ArrayOfValues(4)= "Coil R 11"');
invoke(MN6, 'processCommand', 'ArrayOfValues(5)= "Coil L 11"');
```

```
invoke(MN6, 'processCommand', 'ArrayOfValues(6)=" Coil L 12" ');
invoke(MN6, 'processCommand', 'ArrayOfValues(7)=" Coil R 12" ');
invoke(MN6, 'processCommand', 'ArrayOfValues(8)=" Coil L 17" ');
invoke(MN6, 'processCommand', 'ArrayOfValues(9)=" Coil R 17" ');
invoke(MN6, 'processCommand', 'ArrayOfValues(10)=" Coil R 18" ');
invoke(MN6, 'processCommand', 'ArrayOfValues(11)=" Coil L 18" ');
invoke(MN6, 'processCommand', 'ArrayOfValues(12)=" Coil R 23" ');
invoke(MN6, 'processCommand', 'ArrayOfValues(13)=" Coil L 23" ');
invoke(MN6, 'processCommand', 'ArrayOfValues(14)=" Coil L 24" ');
invoke(MN6, 'processCommand', 'ArrayOfValues(15)=" Coil R 24" ');
invoke(MN6, 'processCommand', 'Call getDocument().makeSimpleCoil(1,
    ArrayOfValues)');
```

A.6.6 CalculateSlotArea

```
% Calculates the stator slot area based on current design points
% Divides half of the slot area into 7 simple sectors
% Then doubles result to find total slot area
A1 = ((Gx-Ex)*(Ey-Gy))/2;
A2 = (Ax-Gx)*(Ey-Gy);
A3 = ((Ax-Gx)*(Gy-Ay))/2;
A4 = ((Cx-Ex)*(Cy-Ey))/2;
A5 = (Cx-Ax)*(Ey-Ay);
A6 = ((Bx-Cx)*(Cy-By))/2;
Alpha = (SS*0.5*Rad)-(atan(By/Bx));
Chyp = sqrt((Cx^2)+(Cy^2));
Arc = ((Alpha)*(Chyp^2)*0.5);
Tri = (((sin(Alpha/2))*Chyp)*((cos(Alpha/2))*Chyp));
A7 = ((Alpha)*(Chyp^2)*0.5)-(((sin(Alpha/2))*Chyp)*((cos(Alpha/2))*Chyp));
SlotArea = 2*(A1+A2+A3+A4+A5+A6+A7);

% Strand cross sectional area based on packing factor (Pf) in slot area,
    converted to m^2
StrandArea = (SlotArea*Pf*1e-6)/(2*Zq);

% Imports values into MagNet
invoke(MN6, 'processCommand', ['Call setvariant(1,',num2str(StrandArea),')']);
invoke(MN6, 'processCommand', 'StrandArea = getVariant(1)');
```

A.6.7 SetCircuitLdq

```
% Generates circuit for calculating Ldq with multiple current sources
% Insert Coils and Current Sources into Circuit
invoke(MN6, 'processCommand', 'Call getDocument().newCircuitWindow()');
invoke(MN6, 'processCommand', 'Call getDocument().getCircuit().insertCoil("Coil
    A", 200, 120)');
invoke(MN6, 'processCommand', 'Call getDocument().getCircuit().
    insertCurrentSource(100, 120)');
invoke(MN6, 'processCommand', 'Call getDocument().getCircuit().
    insertCurrentSource(100, 210)');
invoke(MN6, 'processCommand', 'Call getDocument().getCircuit().
    insertCurrentSource(100, 300)');
invoke(MN6, 'processCommand', 'Call getDocument().getCircuit().
    insertCurrentSource(100, 390)');
invoke(MN6, 'processCommand', 'Call getDocument().getCircuit().insertGround(700,
    160)');
```

```
% Rename Current Sources
invoke(MN6, 'processCommand', 'Call getDocument().renameObject("I1", "Ia_q")');
invoke(MN6, 'processCommand', 'Call getDocument().renameObject("I4", "Ia_deltaq")
    ');
invoke(MN6, 'processCommand', 'Call getDocument().renameObject("I7", "Ia_d")');
invoke(MN6, 'processCommand', 'Call getDocument().renameObject("I10", "Ia_deltad
    ")');

% Connect Source T2 to Coil T1
invoke(MN6, 'processCommand', 'Call getDocument().getCircuit().
    getPositionOfTerminal("Ia_q,T2", TX1, TY1)');
invoke(MN6, 'processCommand', 'Call getDocument().getCircuit().
    getPositionOfTerminal("Coil A,T1", TX2, TY2)');
invoke(MN6, 'processCommand', 'REDIM XArrayOfValues(1)');
invoke(MN6, 'processCommand', 'XArrayOfValues(0)= TX1');
invoke(MN6, 'processCommand', 'XArrayOfValues(1)= TX2');
invoke(MN6, 'processCommand', 'REDIM YArrayOfValues(1)');
invoke(MN6, 'processCommand', 'YArrayOfValues(0)= TY1');
invoke(MN6, 'processCommand', 'YArrayOfValues(1)= TY2');
invoke(MN6, 'processCommand', 'Call getDocument().getCircuit().insertConnection(
    XArrayOfValues, YArrayOfValues)');
% Connect Coil T2 to Source T1
invoke(MN6, 'processCommand', 'Call getDocument().getCircuit().
    getPositionOfTerminal("Coil A,T2", TX1, TY1)');
invoke(MN6, 'processCommand', 'Call getDocument().getCircuit().
    getPositionOfTerminal("Ia_q,T1", TX2, TY2)');
invoke(MN6, 'processCommand', 'REDIM XArrayOfValues(3)');
invoke(MN6, 'processCommand', 'XArrayOfValues(0)= TX1');
invoke(MN6, 'processCommand', 'XArrayOfValues(1)= 245');
invoke(MN6, 'processCommand', 'XArrayOfValues(2)= 100');
invoke(MN6, 'processCommand', 'XArrayOfValues(3)= TX2');
invoke(MN6, 'processCommand', 'REDIM YArrayOfValues(3)');
invoke(MN6, 'processCommand', 'YArrayOfValues(0)= TY1');
invoke(MN6, 'processCommand', 'YArrayOfValues(1)= 60');
invoke(MN6, 'processCommand', 'YArrayOfValues(2)= 60');
invoke(MN6, 'processCommand', 'YArrayOfValues(3)= TY2');
invoke(MN6, 'processCommand', 'Call getDocument().getCircuit().insertConnection(
    XArrayOfValues, YArrayOfValues)');
% Connect Coil T2 to Ground
invoke(MN6, 'processCommand', 'Call getDocument().getCircuit().
    getPositionOfTerminal("Coil A,T2", TX1, TY1)');
invoke(MN6, 'processCommand', 'Call getDocument().getCircuit().
    getPositionOfTerminal("G1,T1", TX2, TY2)');
invoke(MN6, 'processCommand', 'REDIM XArrayOfValues(2)');
invoke(MN6, 'processCommand', 'XArrayOfValues(0)= TX1');
invoke(MN6, 'processCommand', 'XArrayOfValues(1)= 245');
invoke(MN6, 'processCommand', 'XArrayOfValues(2)= TX2');
invoke(MN6, 'processCommand', 'REDIM YArrayOfValues(2)');
invoke(MN6, 'processCommand', 'YArrayOfValues(0)= TY1');
invoke(MN6, 'processCommand', 'YArrayOfValues(1)= 160');
invoke(MN6, 'processCommand', 'YArrayOfValues(2)= TY2');
invoke(MN6, 'processCommand', 'Call getDocument().getCircuit().insertConnection(
    XArrayOfValues, YArrayOfValues)');

% Connect Sources for Coil A
invoke(MN6, 'processCommand', 'Call getDocument().getCircuit().
    getPositionOfTerminal("Ia_q,T1", TX1, TY1)');
```

```
invoke(MN6, 'processCommand','Call␣getDocument().getCircuit().
    getPositionOfTerminal("Ia_deltaq,T1",␣TX2,␣TY2)');
invoke(MN6, 'processCommand','REDIM␣XArrayOfValues(1)');
invoke(MN6, 'processCommand','XArrayOfValues(0)=␣TX1');
invoke(MN6, 'processCommand','XArrayOfValues(1)=␣TX2');
invoke(MN6, 'processCommand','REDIM␣YArrayOfValues(1)');
invoke(MN6, 'processCommand','YArrayOfValues(0)=␣TY1');
invoke(MN6, 'processCommand','YArrayOfValues(1)=␣TY2');
invoke(MN6, 'processCommand','Call␣getDocument().getCircuit().insertConnection(
    XArrayOfValues,␣YArrayOfValues)');
invoke(MN6, 'processCommand','Call␣getDocument().getCircuit().
    getPositionOfTerminal("Ia_deltaq,T1",␣TX1,␣TY1)');
invoke(MN6, 'processCommand','Call␣getDocument().getCircuit().
    getPositionOfTerminal("Ia_d,T1",␣TX2,␣TY2)');
invoke(MN6, 'processCommand','REDIM␣XArrayOfValues(1)');
invoke(MN6, 'processCommand','XArrayOfValues(0)=␣TX1');
invoke(MN6, 'processCommand','XArrayOfValues(1)=␣TX2');
invoke(MN6, 'processCommand','REDIM␣YArrayOfValues(1)');
invoke(MN6, 'processCommand','YArrayOfValues(0)=␣TY1');
invoke(MN6, 'processCommand','YArrayOfValues(1)=␣TY2');
invoke(MN6, 'processCommand','Call␣getDocument().getCircuit().insertConnection(
    XArrayOfValues,␣YArrayOfValues)');
invoke(MN6, 'processCommand','Call␣getDocument().getCircuit().
    getPositionOfTerminal("Ia_d,T1",␣TX1,␣TY1)');
invoke(MN6, 'processCommand','Call␣getDocument().getCircuit().
    getPositionOfTerminal("Ia_deltad,T1",␣TX2,␣TY2)');
invoke(MN6, 'processCommand','REDIM␣XArrayOfValues(1)');
invoke(MN6, 'processCommand','XArrayOfValues(0)=␣TX1');
invoke(MN6, 'processCommand','XArrayOfValues(1)=␣TX2');
invoke(MN6, 'processCommand','REDIM␣YArrayOfValues(1)');
invoke(MN6, 'processCommand','YArrayOfValues(0)=␣TY1');
invoke(MN6, 'processCommand','YArrayOfValues(1)=␣TY2');
invoke(MN6, 'processCommand','Call␣getDocument().getCircuit().insertConnection(
    XArrayOfValues,␣YArrayOfValues)');
invoke(MN6, 'processCommand','Call␣getDocument().getCircuit().
    getPositionOfTerminal("Ia_q,T2",␣TX1,␣TY1)');
invoke(MN6, 'processCommand','Call␣getDocument().getCircuit().
    getPositionOfTerminal("Ia_deltaq,T2",␣TX2,␣TY2)');
invoke(MN6, 'processCommand','REDIM␣XArrayOfValues(1)');
invoke(MN6, 'processCommand','XArrayOfValues(0)=␣TX1');
invoke(MN6, 'processCommand','XArrayOfValues(1)=␣TX2');
invoke(MN6, 'processCommand','REDIM␣YArrayOfValues(1)');
invoke(MN6, 'processCommand','YArrayOfValues(0)=␣TY1');
invoke(MN6, 'processCommand','YArrayOfValues(1)=␣TY2');
invoke(MN6, 'processCommand','Call␣getDocument().getCircuit().insertConnection(
    XArrayOfValues,␣YArrayOfValues)');
invoke(MN6, 'processCommand','Call␣getDocument().getCircuit().
    getPositionOfTerminal("Ia_deltaq,T2",␣TX1,␣TY1)');
invoke(MN6, 'processCommand','Call␣getDocument().getCircuit().
    getPositionOfTerminal("Ia_d,T2",␣TX2,␣TY2)');
invoke(MN6, 'processCommand','REDIM␣XArrayOfValues(1)');
invoke(MN6, 'processCommand','XArrayOfValues(0)=␣TX1');
invoke(MN6, 'processCommand','XArrayOfValues(1)=␣TX2');
invoke(MN6, 'processCommand','REDIM␣YArrayOfValues(1)');
invoke(MN6, 'processCommand','YArrayOfValues(0)=␣TY1');
invoke(MN6, 'processCommand','YArrayOfValues(1)=␣TY2');
```

```
invoke(MN6, 'processCommand','Call getDocument().getCircuit().insertConnection(
    XArrayOfValues, YArrayOfValues)');
invoke(MN6, 'processCommand','Call getDocument().getCircuit().
    getPositionOfTerminal("Ia_d,T2", TX1, TY1)');
invoke(MN6, 'processCommand','Call getDocument().getCircuit().
    getPositionOfTerminal("Ia_deltad,T2", TX2, TY2)');
invoke(MN6, 'processCommand','REDIM XArrayOfValues(1)');
invoke(MN6, 'processCommand','XArrayOfValues(0)= TX1');
invoke(MN6, 'processCommand','XArrayOfValues(1)= TX2');
invoke(MN6, 'processCommand','REDIM YArrayOfValues(1)');
invoke(MN6, 'processCommand','YArrayOfValues(0)= TY1');
invoke(MN6, 'processCommand','YArrayOfValues(1)= TY2');
invoke(MN6, 'processCommand','Call getDocument().getCircuit().insertConnection(
    XArrayOfValues, YArrayOfValues)');
% """ Repeated for Phase B and Phase C """ %
```

A.6.8 ThermalRatedLoad

```
T6 = 0;
I_Peak = 0.01;
I_inc = 0.01;

while T6 < 40
% MAKE SURE ALL MEASUREMENTS ARE CONVERTED INTO M AND NOT MM!!!
% Conversions
r_so = SOR*1e-3;                % Radius of outer stator converted to m
r_bi = (SOR-BI)*1e-3;           % Radius of back iron converted to m
r_tt = (SIR+TT)*1e-3;           % Radius of tooth tip converted to m
r_outer = r_bi-((r_bi-r_tt)/3); % Radial distance to outer slot node in m
r_inner = r_tt+((r_bi-r_tt)/3); % Radial distance to inner slot node in m
r_si = SIR*1e-3;                % Radius of inner stator converted to m
r_housing = r_so+(HT*1e-3);     % Radial distance to external of housing in m
l_st = Lstack*1e-3;             % Stack length converted to m
A_Slot = (SlotArea*1e-6)/2;     % Area of the Slot inc. conversion to m^2
t_tw = TW*0.5*1e-3;             % Half the TW converted to m
t_tb = TB*1e-3;                 % TB converted to m
t_bi = BI*1e-3;                 % BI converted to m
t_housing = HT*1e-3;            % Aluminium housing thickness
t_liner = 0.001;                % Slot liner thickness
t_lam = 0.0005;                 % Thickness of Lamination
t_Fe_Al = 0.000035;             % Effective AG for iron to Al housing

%%% Thermal Conductivities & Coeffients %%%
k_air = 0.014;          % Thermal conductivity of air
k_water = 0.6;          % Thermal cond of water
k_liner = 0.11;         % Thermal cond of Nomex slot liner
k_housing = 209;        % Thermal cond for aluminum housing
k_slot = 2.94;          % Thermal cond for slots w insulation & Pf accounted
k_stator = 28;          % Thermal cond for stator iron with laminations (radial)
k_cu = 386;             % Thermal cond of copper winding
k_r = 0.2;              % Thermal cond of resin
k_Fe_Al = 760;          % Effective thermal cond between Al frame & stator
h_conv = 26.29;         % Heat transfer coefficient for conv

%%% Copper Losses %%%
k_w = (k_cu*k_r)/((Pf*k_r)+((1-Pf)*k_cu)); % Equiv Thermal Cond of Winding (k_w)
```

```
Alpha_cu = 0.39;                                % Temp coefficient of copper resistance
A_cu = A_Slot*Pf;                               % Copper area based on Pf
R_cu_20 = 1.7241e-008;                          % Resistivity of copper at 20C
R_cu_120 = R_cu_20*(1+(Alpha_cu*100));          % Resistivity of copper at 100C
W = (2*Pi*(r_si+(0.5*(r_so-r_si))))*(1/Ns);
l_av = l_st;
P_cu = ((I_Peak/sqrt(2))^2)*((R_cu_120/Pf)*(l_av/(A_cu)));

%%%  Iron Losses %%%
k_h = 0.00754619;           % Obtained from MagNet
k_e = 6.35506e-5;           % Obtained from MagNet
Alpha_Fe = 1.29512;         % Obtained from MagNet
Beta_Fe = 1.79621;          % Obtained from MagNet
f = freq_elec;              % Frequency of flux density waveform
B_m = 1.5;                  % Peak flux density
R_Fe = 4.2e-7;              % Resistivity of iron lamination
Rho_Fe = 7650;              % Density of iron
% Hysteresis Loss (W/kg)
P_h = k_h*f*(B_m^Alpha_Fe);
% Classical eddy current loss (W/kg)
P_ce = ((t_lam^2*Pi^2)/(6*R_Fe*Rho_Fe))*f^2*B_m^2;
% Excess eddy current loss (W/kg)
P_ee = 8.67*k_e*f^1.5*B_m^1.5;

% Tooth volume with approximation for bridge and converted into m^2
A_Tooth = (((SOR-SIR)*(TW/2))+((Gx-Fx)*(Gy-Ay))+((Ax-Gx)*(Gy-Ay)*0.5))*1e-6;
V_Tooth = A_Tooth*l_st;
% Back Iron volume with approximation for bridge and converted into m^2
A_BI = (((SS/2)/360)*Pi*(SOR^2)-((SS/2)/360)*Pi*((SOR-BI)^2))*1e-6;
V_BI = A_BI*l_st;

P_Tooth = (V_Tooth*Rho_Fe)*(P_h+P_ce+P_ee);     % Iron losses for tooth
P_BI = (V_BI*Rho_Fe)*(P_h+P_ce+P_ee);           % Iron losses for BI

%%% Thermal resistances for nodel circuit %%%
sector = (2*Pi*SS*l_st)/(2*360);  % Multiplier for half slot span sector
a_conv = r_housing*sector;        % Surface area of housing for conv cooling

% Rth for convection to water jacket
Rth_12_1 = 1/(h_conv*a_conv);
% Rth for conduction from housing to water jacket
Rth_12_2 = (t_housing/2)/(k_housing*((r_so+(t_housing*0.75))*sector));
% Series thermal resistance between nodes 1 and 2
Rth_12 = Rth_12_1+Rth_12_2;

% Rth for conduction from BI to housing
Rth_23_1 = (t_housing*0.5)/(k_housing*(sector*(r_so+(t_housing/4))));
% Rth for conduction across effective interface airgap between BI and housing
Rth_23_2 = t_Fe_Al/(k_Fe_Al*(sector*r_so));
% Rth for conduction from BI to housing
Rth_23_3 = (t_bi*0.5)/(k_stator*(sector*(r_so-(t_bi/4))));
% Series thermal resistance between nodes 2 and 3
Rth_23 = Rth_23_1+Rth_23_2+Rth_23_3;

% Rth for conduction through tooth to BI (3 to 4)
Rth_34 = ((((r_so-t_bi)-r_si)/3)+(t_bi*0.5))/(k_stator*t_tw*l_st);
```

```
% Calculation for the thermal thickness of slot between 4 and 6
t_upperslot = (((2*Pi*r_outer)/Ns)-t_tw)*0.5;
% Rth for conduction through tooth from 4 to node 6
Rth_46_1 = (t_tw*0.5)/(k_stator*((r_bi-r_tt)*0.5)*l_st);
% Contact resistance between slot and tooth
Rth_46_2 = t_liner/(k_liner*((r_bi-r_tt)*0.5)*l_st);
% Rth for conduction through slot from 6 to 4
Rth_46_3 = t_upperslot/(k_w*((r_bi-r_tt)*0.5)*l_st);
% Series thermal resistance between nodes 4 and 6
Rth_46 = Rth_46_1+Rth_46_2+Rth_46_3;

% Calculation for the thermal thickness of slot between 4 and 6
t_lowerslot = (((2*Pi*r_inner)/Ns)-t_tw)*0.5;
% Rth for conduction through tooth from 5 to node 7
Rth_57_1 = (t_tw*0.5)/(k_stator*((r_bi-r_si)*0.5)*l_st);
% Contact resistance between slot and tooth
Rth_57_2 = t_liner/(k_liner*((r_bi-r_tt)*0.5)*l_st);
% Rth for conduction through slot from 7 to 5
Rth_57_3 = t_lowerslot/(k_w*((r_bi-r_tt)*0.5)*l_st);
% Series thermal resistance between nodes 5 and 7
Rth_57 = Rth_57_1+Rth_57_2+Rth_57_3;

% Rth for conduction between 4 & 5
Rth_45 = ((r_bi-r_si)*0.5)/(k_stator*t_tw*l_st);
% Rth for conduction between 6 & 7
Rth_67 = ((r_bi-r_tt)*0.5)/(k_w*((r_bi-((r_bi-r_tt)*0.5))*sector));

%%% Conversion to conductivities %%%
G12 = 1/Rth_12;
% """ Repeated for all conductivity nodes """ %
G76 = 1/Rth_67;

G1 = G12;
G2 = G12+G23;
G3 = G23+G34;
G4 = G34+G45+G46;
G5 = G45+G57;
G6 = G46+G67;
G7 = G57+G67;

%%% Conductivity Matrix (A) %%%
A = [   G2   -G23  0     0     0     0;
        -G32 G3   -G34  0     0     0;
        0    -G43  G4    -G45  -G46  0;
        0    0     -G54  G5    0     -G57;
        0    0     -G64  0     G6    -G67;
        0    0     0     -G75  -G76  G7];
%%% Heat source matrix (B) %%%
B = [   0;
        P_BI;
        P_Tooth/2;
        P_Tooth/2;
        P_cu/2;
        P_cu/2];
%%% Resultant of temperature matrix (X) %%%
X = A\B;
```

```
T6 = X(5);
I_Peak = I_Peak + I_inc;
end
% After exiting the while loop I_Peak is calculated
RatedLoad_Peak = I_Peak-(2*I_inc);
```

Appendix B: Paper Publications

B.1 PEMD, March 2012

B.2 WEMDCD, March 2013